UNRAVELING THE COMPLEXITY OF GAS-PHASE LITHIUM-CATIONIZED CARBOHYDRATE CHEMISTRY AND STRUCTURES

Paul S. Soma

A dissertation submitted to the faculty at the University of North Carolina at Chapel Hill in partial fulfillment of the requirements for the degree of Doctor of Philosophy in the Department of Chemistry

Chapel Hill
2021

Approved by:

Gary L. Glish

Leslie M. Hicks

Brandie M. Ehrmann

Frank A. Leibfarth

Matthew R. Lockett

ABSTRACT

Paul S. Soma: Unraveling the Complexity of Gas-Phase Lithium-Cationized Carbohydrate Chemistry and Structures
(Under the direction of Gary L. Glish)

Complete structural elucidation of carbohydrate molecules remains a prominent challenge in analytical chemistry. Much of the structural intricacy of carbohydrates stems from the various isomeric monosaccharide subunits that are linked together. To date, there are few analytical techniques capable of differentiating monosaccharide isomers. Mass spectrometry-based technologies are promising for differentiation of monosaccharides because of their high selectivity and sensitivity, and short analysis times. Mass spectrometry analysis first requires generation of gas-phase ions from solution-phase molecules, which are then separated based on their mass-to-charge ratio (*m/z*). Monosaccharide isomers cannot be distinguished by mass spectrometry alone because they have identical *m/z*. Tandem-mass spectrometry (MS/MS) techniques rely on gas-phase chemistry to differentiate isomers and stereoisomers within the mass spectrometer. Two examples of gas-phase chemistries that are useful for isomer differentiation are unimolecular dissociation or an ion/molecule reaction. The MS/MS response, or gas-phase chemistry, of an ion will depend on ion structure and the charge carrier (H^+/Na^+/Li^+/etc.), which is affected by the mode of ionization.

Electrospray ionization (ESI) is commonly employed for ionization of carbohydrates. Because monosaccharides have a high metal cation affinity and because sodium is ubiquitous in solvents, ESI of a monosaccharide solution results in sodium-cationized monosaccharides.

Alternatively, lithium salts can be added into the ESI solution to generate lithium-cationized monosaccharides. Monosaccharide oxygen atoms form multidentate (bi-/tri-/tetradentate) coordinations with lithium, and multiple potential sites for cation coordination exist on a monosaccharide molecule.

To differentiate monosaccharide isomers, the ion distribution that each isomer forms must have measurable differences in gas-phase chemistry. The most common MS/MS technique is collision-induced dissociation (CID), but, in general, CID response is not disparate enough between lithium-cationized monosaccharide isomers for differentiation. Another MS/MS technique that has been able to differentiate isomeric monosaccharides is the water adduction ion/molecule reaction. Using a combination of computational data and experimental water adduction data the structures of solution- and gas-phase lithium-cationized monosaccharide ions were explored, and the chemistry and mechanism of the water adduction reaction was investigated. Finally, using CID and water adduction, the gas-phase dissociation chemistry and product ion structures of lithium cationized hexoses were shown to be more complex than previously postulated.

To my nephew, Rory.

Live passionately.

ACKNOWLEDGEMENTS

Mentorship has presented itself to me in many ways, within science and in other aspects of life. I have had many mentors in science over the years, beginning with my high school chemistry teacher, Mrs. Diksa, who invested a lot of her time. My college mentors in science, Dr. You and Dr. Starn, introduced me to mass spectrometry and encouraged me with the words, "never sell yourself short." I would not be writing this document without those few words of encouragement. Brandie and Gary, thank you for allowing me to learn at my own pace. You allowed me to work when I felt inspired, to produce science that I am proud of, and to maintain my passion for chemistry and mass spectrometry. I am grateful for the experience, and I will miss it, but I will continue to seek new mentorship, knowledge, and experiences.

The support of my family has meant more than a few words can express. Many times, over the past five (28, truly) years I have needed their guidance. My parents are the most selfless people I know. As much as they wish I were not living many states away, they still encourage me to pursue exciting opportunities. Wherever I end up, I will always remember that home is with my family. My grandfather was my first mentor in science. Slowly, but surely, throughout my childhood he introduced me to many aspects of science and guided me towards higher education. He prepared me for the frustrations of graduate school and always reminded me of the reward of success after persevering through failure.

To all the friends I have made along the way, you have made life exciting and full.

TABLE OF CONTENTS

LIST OF TABLES x

LIST OF FIGURES xi

LIST OF ABBREVIATIONS AND SYMBOLS xvi

CHAPTER 1: INTRODUCTION TO MASS SPECTROMETRY BASED STRUCTURAL ELUCIDATION OF CARBOHYDRATES 1

1.1 Carbohydrate Structure 1

1.2 Introduction to Carbohydrate Analysis 4

1.3 Water Adduction Ion/Molecule Reaction 6

1.4 Summary 8

CHAPTER 2: EXPERIMENTAL 11

2.1 Materials 11

2.2 Mass Spectrometry 11

2.3 Water Adduction Ion/Molecule Reaction 16

2.4 CID-Water Adduction 18

2.5 Kinetic Method 18

2.6 Hydrophilic Interaction Liquid Chromatography 19

2.7 Cyclic Ion Mobility-Time of Flight Mass Spectrometry 19

2.8 Theoretical Calculations 21

2.9 Nuclear Magnetic Resonance 22

CHAPTER 3: MECHANISTIC INSIGHTS TO THE WATER ADDUCTION ION/MOLECULE REACTION 24

3.1 Hexoses and Monodeoxy Glucoses 24

3.2 Water Adduction to Inositols.....45

3.3 Hexose Gas-Phase Lithium Cation Affinities Correlate to Unreacted Fraction.....58

3.4 Probing the Lithium-H_2O Bond Strengths of $[Hexose+Li+H_2O]^+$.....70

3.5 Summary.....81

CHAPTER 4: EFFECT OF INSTRUMENT PARAMETERS ON THE WATER ADDUCTION ION/MOLECULE REACTION.....83

4.1 Collisionally-Induced Ion Structural Changes in the Mass Spectrometer Ion Optics.....83

4.2 Water Adduction during Ion Accumulation in the Ion Trap.....90

4.3 Drive rf Voltage Amplitude during the Scan Delay.....96

4.4 Summary.....104

CHAPTER 5: PRE- AND POST-IONIZATION SEPARATION OF CARBOHYDRATE STRUCTURAL CONFORMATIONS.....105

5.1 Ion Mobility Spectrometry and Ion-Neutral Collision Cross Sections.....105

5.2 HILIC LC Separation and CID of Hexose Anomers.....108

5.3 Cyclic Ion Mobility of Lithium Cationized Hexoses.....111

5.4 cIM and HILIC LC of Reducing and Non-reducing Disaccharides.....116

5.5 Summary.....118

CHAPTER 6: UNVEILING THE ISOMERIC COMPLEXITY OF LITHIATED HEXOSE PRODUCT IONS.....120

6.1 Introduction to Dissociation Technologies for Gas-phase Carbohydrates.....120

6.2 Collision-Induced Dissociation of Unlabeled and ^{13}C-Labeled Hexose Epimers.....123

6.3 Water Adduction to Unlabeled Hexose Product Ions.....141

6.4 Water Adduction to Mass Resolved A and X Cross-ring Cleavages.....144

6.5 Summary.....150

CHAPTER 7: SUMMARY AND FUTURE DIRECTIONS.....152

7.1 General Summary.....152

7.2 CID-Water Adduction for *de novo* Carbohydrate Structure Elucidation 154

7.3 Anomerically-locked Methyl Pyranosides for Mechanistic Studies 163

7.4 Structural Differentiation of Glycolipids using CID and Water Adduction............... 166

REFERENCES 174

LIST OF TABLES

Table 3.1 Unreacted fractions reported with 1 standard deviation for all sugars studied ($n \geq 7$). 28

Table 3.2 Relative energies in kcal/mol for DFT solution- and gas-phase optimized structures of *scyllo*-inositol 47

Table 3.3 Relative energies in kcal/mol for DFT solution- and gas-phase optimized structures of *neo*-inositol......49

Table 3.4 Relative energies in kcal/mol for DFT solution- and gas-phase optimized structures of *chiro*-inositol 51

Table 3.5 Relative energies in kcal/mol for DFT solution- and gas-phase optimized structures of *cis*-inositol 53

Table 3.6 Relative energies in kcal/mol for DFT solution and gas phase optimized structures of *epi*-inositol......55

Table 3.7 Relative energies in kcal/mol for DFT solution and gas phase optimized structures of *myo*-inositol......57

Table 3.8 Comparison of beam-type CID and ion trap CID product ion yield (PIY) for $[\text{Hexose+Li+}^{13}\text{C}_6\text{-Glc}]^+$ dimer dissociation 69

Table 4.1 Estimated q_2 value and velocity of a $[\text{Glc+Li}]^+$ ion during the ion trap scan delay as a function of 'scan begin' value (m_1)......101

Table 5.2 Relative energies and Boltzmann abundances of lithium cationized β-methylglucoside structures......113

Table 6.1 CID of unlabeled hexose epimers. Yield of each ion type as a percentage of the initial parent ion population at the optimal hexose CID settings......126

Table 6.2 List of all hypothetically possible lithiated hexose cross-ring cleavages 132

Table 6.3 Measured R_U and ion yield for mass-resolved ^{0,2}A and ^{0,4}X ions, linear combination estimated R_U of the ion mixture, and the measured R_U for the unlabeled (UL) mixture. 145

LIST OF FIGURES

Figure 2.1 The ion trap scan function..15

Figure 2.2 Schematic of the electrospray ionization – ion trap mass spectrometry system used for CID and water adduction experiments. 18

Figure 2.3 A custom Waters Synapt G2-Si Q-cIM-ToF...20

Figure 3.1 a) The primary tridentate lithium coordination structure for β-glucose with oxygen and carbon number labels in blue and green text, respectively. b) C2 deoxygenation of epimers glucose and mannose results in the same molecule. c) An exhaustive list of monodeoxy glucopyranoses. 25

Figure 3.2 Water adduction reaction curves for the 5 monodeoxy glucoses studied................26

Figure 3.3 Gas-phase DFT optimized structures for lithiated α- and β-Glc..............................29

Figure 3.4 Gas-phase DFT optimized structures for the reactive bidentate structures of 1dGlc..31

Figure 3.5 Unreacted fraction for $[M+Li]^+$ as a function of capillary/skimmer cone voltage difference...33

Figure 3.6 Gas-phase DFT optimized structures for lithiated α- and β-6dGlc. 35

Figure 3.7 Relative energies of DFT calculated local minima, represented as dots, for α- and β-6dGlc in solution and *in vacuo*. 37

Figure 3.8 Gas phase DFT optimized structures for α- and β-Man...39

Figure 3.9 Gas-phase DFT optimized structures for α- and β-2dGlc.......................................40

Figure 3.10 Gas phase DFT optimized structures for α- and β-3dGlcglucose. 42

Figure 3.11 Gas phase DFT optimized structures for α- and β-allose......................................43

Figure 3.12 Gas phase DFT optimized structures for α- and β-4dGlc......................................45

Figure 3.13 Structures of six inositol isomers used in this study..46

Figure 3.14 Gas-phase DFT optimized structures for lithiated *scyllo*-inositol...........................48

Figure 3.15 a) Water adduction curves for six inositol isomers, their b) final R_U values and c) reaction rates....48

Figure 3.16 Gas-phase DFT optimized structures for lithiated *neo*-inositol. 50

Figure 3.17 Gas-phase DFT optimized structures for lithiated *chiro*-inositol. 51

Figure 3.18 Gas-phase DFT optimized structures for lithiated *cis*-inositol. 53

Figure 3.19 Gas-phase DFT optimized structures for lithiated *epi*-inositol. 56

Figure 3.20 Gas-phase DFT optimized structures for lithiated *myo*-inositol. 58

Figure 3.21 a) CID of a hypothetical lithium-bound heterodimer in which M_1, a monosaccharide, has a bidentate coordination and $^{13}C_6$-Glc has a monodentate coordination to the lithium cation. 62

Figure 3.22 Mass spectrum as a result of isolation and dissociation of the $[Glc+Li+^{13}C_6\text{-}Glc]^+$ heterodimer where each monosaccharide retains the lithium cation equally. 63

Figure 3.23 Energy-resolved CID of heterodimers formed between a) Glc and $^{13}C_6$-Glc, b) Tal and $^{13}C_2$-Tal, c) Tal and $^{13}C_6$-Glc, and d) Glc and $^{13}C_2$-Tal. 65

Figure 3.24 PIY versus R_U for 14 monosaccharides displaying a correlation between gas-phase lithium affinity and water adduction unreacted fraction. 66

Figure 3.25 R_U and PIY values for fourteen monosaccharides. 68

Figure 3.26 Energy-resolved CID of the $[Idose+Li+^{13}C_6\text{-}Glc]^+$ heterodimer using a) beam-type and b) ion trap CID....70

Figure 3.27 a) Electrostatic potential maps calculated via DFT for a hexose(1-6) and a hexose(4-5) structure. b) Li-H_2O bond length in Angstroms as a function of Li-monosaccharide coordination denticity. 71

Figure 3.28 Full scan mass spectrum of lithiated glucose at an ion trap accumulation time of (top) 100 ms and (bottom) 1000 ms. 74

Figure 3.29 (top) Reaction scheme for the dissociation of $[Hexose+Li+H_2O]^+$ to $[Hexose+Li]^+$, and back-reaction of $[Hexose+Li]^+$ to $[Hexose+Li+H_2O]^+$. (bottom) Energy-resolved CID of $[Glc+Li+H_2O]^+$ and $[Tal+Li+H_2O]^+$. 77

Figure 3.30 a,b) Relative abundances of *m/z* 187 and 205 for Tal and Glc at various isolation widths with and without 0 V fragmentation amplitude applied for a static activation time of 40 ms. c,d) Relative abundances of *m/z* 187 and 205 for Tal and Glc at increasing activation times with 0 V fragmentation amplitude applied, using a static 3 Da isolation width. 78

Figure 3.31 Correlation between SY205 values and water adduction characteristics for six hexoses 80

Figure 4.1 Schematic of the Bruker HCT system 84

Figure 4.2 a) R_U as a function of capillary/skimmer voltage difference for 9 monosaccharides. 88

Figure 4.3 (left) Glc diagnostic ion ratio measured in the full scan mass spectrum as a function of ion trap accumulation time. 93

Figure 4.4 Glc final R_U measured as a function of ion trap accumulation time. 94

Figure 4.5 a) Schematic of a quadrupole ion trap. b) Illustration of the drive rf voltage amplitude during important steps of the ion trap scan function for an MS experiment. 97

Figure 4.6 Scan begin value effect on V_{rf} during scan delay. 99

Figure 4.7 R_U values for Glc measured after 1000 ms scan delay at various 'scan begin' values. 100

Figure 4.8 Water adduction curves for $[C_2H_4O_2+Li]^+$ at various scan begin (m_1) values. 103

Figure 5.1 Increasing number of cIM passes improves feature resolution for $[Fructose+Li]^+$. 107

Figure 5.2 HILIC LC separation of hexose anomers. 109

Figure 5.3 Ion trap CID product ion spectra of HILIC-LC separated hexose anomers. 111

Figure 5.4 Individually measured ATDs after 5 passes in the cIM for the anomerically-locked methylglucosides. 112

Figure 5.5 ATDs after 11 passes in the cIM for the three lithiated hexoses studied. (inset) After 20 passes for Man a low abundance feature was resolved. 114

Figure 5.6 a) The distance between the O2 bound hydrogen and O1 is shorter for α-Glc than for β-Glc. b,c) Post-cIM dissociation spectra for mobility resolved species of Glc and Gal. 116

Figure 5.7 ATDs for 2 non-reducing and 6 reducing lithium cationized disaccharides. 117

Figure 5.8 HILIC chromatograms of 1 non-reducing and 2 reducing disaccharides. 118

Figure 6.1 a) Pyranose form of four epimeric hexoses and hexose carbon numbering. b) Hexose cross-ring cleavage notation and lithiated product ion mass-to-charge values with and without carbon-13 labels at the C1 and C2 positions (reducing end). 121

Figure 6.2 CID product ion spectra of two lithiated hexoses: unlabeled Tal (left) and 1,2-$^{13}C_2$-talose (right). 124

Figure 6.3 Comparison of CID product ion yields for unlabeled (UL) and carbon-13 labeled (^{13}C) hexoses. 128

Figure 6.4 1-$^{13}C_1$-Galactose carbon NMR spectrum with proton decoupling – 13C{H1} 1D. 130

Figure 6.5 1,2-$^{13}C_2$-Glucose carbon NMR spectrum with proton decoupling – 13C{H1} 1D. 131

Figure 6.6. Mechanism of hexose cross-ring cleavage and pyranose ring bond numbers........134

Figure 6.7 Product ion mass spectra insets of four carbon-13 labeled hexoses showing the formation of (top) $^{0,2}A$ and $^{0,4}X$ ions and (middle) $^{0,3}A$ and $^{0,3}X$ ions. The $^{0,3}X$ and $^{0,4}X$ ion yields calculated for each hexose epimer are listed in the table at the bottom of the figure. ..136

Figure 6.8. X ion yields as a function of fragmentation amplitude. 137

Figure 6.9 a) Chromatographic separations of hexose anomers using zwitterionic HLIC-LC. b) $^{0,3}X$ ion yield and c) $^{0,4}X$ ion yield for each hexose anomer or structural feature. 138

Figure 6.10 CID product ion spectra of lithiated 1,2-$^{13}C_2$-Glc cross-ring cleavage ions and lithiated glyceraldehyde. 141

Figure 6.11 Unreacted fraction (R_U) measurements of unlabeled [Hexose+Li]$^+$ for four epimeric hexoses, and their dehydration and cross-ring cleavage CID product ions. 142

Figure 6.12 R_U values measured for mass-resolved $^{0,2}A$, *m/z* 127, and $^{0,4}X$, *m/z* 128 or 129, ions (left) and mass resolved $^{0,3}A$, *m/z* 97, and $^{0,3}X$, *m/z* 98 or 99, ions (right). 146

Figure 6.13 Gas-phase DFT optimized structures for lithiated $^{0,4}X$ (left) and $^{0,2}A$ (right) cross-ring cleavage ions (*m/z* 127). 148

Figure 6.14 Gas-phase DFT optimized structures for lithiated $^{0,3}X$ (left) and $^{0,3}A$ (right) cross-ring cleavage ions (*m/z* 97). 149

Figure 6.15 Gas-phase DFT optimized structures for lithiated $^{0,3}X$ (left) and $^{0,3}A$ (right) cross-ring cleavage ions (*m/z* 67). 150

Figure 7.1 Domon-Costello nomenclature for glycan dissociation, and structural features required for complete glycan characterization. 155

Figure 7.2 Three MS^n experiments that allow redundant measurement of each monosaccharide subunit. 159

Figure 7.3 a) Architecture of a feed-forward artificial neural network.
b) Weighting of inputs prior to the neuron. c) All inputs feed into every neuron in the hidden layer for transformation. 161

Figure 7.4 a) A schematic of supervised learning. b) Unsupervised learning where the neural network learns a unique representation of the input data. 162

Figure 7.5 Mutarotation of Glc occurs upon pyranose ring opening in protic solvent. 163

Figure 7.6 Reaction of a mixture of Glc anomers with acetyl chloride in methanol to produce anomerically-locked methyl glucopyranosides. 164

Figure 7.7 Three example glycolipids. 167

Figure 7.8 Full scan MS of PI(8:0/8:0) and CID-water adduction of *m/z* 593. 169

Figure 7.9 CID-water adduction of *m/z* 599 from PI(8:0/8:0). 170

Figure 7.10 MS/MS product ion spectra of GlcSph and GalSph... 171

Figure 7.11 MS/MS level CID-water adduction product ion ratios for GlcSph and GalSph. 172

LIST OF ABBREVIATIONS AND SYMBOLS

1dGlc	1-deoxyglucose
2dGlc	2-deoxyglucose
3dGlc	3-deoxyglucose
4dGlc	4-deoxyglucose
6dGlc	6-deoxyglucose
$^{0,2}A$	example hexose reducing end cross-ring cleavage notation
$^{0,4}X$	example hexose non-reducing end cross-ring cleavage notation
Å	Angstrom
All	allose
ATD	arrival time distribution
B3LYP	Becke, 3-parameter, Lee-Yang-Parr
CAD	computer aided drawing
CCS	collision cross section
°C	degrees Celsius
CE	capillary electrophoresis
CID	collision-induced dissociation
cIM	cyclic ion mobility
Cpcm	conductor-like polarization continuum solvation model
Da	Dalton
DFT	density functional theory
DIMS	differential ion mobility spectrometry
DNA	deoxyribonucleic acid
ESI	electrospray ionization
ESI-MS	electrospray ionization-mass spectrometry
Gal	galactose
GalSph	galactosphingosine
GC	gas chromatography

Glc	glucose
GluSph	glucosphingosine
ΔG	the change in Gibbs free energy
HCT	high-capacity trap
HILIC	hydrophilic interaction chromatography
HPLC	high-performance liquid chromatography
i187	mass spectrometry peak area for mass-to-charge ratio 187
i205	mass spectrometry peak area for mass-to-charge ratio 205
ICC	ion charge control
IMoS	ion mobility suite
IMS	ion mobility spectrometry
K	rate constant
K	ion mobility
kcal/mol	kilocalories per mole
KE	kinetic energy
kHz	kilohertz
kV	kilovolts
L/min	liters per minute
LC	liquid chromatography
Li^+	lithium cation
LiAc	lithium acetate
LiCl	lithium chloride
$Li\text{-}H_2O$	lithium-water bond formed upon water adduction reaction
Li-O	lithium-oxygen coordination formed between lithium and a carbohydrate
m/z	mass-to-charge
$[M+Li]^+$	lithium cationized molecule
$[M+Li+H_2O]^+$	lithium cationized and water adducted molecule
$[M+Na]^+$	sodium cationized molecule
Man	mannose

MeGlc	methylglucoside
MeOH	methanol
MHz	megahertz
mm	millimeter
mM	millimolar
μL	microliter
μL/min	microliters per minute
μM	micromolar
MP	mobile phase
MS	mass spectrometry or mass spectrometer
ms	millisecond
MS/MS	tandem mass spectrometry
MS^n	n stages of tandem mass spectrometry
Na^+	sodium cation
NMR	nuclear magnetic resonance spectroscopy
NPA	natural population analysis
PI	phosphoinositide
PIY	product ion yield
ppm	parts per million
Q	quadrupole
q_z	Mathieu parameter of an ion
r_0	radial dimension of the quadrupole ion trap
rf	radiofrequency
RNA	ribonucleic acid
R_R	reacted fraction of ions
RRKM	Rice-Ramsperger-Kassel-Marcus theory
R_U	unreacted fraction of ions
SY	survival yield
Tal	talose

TOF	time-of-flight
V	voltage
V_{rf}	alternating current voltage amplitude of the ion trap drive rf
$2z_0$	axial dimension of the quadrupole ion trap
ε	ion internal energy
ε_o	critical energy for unimolecular dissociation
Ω	frequency of the ion trap drive rf voltage

CHAPTER 1: INTRODUCTION TO MASS SPECTROMETRY BASED STRUCTURAL ELUCIDATION OF CARBOHYDRATES

1.1 Carbohydrate Structure

Structural characterization of biomolecules is a prominent analytical challenge because of the implications on the understanding of human physiology. The human genome has been mapped[1] and well-established methods exist to study the human proteome[2–4], but improved technologies for carbohydrate structural characterization are needed. In 2012 the National Academy of Sciences called for a transformation of glycoscience by urging development of methods to identify and elucidate the structures of all biologically relevant carbohydrates[5, 6]. Carbohydrates are the most abundant natural biopolymers and are involved in the fundamental functions of all multicellular organisms through glycosylation of proteins and lipids. Enzymatic production of carbohydrates, unlike template-guided protein translation, is a competitive non-template regulated mechanism and as a result carbohydrates are the most structurally diverse natural biopolymers[7]. Larger carbohydrates are enzymatically synthesized *via* linkage of monosaccharides. As the carbohydrate chain is lengthened the linkage can occur via one of many hydroxyl groups on the monosaccharide resulting in either linear or branched polymer chains. If one or both anomeric hydroxyl group(s) is incorporated into the glycosidic bond, then the linkage(s) can either be in the α or β configuration.

As the building blocks of larger carbohydrates, monosaccharides are a widely studied class of molecules. Various classes of monosaccharides exist and within a single monosaccharide class there are multiple isomers. Monosaccharide epimers are stereoisomers that have varying oxygen atom orientations around the multiple asymmetric carbons. Hexoses are monosaccharides that are commonly found in biology with the simple chemical formula, $C_6H_{12}O_6$, but encompass a vast structural landscape. The pyranose form of glucose (Glc), an aldohexose, is shown in Figure 1.1a with carbon numbers labeled in blue. These aldohexoses have three stereocenters (excluding the anomeric center at C1), producing 8 diastereomers (Figure 1.1b). Aldohexoses can exist as a straight chain aldehyde, a five-membered cyclic hemiacetal (furanose), or a six-membered cyclic hemiacetal (pyranose). Measurement of aldohexoses is often a convolution of cyclic and acyclic forms, all of which establish equilibrium in solution[8]. The pyranose and furanose forms can each adopt two configurations, α or β, about the C1 anomeric center which establish equilibria of their own. The Glc pyranose anomers are shown in Figure 1.1a. In aqueous solution the six-membered pyranose rings of α-Glc and β-Glc are in equilibrium (α:β = 37.63:61.96) constituting 99.6% of existing Glc structures, the remaining 0.4% are acyclic and furanose forms. The pyranose ring of Glc is most stable in the $^4C_1$ chair conformation due to its equatorial hydroxyl groups that alternate on opposite sides of the "plane" of the ring, minimizing steric interactions such as unfavorable 1,3-diaxial strain. Even though the $^4C_1$ chair of Glc is favorable it can be distorted to boat, skew boat or envelope conformations called "puckering geometries"[9, 10]. Puckering geometries of ribose, a pentose, are known to effect RNA and DNA structure[11, 12].

Glc in the pyranose ring contains only equatorial hydroxyl groups at the C2/C3/C4 positions, but other hexose epimers have axial hydroxyl groups incorporated into the pyranose ring. The axial hydroxyl groups of other hexose epimers alter the solution-phase equilibria between pyranose anomers and furanose anomers[8], and even the stability of different ring puckering states. These slight differences in stereochemistry and solution-phase structure equilibria are difficult to differentiate; hence, technologies to elucidate all structural features of hexoses and larger carbohydrates are still being developed.

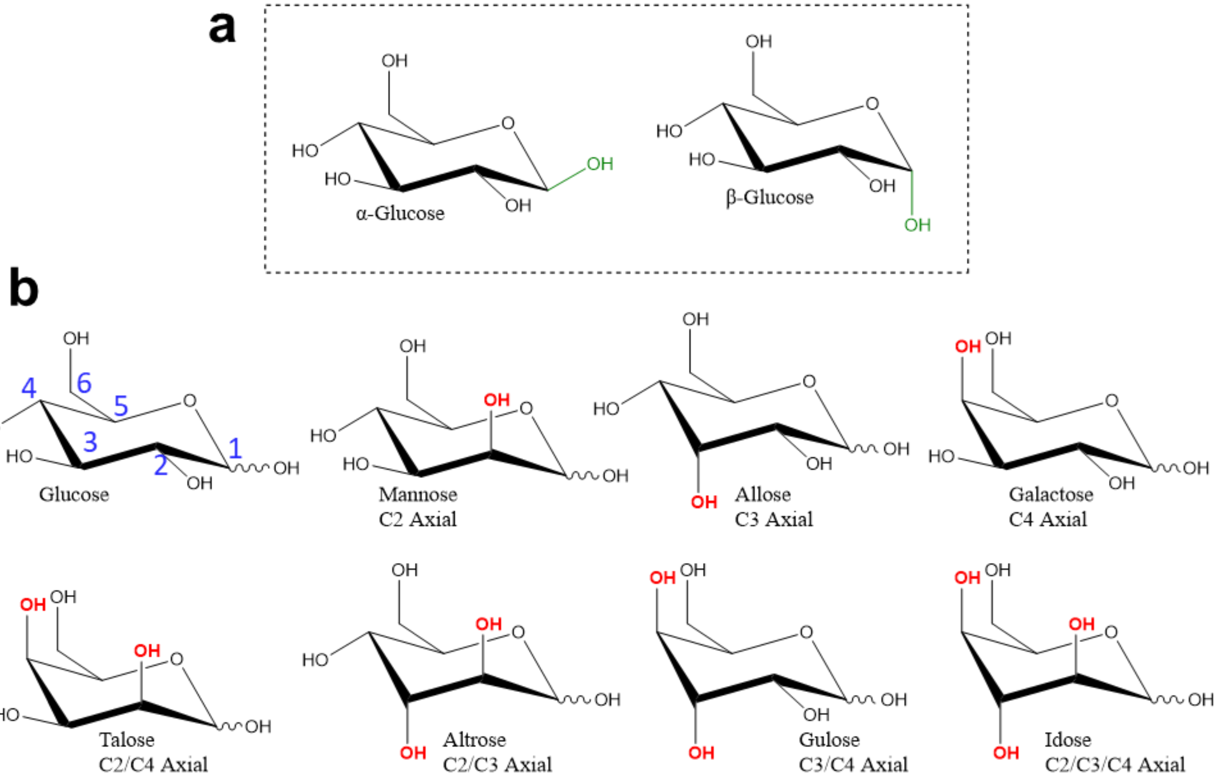

Figure 1.1 a) Alpha and beta anomers of the glucose pyranose ring. b) Eight D-hexose epimers shown in their aldohexopyranose ring conformations with undefined anomeric configurations at C1 anomeric center. Carbon numbering is shown in blue on the glucose molecule.

Thus far, the stereochemistry and solution-phase structure equilibria of hexoses have been discussed. However, hexose gas-phase ion structures must also be considered for mass spectrometry experiments. When an aqueous solution of a hexose is introduced into the electrospray ionization (ESI) process the hexose solution-phase structures (pyranose, furanose, etc.) can coordinate a lithium cation and be released as a gas-phase ion for subsequent mass spectrometry analysis. Multiple solution-phase structures compounded with many possible lithium cation coordination sites for each structure suggests significant structural heterogeneity of the gas-phase ions that are produced by ESI. Each hexose isomer forms a unique distribution of ion structures with various multidentate lithium-oxygen (Li-O) coordinations. This ion structural heterogeneity can potentially complicate carbohydrate analysis, but in some cases the different ion structures and their chemistries can be leveraged for differentiation.

1.2 Introduction to Carbohydrate Analysis

The challenge of deciphering the vast number of carbohydrate structural isomers has been met with many technologies, each of which provides a small piece of the puzzle. Nuclear magnetic resonance (NMR) is effective for determining carbohydrate stereochemistry and sequence[8, 13–15]. But because NMR requires pure samples at millimolar concentrations its utility for biological samples is hindered. Preparing samples from biological matrices for NMR entails extensive purification to increase concentration and reduce chemical background. Therefore, methods that are less labor intensive and more sensitive are desirable. Mass spectrometry (MS) separates ions based on their mass-to-charge ratio (*m/z*), providing high sensitivity and selectivity, and enabling analysis of small amounts of material in complex matrices[7]. However, isomers cannot be distinguished by MS alone and many isomeric carbohydrates exist. Separation of isomers may be achieved prior to the mass spectrometer or certain tandem mass spectrometry (MS/MS) techniques may be able to differentiate isomers.

Pre-ionization separations can be used to separate carbohydrate isomers prior to ESI (or other ionization technique). Liquid chromatography (LC) has been used to separate carbohydrate isomers[7, 16], but separations last minutes to hours. Typical reversed-phase LC is unable to retain and resolve isomeric sugars, therefore a chemical derivatization step such as permethylation is necessary to increase hydrophobicity[17, 18]. Hydrophilic interaction (HILIC) LC has been used for carbohydrate analysis without prior derivatization[19–21], but HILIC is not as common as reversed-phase LC. Gas chromatography (GC) is often used to separate gas phase carbohydrate molecules prior to ionization and MS analysis, but also requires derivatization to increase sugar volatility[22]. Chromatography often separates carbohydrate anomers which, in many cases, is undesirable and complicates the experiment. To prevent chromatographic anomer separation a further derivatization step is required to reduce the anomeric center.

Ion mobility spectrometry (IMS) is a gas-phase post-ionization separation that occurs on the millisecond timescale[23], as opposed to lengthy chromatography separations. IMS has been employed to separate isomeric glycans prior to MS[24–26]. Success has been found with IMS for separation of larger carbohydrates because of their propensity to have greater differences in ion mobility. But most current IMS devices lack the resolving power to separate monosaccharide isomers.

The separation techniques discussed all occur prior to the mass spectrometer, but experiments can be done within the mass spectrometer to gain ion structural information and attempt to differentiate monosaccharide isomers. Tandem mass spectrometry (MS/MS) involves multiple stages of mass selection typically with ion dissociation between MS steps. Dissociative techniques generally involve an ion activation step and subsequent unimolecular ion dissociation. The ion activation mechanism, timescale and amount of internal energy imparted into the ion can vary based on the activation mode and scenario[27]; all of which have implications on the types of product ions formed. MS/MS can be used with or without prior LC, GC or IMS separation. The goal of MS/MS experiments for carbohydrate analysis is to determine monosaccharide connectivity and identify the monosaccharide subunits. It is often necessary to use multiple types of MS/MS to achieve this goal. Collision-induced dissociation (CID) has been employed to identify glycosidic bond stereochemistry and glycan connectivity [28–30], and to aid theoretical studies of carbohydrate dissociation pathways[31–34]. Photodissociation, and electron activated dissociation of ions in the mass spectrometer have been shown to provide product ions that are complementary to CID[35, 36]. MS/MS involving ion/molecule reactions such as hydrogen-deuterium exchange has been used to distinguish isomers and/or gas-phase conformers[37–40]. But these techniques have found most success with larger carbohydrates.

Identification of the monosaccharides using only CID is difficult. CID of hexose epimers often generates identical product ions that do not promote differentiation, although CID of ammonium adducted hexose ions has been reported to generate some unique MS/MS and MS^3 product ions[41, 42]. Specialized dissociation techniques, such as the kinetic method[43] and fixed-ligand kinetic method[44, 45] can be used to differentiate monosaccharide isomers. The kinetic method and the fixed-ligand kinetic method require the use of ternary and quaternary mixtures, respectively, to form metal-bound dimeric and metal-bound trimeric ion clusters. These previously reported methods required high concentrations of the monosaccharide and each reagent because the necessary ion complexes do not favorably form upon ESI; therefore, the desired ion cluster abundances were low. To date, there are few mass spectrometry technologies capable of differentiating stereoisomeric monosaccharides that are amenable to low concentrations and require minimal reagents.

1.3 Water Adduction Ion/Molecule Reaction

Gas-phase ion/molecule reactions can be integrated into tandem mass spectrometry experiments to probe intermolecular reactivity. Water adduction is a gas-phase ion/molecule reaction that occurs inside of an ion trap mass spectrometer. The water adduction ion/molecule reaction has distinguished stereoisomeric D-aldohexoses, D-pentoses, hexosamines, N-acetylhexosamines and isomeric monodeoxy glucoses[46–48]. Collision-induced dissociation in tandem with water adduction revealed glycosidic linkage position and anomeric configuration of glucose-glucose disaccharides[49]. Water adduction does not require carbohydrate derivatization or instrument modification, and only requires addition of lithium salt to a sample. The ability of the water adduction reaction to probe stereochemical differences, and its simplicity, gives it an advantage over many current technologies. This ion/molecule reaction is only observed for the lithium cationized species in a low-energy trapping instrument in which ions have a long residence time (tens of milliseconds or longer) such as a quadrupole ion trap.

Electrospray ionization (ESI) of many molecular classes generates protonated, $[M+H]^+$, ions. Carbohydrates have high affinity for metal cations, thus, ESI of a carbohydrate solution produces sodium cationized carbohydrates, $[M+Na]^+$. Adventitious sodium cations favorably complex with the oxygen atoms of carbohydrates, but upon addition of a lithium salt to the ESI solution, Li^+ out-competes Na^+ to generate $[M+Li]^+$. Lithium cationized carbohydrates, $[M+Li]^+$, are transferred from an aqueous solution of lithium salt and the carbohydrate to the gas phase via ESI and isolated in an ion trap mass spectrometer. A residual water molecule within the vacuum chamber of the mass spectrometer can interact with the lithium cationized sugar in the ion trap. Ions are stored in the trap for a user specified delay time and varying this delay time allows control of the water adduction reaction time. Kinetics experiments that yield the water adduction reaction rate are run by varying the reaction time. Water molecules will adduct to a fraction of the population of $[M+Li]^+$ ions, generating a population of $[M+Li+H_2O]^+$ ions, which are detected 18 mass-to-charge units higher. At long reaction times, the portion of the $[M+Li]^+$ population that is not observed to adduct water is termed the unreacted fraction (R_U). The water adduction reaction rate and R_U are unique to individual lithium cationized hexoses.

Hexoses have six oxygen atoms available to coordinate a lithium cation and, generally, multidentate lithium-oxygen (Li-O) coordinations are formed during ESI. The presence of both reacted, [Hexose+Li+H_2O]$^+$, and unreacted, [Hexose+Li]$^+$, ions for a given hexose implies different sites of lithium coordination[48]. Reactivity of a given [M+Li]$^+$ structure is dependent on the number of oxygen atoms coordinated to the lithium cation. Hexose anomeric and stereochemical configuration determine oxygen atom arrangement around the pyranose ring, therefore, dictating the [Hexose+Li]$^+$ structures formed.

To study the potential lithium binding sites of each hexose isomer, density functional theory (DFT) methods were used. DFT was used to determine the preferred lithium binding sites for hexose epimers in solution and *in vacuo*. The pyranose ring was the focus of DFT studies because it is the major structure in aqueous solution for all hexose epimers. DFT calculations suggest that hexoses generally form bi-, tri- or tetradenate Li-O coordinations. Based on the DFT calculation results paired with water adduction experimental results, lithium cationized carbohydrate structures with bidentate Li-O coordinations are observed to form [M+Li+H_2O]$^+$, while ions with tri- or tetradentate Li-O coordinations are not observed to adduct water[48]. Relative abundances of reacted and unreacted theoretical structures for each hexose aided understanding of experimental R_U values. Computational DFT structures and experimental water adduction ion/molecule reaction results proved to be synergistic. This combination of theory and experiment provided insight to the lithium cationization of monosaccharides, the mechanism of the water adduction ion/molecule reaction and the isomeric heterogeneity of hexose CID product ions.

1.4 Summary

Chapter 1 was intended to summarize current methodology for carbohydrate structural elucidation technologies, and to introduce the water adduction ion/molecule reaction that has been developed to differentiate carbohydrate stereoisomers. This dissertation investigates the mechanism of the water adduction ion/molecule reaction and how multidentate Li-O coordinations produce unique reaction rates and R_U values for carbohydrate stereoisomers. By studying the water adduction mechanism, much was learned about lithium cationization of carbohydrates and the many solution- and gas-phase structures that form during ESI. Pre- and post-ionization separations, tandem mass spectrometry experiments and theoretical calculations are combined to explore the structural landscape of gas-phase lithium cationized carbohydrate ions and how these structures affect gas-phase chemistry.

In **Chapter 2** the materials and experimental methods used throughout the studies in this dissertation are described.

In **Chapter 3** the structural landscape of lithium cationized monosaccharides (hexoses, monodeoxy glucoses and inositols) are explored with DFT and experimental R_U values to provide insight to the water adduction mechanism. To further corroborate the importance of multidentate Li-O coordinations on water adduction results, the relative order of gas-phase lithium cation affinities of monosaccharides was measured and correlated to R_U. Lastly, lithium-water (Li-H_2O) bond strengths that hexose epimers form upon water adduction were probed.

In **Chapter 4** the effects of mass spectrometer parameters on water adduction ion/molecule reaction results are discussed and well-controlled experiments and calibration for cross-platform or cross-laboratory studies are encouraged.

In **Chapter 5** the question of whether the gas-phase carbohydrate structures resolved by ion mobility spectrometry are due to carbohydrate anomers or different metal cationization sites is discussed.

In **Chapter 6** the isomeric complexity of lithium cationized hexose product ions formed upon collision-induced dissociation is unveiled and differences in dissociation chemistry for hexose epimers are discussed.

Chapter 7 is a summary of the lessons learned throughout this dissertation and groundwork is provided for future studies centered around the water adduction ion/molecule reaction.

CHAPTER 2: EXPERIMENTAL

2.1 Materials

Optima grade methanol, Optima grade water and Optima grade acetonitrile were purchased from Fischer Scientific (Fairlawn, NJ, USA). D-glucose (Glc), D-mannose (Man), D-galactose (Gal), D-1,2-$^{13}C_2$-glucose, D-$^{13}C_6$-Glucose and lithium acetate were purchased from Sigma Aldrich (St. Louis, MO, USA). D-allose (All), 1,5-Anhydroglucitol (1dGlc), 2-deoxy-D-glucose (2dGlc), 3-deoxy-D-glucose (3dGlc), 4-deoxy-D-glucose (4dGlc), 6-deoxy-D-glucose (6dGlc), methyl a-D-glucopyranoside (α-MeGlc), methyl b-D-glucopyranoside (β-MeGlc), D-Talose (Tal), epi-Inositol, 1D-chiro-Inositol, cis-Inositol, scyllo-Inositol, neo-Inositol and glyceraldehyde were purchased from Carbosynth (Berkshire, UK). D-1,2-$^{13}C_2$-Talose was purchased from Omicron Biochemicals (South Bend, Indiana). D-1-$^{13}C_1$-galactose and D-1-$^{13}C_1$-mannose were purchased from Cambridge Isotope Laboratories (Tewksbury, MA).

2.2 Mass Spectrometry

All sugars were individually analyzed at a concentration of 25 or 50 μM with 100 μM lithium acetate in pure water or pure methanol. The sugar and lithium salt solution was delivered at 2 μL/min to the electrospray ionization (ESI) emitter of a Bruker HCTultra quadrupole ion trap mass spectrometer. The ESI emitter was grounded, and the MS inlet capillary was -4.5 kV for positive ion generation. Nitrogen nebulization gas was constant at 20 psi and the desolvation gas was held at 5 L/min and 300 °C. Positive ions and desolvation gas are pulled through the MS inlet capillary by a pressure gradient between atmosphere and the first differentially pumped region of the vacuum system. The pressure gradient pulls ions past the electric field of the capillary exit voltage (101.8 V) and ions are subsequently accelerated by the skimmer cone voltage (40.0 V). Beyond the skimmer cone ions are transferred through an rf only octopole (126.2 V_{p-p}) with accelerating entrance and exit dc voltages of 8 and 1.7 V, then through a set of static potential lenses (-5 and -60 V) for injection into the ion trap. All the voltages within the entrance ion optics can be controlled to optimize or block ion transmission to the ion trap. The trap drive was set to 43.6 arbitrary units and the mass range *m/z* 50 to 500 was scanned at 26,000 Da/s ("Ultra Scan"). Spectrum averaging was set to 10 and rolling averaging was turned off. The Bruker ion charge control (ICC SmartTarget) was set to 200,000 counts with a maximum accumulation time of 300 ms. After ion accumulation, precursor ions were isolated for tandem-MS with a 1 Da window. Two stages of mass spectrometry are referred to as a tandem mass spectrometry or an MS/MS experiment. The tandem mass spectrometry experiments employed in this dissertation involved collision-induced dissociation (CID), the water adduction ion/molecule reaction, or a combination of the two. Many stages of mass analysis, MS^n, are possible with an ion trap mass analyzer, where n is the number of stages of mass analysis. MS^n is possible with an ion trap because of its unique separation-in-time mode of operation.

Some mass analyzer types, such as quadrupoles (Q), time-of-flight (TOF) or sectors, separate ions by their *m/z* in space. During separation in space, ions are constantly in transit through the mass spectrometry system. As ions traverse the mass analyzer, depending on the type of analyzer, they are separated by an electric (Q) or magnetic (sector) field, or pulsed into a field free region and separated based on velocity (TOF). Ions are constantly being generated at the electrospray ionization source, and for separation-in-space mass spectrometry systems

(Q, TOF, sector) there is a constant ion flux through the system for mass analysis and detection.

Ion traps are unique in that they separate ions in time within a confined volume. The ion trap experiment is often described by the 'scan function,' which details rf voltage amplitudes, and other relevant voltages within the mass spectrometry system, as a function of time (Figure 2.1). Because mass analysis using an ion trap occurs within the confined volume of the trap, a constant ion flux into the trap is not amenable to the experiment. Ions must be transmitted through the entrance ion optics (capillary exit voltage, skimmer voltage, lens voltages, etc.) to fill the ion trap with ions, but when an MS^n experiment is underway the ion flux must be blocked. To address this need, for a short time, the entrance ion optics are set for optimal transmission of ions into the trap (Figure 2.1, step 2, accumulation). After ion accumulation, the entrance ion optics voltages are changed to completely block ion transmission to the ion trap. The Skimmer 2 voltage is shown in Figure 2.1 to be high (block ions) during all steps of the scan function besides the accumulation step (low voltage, transmit ions). Much more discussion on the accumulation step is provided in Chapter 4.2.

Using alternating current radiofrequency (rf) voltages, the ion trap stabilizes and 'traps' a cloud of ions within the confined volume of the ion trap. The primary 'drive' rf voltage creates the main trapping electric field within the ion trap. Prior to ion accumulation, the drive rf voltage amplitude is lowered to reduce the trapping field, destabilize ions, and clear the trap of all ions (Figure 2.1, step 1, clear trap). During the rest of the scan function, the drive rf is used to stabilize ions of interest or it is linearly ramped to sequentially destabilize (eject) ions for mass analysis and detection (step 5, mass analysis). The linear ramp of the drive rf voltage is known as the analytical scan. Auxiliary rf voltages are also used to manipulate ions (isolation, activation) for MS^n experiments and for resonance ejection mass analysis for *m/z* determination[50].

Mass analysis with separation-in-space mass analyzers (Q, TOF, sector) occurs on the timescale of ion transit time through the mass analyzer (tens to hundreds of microseconds). Ion trap MS experiments occur on the millisecond to second timescale, depending on the experiment. Once ions are stable in the ion trap they can be stored and manipulated for many seconds without significant ion loss. Step 4 of the scan function in Figure 2.1 is called the scan delay. The scan delay is a controllable delay time prior to the analytical scan. Typically, the scan delay is used for collisional cooling of ions to ensure accurate and precise *m/z* determination upon mass analysis. In this dissertation the scan delay is used in an unorthodox manner, to control the reaction time for the gas-phase water adduction ion/molecule reaction. The drive rf voltage amplitude during the scan delay is dependent on user-defined parameters of the experiment and can change the results of the water adduction ion/molecule reaction. Much more discussion on the drive rf voltage during the scan delay is provided in Chapter 4.3.

The experiment discussed thus far has been a single stage of mass analysis (full scan MS) and does not include isolation/activation events. Full scan MS experiments are used to detect all ions that are accumulated and stabilized in the ion trap. The scan function in Figure 2.1 illustrates an MS/MS experiment, including one isolation/activation event and the analytical scan for ion ejection and detection. MS^n experiments involve multiple stages of mass selection and analysis. A very common type of mass selection is isolation of a specific *m/z* of interest for further ion manipulation. While there are various methods, isolation of a single *m/z*, or a small range of *m/z*, is achieved by controlling the drive and auxiliary rf voltages, often using specialized auxiliary rf waveforms[51–53]. Isolation maintains stability of the desired ions and excites and ejects all other unwanted ions from the trap. After isolation, the ions of interest can be subjected to a myriad of experiments; for example, activation (for dissociation) and/or ion/molecule reactions. Product ions that are formed by dissociation or reaction can then be isolated for further ion manipulation. MS^n experiments typically involve multiple stages of isolation, and the accompanying activation or reaction step, and end with analytical scan for ejection and detection.

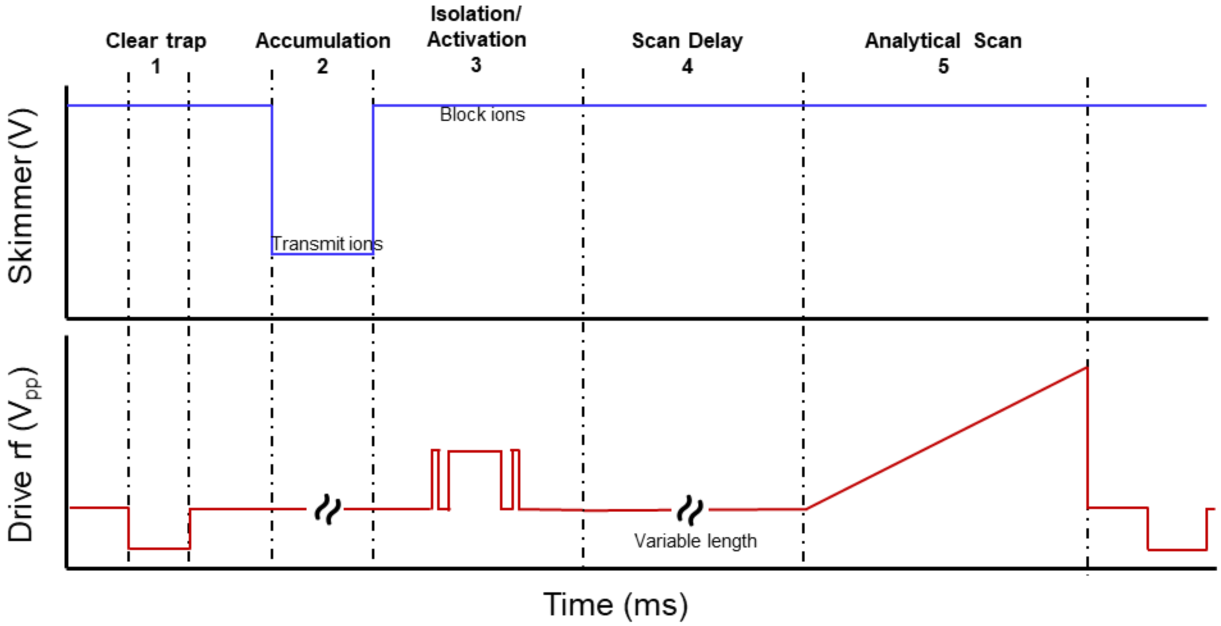

Figure 2.1 The ion trap scan function showing the skimmer dc voltage and drive rf voltage amplitude as a function of time. Step 1: Clear trap. Skimmer voltage is set to block ion transmission. Drive rf voltage amplitude is lowered briefly to reduce the trapping field and destabilize all ions. Step 2: Accumulation. Skimmer voltage is set to transmit ions. Drive rf voltage amplitude is raised to create the trapping field. Step 3: Isolation and activation events can be used or omitted. Complex auxiliary rf waveforms are often applied (not pictured). If no isolation events are used, it is an MS experiment. Using one isolation event is an MS/MS experiment, and *n* isolation events is MS^n. Step 4: Scan delay. Step 5: Mass analysis for *m/z* determination.

2.3 Water Adduction Ion/Molecule Reaction

Lithiated carbohydrate ions, $[M+Li]^+$, stored in the ion trap MS will interact with residual water molecules in the MS vacuum chamber to generate $[M+Li+H_2O]^+$. Following precursor ion isolation a delay time can be applied to increase ion storage duration prior to the analytical scan for detection. This controllable delay time ('scan delay'), a segment of the ion trap scan function, effectively modulates the reaction time for the water adduction experiment. A detailed discussion of the ion trap scan function and the scan delay is provided in Chapter 4.3. Depending on ion structure, some water adduction may occur without a scan delay, but changing the scan delay (reaction time) enables kinetics experiments. As reaction time is varied the abundances of $[M+Li]^+$ and $[M+Li+H_2O]^+$ are monitored. Long reaction times (≥1000 ms) are used to measure the abundances of $[M+Li]^+$ and $[M+Li+H_2O]^+$ once the reaction has reached the asymptotic ratio of $[M+Li]^+/([M+Li]^+ + [M+Li+H_2O]^+)$. The asymptotic value of the ratio is called the final unreacted fraction (R_U) and is dependent on carbohydrate ion structure. From here forward any mention of 'R_U' or 'unreacted fraction' will refer to the final unreacted fraction measured with a 1000 ms reaction time or greater.

The change in $[M+Li]^+/([M+Li]^+ + [M+Li+H_2O]^+)$ at short reaction times (11.3, 21.3, 31.3, 41.3, 51.3 and 61.3 ms) is used to calculate the water adduction reaction rate. Because the water concentration in the ion trap is much greater than the ion concentration, pseudo-first-order kinetics are assumed. The water concentration is unknown, so the determined reaction rates are a function of $[H_2O] \times k$, where k is the rate constant and $[H_2O]$ is the water concentration. Only the reactive portion of ions are included in the rate calculation; the following equation was used to determine the portion of reactive ions remaining at a given scan delay time (R_R).

$$R_R = \frac{(1 - R_U)\left(I_{[M+Li]+} + I_{[M+Li+H2O]+}\right) - I_{[M+Li+H2O]+}}{(1 - R_U)\left(I_{[M+Li]+} + I_{[M+Li+H2O]+}\right)}$$

Plotting ln(R_R) versus time results in a linear relationship and provides the reaction rate ([H_2O] × k). The scan delay times used to determine R_U and reaction rate were chosen based on the water concentration within the ion trap, which has not changed drastically over years of repeated experimentation in a temperature and humidity-controlled laboratory. If the water concentration is intentionally raised by doping it directly into the ion trap, the reaction rate ([H_2O] × k) would increase accordingly and shorter scan delay times could be used to measure reaction rates and the asymptotic R_U values.

R_U of lithiated hexoses has been extensively studied in the Glish laboratory through experimentation and density functional theory (DFT) calculations. Information about ion structure can be deduced from R_U measurements. R_U is dependent on the multidentate Li-O coordinations that hexoses form during the ESI process. Multidentate Li-O coordinations that form is dependent on oxygen atom arrangement of the molecule and, therefore, stereochemistry. Ions that remain unreacted, and therefore are observed as the precursor ion in the spectrum, have tri- or tetradentate Li-O coordinations. Ions that are observed as the water adducted precursor ion in the spectrum (reacted) contain bidentate lithium-oxygen coordinations.

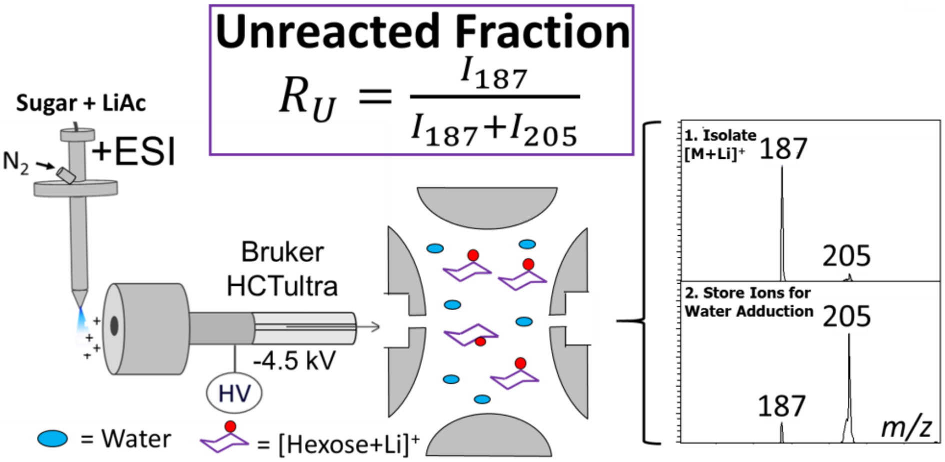

Figure 2.2 Schematic of the electrospray ionization – ion trap mass spectrometry system used for CID and water adduction experiments.

2.4 CID-Water Adduction

Most individual CID experiments, or individual water adduction experiments, discussed in this thesis are at the MS/MS level unless otherwise noted. To measure the water adduction characteristics of lithiated hexose product ions, $[P+Li]^+$ we must use CID and water adduction experiments in tandem. All CID-water adduction experiments on lithiated hexose product ions are at the MS^3 level (MS^1, isolate precursor → CID → MS^2, isolate product ion → water adduction → MS^3, analytical scan). CID must also be used to first dissociate larger carbohydrates (disaccharides and larger) into their monosaccharide substituent prior to the water adduction reaction. All the MS and MS/MS parameters discussed previously were maintained for CID-water adduction experiments.

2.5 Kinetic Method

The kinetic method[54, 55] was used to measure relative gas-phase lithium affinities of monosaccharides. Kinetic method theory is discussed in more detail within Chapter 3.3. A solution of monosaccharide, $^{13}C_6$-glucose and lithium acetate was delivered to the ESI emitter to form lithium-bound heterodimers between the two sugars. The dimers, [Monosaccharide+Li+$^{13}C_6$-glucose+Li]$^+$,were isolated in the ion trap with a wide isolation window (5 Da) to prevent dissociation of the dimer during isolation. After isolation the heterodimer was subjected to energy-resolved CID where the fragmentation amplitude was stepped from 0.0 to 1.0 V in increments of 0.01 V. Dissociation of the dimer results in one of the two sugar molecules retaining the lithium cation; the other sugar molecule becomes neutralized and is not detected. The relative abundance of [Monosaccharide+Li]$^+$ and [$^{13}C_6$-glucose+Li]$^+$ represents the monosaccharide gas-phase lithium affinity relative to $^{13}C_6$-glucose. The gas-phase lithium affinities of deoxyglucoses and hexoses were measured relative to $^{13}C_6$-glucose. Gas-phase lithium affinity is related to the denticity of lithium-oxygen coordinations each monosaccharide can form and is dependent on stereochemistry.

2.6 Hydrophilic Interaction Liquid Chromatography

An Agilent Infinity II HPLC was used for gradient mobile phase delivery through a SeQuant ZIC-cHILIC column (3 µm, 100 Å, 150 x 4.6 mm). Mobile phase A was water and B was acetonitrile. The LC flow rate was set to 0.6 mL/min. Monosaccharides were eluted over an 18-minute run where MP B was 90% (0-2 min), 60% (12-14 min), 90% (14.5-18min). Disaccharides and trisaccharides were eluted over a 40-minute run where MP B was 90% (0-0.5 min), 60% (30.5-34.5 min), 90% (35-40 min). Three microliters of 200 µM sugar was injected onto the column. A 1.5 µL/min post-column infusion of 10 mM lithium acetate (aqueous) was teed in prior to the divert valve. Flow from the divert valve was delivered to the electrospray ionization (ESI) source of a Bruker HCTultra quadrupole ion trap.

2.7 Cyclic Ion Mobility-Time of Flight Mass Spectrometry

A modified Waters Synapt G2-Si Q-IM-TOF mass spectrometer (Figure 2.3) with the TriWave traveling wave ion mobility cell replaced by a cyclic traveling wave ion mobility spectrometer (cIM)[56, 57] was used for cIM experiments. The quadrupole isolation window was set to 3 Da window to transmit ions into the ion accumulator (10 ms accumulation) and helium cell (flow 80 mL/min) prior to injection to the cIM for separation A multidirectional traveling wave array (T-Wave array) controlled the ion path through the cIM device (Figure 2.2c-e). The cIM pathlength was 98 cm and estimated ion cycle time was 10 ms/pass; T-wave height was either 22 or 35 V. Ions were separated in the cIM based on their collision cross sections (CCS) with N_2 gas flowing at 35 mL/min. After ejection from the cIM, ions were either measured as intact $[M+Li]^+$ species or subjected to post-mobility CID prior to mass analysis and detection.

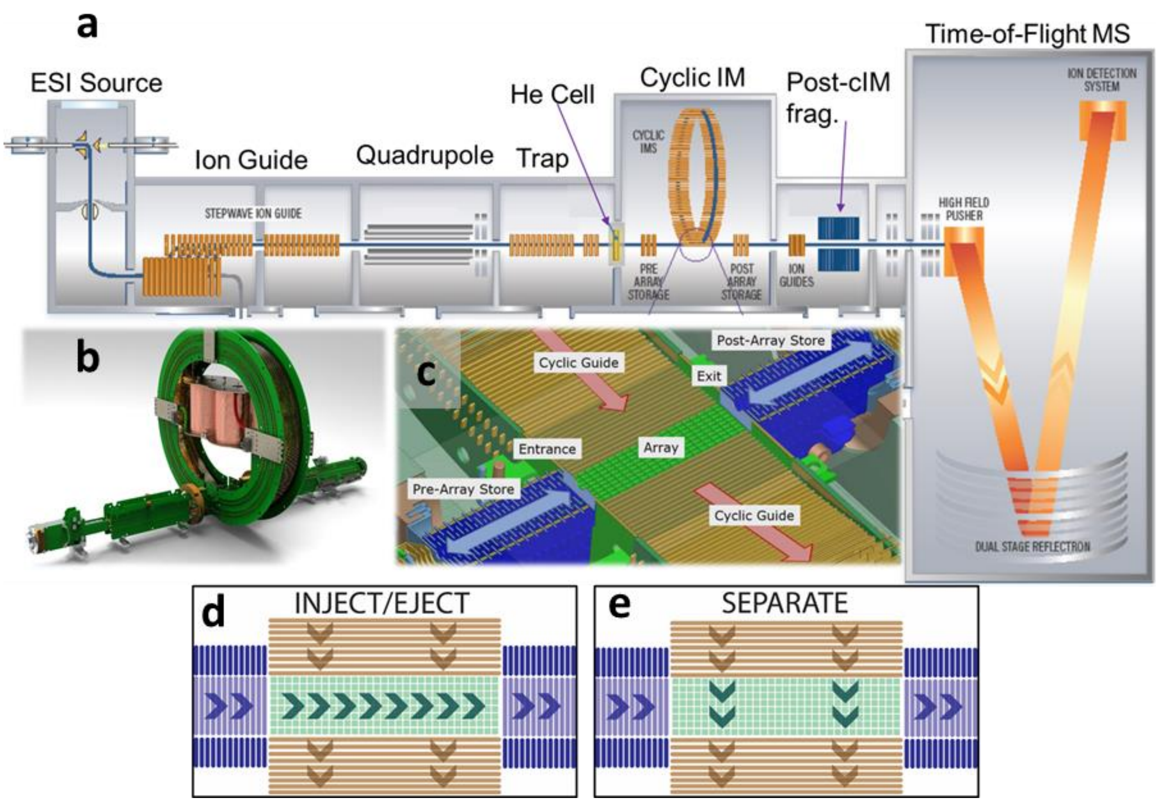

Figure 2.3 a) A custom Waters Synapt G2-Si Q-cIM-ToF. b) CAD rendering of the cyclic traveling wave mobility cell. c) Schematic of the multidirectional traveling wave array. d,e) Direction of T-Wave array during ion inject/eject and separation experiment.

2.8 Theoretical Calculations

Density Functional Theory (DFT) calculations performed with Gaussian 09[58] were used to determine, and calculate the relative energy of, all possible lithium binding sites for the chair, boat and skew-boat ring conformations for the hexoses, deoxyglucoses and inositols studied. Geometry optimizations and frequency calculations were performed with the B3LYP functional and 6-311++G(d,p) basis set[59, 60]. Gibbs free energies for the $^4C_1$ chair structures for both anomers of D-glucose, D-galactose, and D-mannose were compared to the previously reported global minima. For D-allose, and the monodeoxy hexoses, multiple variations in the hydrogen bonding network and the gauche-gauche, gauche-trans and trans-gauche hydroxymethyl rotamers were considered to find the lowest energy $^4C_1$ chair structure for each. Inositols do not contain the hydroxymethyl group or the ring oxygen, so it was only necessary to explore various hydrogen bond networks. The axial $^1C_4$ chair, boat, and skew-boat minimum energy structures were determined by optimizing the same structural variants. From the starting structure of each monosaccharide many lithium coordinated structures were generated. Lithium atoms were arranged at each of the four vertices of a tetrahedron around each oxygen atom at a distance of 1.8 Å. Adding one lithium atom to each of the 4 vertices of 6 oxygen atoms generated 24 different structures. All 24 structures were then optimized at the B3LYP/3-21G level of theory with conductor-like polarization continuum solvation model (cpcm) with water as the solvent. These structures were re-optimized, and frequency calculations were performed, at a higher level of theory using B3LYP\6-311++G(d,p) and the implicit solvent. The high-level optimized solvated $[M+Li]^+$ structures were then optimized and frequency calculations performed at the B3LYP\6-311++G(d,p) level of theory in the gas phase. The solution phase calculations were followed by gas phase calculations to model the generation of $[M+Li]^+$ in the electrospray process where complexation occurs in the droplet and the molecular ion is subsequently released into the gas phase. Once in the gas phase a single explicit water molecule is added to each structure, which is optimized at the 3-21G level followed by optimization and frequency calculation with the 6-311++G(d,p) basis set.The relative abundances of each $[M+Li]^+$ structure were estimated based on a Boltzmann distribution at 400 K using solution-phase Gibbs free energies. The abundance calculation for each hexopyranose was restricted to the aqueous solution anomeric ratio as measured by NMR. For example, the combined abundance of all α-Glc structures were restricted to 37.63% of the total population and β-Glc structures were restricted to 61.96%. The anomeric ratio for the aldohexoses, and monodeoxy glucoses were previously measured.

Ion Mobility Suite (IMoS) was used to employ the trajectory method to predict ion-neutral collision cross sections (CCS) of the gas-phase optimized $[M+Li]^+$ structures in a nitrogen drift gas. Each ion structure was optimized using the B3LYP/6-311++(d,p) functional and basis set with the natural population analysis (NPA) method for partial charge derivation. Each gas-phase $[M+Li]^+$ structure had a unique theoretical CCS value. The gas-phase structures have corresponding solution-phase structures from which they were generated. The Gibbs free energies of the corresponding solution-phase structures (from the frequency calculations at B3LYP\6-311++G(d,p)) were used to invoke a Boltzmann distribution at 400 K. For each hexose, the Boltzmann distribution was restricted to the anomeric ratio measured in solution by NMR. From the Boltzmann calculation, relative abundances of the $[M+Li]^+$ structures released into the gas phase by ESI was predicted. Relative abundances were then used to calculate a weighted CCS value for each hexose anomer.

2.9 Nuclear Magnetic Resonance

Measuring the cross-ring cleavage reducing-end yields of the hexose epimers is heavily reliant on accurate regiospecific carbon-13 labeling. The carbon-13 positions for 1,2-$^{13}C_2$-Glc and 1-$^{13}C_1$-Gal were confirmed using carbon-13 NMR with proton decoupling (13C{1H} 1D) with a Bruker AVANCE III 600 MHz NMR spectrometer equipped with a QNP cryoprobe. For analysis, each ^{13}C-hexose was dissolved in D_2O at a concentration of 110 mM. To confirm C1 labeling for both 1,2-$^{13}C_2$-Glc and 1-$^{13}C_1$-Gal, the measured chemical shifts were compared to literature values, and C2 labeling of 1,2-$^{13}C_2$-Glc was confirmed using peak splitting patterns. Peak splitting is not typically observed for natural carbon-13 abundance experiments but was readily observed for 1,2-$^{13}C_2$-Glc because C1 and C2 are 99% enriched carbon-13.

CHAPTER 3: MECHANISTIC INSIGHTS TO THE WATER ADDUCTION ION/MOLECULE REACTION

3.1 Hexoses and Monodeoxy Glucoses

Distinguishing Hexoses and Monodeoxy Glucoses

Hexoses have six oxygen atoms available to coordinate to a metal cation, creating many possible multidentate binding sites. Coordination of a metal cation to a hexopyranose depends on anomeric and stereochemical configuration and pyranose ring conformation, all of which are intertwined to create a unique oxygen atom orientation. One example tridentate Li-O coordination formed by Glucose (Glc), along with the carbon and oxygen labels, is shown in Figure 3.1a. A computational study on the interaction of Na^+ with Glc in aqueous solution exhibited the relationship between pyranose conformation and the available variety of metal cation coordinations[61]. The research presented herein applies a similar computational strategy. DFT is used to determine the possible multidentate lithium-oxygen coordinations, and their relative stabilities in both the solution and gas phase, across the complete pyranose structural landscape of 4 hexoses and 5 monodeoxy hexoses. A comprehensive set of DFT optimized lithium cationized hexoses provide a structural framework to complement the water adduction ion/molecule reaction in an ion trap MS and promote understanding of lithium cationization of hexoses.

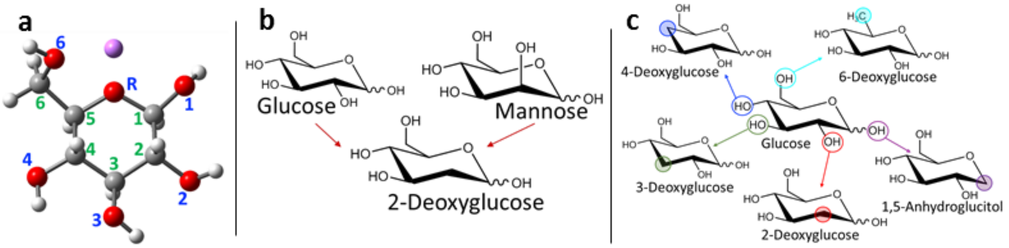

Figure 3.1 a) The primary tridentate lithium coordination structure for β-glucose with oxygen and carbon number labels in blue and green text, respectively. b) C2 deoxygenation of epimers glucose and mannose results in the same molecule. c) An exhaustive list of monodeoxy glucopyranoses.

Axial epimers of Glc provide insight towards the effect of stereochemistry on lithium cationization and water adduction reactivity. A unique relationship exists between Glc, mannose (Man) and 2-deoxyglucose (2dGlc) that allows comparison of an equatorial, axial and absent hydroxyl group (Figure 3.1b). This relationship extends to the C3 and C4 positions with allose/3-deoxyglucose and galactose/4-deoxyglucose. An exhaustive list of monodeoxy glucopyranoses (Figure 3.1c) was studied to probe the contribution of each hydroxyl group to lithium cationization around the pyranose ring and water adduction unreacted fraction. Computational modeling of the lithium cationized hexoses aids interpretation of the experimental water adduction data.

Decay curves were measured for each hexose and monodeoxy hexose by isolating $[M+Li]^+$ in the ion trap and varying reaction time by applying a delay prior to mass analysis. The scan delay was incremented between 0–1000 ms, and at each reaction time the ratio of intensities of $[M+Li]^+ / ([M+Li]^+ + [M+Li+H_2O]^+)$ was measured. The decay curves plotted in Figure 3.2 show that all the monodeoxy hexoses finish reacting (asymptote) in less than 1000 ms, which was also true for the hexoses. The unreacted fraction at which each sugar asymptotes is the final R_U, and the change in the unreacted fraction ratio at short reaction times informs of the reaction rate[47]. The five monodeoxy hexoses and four hexoses were completely distinguished by their final unreacted fractions, meaning that each sugar adopted different amounts of reactive and unreacted forms of $[M+Li]^+$. The final R_U values for all 9 sugars are reported in Table 3.1.

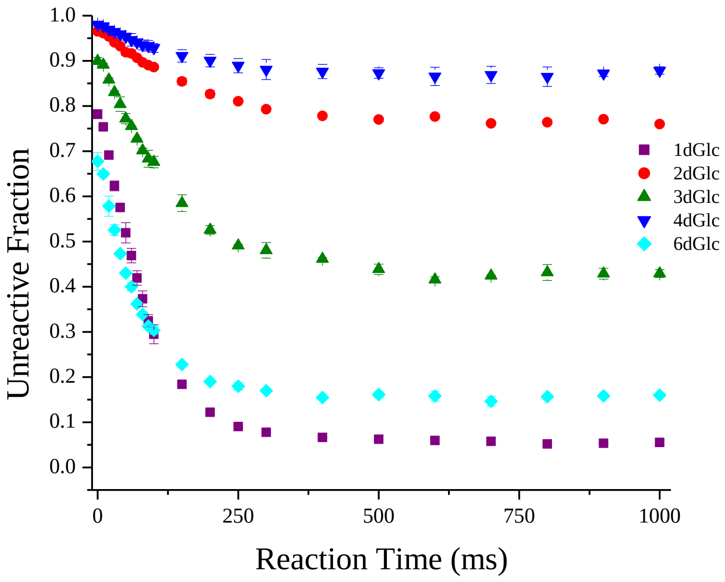

Figure 3.2 Water adduction reaction curves for the 5 monodeoxy glucoses studied.

The structures for all the monodeoxy hexose molecules are shown in Figure 3.1c. The deoxyhexose 1,5-anhydroglucitol (1dGlc) is simply glucose with a hydrogen in place of the hydroxyl at the anomeric C1 position. The C2 hydroxyl is replaced by a hydrogen on 2-deoxyglucose with which the nomenclature is consistent for the remaining monodeoxy glucose structures. A general naming scheme for each lithium cationized hexose structure will be used for the remainder of this discussion: *anomer*-Hexose(LiBoundOxygen-LiBoundOxygen). For example, the model of β-Glc in Figure 3.1a has a tridentate interaction with lithium where the oxygen atom of the C1 and C6 hydroxyls and the ring oxygen are coordinated to lithium and is denoted β-Glc(1-R-6).

Lithium coordinations to different oxygen atoms of the pyranose ring are formed in the electrospray process. The absence of a hydroxyl group from different positions around the pyranose ring has a varying impact on the reaction of $[M+Li]^+$ with water in the ion trap. Removal of a single hydroxyl group from the sugar ring eliminates at least two potential sites for lithium coordination. For example, absence of the C2 hydroxyl eliminates the bidentate coordination site between the C1 and C2 hydroxyls, as well as the bidentate coordination site between the C2 and C3 hydroxyls. With the (1-2) and (2-3) coordinations becoming impossible, the measured water adduction unreacted fraction is solely a product of the remaining possible sites. One- and 6-Deoxyglucose had low unreacted fractions whereas 2- and 4-Deoxyglucose had high unreacted fractions. Three-Deoxyglucose had an intermediate unreacted fraction when compared to the other deoxy sugars. Differences between hexose unreacted fractions show that water adduction in the ion trap can measure differences in lithium cation binding, due to the removal of binding sites via deoxygenation or due to differences in stereochemistry. The effect of stereochemistry, deoxygenation, anomeric configuration, and pyranose ring conformation on water adduction unreacted fraction will be discussed in forthcoming sections.

Table 3.1 Unreacted fractions reported with 1 standard deviation for all sugars studied (n ≥ 7).

Hexose	**Unreacted Fraction**	**Axial Hydroxyl**
Glucose (Glc)	0.289 ± 0.003	-
Mannose (Man)	0.733 ± 0.009	C2
Allose (All)	0.239 ± 0.005	C3
Galactose (Gal)	0.348 ± 0.001	C4
1,5-Anhydroglucitol (1dGlc)	0.056 ± 0.002	-
2-Deoxyglucose (2dGlc)	0.743 ± 0.009	-
3-Deoxyglucose (3dGlc)	0.424 ± 0.008	-
4-Deoxyglucose (4dGlc)	0.882 ± 0.010	-
6-Deoxyglucose (6dGlc)	0.183 ± 0.009	-

1-Deoxyglucose and Glucose

To study the reactivity of bi- and tridentate lithium coordinations, Glc and the anomerically-locked methylglucosides were used. The primary $^4C_1$ tridentate (unreacted) structure for β-Glc, denoted β-Glc(1-R-6), binds lithium to the C1 and C6 hydroxyls, and the ring oxygen. Based on theoretical calculations, the (1-R-6) interaction only exists for β-Glc and not for α-Glc because the anomeric hydroxyl is opposite the hydroxymethyl (C6 hydroxyl) with respect to the "plane" of the ring. DFT calculations allow investigation of individual anomers, but experimental results from Glc are always a measurement of an anomeric mixture. The DFT energy minimized structures for lithium cationized α- and β-Glc are shown in Figure 3.3.

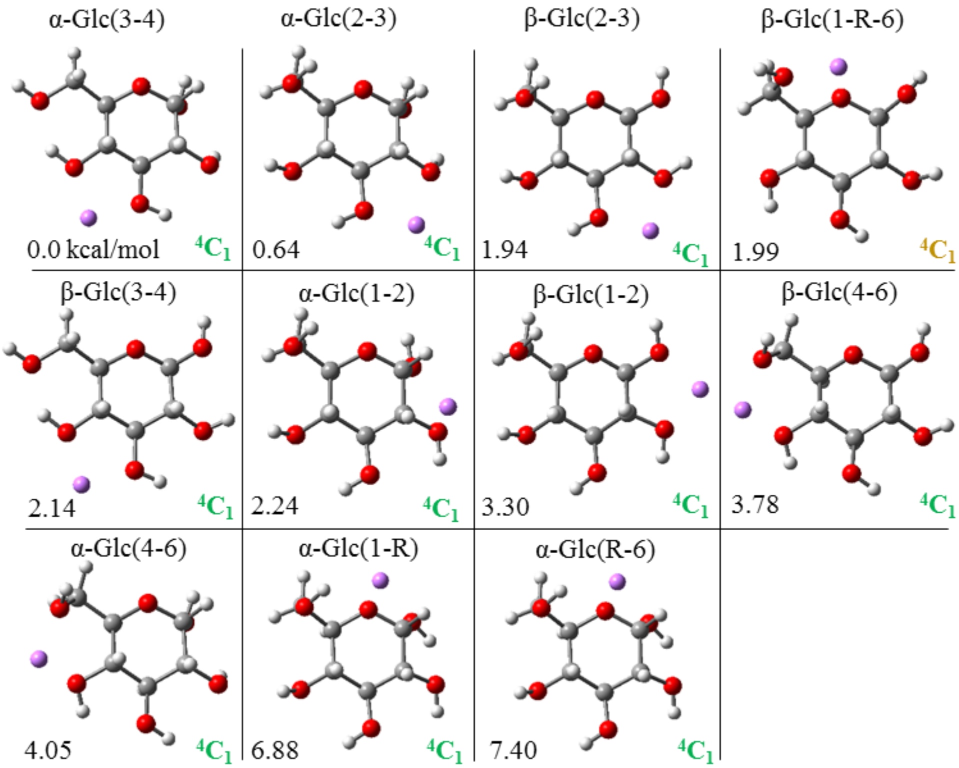

Figure 3.3 Gas-phase DFT optimized structures for lithiated α- and β-Glc. Relative Gibbs free energies expressed in kcal/mol are based on solution-phase vibrational calculations. Pyranose ring conformation is labeled and color coded to represent the number of oxygen atoms coordinated to lithium (green = bidentate, yellow = tridentate, red = tetradentate).

Anomerically-locked α- and β-methylglucosides were used to experimentally measure the individual Glc anomers. Methylglucosides (MeGlc) have a methoxy group at the C1 position, instead of a hydroxyl group, preventing them from ring-opening and mutarotating in solution. Replacement of a hydroxyl with a methyl group was found not to affect metal cation complexation in solution[62], nor did it alter the chair conformation equilibria of Glc, Man or Gal[63]. The methoxy group was found not to alter water adduction reactivity of Glc by measuring the unreacted fraction of a mixture of α- and β-MeGlc that matched the natural anomeric ratio of Glc. The water adduction metrics of $[M+Li]^+$ for the anomerically locked α- and β-MeGlc were reported previously[48]. The unreacted fractions were 0.045 and 0.261 for α-MeGlc and β-MeGlc, respectively. The inability to mutarotate to the β-anomer reduced the unreacted fraction of α-MeGlc, because in the $^4C_1$ conformation it cannot form tridentate interactions with lithium. The small fraction of unreacted $[\alpha\text{-MeGlc+Li}]^+$ must arise from the $^1C_4$ chair, boat or skew-boat conformations. All of the hydroxyls are oriented axially in the $^1C_4$ chair of MeGlc which creates tri- and tetradentate lithium binding sites. Water adduction results for MeGlc show that the β-anomer of Glc is the main contributor to unreacted structures.

The contribution of the β-Glc(1-R-6) structure to the final unreacted fraction of Glc was highlighted using 1dGlc. The anomeric hydroxyl of Glc is replaced by a hydrogen to generate 1dGlc eliminating the possibility for (1-2) and (1-R-6) interactions. The absence of an oxygen at the C1 position yielded an experimental final unreacted fraction of 0.056 ± 0.002. DFT calculations predicted there would be no tridentate interactions for 1dGlc in the $^4C_1$ conformation, which correlated well to the experimental unreacted fraction. Four gas-phase lithium cationized structures for the $^4C_1$ conformation, and two other conformations, of 1dGlc are shown in Figure 3.4.

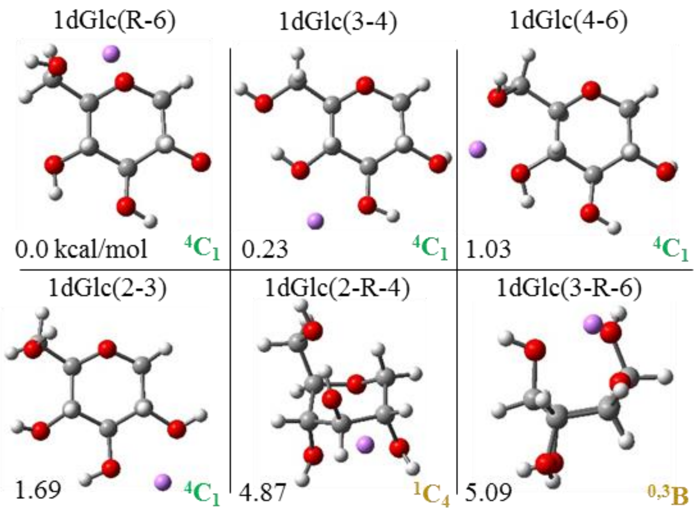

Figure 3.4 Gas-phase DFT optimized structures for the reactive bidentate structures of 1dGlc in the $^4C_1$ conformation and two unreacted tridentate structures. Relative Gibbs free energies expressed in kcal/mol are based on vibrational calculations with water as the implicit solvent.

When considering only the $^4C_1$ conformation of [1dGlc+Li], a tri- or tetradentate interaction cannot exist and complete reaction would be expected (unreacted fraction = 0.00). As previously mentioned, and as indicated by the nonzero experimental unreacted fraction of 1dGlc, the entire conformational space of sugar ring conformation and cation binding positions must be considered. The $^1C_4$ chair, as well as all boat and skew-boat conformations were modeled. Two tridentate structures (Figure 3.4) were within 5 kcal/mol of the most stable 1dGlc(R-6) structure in solution which may explain the small portion of unreacted [1dGlc+Li]$^+$. Based on a Boltzmann distribution at 400 K, the two tridentate structures had a combined estimated abundance of 0.18% of the total [M+Li]$^+$ population. Solution-phase abundance estimates failed to describe the 5% unreacted fraction of 1dGlc, assuming no internal energy was added to [M+Li]$^+$ in the MS ion optics to induce isomerization.

In the electrospray droplet $[M+Li]^+$ complexes are solvated, adopting various structures that are favorable in the solution phase. When $[M+Li]^+$ are released into the gas phase they become kinetically trapped as the solution phase structures unless energy is provided for isomerization. The ion optics of the MS were used to impart internal energy into $[M+Li]^+$. The region between the MS inlet capillary and skimmer cone is held around 1.3 mbar, and upon increasing the capillary/skimmer voltage difference $[M+Li]^+$ underwent increasingly energetic collisions with neutral gas molecules. Increasing the voltage difference between the capillary and skimmer yielded an increase in unreacted fraction for some lithium cationized hexoses (see Figure 3.5 and Chapter 4.1). The increasing unreacted fraction for $[M+Li]^+$ was attributed to isomerization of kinetically trapped bidentate structures that are favorable in the solution phase to tridentate structures that are more favorable in the gas phase.

The unreacted fractions of $[M+Li]^+$ as a function of the capillary/skimmer voltage difference for 5 of the hexoses in this study are shown in Figure 3.5. Internal energy was imparted into [α-MeGlc+Li]$^+$ in the MS ion optics and an increased unreacted fraction was measured. The increase was attributed to isomerization of bidentate $^4C_1$ structures to unreacted boats or skew-boats[48]. The onset of change in unreacted fraction for α-MeGlc was between a capillary/skimmer voltage difference of 60 and 70 V. The onset of change for Glc was also observed between 60 and 70V, suggesting that bidentate structures of α-MeGlc and α-Glc isomerize to tri- or tetradentate structures at similar critical energies. Imparting internal energy into β-MeGlc resulted in minimal change in unreacted fraction. β-MeGlc forms bidentate and some tridentate $[M+Li]^+$ structures in the electrospray droplet. Upon gaining internal energy the bindentate structures cannot gain enough energy to isomerize in the ion optics. These ion optics isomerization experiments were complementary to the solution and gas-phase DFT optimized structures, as discussed for 6dGlc below.

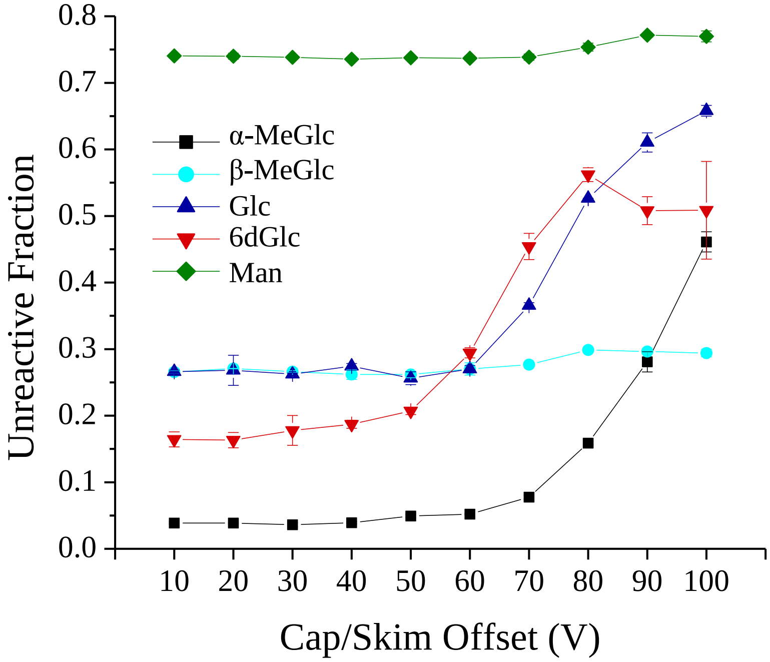

Figure 3.5 Unreacted fraction for $[M+Li]^+$ as a function of capillary/skimmer cone voltage difference

6-Deoxyglucose and Glucose

Replacing the exocyclic hydroxyl group at the C6 position of Glc with a hydrogen results in 6dGlc. Because the hydroxyl at C1 is present, 6dGlc can exist as either the α- or β-anomer. The primary tridentate β-Glc(1-R-6) chair structure cannot exist for β-6dGlc, and α-6dGlc still cannot form tridentate coordinations in the $^4C_1$ chair. An unreacted fraction of 0.183 ± 0.009 was measured for 6dGlc, but an unreacted fraction similar to that of 1dGlc was initially hypothesized. Theoretical calculations and ion optics isomerization experiments both provide insight into the near 20% unreacted fraction. 6dGlc was observed to ring pucker at relatively low voltages; upon increasing the internal energy of $[M+Li]^+$ as seen in Figure 3.5 the unreacted fraction of 6dGlc increased from 0.18 to 0.56. The unreacted fraction of 6dGlc began to rise at a capillary/skimmer voltage difference of 50V, a lower voltage than all other sugars. The onset of isomerization at lower capillary/skimmer voltages for 6dGlc suggested that it can readily pucker from bidentate $^4C_1$ chair structures to tridentate structures in other ring conformations. One possible explanation for the low activation barrier for ring puckering of 6dGlc is the absence of the exocyclic C6 hydroxyl group. The C6 hydroxyl of Glc can rotate freely about the C5-C6 bond and create consecutive hydrogen bonding around the pyranose ring. Fewer consecutive hydrogen bonds may account for the lower critical energy required for ring puckering upon collisional activation. Also, isomerization of the 6dGlc $^4C_1$ chair to other conformations has a lower activation barrier because they experience less steric hindrance in the absence of the far-reaching C6 hydroxyl.

Eight solution-phase structures were within 5 kcal/mol of one another for 6dGlc (Figure 3.6). One of the eight solution phase structures had a tridentate (1-R-4) lithium coordination for α-6dGlc in the $^5S_1$ conformation that was 4.12 kcal/mol higher than the most stable $^4C_1$ structure. This (1-R-4) tridentate solution phase structure was more stable than the (1-R) interaction because puckering to the $^5S_1$ skew boat from the $^4C_1$ chair enabled another stabilizing lithium coordination. Additionally, the $^5S_1$ conformation of 6dGlc was relatively stable because of the absent C6 hydroxyl. If present, the C6 hydroxyl would be unfavorably positioned above the pyranose ring (see structure α-6dGlc(1-R-4) in Figure 3.6).

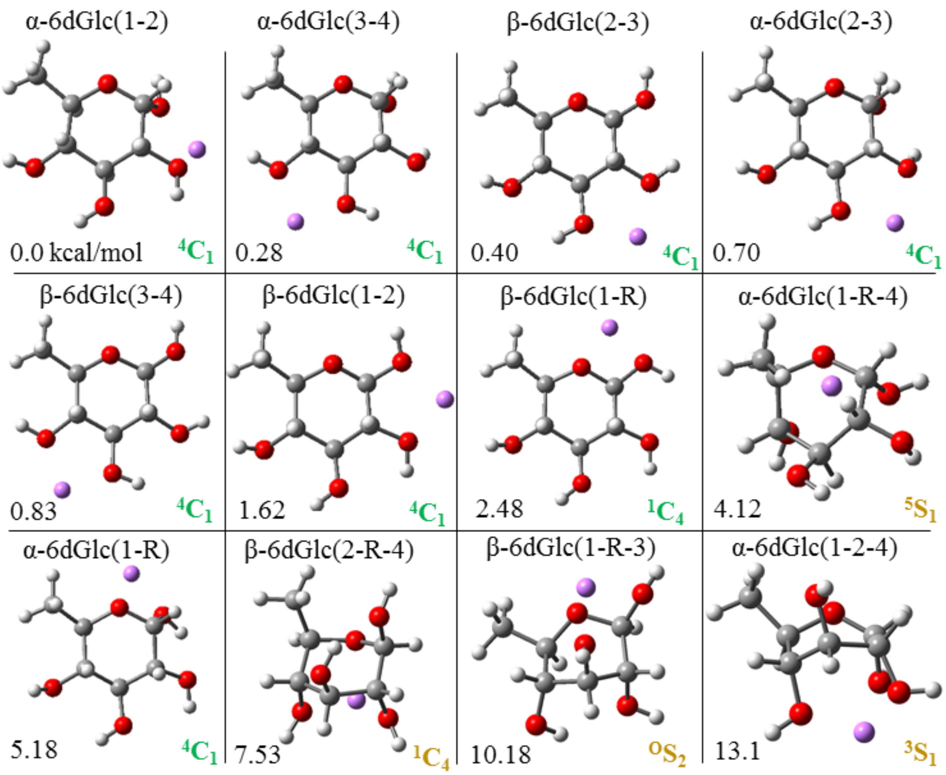

Figure 3.6 Gas-phase DFT optimized structures for lithiated α- and β-6dGlc. Relative solution phase Gibbs free energies are reported in kcal/mol. Sugar ring conformation is provided and labeled green or yellow for bidentate or tridentate interactions, respectively.

Equally important to solution phase energies was the gas-phase stability of the $^3S_1$ and $^OS_2$ skew boats, as well as the $^1C_4$ chair that have tridentate interactions with lithium. These three tridentate structures were unfavorable in solution phase (>7.5 kcal/mol) but became more favorable *in vacuo* (Figure 3.7). The increased stability *in vacuo* suggested that a third coordination to lithium overcomes the steric hindrance and ring strain of the axial chair and skew boat conformations. The tridentate $^3S_1$ skew boat, α-6dGlc(1-2-4), was 13.11 kcal/mol less stable in solution than the most stable bidentate chair, α-6dGlc(1-2). Conversely, *in vacuo* the $^3S_1$ skew boat α-6dGlc(1-2-4) was 1.12 kcal/mol more stable than the $^4C_1$ chair, α-6dGlc(1-2)

To visualize the change in relative stabilities between the solution and gas phases, DFT optimized structures for α- and β-6dGlc are represented as dots in order of relative Gibbs free energies in Figure 3.7, where green dots are bidentate (reactive) and yellow dots are tridentate (unreacted) structures. On the left side of Figure 3.7 the solvated structures are in order of relative solution-phase Gibbs free energies, and the corresponding gas-phase structures and their relative Gibbs free energies are also plotted. Solvated structures without a ring conformation label are in the $^4C_1$ chair conformation. The labeled solution-phase skew boat and axial chair structures are matched to their gas-phase structures with an asterisk of the same color. Dashed arrows in Figure 3.7 correlate bidentate solution-phase structures to their gas-phase relative energies. Solid arrows represent proposed gas-phase isomerization from the kinetically trapped bidentate coordination to a more favorable tridentate structure. The proposed isomerization scheme for the $^4C_1$ chair, α-6dGlc(1-2), to the α-6dGlc(1-2-4) $^3S_1$ skew boat, denoted by the red arrows, is shown on the right hand side of Figure 3.7.

If enough internal energy is provided to α-6dGlc(1-2) in the MS ion optics it can isomerize to the more stable $^3S_1$ tridentate structure, α-6dGlc(1-2-4). The red arrows in Figure 3.7 show the progression of α-6dGlc(1-2) from solution to the gas phase, followed by isomerization to an unreacted structure. The blue arrows in Figure 3.7 represent the progression of β-6dGlc(1-R) from solution to gas phase, followed by isomerization to the unreacted $^OS_2$ skew boat β-6dGlc(1-R-3). These theoretical results supported the experiment, where 6dGlc unreacted fraction reached 0.56 as internal energy was imparted (Figure 3.5). The two bidentate structures that were proposed to undergo isomerization, α-6dGlc(1-2) and β-6dGlc(1-R), had estimated relative abundances of 16.98% and 2.50%, respectively. These two structures constituted 19.48% of the structures formed during electrospray, helping to account for the increased 6dGlc unreacted fraction as the capillary/skimmer voltage difference was raised.

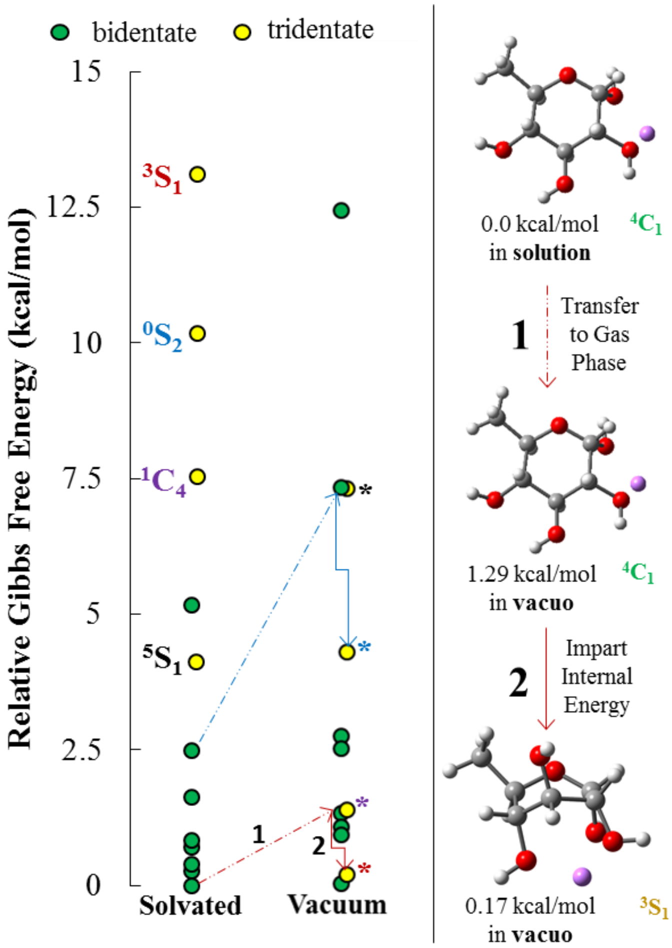

Figure 3.7 (Left) Relative energies of DFT calculated local minima, represented as dots, for α- and β-6dGlc in solution and *in vacuo.* All solution-phase dots without a ring conformation label are in the $^4C_1$ chair. An asterisk next to tridentate gas-phase structures denotes the corresponding solution-phase structures by color. The arrows are proposed isomerization schemes and are detailed in the text. (Right) Proposed reaction coordinate for the gas-phase isomerization of the $^4C_1$ chair, α-6dGlc(1-2), to the α-6dGlc(1-2-4) $^3S_1$ skew boat.

Mannose, 2-Deoxyglucose and Glucose

Glc and Man are epimeric aldohexoses that differ at the C2 position, and the water adduction characteristics of these epimers are vastly different (Table 3.1). The axial C2 hydroxyl of Man stabilizes the alpha anomer, inducing an anomeric ratio (α:β = 66.23:32.85) that is opposite of Glc (α:β = 37.63:61.96)[8]. Because the axial C2 hydroxyl of Man is oriented on the same side of the pyranose ring as the exocyclic hydroxymethyl, there are many potential tridentate lithium coordination sites for both α- and β-Man anomers. The high unreacted fraction of Man (0.733 ± 0.009) suggested favorable tridentate solution-phase structures. The optics isomerization experiment (Figure 3.5) for Man showed minor change in unreacted fraction as increased internal energy was imparted into $[\mathrm{Man+Li}]^+$, which was consistent with DFT calculations that predicted unreacted Man structures to be most favorable both in solution and *in vacuo*.

Thirteen unique DFT optimized structures for Man were within 5.46 kcal/mol in solution, and their relative Gibbs free energies (solution and *in vacuo*) are portrayed using dots in Figure 3.8. The four most favorable solution-phase structures had tri- or tetradentate coordinations with lithium with relative Gibbs free energies of 0.0, 0.12, 0.18 and 0.98 kcal/mol, respectively. Based on a Boltzmann distribution at 400 K, the percent abundances of the four unreacted structures summed to 71.98% (abundances were 45.38, 11.79, 10.84 and 3.97%, respectively). The calculated abundance of unreacted Man structures in solution closely matches the experimentally measured unreacted fraction. Solution-phase structures explained the high water adduction unreacted fraction of Man, and corresponding gas phase structures detail its minimal change when internal energy was added in the MS ion optics. Unlike 6dGlc, Man prefers tri- or tetradentate lithium coordinations both in solution and *in vacuo*. Imparting internal energy into

[Man+Li]⁺ either induces isomerization from unreacted structures to other unreacted structures or little isomerization of bidentate structures occurs, rendering the R_U mostly unaffected.

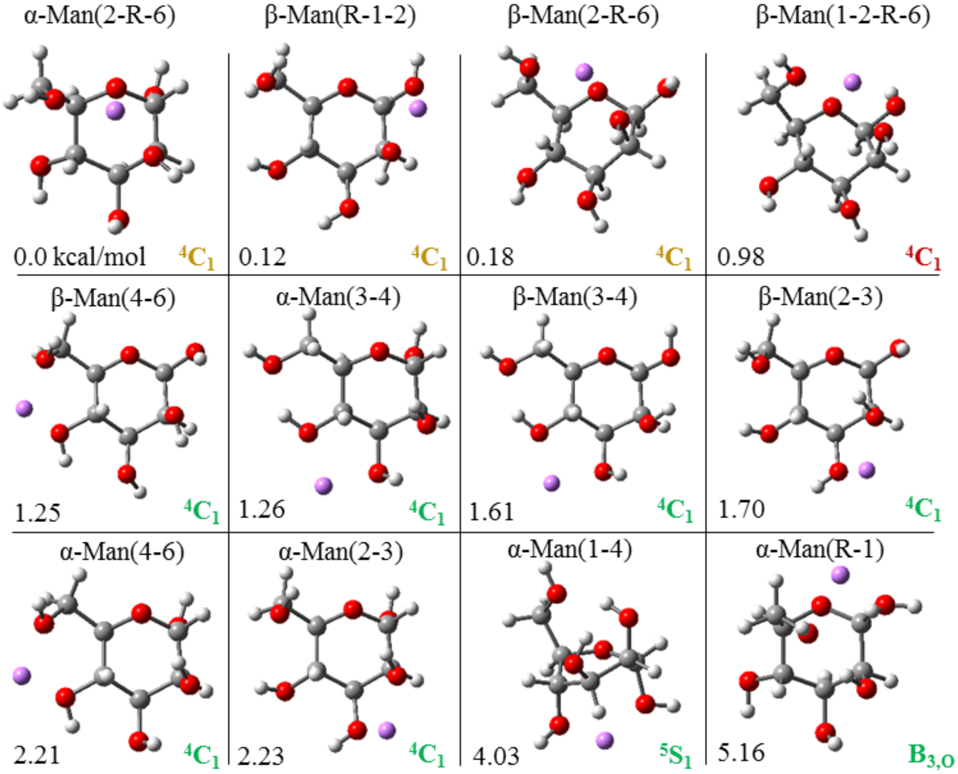

Figure 3.8 Gas phase DFT optimized structures for α- and β-Man. Relative solution phase Gibbs free energies are reported in kcal/mol. Sugar ring conformation is provided and labeled green, yellow, or red for bidentate, tridentate, or tetradentate interactions, respectively.

Upon deoxygenation at the C2 position of either Glc or Man, 2dGlc is formed (Figure 3.1b). Nearly identical unreacted fractions were measured for mannose (0.733 ± 0.009) and 2dGlc (0.743 ± 0.009). The β-2dGlc(1-R-6) tridentate structure was most favorable in solution but was accompanied by six bidentate structures ranging from 0.19 to 3.42 kcal/mol and five tridentate structures ranging from 4.21 to 7.46 kcal/mol (Figure 3.9). The β-2dGlc(1-R-6) structure had an estimated abundance of 43.20%, and the remaining five tri- and tetradentate structures combined for 0.28% estimated abundance in solution. Based on these calculations, the high unreacted fraction of 2dGlc is not solely due to tri- and tetradentate solution-phase structures (which was the case for Man). The high unreacted fraction for 2dGlc may be due to very low isomerization activation barriers for bidentate structures of 2dGlc.

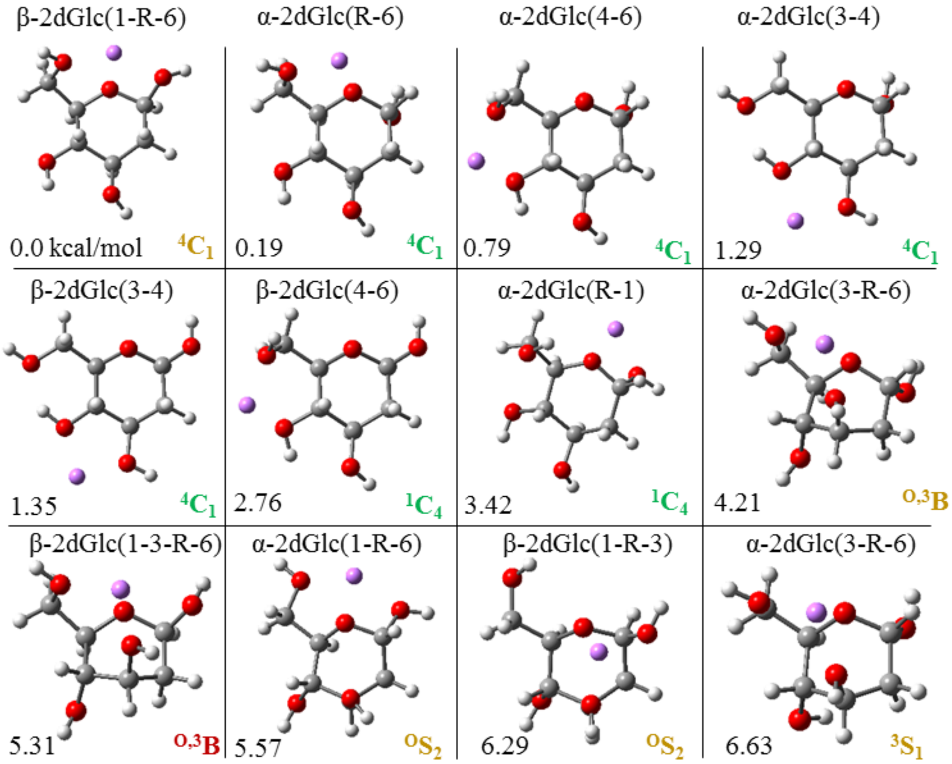

Figure 3.9 Gas-phase DFT optimized structures for α- and β-2dGlc. Relative solution phase Gibbs free energies are reported in kcal/mol. Sugar ring conformation is provided and labeled green, yellow or red for bidentate, tridentate or tetradentate interactions, respectively.

Comparison of Glc, Man and 2dGlc revealed that the equatorial C2 hydroxyl of hexopyranoses is a major contributor to overall water adduction reactivity. Man is highly unreacted due to its axial C2 hydroxyl creating many possible tridentate lithium coordinations. Loss of the (1-2) and (2-3) lithium binding sites for 2dGlc, concurrent with a high unreacted fraction for 2dGlc indicates that these bidentate lithium coordination sites are important contributors to the population of Glc structures that react.

Allose, 3-Deoxyglucose and Glucose

Allose (All) is the axial epimer of glucose at the C3 position and deoxygenation at the C3 position from either epimer generates 3dGlc. The unreacted fractions measured for Glc, All and 3dGlc were 0.289 ± 0.003, 0.239 ± 0.005 and 0.424 ± 0.008, respectively (Table 1). Deoxygenation at C3 resulted in an unreacted fraction for 3dGlc that is greater than for Glc. The structures for 3dGlc are shown in Figure 3.10. The higher unreacted fraction of 3dGlc was attributed to a higher probability for the most favorable β-3dGlc(1-R-6) to exist due to inability to form the (2-3) and (3-4) bidentate coordinations. The β-3dGlc(1-R-6) structure was estimated to be 36.94% abundant, contributing greatly to the unreacted fraction of 3dGlc. Additionally, the $^1C_4$ chair of 3dGlc was notably stable yielding the unreacted α-3dGlc(2-R-4) structure that was only 1.51 kcal/mol (estimated 1.95% abundance) relative to the most favorable $^4C_1$ structure. The $^1C_4$ conformation of α-3dGlc is more stable than that of Glc. Instability of the Glc axial $^1C_4$ chair stems from the unfavorable 1,3-diaxial interactions of the C1, C3 and C6 hydroxyls above the ring for β-Glc (or C3 and C6 hydroxyls above the ring for α-Glc) as well as the C2 and C4 hydroxyls below the ring for both anomers. Because α-3dGlc in the $^1C_4$ chair has no 1,3-diaxial interactions above the ring it has increased stability.

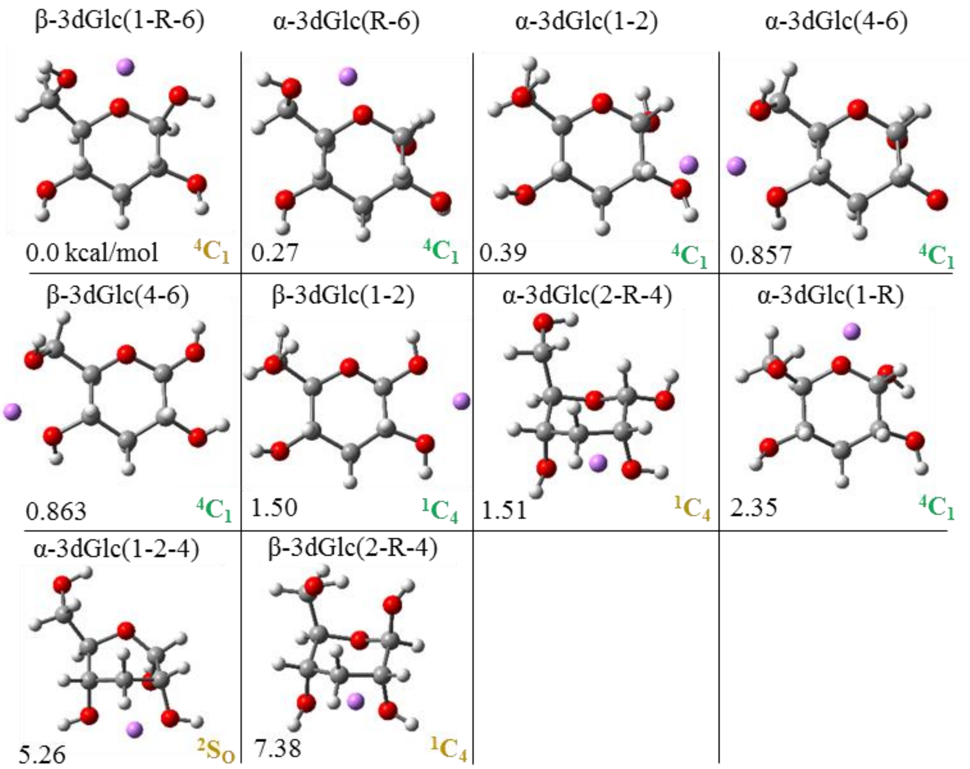

Figure 3.10 Gas phase DFT optimized structures for α- and β-3dGlcglucose. Relative solution phase Gibbs free energies are reported in kcal/mol. Sugar ring conformation is provided and labeled green or yellow for bidentate or tridentate interactions, respectively.

Allose (Figure 3.11) had a lower unreacted fraction than Glc. The structural composition of All in aqueous solution has been measured by NMR to be 91.7% pyranose (allopyranose α:β = 15.9:84.1), 8.29% furanose and 0.01% acyclic[8]. With β-All favored in aqueous solution it may seem counterintuitive that All has a lower unreacted fraction than Glc. A Boltzmann distribution demonstrated that the β-All(1-R-6) structure was only 0.84% abundant. Also, α-All cannot form the (1-2) coordination because the axial C3 hydroxyl is in close enough proximity to interact with the lithium cation, and instead forms the α-All(1-2-3) structure that is relatively favorable at 1.19 kcal/mol (but is estimated to be only 1.5% abundant.) Despite forming β-

All(1-R-6) and other tridentate interactions that are unique to All, the abundances of these structures are estimated to be low, resulting in a low unreacted fraction. The furanose anomers of All are marginally abundant in aqueous solution (as measured by NMR). The furanose structures of Idose and Talose were separated from pyranoses by differential ion mobility and were observed to react in a previous study[64]; furanose structures of All may react similarly.

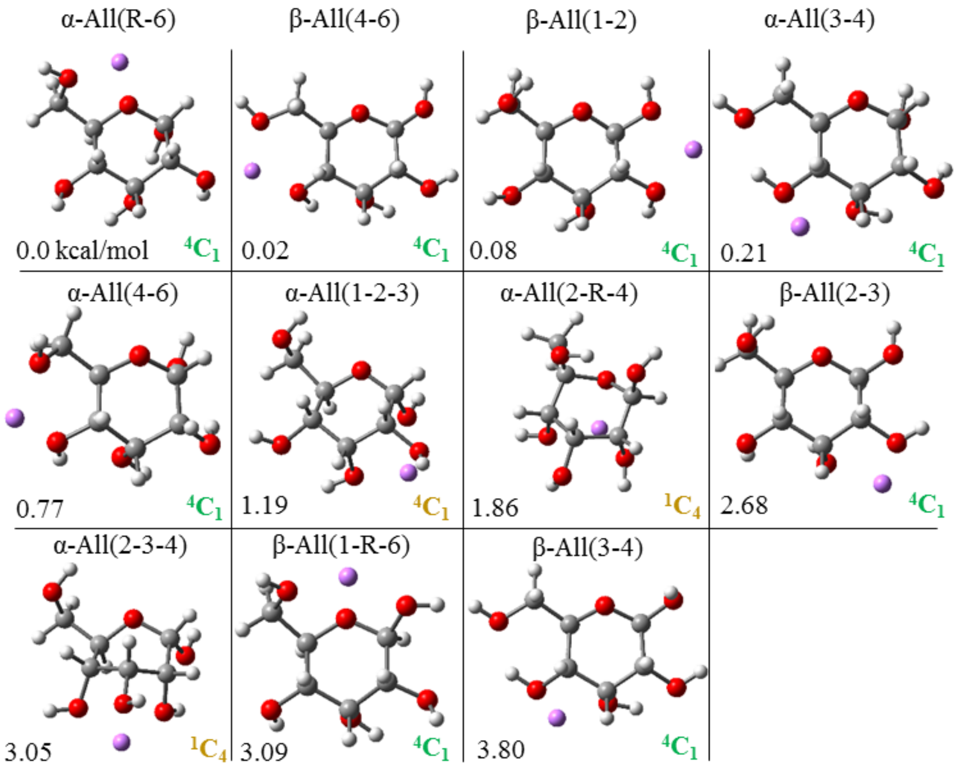

Figure 3.11 Gas phase DFT optimized structures for α- and β-allose. Relative solution phase Gibbs free energies are reported in kcal/mol. Sugar ring conformation is provided and labeled green or yellow for bidentate or tridentate interactions, respectively.

Galactose, 4-Deoxyglucose and Glucose

The relationship of Glc, Gal and 4dGlc at the C4 position is the same as previously discussed for the C2 and C3 positions. Unreacted fractions for Glc, Gal and 4dGlc were 0.289 ± 0.003, 0.348 ± 0.001 and 0.882 ± 0.010, respectively. The axial C4 hydroxyl of Gal resulted in an unreacted fraction increase relative to Glc, signifying a minor difference in reactivity between hexoses with an axial or equatorial C4 hydroxyl. Gal maintained a low unreacted fraction when compared to Man (axial C2 hydroxyl) suggesting that the equatorial C4 hydroxyl was not as crucial to $[M+Li]^+$ water adduction reactivity as the equatorial C2 hydroxyl. Stereochemistry at the C4 position did not have a major impact on water adduction metrics, but deoxygenation at this site drastically influenced the unreacted fraction.

Of the nine hexoses in this study, 4dGlc was the most unreacted. Absence of the C4 hydroxyl eliminates the (3-4) and (4-6) bidentate lithium binding sites, increasing the probability for lithium to create a tridentate coordination in the $^4C_1$ chair. DFT structures for 4dGlc are shown in Figure 3.12. A unique scenario arises for 4dGlc that is not applicable to the other hexoses discussed. The behavior of the hydroxyl groups adjacent to the deoxygenation site influences the water adduction unreacted fraction. The exocyclic hydroxyl at the C6 position of the pyranose ring can freely rotate about the C5-C6 bond to interact with lithium. If lithium coordinates to the C6 hydroxyl of Glc in solution and solvent is removed from $[Glc+Li]^+$ the lithium can end up in a bidentate (4-6) or tridentate (1-R-6) coordination by way of the rotational freedom of the C6 hydroxyl. This is not true for 4dGlc. When solvent is removed from $[4dGlc+Li]^+$, where Li is coordinated to the C6 hydroxyl, the lithium can only adopt the tridentate (1-R-6) coordination. It is possible that β-2dGlc undergoes a similar mechanism but is less pronounced because the C1 hydroxyl does not extend as far outwards from the ring as the C6 hydroxyl, nor does it have free rotation about a C-C bond.

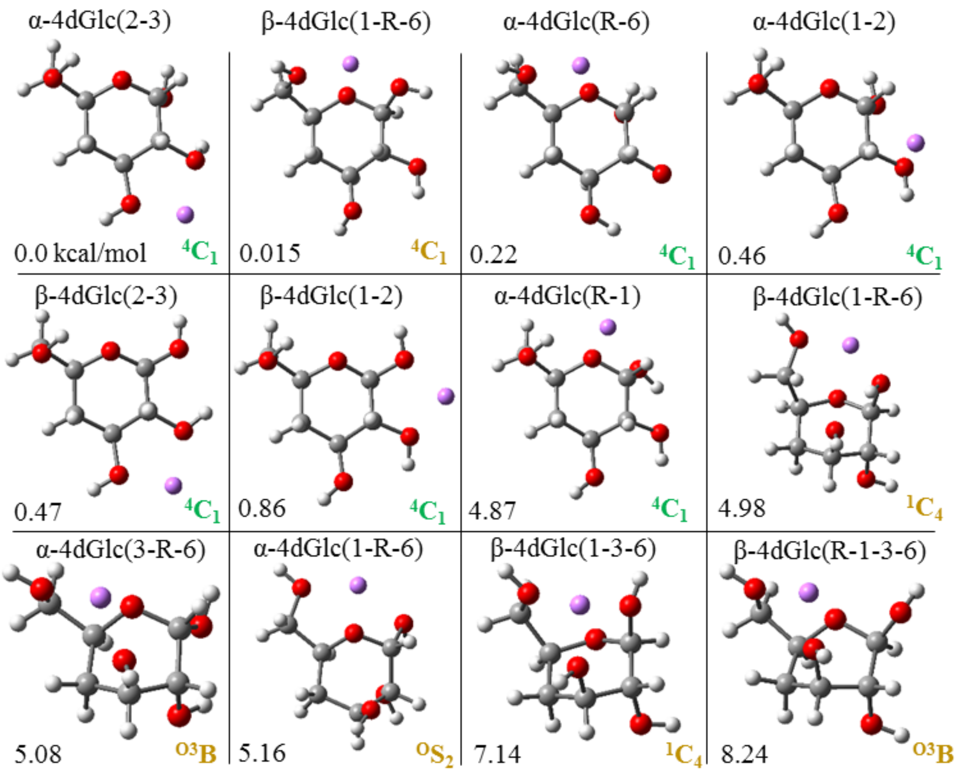

Figure 3.12 Gas phase DFT optimized structures for α- and β-4dGlc. Relative solution phase Gibbs free energies are reported in kcal/mol. Sugar ring conformation is provided and labeled green or yellow for bidentate or tridentate interactions, respectively.

3.2 Water Adduction to Inositols

Inositols are cyclic sugar molecules with the molecular formula $C_6H_{12}O_6$ which makes them isomeric to hexoses. Both inositols and hexoses are prevalent in biology, have multiple stereocenters, can assume various ring-puckering states and contain six-membered rings, but inositols have key structural differences from hexoses that simplify prediction of Li-O coordinations[65]. Hexoses form a six-membered pyranose ring with an oxygen atom contained in the ring and a hydroxymethyl group at the C5 position. The pyranose can ring-open and invert stereochemistry at the anomeric center; therefore, hexoses exist as two anomers. The hydroxymethyl group and anomeric mixture of hexoses complicates the prediction of Li-O coordinations that will form. The structural backbone of inositols is a cyclohexane ring where each carbon is functionalized with one hydroxyl group which can be in various stereochemical configurations (Figure 3.13). Because the inositol cyclohexane ring cannot open to the straight chain, inositols do not exist as a mixture of anomers. Due to the lack of a ring oxygen and hydroxymethyl group, planes of symmetry in inositol structure help reduce the number of unique Li-O coordinations any given inositol stereoisomer can form. Hexoses are most stable in the $^4C_1$ chair conformation and, thus, it is conventional to illustrate hexoses in the $^4C_1$ chair. Inositols are generally illustrated in the $^1C_4$ chair conformation, and any mention of the inositol chair structure relates to the $^1C_4$ chair (see Figure 3.13).

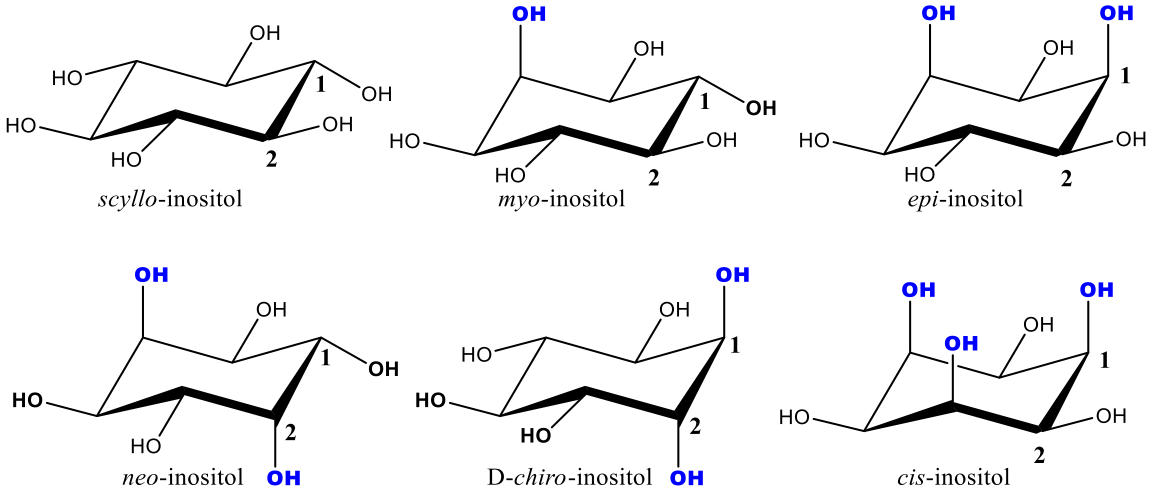

scyllo-inositol *myo*-inositol *epi*-inositol

neo-inositol D-*chiro*-inositol *cis*-inositol

Figure 3.13 Structures of six inositol isomers used in this study. Axial hydroxyl groups are colored blue and equatorial hydroxyl groups are black.

Considering only the chair conformations shown in (Figure 3.13), *scyllo*, *neo*, and *chiro*-inositol can be predicted to form mainly bidentate Li-O coordinations. Equatorial hydroxyl groups are oriented towards the peripheral of the cyclohexane ring further from one another, promoting bidentate coordinations. Tri- and tetradentate Li-O coordinations often form in the presence of axial hydroxyl groups because they are oriented towards the center of the ring. Because *scyllo* has only equatorial hydroxyl groups in the chair conformation, no three or four oxygen atoms can coordinate the lithium in concert to create a tri- or tetradentate coordination. Therefore, *scyllo* was predicted to form many bidentate Li-O coordinations and to have a low R_U. DFT calculations for chair, boat and skewboat ring conformations show that *scyllo* only forms bidentate Li-O coordinations. The gas-phase optimized DFT structures for *scyllo* are shown in Figure 3.14 with their relative solution-phase energies in kcal/mol (expected in solution prior to ionization by ESI) and ring conformations noted. In Table 3.2, the relative solution-phase and gas-phase energies of each *scyllo* structure are listed in kcal/mol. As expected for *scyllo*, only bidentate Li-O coordinations are possible in the chair, boat and skewboat conformations resulting in a low R_U value and coinciding with a high water adduction reaction rate (Figure 3.15).

Table 3.2 Relative energies in kcal/mol for DFT solution and gas phase optimized structures of *scyllo*-inositol

Structure	Conformation	ΔG_{solv} (kcal/mol)	ΔG_{gas} (kcal/mol)
scyllo(4-5)	$^1C_4$	**0.00**	0.06
scyllo(1-2)	$^1C_4$	0.27	**0.00**
scyllo(3-4)	$^1C_4$	0.39	0.17
scyllo(5-6)	$^1C_4$	0.95	0.11
scyllo(1-6)	$^1C_4$	0.98	0.19
scyllo(2-3)	$^1C_4$	3.60	0.10

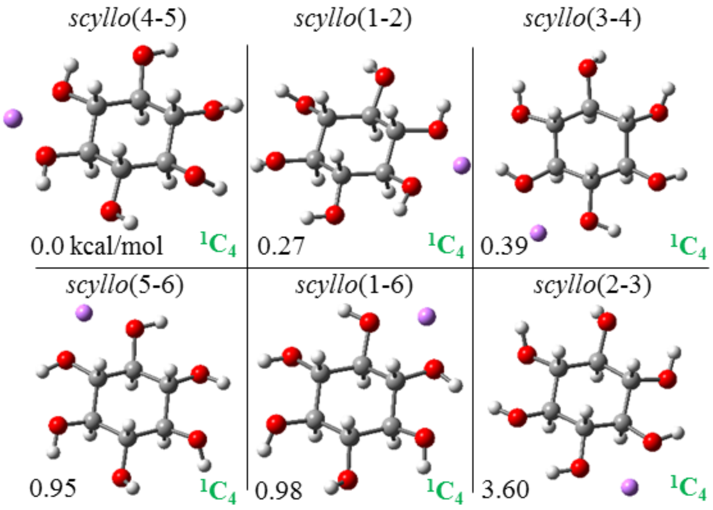

Figure 3.14 Gas-phase DFT optimized structures for lithiated *scyllo*-inositol. Relative solution phase Gibbs free energies are reported in kcal/mol. Inositol ring conformation is provided and labeled green or yellow for bidentate or tridentate interactions, respectively.

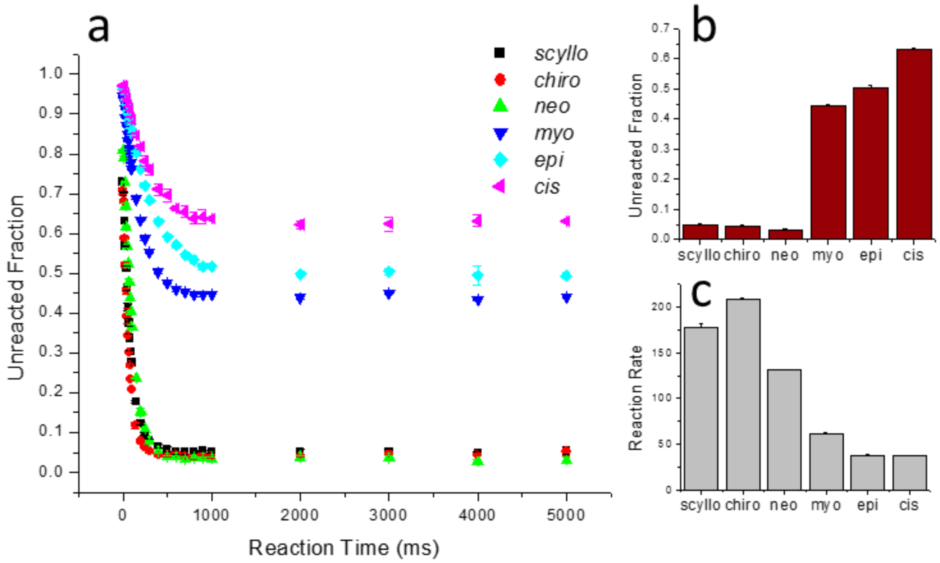

Figure 3.15 a) Water adduction curves for six inositol isomers, their b) final R_U values and c) reaction rates.

Neo and *chiro* have two axial hydroxyl groups each, but they are opposite one another with respect to the plane of the cyclohexane ring. Six chair and two skewboat DFT optimized structures of *neo* are shown in Figure 3.16, and their relative solution- and gas-phase energies are listed in Table 3.3. The C2 and C5 axial hydroxyl groups of *neo* are opposite one another with respect to both ring position and plane. C2 and C5 are adjacent to equatorial hydroxyl groups and another plane of symmetry, perpendicular to the ring plane, extends through C2 and C5. Equatorial/axial bidentate coordinations *neo*(1-2) and *neo*(2-3) are mirrored across the plane of symmetry, as well as the equatorial/axial coordinations *neo*(4-5) and *neo*(5-6). Two equatorial/equatorial bidentate coordinations *neo*(3-4) and *neo*(1-6) are also geometrically identical considering the C2/C5 plane of symmetry. It is impossible for *neo* to form a tridentate coordination in the $^1C_4$ or $^4C_1$ chair conformation, but *neo*(1-2-3) and *neo*(4-5-6) can exist in the $^2S_6$ and $^6S_2$ conformations, respectively. Skewboats are generally less favorable in solution phase than the chairs due to increased ring strain, but often become more favorable in the gas phase where an increased number of Li-O coordinations stabilizes the ring strain energy. The low R_U values measured for *scyllo, neo* and *chiro* corroborate the predicted formation of majority bidentate Li-O coordinations (Figure 3.15).

Table 3.3 Relative energies in kcal/mol for DFT solution and gas phase optimized structures of *neo*-inositol

Structure	Conformation	ΔG_{solv} (kcal/mol)	ΔG_{gas} (kcal/mol)
neo(4-5)	$^1C_4$	**0.00**	2.41
neo(1-2)	$^1C_4$	0.07	0.55
neo(1-6)	$^1C_4$	0.93	4.41
neo(2-3)	$^1C_4$	1.86	0.13
neo(3-4)	$^1C_4$	2.29	**0.00**
neo(5-6)	$^1C_4$	2.87	0.13
neo(1-2-3)	$^2S_6$	6.35	4.67
neo(4-5-6)	$^6S_2$	8.41	1.12

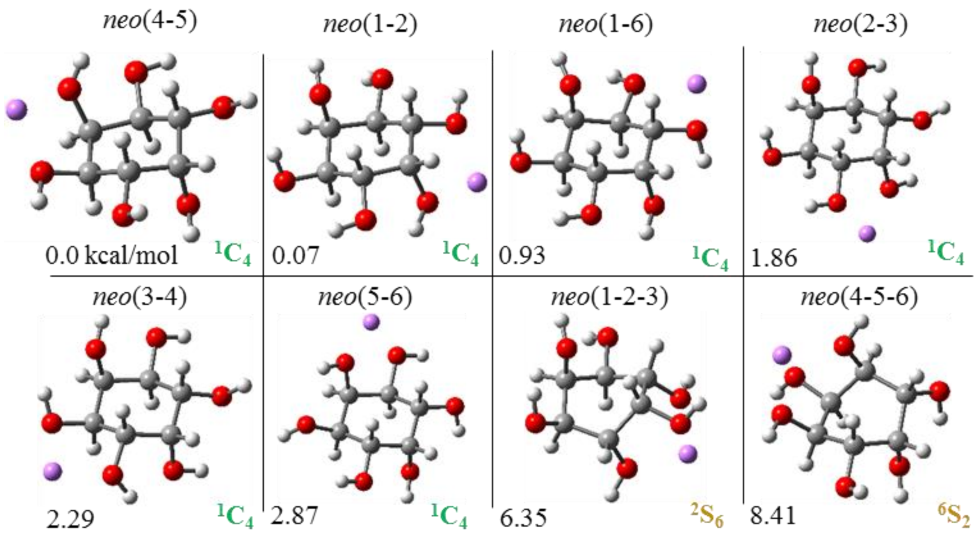

Figure 3.16 Gas-phase DFT optimized structures for lithiated *neo*-inositol. Relative solution phase Gibbs free energies are reported in kcal/mol. Inositol ring conformation is provided and labeled green or yellow for bidentate or tridentate interactions, respectively.

Chiro also has axial hydroxyl groups at the C1 and C2 positions that are on opposite sides of the cyclohexane-ring plane and will only form bidentate Li-O coordinations in the chair conformations. Five chair and two skewboat DFT optimized structures of *chiro* are shown in Figure 3.17, and their relative solution- and gas-phase energies are listed in Table 3.4. *Chiro* can form a tridentate coordination in the $^1S_5$ conformation as *chiro*(2-3-5) and *chiro*(1-5-6), but these structures in the solution phase are 10.26 and 11.96 kcal/mol higher in energy than the most stable solution-phase bidentate *chiro*(1-6) structure. When desolvated and in the gas-phase, the tridentate structures of *chiro* become slightly closer in energy but do not overtake the bidentate structures as most favorable. Because bidentate coordinations being more favorable in both in solution and *in vacuo,* a low R_U and high reaction rate were measured as predicted.

Table 3.4 Relative energies in kcal/mol for DFT solution- and gas-phase optimized structures of *chiro*-inositol

Structure	Conformation	ΔG_{solv} (kcal/mol)	ΔG_{gas} (kcal/mol)
chiro(1-6)	$^1C_4$	**0.00**	3.47
chiro(2-3)	$^1C_4$	0.03	3.70
chiro(3-4)	$^1C_4$	0.52	0.07
chiro(5-6)	$^1C_4$	0.90	0.04
chiro(4-5)	$^1C_4$	2.19	**0.00**
chiro(2-3-5)	$^1S_5$	10.26	5.78
chiro(1-5-6)	$^1S_5$	11.96	5.77

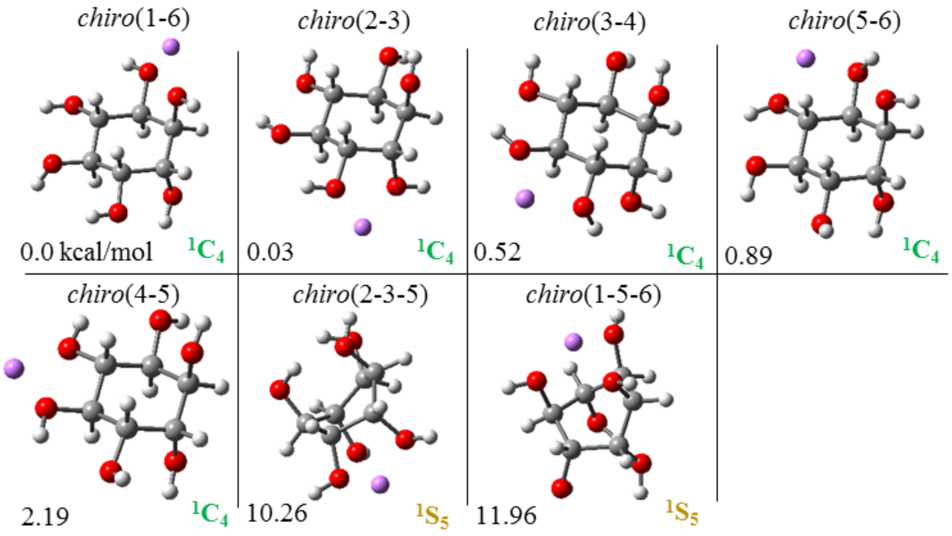

Figure 3.17 Gas-phase DFT optimized structures for lithiated *chiro*-inositol. Relative solution phase Gibbs free energies are reported in kcal/mol. Inositol ring conformation is provided and labeled green or yellow for bidentate or tridentate interactions, respectively.

Cis, epi and *myo* all have relatively high R_U values (Figure 3.15). In the $^1C_4$ chair conformation, *cis* contains three axial hydroxyl groups on the same side of the cyclohexane ring at C1, C3 and C5, as well as three equatorial hydroxyl groups that are oriented in the same direction. In the ESI droplet (based on solution phase DFT calculations) *cis*-inositol in the chair conformation can form tridentate, or hypothetically bidentate coordinations; regarding the latter, the lithium cation remains on the peripheral of the inositol structure and is slightly solvated by the surrounding solvent. Without surrounding solvent molecules to solvate the lithium it is more energetically favorable for lithium to form a tridentate coordination between the closely positioned oxygen atoms of *cis*. Therefore, the bidentate coordinations in solution transition to tridentate coordinations *in vacuo;* and, based on DFT calculations, *cis* in the chair conformation was expected to only exist with tridentate Li-O coordinations in the gas phase. Four chair, one boat and seven skewboat structures of *cis* are shown in Figure 3.18, and their relative solution and gas phase energies are listed in Table 3.5. The relative solution-phase energies of bidentate *cis* structures range from 5.74 to 6.20 kcal/mol higher than the most favorable structure, but once in the gas-phase the bidentate structures range 14.02 to 18.06 kcal/mol higher in energy. The unfavorable nature of bidentate gas-phase coordinations for *cis* stems from increased ring strain without a third Li-O coordination to stabilize the structure. DFT calculations strongly suggest that only tridentate coordinations should form for *cis*. Only tridentate coordinations would hypothetically result in an R_U close to 1, but for *cis* the measured R_U = 0.637. A sizeable fraction of $[$*cis*$+Li]^+$ ions are observed to adduct a water molecule in the ion trap, suggesting that either the complete array of structures is not known, or that specific tridentate coordinations may be able to adduct a water molecule and survive the process of ejection from the ion trap and detection. The strengths of Li-H_2O bonds of water-adducted sugars will be discussed in Section 3.5; and how the environment within the ion trap, and ion energy, may affect the stability of Li-H_2O coordinations, and ultimately the observed RU, are discussed in Chapter 4.

Table 3.5 Relative energies in kcal/mol for DFT solution and gas phase optimized structures of *cis*-inositol

Structure	Conformation	ΔG_{solv} (kcal/mol)	ΔG_{gas} (kcal/mol)
cis(1-3-5)	$^{1}C_{4}$	**0.00**	**0.00**
cis(1-2-3)	$^{1}C_{4}$	0.70	1.99
cis(3-4-5)	$^{1}C_{4}$	0.88	1.96
cis(1-5-6)	$^{1}C_{4}$	3.86	1.96
cis(2-3-4)	$^{2}S_{6}$	5.68	6.38
cis(1-4-5)	$^{1}S_{3}$	5.73	2.91
cis(2-3)	$^{5}S_{1}$	5.74	17.33
cis(1-6)	$^{6}S_{2}$	5.84	14.72
cis(1-2)	$^{1,4}B$	5.93	18.06
cis(5-6)	$^{3}S_{1}$	6.20	17.90
cis(4-5)	$^{2}S_{6}$	6.71	14.02
cis(3-4)	$^{1}S_{5}$	6.98	14.02

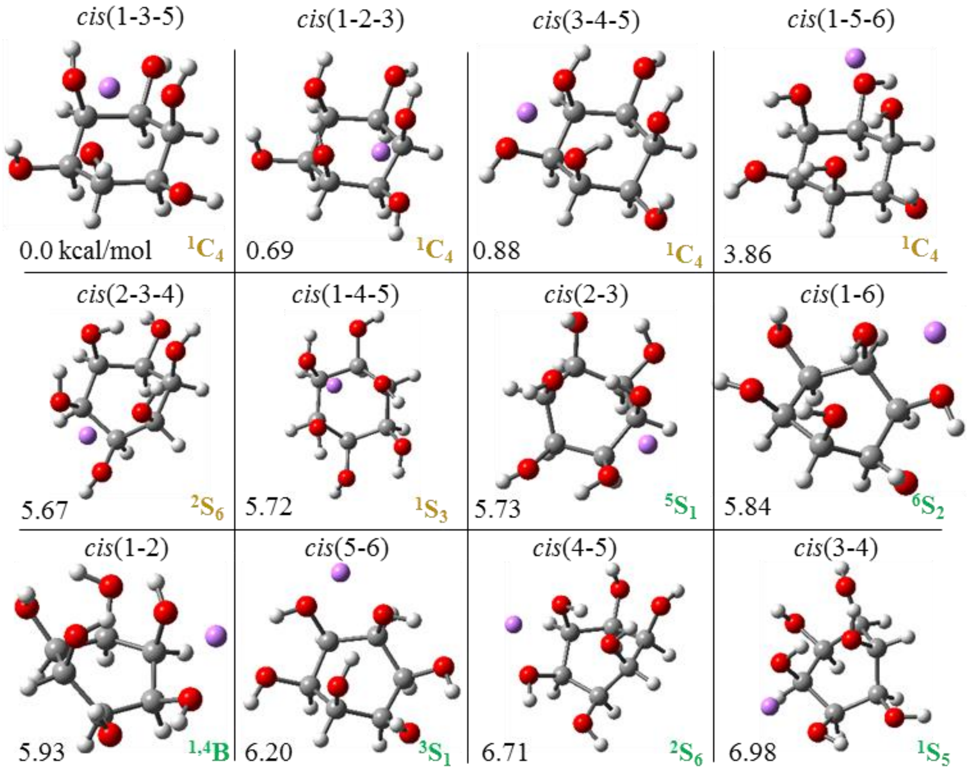

Figure 3.18 Gas-phase DFT optimized structures for lithiated *cis*-inositol. Relative solution phase Gibbs free energies are reported in kcal/mol.

Epi-inositol has 2 axial hydroxyl groups at the C1 and C5 positions both oriented "up" on the same side of the cyclohexane ring plane, 3 equatorial hydroxyl groups at the C2/C4/C6 positions also oriented "up" and 1 equatorial group oriented "down" at the C3 position for 4 total equatorial hydroxyl groups. With 1 axial and 3 equatorial hydroxyl groups on the same side of the ring plane, epi was predicted to form both bidentate and tridentate Li-O coordinations in the chair conformation. Six chair and six skewboat structures of *epi* are shown in Figure 3.19, and their relative solution and gas phase energies are listed in Table 3.6. The 1,3-axial hydroxyl groups at C1 and C5 flank the equatorial C6 hydroxyl group creating a geometry that is favorable to form the tridentate *epi*(1-5-6) structure that is 0.62 kcal/mol in solution and the most favorable structure in the gas phase. Equatorial/equatorial bidentate coordinations can form in the chair conformation between O2/O3 or O3/O4 to create *epi*(3-4) and *epi*(2-3) which are 1.38 and 1.52 kcal/mol in solution, respectively. These equatorial/equatorial bidentate interactions become relatively less stable in the gas phase. Axial/equatorial bidentate coordinations can form in the chair conformation between O1/O2 or O4/O5 to create *epi*(4-5) and *epi*(1-2). The *epi*(4-5) and *epi*(1-2) structures are the first and third most favorable structures in solution at 0.0 and 0.90 kcal/mol, respectively. These bidentate equatorial/equatorial and bidentate equatorial/axial all contribute to the [*epi*+Li]$^+$ ions that are observed to adduct a water molecule. The stereochemistry of *epi* lends itself to forming tridentate structures in boat or skewboat conformations, as is seen in Table 3.6 and Figure 3.19. The skewboat conformations of *epi* are generally less stable than chair conformations, so it is likely that the majority of unreacted [*epi*+Li]$^+$ ions result from the tridentate chair structure, *epi*(1-5-6). Because of the possibility for *epi* to form tridentate structures in the chair, skewboat and boat conformations it has a relatively high R_U = 0.518.

Table 3.6 Relative energies in kcal/mol for DFT solution and gas phase optimized structures of *epi*-inositol

Structure	Conformation	ΔG_{solv} (kcal/mol)	ΔG_{gas} (kcal/mol)
epi(4-5)	$^1C_4$	**0.00**	12.30
epi(1-5-6)	$^1C_4$	0.62	**0.00**
epi(1-2)	$^1C_4$	0.90	8.69
epi(3-4)	$^1C_4$	1.38	14.51
epi(2-3)	$^1C_4$	1.52	11.77
epi(1-2-6)	$^3S_1$	5.91	6.31
epi(1-4-6)	$^1S_5$	6.96	5.80
epi(4-5-6)	$^6S_2$	7.18	6.39
epi(5-6)	$^1C_4$	7.53	13.48
epi(1-2-5)	$^2S_6$	8.55	9.38
epi(1-2-4)	$^1S_3$	8.76	6.21
epi(2-4-5)	$^2S_6$	10.52	5.97

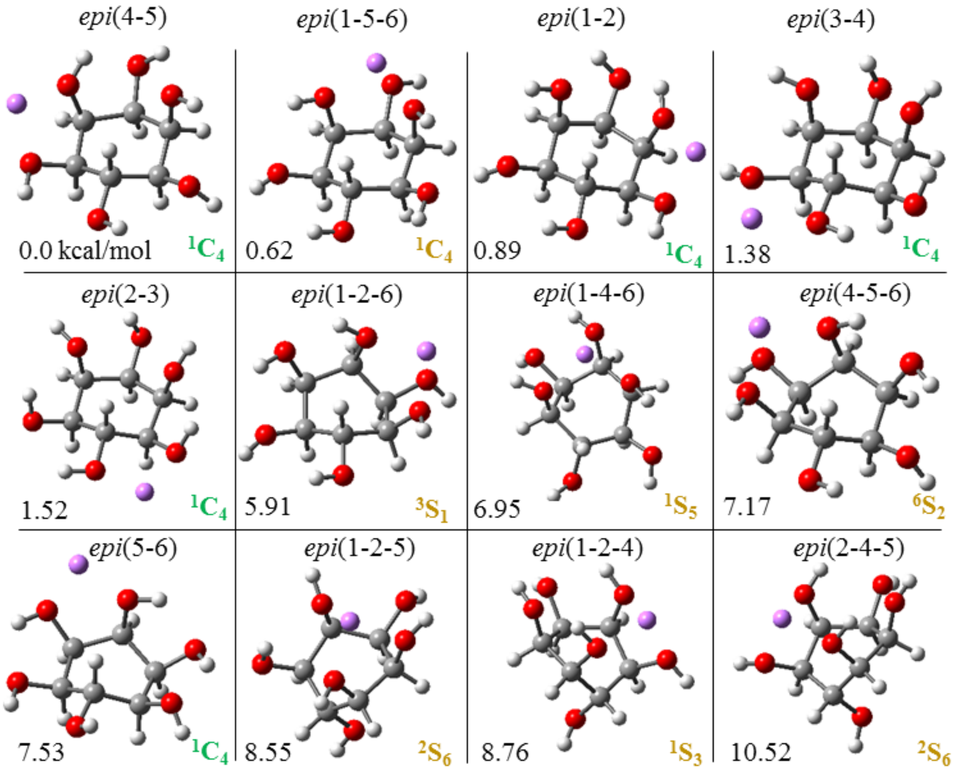

Figure 3.19 Gas-phase DFT optimized structures for lithiated *epi*-inositol. Relative solution phase Gibbs free energies are reported in kcal/mol. Inositol ring conformation is provided and labeled green or yellow for bidentate or tridentate interactions, respectively.

Myo-inositol contains one axial hydroxyl group oriented "up" at the C5 position, 3 equatorial hydroxyl groups oriented "up" at C2, C4 and C6, and 2 equatorial hydroxyl groups oriented "down" at C1 and C3. Five chair and three skewboat structures of *myo* are shown in Figure 3.20, and their relative solution and gas phase energies are listed in Table 3.7. In the chair conformation *myo* was only predicted by DFT to form bidentate Li-O coordinations. Equatorial/axial bidentate coordinations exist in the chair conformation for *myo*(4-5) and *myo*(5-6), while *myo*(3-4), *myo*(1-6) and *myo*(1-2) are equatorial/equatorial coordinations. Three skewboat tridentate coordinations for *myo* may contribute to the R_U value of 0.448. While the tridentate coordinations are not favorable in the solution phase, they become relatively more stable in the gas phase. It is possible that inositols have low ring-puckering activation barriers because they lack the hydroxymethyl group, similar to 6dGlc (Figure 3.7). A low ring-puckering activation barrier may lead to structural changes upon collisional activation in the ion optics of the mass spectrometer. Adding internal energy to ions in the ion optics of the MS can convert solution-phase favorable bidentate structures that are kinetically trapped after ESI into gas-phase favorable tridentate structures. This conversion occurs in the ion optics, prior to the mass spectrometer, so the ion structures that undergo water adduction may reflect gas-phase favorable structures. This phenomenon is discussed in more detail in Chapter 4.

Table 3.7 Relative energies in kcal/mol for DFT solution and gas phase optimized structures of *myo*-inositol

Structure	**Conformation**	**ΔG_{solv} (kcal/mol)**	**ΔG_{gas} (kcal/mol)**
myo(3-4)	$^{1}C_{4}$	**0.00**	0.32
myo(1-6)	$^{1}C_{4}$	0.55	3.82
myo(5-6)	$^{1}C_{4}$	1.55	**0.00**
myo(1-2)	$^{1}C_{4}$	1.72	1.11
myo(4-5)	$^{1}C_{4}$	3.27	0.03
myo(4-5-6)	$^{6}S_{2}$	6.74	2.27
myo(2-4-5)	$^{2}S_{6}$	10.33	1.78
myo(2-5-6)	$^{5}S_{1}$	10.51	1.77

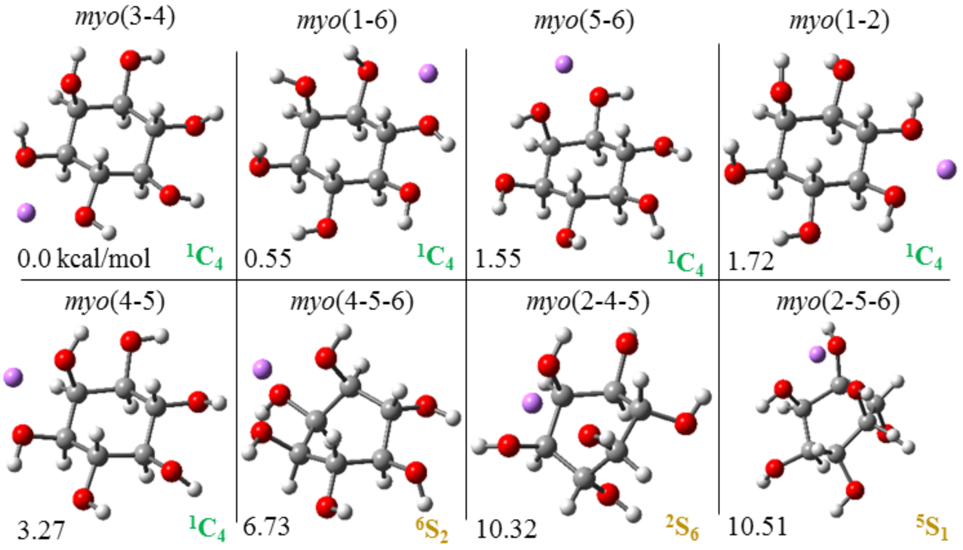

Figure 3.20 Gas-phase DFT optimized structures for lithiated *myo*-inositol. Relative solution phase Gibbs free energies are reported in kcal/mol. Inositol ring conformation is provided and labeled green or yellow for bidentate or tridentate interactions, respectively

3.3 Hexose Gas-Phase Lithium Cation Affinities Correlate to Unreacted Fraction

ESI of a hexose and lithium acetate produces both $[\text{Hexose+Li}]^+$ and $[\text{Hexose+Li+Hexose}]^+$, a lithium-bound dimer. When only one hexose isomer is electrosprayed lithium-bound homodimers are formed, but a second hexose isomer can be put in solution to also form lithium-bound heterodimers, $[\text{Hexose}_1\text{-Li-Hexose}_2]^+$. Generally, homodimers and heterodimers of isomeric hexoses have the same *m/z* value (*m/z* 367) and, therefore, cannot be distinguished from one another by MS. If a heavy-isotope labeled hexose, such as $^{13}C_6$-Glc, is placed in solution with a non-heavy-isotope labeled hexose the hexose homodimer will be observed as *m/z* 367, the $^{13}C_6$-Glc homodimer will be observed as *m/z* 379, and the heterodimer $[\text{Hexose+Li+}^{13}\text{C}_6\text{-Glc}]^+$ will be observed as *m/z* 373. The heterodimer can consist of Glc and $^{13}C_6$-Glc, or any monosaccharide that is electrosprayed with $^{13}C_6$-Glc. Using CID, the gas-phase lithium affinities of fourteen monosaccharides were measured relative to $^{13}C_6$-Glc based on lithium cation retention.

CID in a quadrupole ion trap MS is considered a slow-heating process, referring to the slow addition (in small increments) of internal energy, ε, into ions. This can be opposed to 'fast' processes that provide large amounts of ε in one or a few events such as beam-type CID, surface induced dissociation, UV photodissociation, and electron impact. For beam-type CID, a 'fast' activation process, ions are accelerated on the axis of a collision cell for a few high-velocity collisions with nitrogen or argon gas that cause dissociation. Because of the high ion velocities and more massive (than helium) neutral gases, beam-type CID induces larger increments of ε than slow-heating CID in a quadrupole ion trap; also, in beam-type CID, product ions can be activated and undergo, often unwanted, sequential dissociation. CID in a quadrupole ion trap involves mass-to-charge specific ion acceleration and collisions with He gas that increase ion internal energy in relatively small steps such that a single (or a few) collision event(s) cannot overcome the critical energy, ε_o, (activation energy barrier) of unimolecular ion dissociation; therefore, many collision events must occur. Mass-to-charge selectivity of CID in an ion trap is an advantage; after dissociation, product ions that have a different *m/z* are stable in the ion trap but are not activated further. For tens to hundreds of milliseconds ions undergo collisions in the ion trap, shifting the Boltzmann distribution of ion energies to higher ε values[27]. Therefore, after some activation time, ions at the upper end of the ε distribution will have enough energy to dissociate ($\varepsilon > \varepsilon_o$) where ε_o is the critical energy, activation barrier, for a given dissociation reaction and some ions will have $\varepsilon < \varepsilon_o$.

Upon each collision for a single ion (no longer discussing the total ion population), ion ε increases and is statistically distributed across all available vibrational modes of the molecular ion. RRKM theory addresses the statistical process of ε distribution into an ion, describing the ‘sum of states’ which is a representation of all the ways to distribute energy among molecular vibrational modes of an ion[66]. There are two statistical extremes that, although improbable, help explain this phenomenon of intramolecular vibrational redistribution as it pertains to unimolecular dissociation of ions. First, hypothetically, if the ion ε gained from each collision was solely channeled into a single vibrational mode then the bond involved in that vibration would quickly reach a value of $\varepsilon > \varepsilon_o$ and dissociation of that bond would occur; the result is a fast dissociation rate. Second, hypothetically, if ion internal energy gained from each collision was evenly redistributed throughout all ion vibrational modes, then the weakest bond (the lowest ε_o dissociation pathway) would be expected to dissociate, but at a slower reaction rate. While the slow-heating process is generally observed to access the low ε_o dissociation pathways, it is statistically improbable that ε is channeled into one vibrational mode, or that ε distribution is uniform across all vibrational modes.

Relatively large differences in critical energies ($\Delta\varepsilon_o$) values are observed between rearrangement dissociations, where bonds are both broken and created resulting in lower ε_o values, and simple cleavage dissociations, where a single bond is broken. Slow-heating CID, therefore, may be able to raise the ε of an ion above the ε_o(rearrangement) but not above the ε_o(simple cleavage). The rearrangement would then occur at a rate fast enough to be observed on the timescale of the CID experiment, but the simple cleavage would not be observed. Rearrangement and simple cleavage reaction rates eventually converge as ε increases slightly above the ε_o(simple cleavage). When ε is greatly above both the ε_o (rearrangement) and ε_o(simple cleavage), there is plentiful excess ε ($\varepsilon > \varepsilon_o$) for either reaction to occur; though, the reaction rate for the simple cleavage would be higher based on the greater probability of sufficient energy being distributed into a single vibrational mode, rather than the many vibrational modes required for a more complex rearrangement transition state structure.

Dissociation of lithium-bound monosaccharide dimers does not require rearrangement, rather simple cleavage of Li-O coordinations that are weaker than the typical covalent carbon-carbon or carbon-hydrogen bonds. When a lithium-bound heterodimer, $[\text{Hexose+Li+}^{13}\text{C}_6\text{-Glc}]^+$, is isolated in the ion trap and subsequently subjected to slow-heating CID there is competition between the two monosaccharide units for charge (lithium cation) retention and, therefore, competition to remain ionized. The weakest bonds in the dimer structure are the Li-O coordinations, so the competition is between either loss of Hexose or $^{13}\text{C}_6$-Glc from $[\text{Hexose+Li+}^{13}\text{C}_6\text{-Glc}]^+$. Of multiple competing simple cleavage dissociation pathways, the pathway that is expected to be observed at a given ε depends on the $\Delta\varepsilon_o$ between the pathways (Figure 3.21). The $\Delta\varepsilon_o$ of these competing pathways is expected to be relatively small. Slight disparity between energy requirements ($\Delta\varepsilon_o$), and reaction rate, at a given ε for each pathway is observed as a difference in relative abundance for $[\text{Hexose+Li}]^+$ and $[^{13}\text{C}_6\text{-Glc+Li}]^+$ after CID. The monosaccharide subunit that has a higher coordination denticity (more Li-O coordinations) will retain the lithium cation and remain ionized. The monosaccharide subunit that does not retain the lithium will become neutral, and therefore is no longer able to be manipulated by electric fields in the ion trap and cannot be detected.

As discussed in previous sections, hexose and inositol stereochemistry dictate the denticity of Li-O coordinations for $[\text{Hexose+Li}]^+$ and $[\text{Inositol+Li}]^+$, and as a result the water adduction characteristics are driven by stereochemistry. Monosaccharides that form more tri- and tetradentate Li-O coordinations are measured to have high R_U values during the water adduction ion/molecule reaction. The denticity of Li-O coordinations for a given monosaccharide within a lithium-bound heterodimer should also be dictated by stereochemistry; therefore, stereochemistry should dictate the gas-phase lithium affinity of monosaccharides. Ideally, monosaccharide stereochemistry, gas-phase lithium affinity and water adduction ion/molecule reaction characteristics can be related. A correlation between gas-phase lithium affinity and water adduction characteristics further confirmed the proposal that the water adduction unreacted fraction is related to bi- versus tri- and tetradentate Li-O coordinations. Heterodimers were individually formed between $^{13}C_6$-Glc and a suite of non-heavy-isotope enriched monosaccharides: all 8 D-aldohexose epimers, fructose, and five deoxyglucoses.

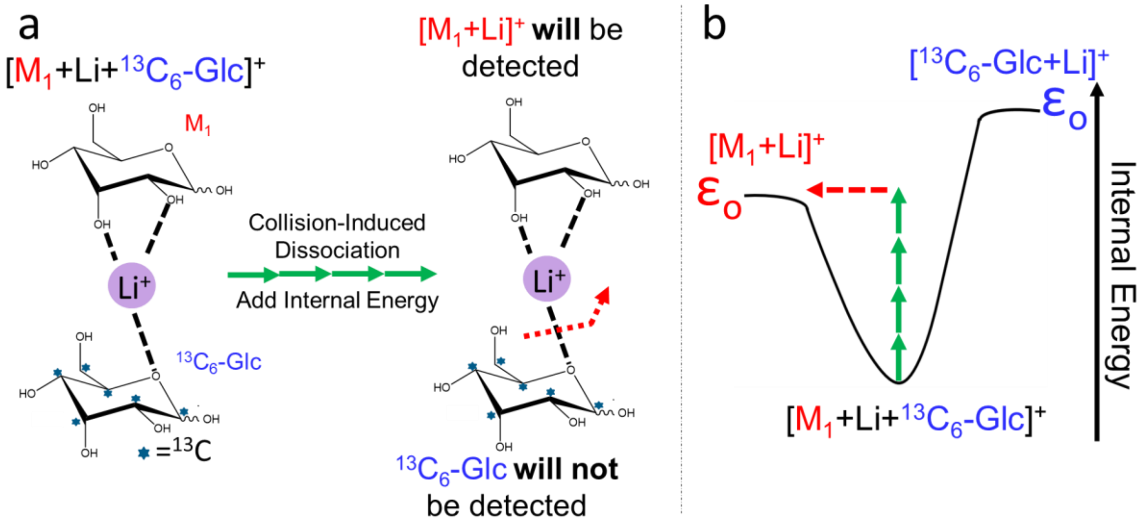

Figure 3.21 a) CID of a hypothetical lithium-bound heterodimer in which M_1, a monosaccharide, has a bidentate coordination and $^{13}C_6$-Glc has a monodentate coordination to the lithium cation. When internal energy is added to the heterodimer by slow heating via CID in a quadrupole ion trap MS the weakest bond will break; the lowest critical energy (ε_o) dissociation pathway will occur. The monodentate coordination between $^{13}C_6$-Glc and lithium dissociates, and M_1 retains the lithium. b) Potential-energy surface illustration of the heterodimer undergoing CID in a quadrupole ion trap MS. The ε_o to form $[M_1+Li]^+$ is lower than for $[^{13}C_6$-Glc$+Li]^+$. Small energy increments (green arrows) raise the heterodimer internal energy slowly.

After heterodimer isolation and dissociation, the relative abundance of lithiated monosaccharide versus $^{13}C_6$-Glc was determined. If the monosaccharide is of higher abundance than $^{13}C_6$-Glc, then the monosaccharide has a higher gas-phase lithium affinity than glucose. If the monosaccharide is of lower abundance than $^{13}C_6$-Glc, then the monosaccharide has a lower gas-phase lithium affinity than glucose. The relative order of gas-phase lithium affinities of 14 monosaccharides were measured by comparison to $^{13}C_6$-Glc. Dissociation of $[Glc+Li+^{13}C_6\text{-}Glc]^+$ heterodimers results in an equal abundance of $[Glc+Li]^+$ and $[^{13}C_6\text{-}Glc+Li]^+$ ions (Figure 3.22). Because Glc and $^{13}C_6$-Glc have identical stereochemistries and oxygen atom orientations, they form the same Li-O coordinations within the heterodimer strutures and have equivalent gas-phase lithium affinities.

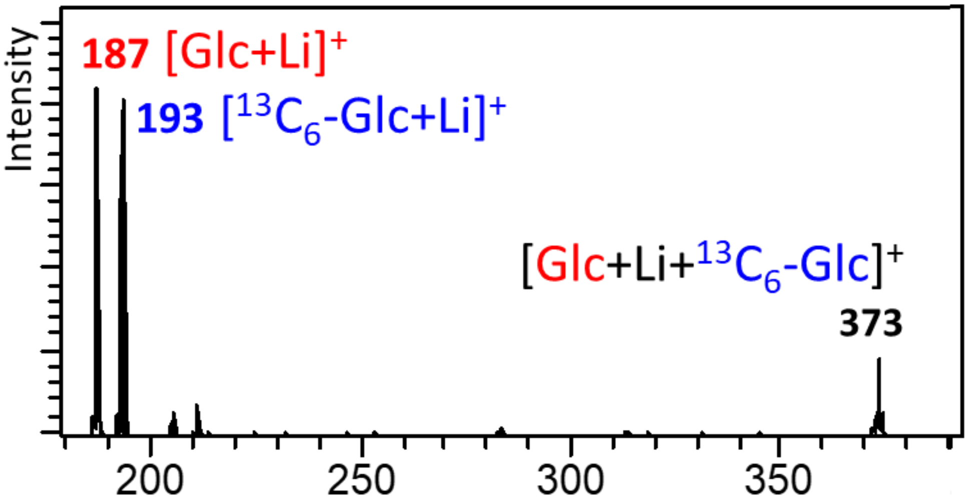

Figure 3.22 Mass spectrum as a result of isolation and dissociation of the $[Glc+Li+^{13}C_6\text{-}Glc]^+$ heterodimer where each monosaccharide retains the lithium cation equally.

Energy-resolved CID of the $[Glc+Li+^{13}C_6\text{-}Glc]^+$ heterodimer shows equal yield of both product ions at various fragmentation amplitudes (Figure 3.23a). Dissociation of $[Tal+Li+^{13}C_2\text{-}Tal]^+$ heterodimers also showed Tal and $^{13}C_2$-Tal retain the lithium equally (Figure 3.23b), bolstering the claim that monosaccharide stereochemistry dictates the gas-phase lithium affinity and is not affected by heavy-isotope labeling. Tal has two axial hydroxyl groups at the C2 and C4 positions that promote tri- and tetradentate coordinations as shown by DFT calculations[48] and a high R_U of 0.904. Since a large portion of [Tal+Li]+ exists as tri- or tetradentate coordinations, it was also predicted that Tal would form high denticity coordinations in the $[Tal+Li+^{13}C_6\text{-}Glc]^+$ heterodimer. Experimentally, Tal exhibited a high gas-phase lithium affinity as predicted, strongly retaining the lithium with a 91% relative abundance versus $^{13}C_6$-Glc (Figure 3.23c). To further confirm that stereochemistry and Li-O coordination drive the competition for lithium retention (rather than being heavily dependent on mass), the $[Glc+Li+^{13}C_2\text{-}Tal]^+$ heterodimer was assessed and $^{13}C_2$-Tal retained the lithium 91% relative to Glc (Figure 3.23d).

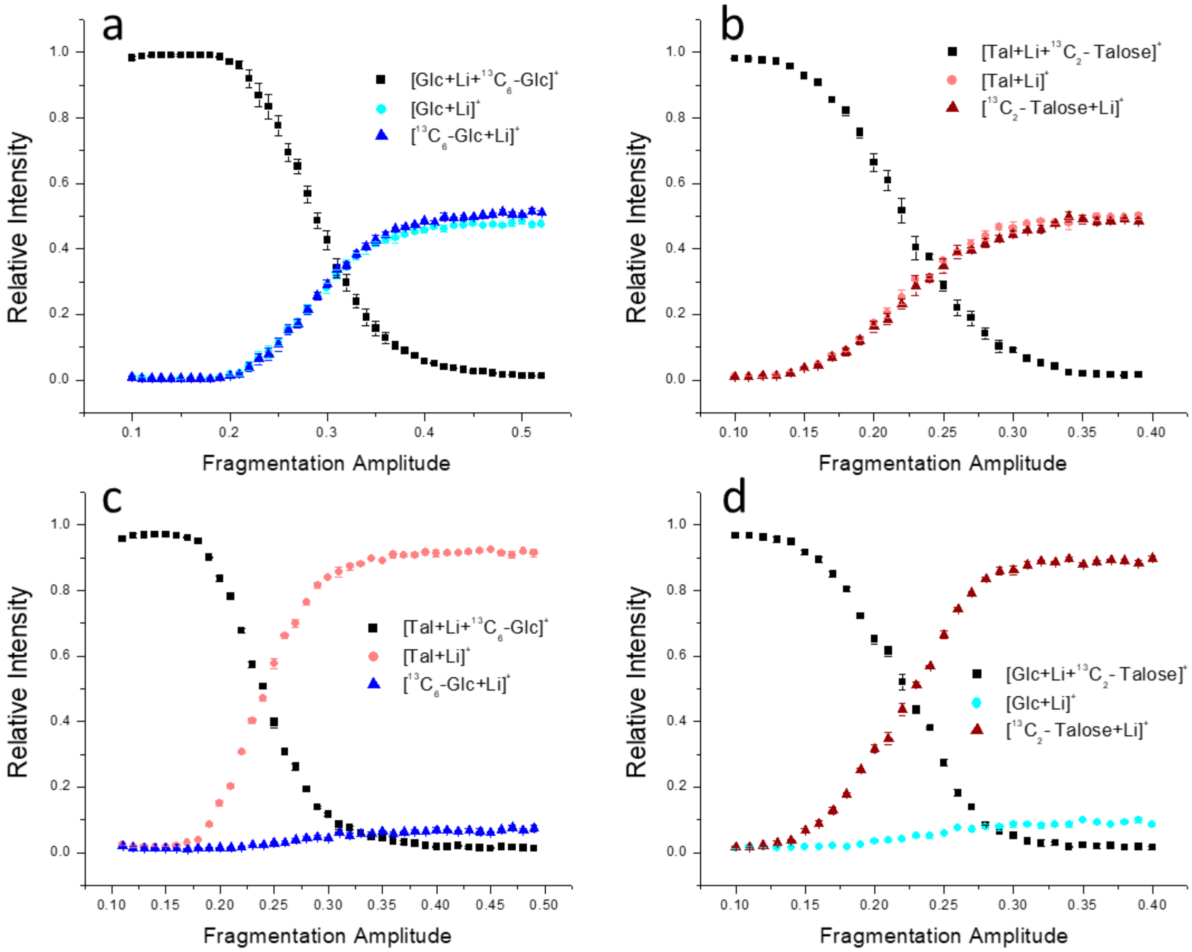

Figure 3.23 Energy-resolved CID of heterodimers formed between a) Glc and $^{13}C_6$-Glc, b) Tal and $^{13}C_2$-Tal, c) Tal and $^{13}C_6$-Glc, and d) Glc and $^{13}C_2$-Tal.

The energy-resolved heterodimer dissociation measurements were made on 14 monosaccharides versus $^{13}C_6$-Glc. The product ion yield (PIY) of the unlabeled monosaccharide at various fragmentation amplitudes was fit to a sigmoidal curve in Origin Pro 6 to determine the final asymptotic PIY value. These PIY values for each monosaccharide are a relative measure of gas-phase lithium affinity. A correlation between gas-phase lithium affinity and water adduction unreacted fraction was found by plotting PIY versus R_U for all monosaccharides (Figure 3.24). Lithium cation affinity is tied to the Li-O coordination denticity, or the total bond strength, between the monosaccharide and lithium cation. The correlation between lithium cation affinity and water adduction R_U has increased our confidence in the definition of water adduction reacted (bidentate) and unreacted (tridentate) structures.

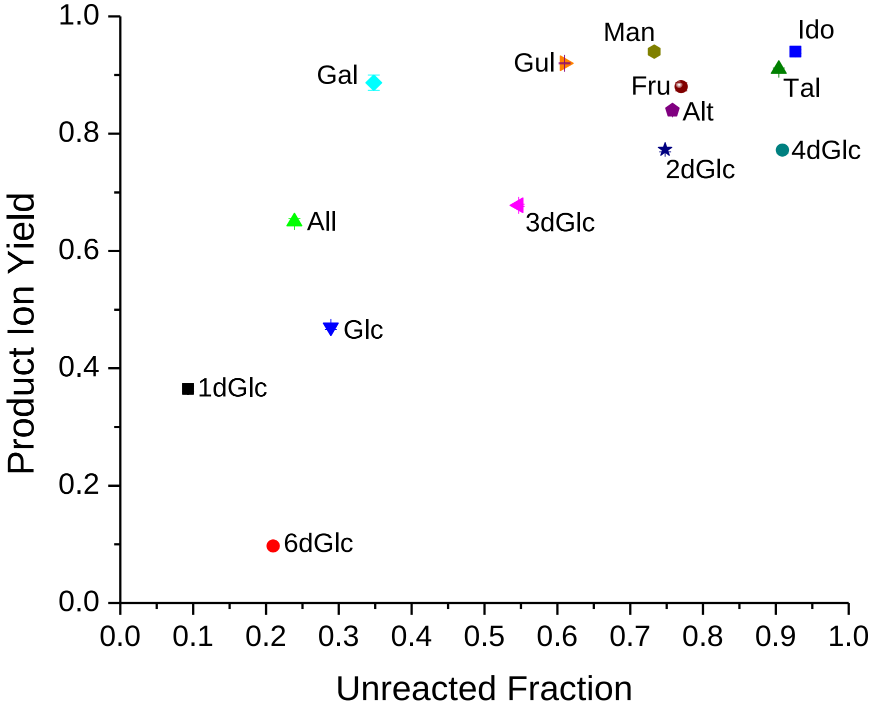

Figure 3.24 PIY versus R_U for 14 monosaccharides displaying a correlation between gas-phase lithium affinity and water adduction unreacted fraction.

Heterodimer complex formation during ESI is complex. Differential ion mobility (DIMS) measurements by our lab have shown that lithium-bound dimers form multiple different structures[67]. The existence of multiple dimer structures is also corroborated by the observed competition for lithium, where at least two subsets of dimer structures exist – dimer structures where M_1 retains lithium and dimer structures where M_2 retains the lithium. Because dimers are complex and multiple structures exist that cannot be easily elucidated, we did not expect a perfect correlation between PIY and R_U. 6-Deoxyglucose is not observed to closely fit the correlation. There are two possible explanations for this, the first regarding water adduction R_U. As discussed earlier in this chapter, 6dGlc cannot form the tridentate Li-O coordination between O1, O6 and the ring oxygen because the hydroxymethyl group (O6) is absent. Lacking the tridentate 6-R-1 coordination 6dGlc was expected to result in an R_U value similar to that of 1dGlc (less than 0.1). Instead, 6dGlc, was observed to have an unexpectedly high R_U value (near 0.2) and it was reasoned that without the bulky hydroxymethyl group, ring-puckering in the ion optics was easier for 6dGlc (Figure 3.7). Therefore, 6dGlc water adduction characteristics are complicated beyond the structures that form during ESI. The second is regarding the importance of the hydroxymethyl group in the lithium-bound dimer structure. The hydroxymethyl group is more sterically "far-reaching" than hydroxyl groups. It is reasonable that the hydroxymethyl group improves lithium cation retention upon dimer dissociation because it can coordinate the lithium even when C5 is not perfectly positioned in the dimer structure. The hydroxymethyl group contributes to many tri- and tetradentate coordinations for $[\text{Hexose+Li}]^+$ ions, therefore it should also increase the number of Li-O coordinations in the dimer structure and improve gas-phase lithium affinity. 6dGlc is an outlier from the correlation because of its high R_U and low PIY, both of which stem from an absence of the bulky hydroxymethyl group.

Visualizing the R_U and PIY data in the form of a bar graph displays the same positive correlation between water adduction R_U and PIY representing gas-phase lithium cation affinity (Figure 3.25). Focusing on the orange bars that display R_U values, we visualize the ability of the water adduction ion/molecule reaction to differentiate the 14 monosaccharides from one another. The blue bars displaying PIY, which contain information about lithium cation affinity, also show differentiation for some monosaccharides. Therefore, by forming lithium bound heterodimers between a monosaccharide and a reference molecule ($^{13}C_6$-Glc in this case) we are also able to differentiate isomeric monosaccharides from one another. Thus, we can differentiate isomeric monosaccharides using only the mass spectrometer by way of the water adduction ion/molecule reaction and lithium bound heterodimer dissociation. Using PIY as discussed here to differentiate hexoses is similar to previous studies where a modified kinetic method, the fix-ligand kinetic method, was used for complete hexose isomer identification[45, 68, 69]. The lithium-bound heterodimer dissociation presented here is a simpler experiment in that it only requires addition of unknown hexose, lithium salt and $^{13}C_6$-Glc to the electrospray solution, whereas the fixed-ligand kinetic method requires addition of hexose, two ligand molecules and a metal salt to form metal-bound trimer complexes with the hexose.

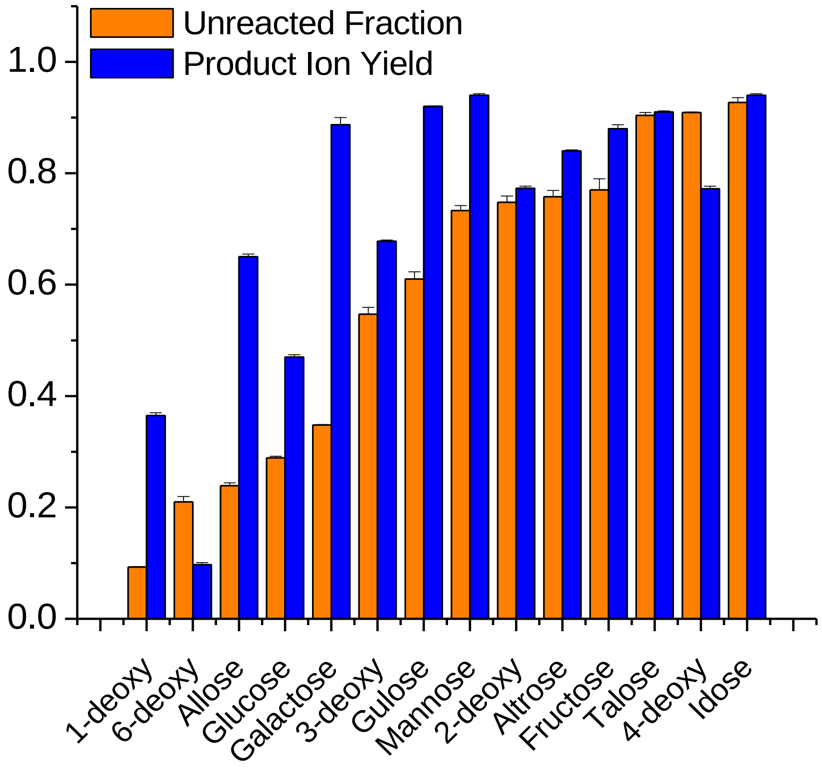

Figure 3.25 R_U and PIY values for fourteen monosaccharides.

Dissociation of lithium-bound heterodimers to measure PIY was expanded to beam-type CID on a Waters Q-TOF Premier instrument and compared to results from the Bruker HCT quadrupole ion trap. After ESI, [Hexose+Li+$^{13}C_6$-Glc]$^+$ dimers were *m/z* selected by the quadrupole (Q) and accelerated through a collision cell filled with argon gas to an electrode that pulses ions for time-of-flight (TOF) mass analysis and detection. The accelerating voltage difference between the quadrupole exit and collision cell entrance (collision voltage/energy) was incremented from 2 to 16.5 V and the relative abundance of [Hexose+Li]$^+$ and [$^{13}C_6$-Glc+Li]$^+$ was monitored to determine PIY. In Table 3.8 the PIY values from both beam-type and ion trap CID are compared.

Table 3.8 Comparison of beam-type CID and ion trap CID product ion yield (PIY) for [Hexose+Li+$^{13}C_6$-Glc]$^+$ dimer dissociation

		[Hexose+Li]$^+$ PIY		
Hexose	**Glc Relation**	**Beam-type**	**Ion trap**	**%Diff**
Glucose	–	0.485 ± 0.001	0.473 ± 0.004	2.54
Allose	C3 epimer	0.684 ± 0.001	0.649 ± 0.005	5.39
Galactose	C4 epimer	0.886 ± 0.001	0.887 ± 0.013	0.11
Talose	C2, C4 epimer	0.903 ± 0.002	0.911 ± 0.002	0.88
Idose	C2, C3, C4 epimer	0.85 ± 0.05	0.941 ± 0.003	9.67

Beam-type and ion trap CID yielded similar results for distinguishing hexoses by lithium-bound heterodimer dissociation, indicating that this method can be transferred across multiple mass spectrometry systems. The disparate results for idose can be explained by the instability of the [Idose+Li+$^{13}C_6$-Glc]$^+$ dimer. Idose has a high lithium affinity due to its three axial hydroxyl groups, which causes a weaker interaction between $^{13}C_6$-Glc and the lithium cation. Because of the weak interaction, $^{13}C_6$-Glc coordinations to lithium are easily dissociated as they are transmitted through QTOF. Dissociation of the dimer prior to the quadrupole results in lower overall signal intensities and larger measurement standard deviations (Figure 3.26). Dimer dissociation is also observed after *m/z* selective transmission through the quadrupole, even at the lowest collision voltages (around 2 V) that are typically only used to attain efficient ion transmission. In the Bruker ion trap MS system the idose heterodimer was seemingly stable during transmission, trapping and isolation, and the slow-heating process of ion trap CID was on display, as the heterodimer was not significantly dissociated at the lowest fragmentation amplitudes.

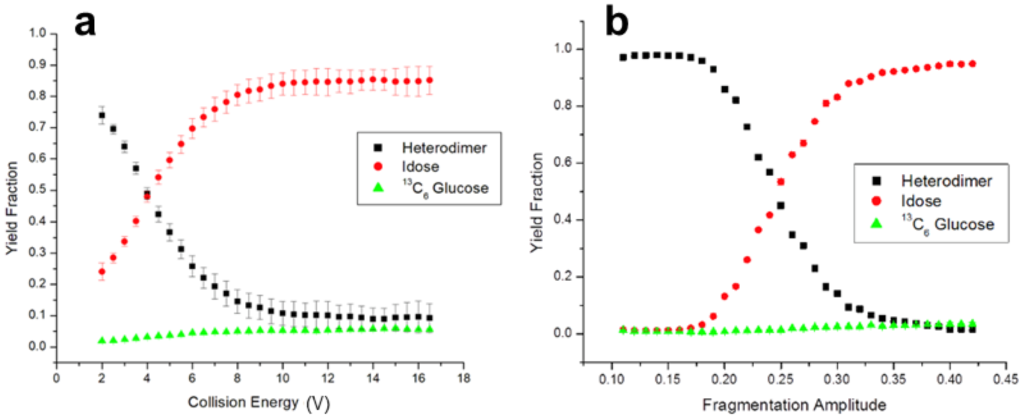

Figure 3.26 Energy-resolved CID of the [Idose+Li+$^{13}C_6$-Glc]$^+$ heterodimer using a) beam-type and b) ion trap CID.

3.4 Probing the Lithium-H_2O Bond Strengths of [Hexose+Li+H_2O]$^+$

Regarding water adduction metrics, specifically the unreacted fraction, we have discussed the importance of the lithium coordination denticity to a hexose molecule, or other monosaccharide type. Given time to adduct a water molecule in the ion trap, an ion with a tri- or tetradentate coordination between lithium and the hexose is observed as the unreacted [Hexose+Li]$^+$ ion. A tridentate coordination between lithium and hexose is stronger than a bidentate coordination, both of which are stronger than a monodentate coordination. Two example electrostatic potential maps for a O1/O6 and a O4/O5 Li-O coordinated hexose are shown in Figure 3.26a, where blue denotes a region of low electron density or a more positive partial charge and red denotes a region of high electron density or a more negative partial charge.

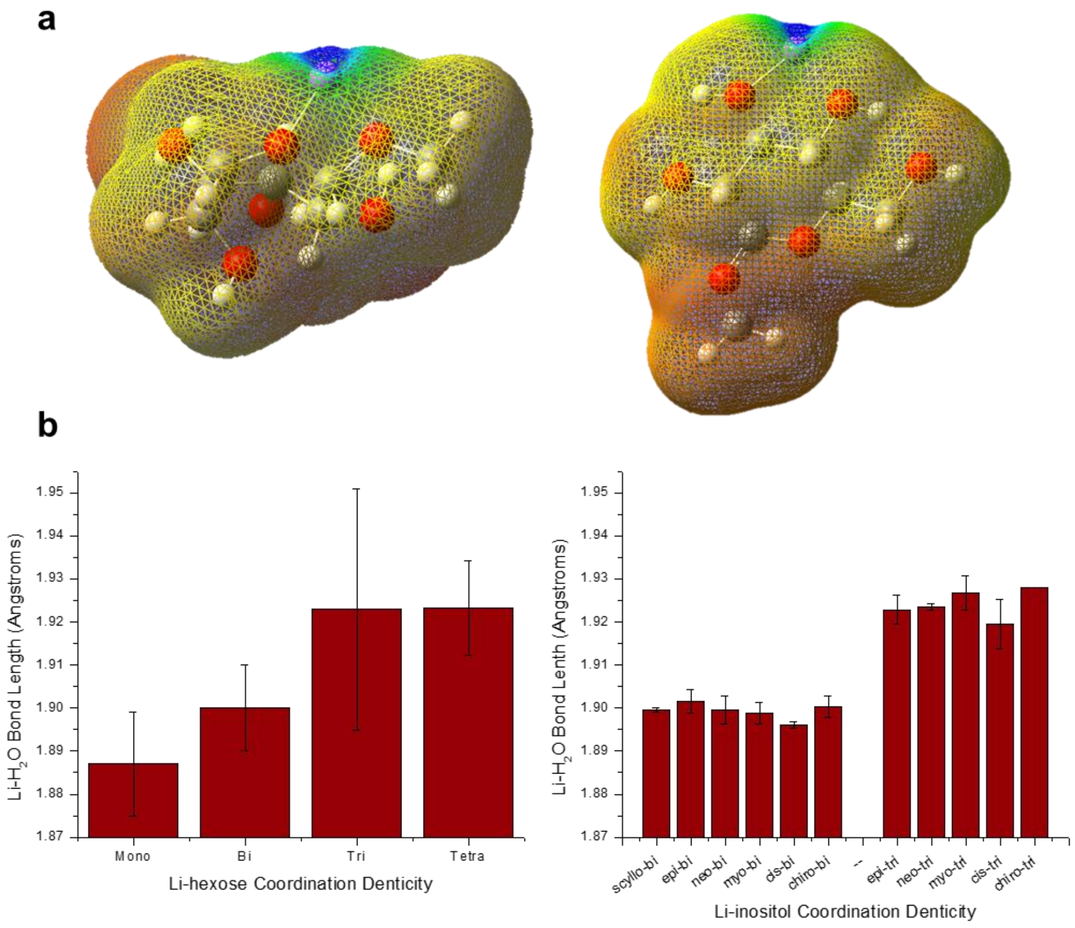

Figure 3.27 a) Electrostatic potential maps calculated *via* DFT for a (left) hexose(1-6) and a (right) hexose(4-5) structure. Blue denotes a region of low electron density, nearest the lithium cation, and red denotes a region of high electron density. b) Li-H_2O bond length in Angstroms as a function of Li-monosaccharide coordination denticity for (left) hexose epimers Glc, Man, Gal and Tal combined, and (right) individual inositols. Bond lengths were determined from DFT structures.

The magnitude of the partial positive charge at the site of water adduction will affect the strength of an interaction between $[Hexose+Li]^+$ and a water molecule. A greater partial positive charge on the lithium cation should create a stronger interaction with the dipole of the water molecule (oxygen partial negative charge). Strong lithium-water dipole interactions are hypothesized to facilitate a faster reaction rate because longer interaction distances are possible. Conversely, a lower partial charge on the lithium cation will result in weaker interactions and possibly slower reaction rates. The denticity of the $[Hexose+Li]^+$ coordination can affect partial positive charge of the lithium cation. Coordination to one oxygen atom of the hexose will decrease the partial positive charge of the lithium. Coordination to two or three oxygen atoms should even further reduce the partial positive charge of the lithium cation. Additionally, the Li-O (Li-hexose) coordination bond distances typically decrease as the denticity increases, pulling the lithium closer to the hexose molecule (Figure 3.27b). Shorter coordination distances result in less surface area for a water molecule to approach the lithium cation. The surface area available for a gas-phase water molecule to approach the lithium cation is dependent on the coordination denticity, but also can be affected by the geometry of the coordination site. The hexose(4-5) structure in Figure 3.27a has a smaller surface area for water molecule approach than does the hexose(1-6), visualized by the blue-colored region of low electron density (high partial positive charge). Although both structures have bidentate Li-O coordinations, the geometries and Li-O bond distances are different, resulting in unique sites for water adduction. These types of unique coordination sites, distinguished by the interaction strength (lithium partial positive charge) and the available interaction surface area (coordination site geometry), are hypothesized to be related to the probability of lithium-water interaction; thus, the water adduction reaction rate.

Whether or not a lithium-water interaction is thermodynamically stable also depends on interaction strength. Therefore, the Li-O (Li-hexose) coordination denticity affects the Li-H_2O bond strength and determines whether the ion is detected as $[Hexose+Li]^+$ or $[Hexose+Li+H_2O]^+$. A bidentate Li-O coordination (compared to tridentate) is expected to have a greater partial positive charge at the lithium. Upon interaction, bidentate structures will therefore have a stronger Li-H_2O bond. Shorter average Li-H_2O bond lengths are estimated by DFT for bidentate Li-hexose and Li-inositol structures when compared to tridentate structures (Figure 3.27b). A shorter bond length is interpreted as a stronger interaction. A strong Li-H_2O bond is a favorable interaction that is stable and will survive collisions with helium gas during ion manipulation within the ion trap and during ejection from the ion trap for detection. Coordination site geometry can also affect the thermodynamic stability of the $[Hexose+Li+H_2O]^+$ ion. For example, $[Hexose+Li+H_2O]^+$ stability would be improved if the water molecule can interact with lithium and hydrogen bond with the hexose.

As already discussed in detail this chapter, hexose stereochemistry dictates the Li-O (Li-hexose) coordination denticity and, as a result, water adduction characteristics. Hexose stereochemistry also dictates the strength of the Li-H_2O bond formed by water adduction in the ion trap. The Li-H_2O bond strengths of six hexose epimers were studied using water adduction and CID in the ion trap at the MS/MS level. Lithium chloride (LiCl) was used for this set of experiments rather than lithium acetate (LiAc). LiAc forms clusters that are observed at the same *m/z* 205 value as $[Hexose+Li+H_2O]^+$ and LiCl does not form the same cluster. For the majority of water adduction experiments the LiAc cluster is not an interferent because the $[Hexose+Li]^+$ ion at *m/z* 187 is isolated prior to water adduction. In this current set of experiments, water adduction is purposefully allowed to occur during ion accumulation in the trap and *m/z* 205 is subsequently isolated; in this specific experiment the LiAc cluster is an interferent. The ion trap accumulation time was set to a static 1000 ms to allow [Hexose+Li]$^+$ to adduct water during accumulation (Figure 3.28) and subsequently the [Hexose+Li+H_2O]$^+$ ions were isolated with a 3 Da window in the first stage of mass analysis. The 3 Da window was used as an attempt to minimize dissociation of the Li-H_2O bond during isolation. Following isolation, the [Hexose+Li+H_2O]$^+$ ions were subjected to CID to dissociate the Li-H_2O bond that formed by water adduction. The resulting ions were then scanned out to be detected and the relative yield of [Hexose+Li]$^+$ and [Hexose+Li+H_2O]$^+$ ions were calculated. Energy-resolved CID of the [Hexose+Li+H_2O]$^+$ water adduct ions of six hexose epimers revealed stark differences in Li-H_2O bond strengths.

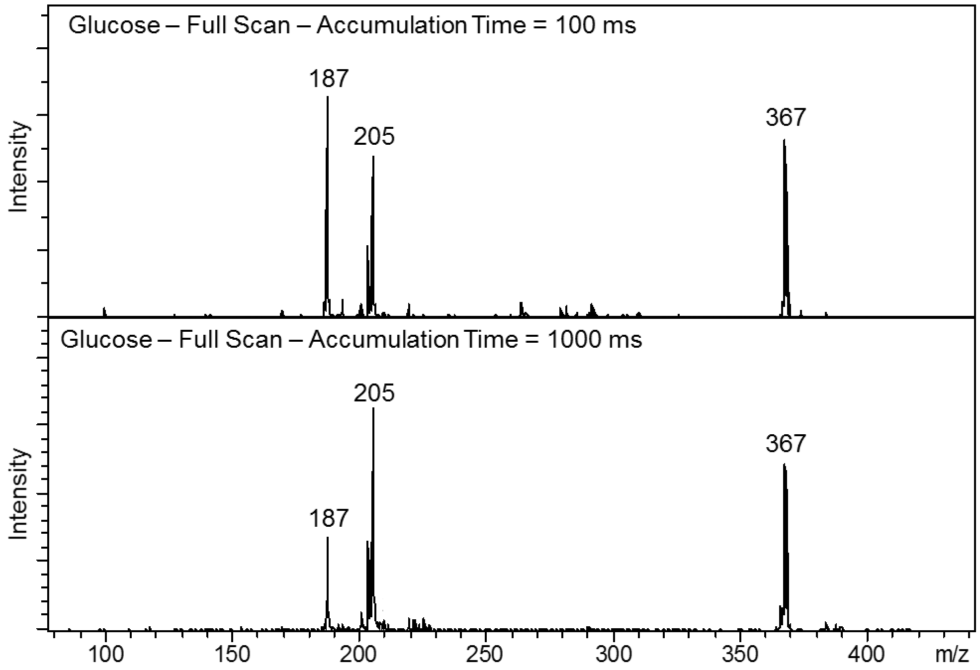

Figure 3.28 Full scan mass spectrum of lithiated glucose at an ion trap accumulation time of (top) 100 ms and (bottom) 1000 ms. Ions can adduct a water molecule while trapped during accumulation. Greater abundance of the water adduct ion at *m/z* 205 is observed in the full scan spectrum at a longer accumulation time.

The lithium-hexose coordination strength hierarchy is as follows: tetradentate > tridentate > bidentate; also, this coordination denticity affects water adduction R_U. As discussed above, the strength of the lithium-hexose coordination is inversely proportional to the strength of the Li-H_2O bond formed during water adduction. For example, a tetradentate lithium-hexose coordination will form the weakest Li-H_2O bond and a bidentate lithium-hexose coordination will form a stronger Li-H_2O bond. After isolation and dissociation of *m/z* 205, the relative abundance of *m/z* 187 ($[Hexose+Li]^+$ ions) and *m/z* 205 ($[Hexose+Li+H_2O]^+$ ions) is dependent on two physical properties, the strength of the Li-H_2O bonds of $[Hexose+Li+H_2O]^+$ ions (as probed by CID) and the water adduction reaction rates of $[Hexose+Li]^+$ ions (affecting back-reaction of *m/z* 187 to *m/z* 205). The experiment reaction scheme and example energy-resolved CID data for $[Tal+Li+H_2O]^+$ are shown in Figure 3.29. From energy-resolved CID of $[Hexose+Li+H_2O]^+$, relative ion yield versus fragmentation amplitude (V) can be plotted. Three regimes exist during this experiment. First, some Li-H_2O bonds break during the 40 ms activation time at 0 V fragmentation amplitude. Second, the fragmentation amplitudes at which the survival yield (SY) of *m/z* 205 is decreasing and the yield of *m/z* 187 is increasing; this regime includes the 50% SY of *m/z* 205. Third, a steady state is reached between dissociation of Li-H_2O bonds by CID and creation of Li-H_2O bonds by water adduction back-reaction. In this regime, the relative abundances of *m/z* 187 and 205 are static.

In the first regime of the energy-resolved CID experiment at 0 V fragmentation amplitude for Tal the SY of *m/z* 205 is less than 1 ($SY_{205} = 0.722$). The product ion yield of *m/z* 187 is inherently 1 – 0.722 ($^{0V}PIY_{187} = 0.278$). Near 30% of all Li-H_2O bonds of $[Tal+Li+H_2O]^+$ dissociated after isolation or during application of 0 V fragmentation amplitude for 40 ms. This dissociation at 0 V fragmentation amplitude will be explored before relating the three data regimes to the water adduction characteristics of the 6 hexose epimers studied. The extent of dissociation for $[Tal+Li+H_2O]^+$ and $[Glc+Li+H_2O]^+$ ions in the first regime was studied by incrementally decreasing the isolation width from 26 to 1 Da with and without subsequently applying a 40 ms activation time and 0 V fragmentation amplitude (Figure 3.30a-b). When no activation was applied the Tal SY_{205} was 0.86. With 40 ms activation at 0 V was applied, Tal $^{0V}SY_{205}$ was 0.72, matching the first regime of the energy-resolved CID experiment. Glc SY_{205} values without activation and with activation were 0.97 and 0.95, respectively. Tal exhibited characteristically weaker Li-H_2O bonds than Glc, as indicated by the lower SY_{205} values. Tal and Glc SY_{205} values were independent of isolation width, indicating a 3 Da isolation window was appropriate for all experiments. More Li-H_2O bonds dissociate as the activation time is increased from 0 to 600 ms, while maintaining 0 V fragmentation amplitude and 3 Da isolation width (Figure 3.30c-d). Both Tal and Glc reach a steady state as activation time (with 0 V fragmentation amplitude) is increased, displaying further that there is some activation of ions even without an applied amplitude. Generally, longer activation times lead to an increasing number of ion-helium collisions in the ion trap and greater amounts of internal energy imparted into the ions. Ion dissociation without an applied activation voltage may be related to accelerating ion-ion interactions (space charging) during ion storage which result in higher energy ion-helium collisions[70–72].

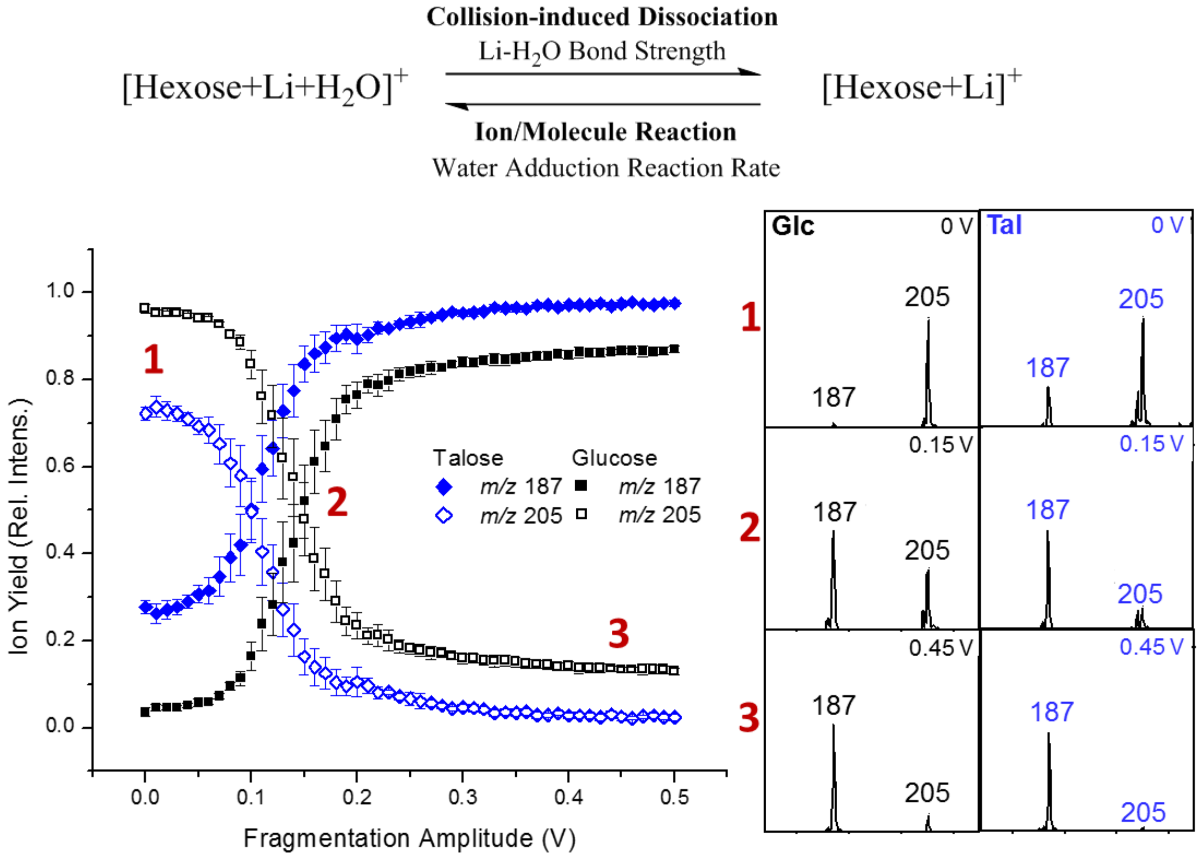

Figure 3.29 (Top) Reaction scheme for the dissociation of $[Hexose+Li+H_2O]^+$ to $[Hexose+Li]^+$, and back-reaction of $[Hexose+Li]^+$ to $[Hexose+Li+H_2O]^+$. After dissociation, there is time for some $[Hexose+Li]^+$ ions to adduct a water molecule during and after the 40 ms CID activation time, and before excitation for ejection from the ion trap. (Bottom) Energy-resolved CID of $[Glc+Li+H_2O]^+$ and $[Tal+Li+H_2O]^+$ with representative mass spectra from each of the three experimental regimes labeled in red. Each regime is discussed in the text.

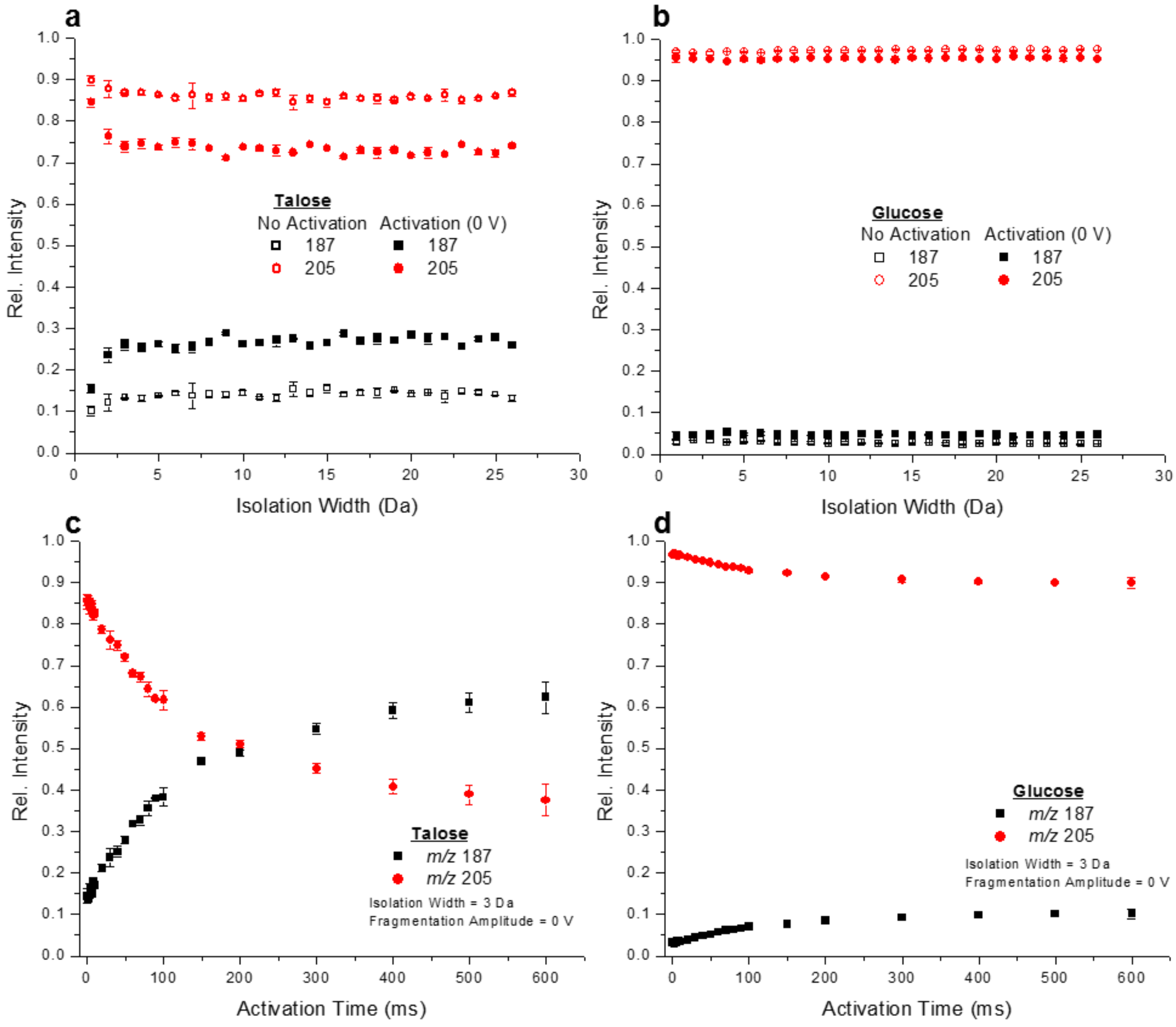

Figure 3.30 a,b) Relative abundances of *m/z* 187 and 205 for Tal and Glc at various isolation widths with and without 0 V fragmentation amplitude applied for a static activation time of 40 ms. c,d) Relative abundances of *m/z* 187 and 205 for Tal and Glc at increasing activation times with 0 V fragmentation amplitude applied, using a static 3 Da isolation width.

Experimental observations in the first regime, defined in Figure 3.29, have been explored. Now all three regimes will be discussed for six hexose epimers. A sigmoidal fit was applied to the SY_{205} values as a function of fragmentation amplitude for each hexose epimer to determine the initial ${}^{R1}SY_{205}$ in regime 1 and the final ${}^{R3}SY_{205}$ in regime 3. For each hexose the initial ${}^{R1}SY_{205}$ and final ${}^{R3}SY_{205}$ were plotted against the respective R_U values, as well as reaction rates (Figure 3.31). In regime 1, the weakest Li-H_2O bonds of the [Hexose+Li+H_2O]$^+$ population dissociate but the stronger Li-H_2O bonds survive. As we have discussed, the ${}^{R1}SY_{205}$ value is related to the Li-H_2O bonds that survive isolation and application of 40 ms activation time at 0 V fragmentation amplitude, and the strength of Li-H_2O bonds is related to the denticity of Li-hexose coordination. A negative linear correlation was observed between ${}^{R1}SY_{205}$ and R_U (Figure 3.31a). A higher R_U value corresponds to a lower initial ${}^{R1}SY_{205}$ value. Tal has two axial hydroxyl groups at C2 and C4 that create greater numbers of tri- and tetradentate Li-hexose coordinations. Tri- and tetradentate Li-hexose coordinations result in weaker Li-H_2O bonds, thus, Tal has the lowest ${}^{R1}SY_{205}$ (and the highest R_U) out of the six hexoses studied here. Conversely, All and Glc form more bidentate Li-hexose coordinations and have the lowest R_U values. Bidentate Li-hexose coordinations result in stronger Li-H_2O bonds, thus, All and Glc have the highest ${}^{R1}SY_{205}$ values. A positive correlation between ${}^{R1}SY_{205}$ and reaction rate values was observed (Figure 3.31b). In general, water adduction reaction rate and R_U are inversely proportional, as seen in Figure 3.15b-c.

To discuss regime 3 of the data we will consider the correlation between ${}^{R3}SY_{205}$ and reaction rate (Figure 3.31d). In regime 3, a high fragmentation amplitude is applied for 40 ms activation time. In regime 3, enough internal energy should be imparted into the ions to dissociate all Li-H_2O bonds. Any *m/z* 205 that is detected in regime 3 should then be due to back reaction (Figure 3.29, top). Back reaction is dependent on [Hexose+Li]$^+$ reaction rate, Li-hexose coordination denticity, and hexose stereochemistry. All and Glc have the highest water adduction reaction rates, so the greatest abundance of back-reacted ions is detected. Notably in regime 2 is the 50% SY_{205} point which is hypothesized to be the energy required to dissociate the median Li-H_2O bond strength for the hexose.

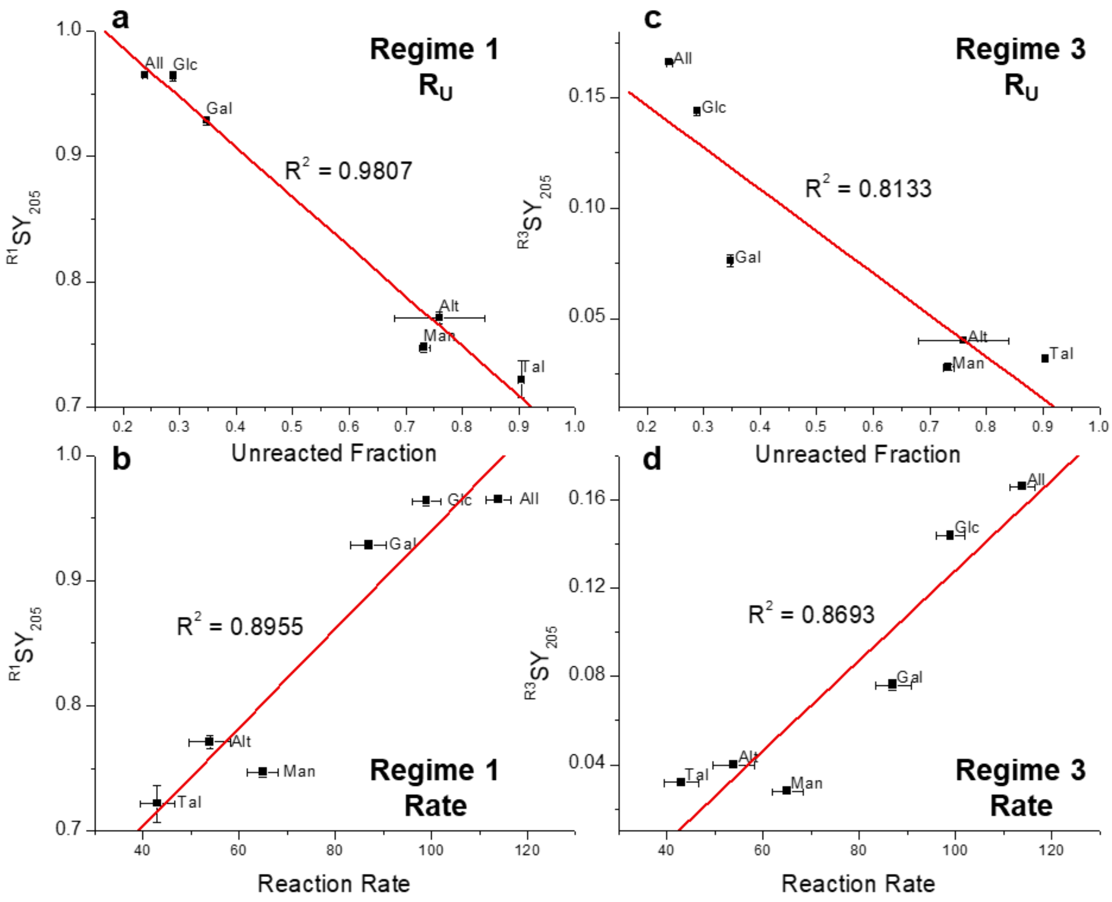

Figure 3.31 Correlation between SY205 values, measured by CID of Li-H2O bonds, and water adduction characteristics for six hexoses. a) Regime 1, initial, $^{R1}SY_{205}$ versus R_U. b) Regime 1, initial, $^{R1}SY_{205}$ versus reaction rate. c) Regime 3, final, $^{R3}SY_{205}$ versus R_U. d) Regime 3, final, $^{R3}SY_{205}$ versus reaction rate.

3.5 Summary

Lithiated gas-phase carbohydrate ions can adduct a water molecule in an ion trap mass spectrometer. The water adduction ion/molecule reaction distinguishes lithiated sugar ions inside of an ion trap mass spectrometer based on reaction rates and R_U. Chapter 3 discussed the mechanisms dictating monosaccharide R_U values and some insights on reaction rates. Ultimately, stereochemistry drives differentiation of isomeric monosaccharides by water adduction. Monosaccharide stereochemistry, the orientation of individual oxygen atoms, dictates all Li-hexose coordinations that are potentially adopted by the $[\text{Hexose+Li}]^+$ ions formed during ESI and introduced into the ion trap MS. It is the denticity of Li-hexose coordinations that affect the water adduction R_U, where bidentate Li-O (Li-hexose) coordinations are observed to react, and tri- and tetradentate may not.

Water adduction experiments and theoretical DFT calculations were used to relate the R_U and rate of water adduction to the potential Li-hexose coordinations formed by various monosaccharides. Regarding hexoses, axial hydroxyl groups on the same side of the pyranose ring (C2 and C4 positions) as the hydroxymethyl group (C5 position) increase R_U values and decrease reaction rates. The axial hexose epimers Gal, Man and Tal all have greater R_U values than Glc which has only equatorial hydroxyl groups. Water adduction to monodeoxyglucoses showed that the absence of a single hydroxyl group from the pyranose ring affects R_U values in a predictable manner by removal of potential Li-hexose coordinations. Inositols are isomeric to hexoses but lack the anomeric center and the hydroxymethyl group; therefore, inositols have more predictable Li-O (Li-inositol) coordinations and were used to further confirm the hypothesis that bidentate coordinations are observed to react, whereas tri- and tetradentate are not.

The gas-phase lithium affinities of fourteen monosaccharides were measured relative to ${}^{13}C_6$-Glc by energy-resolved dissociation of lithium-bound heterodimers and the kinetic method. Monosaccharide stereochemistry affected gas-phase lithium affinity in a way that correlated with water adduction characteristics. Monosaccharides that were measured to have higher R_U values also had higher lithium affinities. Monosaccharides with high lithium affinities form stronger Li-O (Li-monosaccharide) coordinations such as tri- and tetradentate coordinations. Tal and Idose, axial epimers of Glc, have the greatest lithium affinities and the highest R_U values; they also favorably form many tri- and tetradentate Li-O coordinations.

Dissociation of the Li-H_2O bonds formed by water adduction to $[Hexose+Li]^+$ provided insight to the relative strength of Li-H_2O bonds for six hexoses, and helped explain why tri- and tetradentate Li-hexose coordinations may not be observed to react. Hexose epimers with higher R_U values and greater amounts of tri- and tetradentate Li-hexose coordinations formed weaker Li-H_2O bonds upon water adduction. A higher Li-hexose coordination denticity reduces the partial positive charge of the lithium cation on $[Hexose+Li]^+$, creating a weaker interaction with the dipole of the water molecule (partial negative charge of the oxygen). Weaker Li-H_2O bonds may not survive ejection from the ion trap for detection and, in this case, the $[Hexose+Li]^+$ ion is observed in the mass spectrum. Bidentate Li-hexose coordinations result in a greater partial positive charge on the lithium cation of $[Hexose+Li]^+$, resulting in a stronger interaction with the dipole of the water molecule. Strong or favorable Li-H_2O bonds may be stable such that they survive ejection from the ion trap for detection and result in observation of the $[Hexose+Li+H_2O]^+$ ion.

CHAPTER 4: EFFECT OF INSTRUMENT PARAMETERS ON THE WATER ADDUCTION ION/MOLECULE REACTION

4.1 Collisionally-Induced Ion Structural Changes in the Mass Spectrometer Ion Optics

Electrospray ionization generates gas-phase ions from solution-phase molecules at atmospheric pressure. A solution containing analyte and other species is delivered through a capillary and an inert nebulization gas is flowed coaxial around the outside of the capillary. The ESI capillary is positioned near the mass spectrometer inlet and a voltage difference (kilovolts) is applied between the capillary and MS inlet. The solution forms a Taylor cone[73] at the capillary tip and with the help of nebulization gas many small charged droplets are emitted that contain analyte and other species (H^+, Na^+, other molecules, etc.). Initial droplet sizes have micrometer radii but shrink via evaporation to the nanometer range. As ESI droplets desolvate and shrink, clusters containing a few solvent molecules and an ion are ejected[74]. The cluster is then pulled by a pressure differential into the vacuum system of the mass spectrometer through the heated inlet capillary and through a capillary exit voltage typically held at +102 V (Figure 4.1). Once past the capillary exit the ion or cluster is accelerated by the skimmer cone voltage (typically +40 V). This accelerating field is created by the capillary/skimmer voltage difference (62 V) and is referred to as the declustering potential on some other mass spectrometry systems. Between the capillary exit and the skimmer cone is the first differentially pumped region of the MS vacuum chamber that is held around 1.3 mbar. As an ion or a cluster is accelerated through the first differentially pumped vacuum region it will undergo collisions with neutral gas molecules. These energetic collisions result in collisional heating and aid in further desolvation of clusters to eventually result in a completely desolvated gas-phase ion. If a completely desolvated gas-phase ion is accelerated through this region, any ion-neutral collisions will increase the internal energy of the ion and may result in collision-induced dissociation.

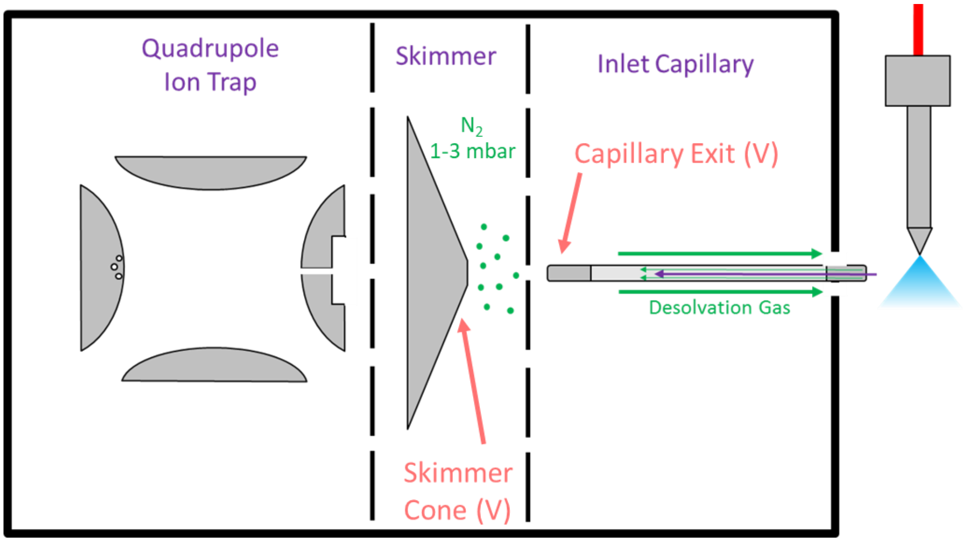

Figure 4.1 Schematic of the Bruker HCT. Pictured from right to left: electrospray emitter, heated glass capillary, metal capillary exit (cap exit voltage), skimmer cone (skimmer voltage). Nitrogen and other neutral gases are depicted in green.

The magnitude of the capillary/skimmer voltage difference can be raised or lowered to increase or decrease the collisional energy ions or clusters are subjected to, respectively. Thus, the capillary/skimmer voltage difference is generally optimized for desolvation and maximum transmission of ions of interest. The optimal capillary/skimmer voltages are often different for various analytes and ion types. The optimal transmission voltages for one ion type (charge magnitude, charge carrier type, molecule type, monomer, dimer, etc.) might poorly transmit another ion type. In some scenarios, the capillary/skimmer voltage differences can raise ion internal energy to the point of dissociation. In-source dissociation of ions has been used for structural diagnosis[75] and has been compared to beam-type CID[76]. The collisions ions or clusters undergo within the ion optics of our Bruker HCT instrument are more similar to the beam-type CID used with triple quadrupole and quadrupole-time of flight mass spectrometry systems. Beam-type CID collisions are energetically different than the collisions that ions undergo inside of the quadrupole ion trap. In the ion optics, ions or clusters will undergo a few relatively energetic collisions with atmospheric gas molecules, mostly nitrogen. In the quadrupole ion trap, ions undergo many collisions with helium gas that are relatively less energetic (Figure 3.21).

The capillary/skimmer voltage difference is generally used to decluster/desolvate ions after ESI and in some cases for in-source dissociation of ions. Here, the capillary/skimmer voltage difference was used to raise the internal energy of lithiated monosaccharide ions over activation barriers for ring-puckering and Li-monosaccharide coordination isomerization. Isomerization of $[\text{Monosaccharide+Li}]^+$ in the ion optics was already briefly mentioned in Chapter 3.1 and was illustrated in Figures 3.6 and 3.7, but will be covered further in this section. $[\text{Monosaccharide+Li}]^+$ ions released by ESI are solution-phase favorable structures that become kinetically-trapped upon release into the gas phase; however, the relative stabilities of all possible ion structures change from the solution to gas phase (Figure 3.7). Therefore, once released into the gas phase, if internal energy is imparted into the kinetically trapped solution-phase structures, it is possible for some ions to isomerize to structures that are more favorable in the gas phase. Past studies have shown that large biomolecules can exhibit this phenomenon[77, 78], and conformational changes of kinetically-trapped 'native' protein ions, specifically structural unfolding events, have been studied by ion mobility spectrometry-mass spectrometry[79]. More closely related to the current study, small molecules have also been shown to exhibit this phenomenon. During ESI, benzocaine[80, 81] and para-aminobenzoic acid[82] were detected as either a solution-phase favored N-protomer or a gas-phase favored

O-protomer. ESI and ion source conditions were varied to alter the protomer population that was detected. Under certain conditions the solution-phase favored N-protomer remained stable and was detected, and under other conditions the kinetically trapped N-protomer was destabilized and convert to the gas-phase favored O-protomer. Here, we show that kinetic trapping of solution-phase ion structures and isomerization in the gas phase extends to lithium cationized monosaccharides.

In the gas phase, monosaccharide ions with tri- and tetradentate Li-O coordinations are generally more stable than bidentate Li-O coordinations based on DFT calculations. But because many ions adduct a water molecule, bidentate structures must exist in the gas phase as kinetically trapped structures. Therefore, water adduction experiments do not measure the most favorable gas phase structures unless the kinetically trapped bidentate structures can isomerize. Monosaccharides with low experimental R_U values have favorable bidentate Li-O coordinations in the solution phase, as determined by DFT. For example, the most favorable solution-phase structures of Glc and 6dGlc have bidentate coordinations as shown in Figures 3.3 and 3.6, respectively. Glc and 6dGlc have among the lowest R_U values for glucose derived monosaccharides. Bidentate structures are favorable in solution because the lithium cation prefers to remain partially solvated by the surrounding water solvent. In solution, a tri- or tetradentate Li-O coordination means that the lithium must sacrifice a portion of the solvation shell, so these coordinations are less favorable. Additionally, monosaccharides without axial hydroxyl groups at the C2/C3/C4 positions often require ring puckering to boat or skewboat structures to form tri- or tetradentate coordinations, such as α-Glc and 6dGlc. Therefore, tri- or tetradentate coordinations that cannot be formed in the $^4C_1$ ring conformation are typically not favorable in solution phase. Conversely, in the gas phase, monosaccharide ring puckering to form tri- or tetradentate coordinations may become favorable. Ring puckering induces unfavorable strain into the molecule, but, in the gas phase, formation of a new favorable Li-O coordination can overcome the unfavorable ring strain to stabilize the ion (Figure 4.2b).

To study isomerization and ring puckering of $[\text{Monosaccharide+Li}]^+$ ions as they are transmitted through the ion optics of the mass spectrometer, internal energy was added into the ions in the ion optics of the MS by increasing the capillary/skimmer voltage difference. Then the water adduction R_U values were measured. R_U values of four hexoses and five monodeoxy glucoses as a function of capillary/skimmer voltage difference are plotted in Figure 4.2a. Most monosaccharides are observed to have changing R_U values as an increasing amount of internal energy is imparted. 1dGlc, 6dGlc, All, Glc, Gal and 3dGlc all begin with a low R_U value at low voltages, and each has an observable increase in R_U at a unique onset voltage, representing different activation energy barriers. The increasing R_U values as are interpreted as isomerization or ring puckering of kinetically trapped solution-phase bidentate structures to more favorable gas-phase tri- or tetradentate structures that are not observed to react. The hypothetical reaction coordinate in Figure 4.2b illustrates the isomerization of a kinetically trapped solution-phase bidentate ion that has been destabilized since being released into the gas-phase. As internal energy is added to the kinetically trapped solution-phase bidentate ion, it may overcome a transition state activation energy barrier and convert to a more gas-phase favorable tridentate ion. The lower capillary/skimmer voltage difference does not overcome the isomerization/ring puckering internal energy barrier of a bidentate structure, but a larger voltage difference does.

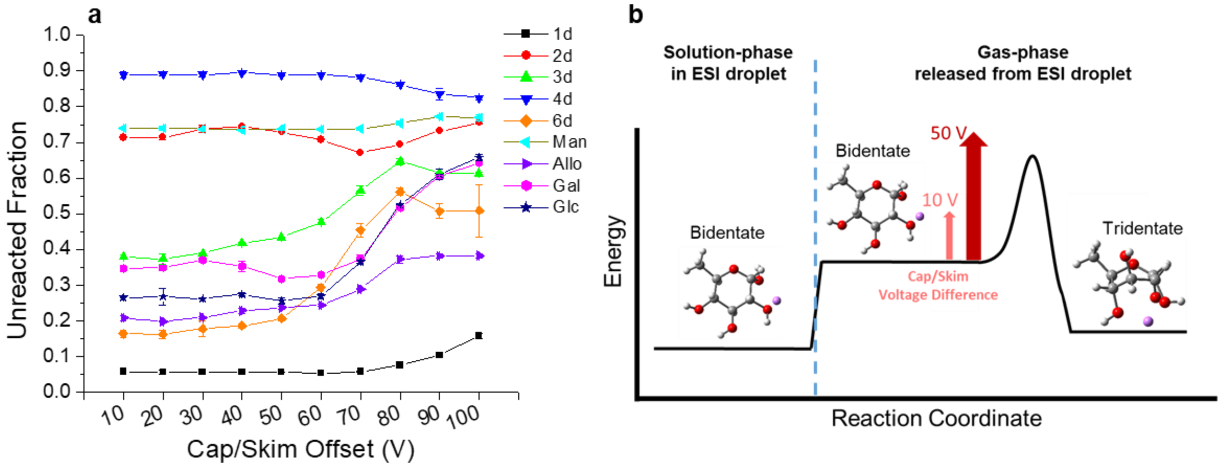

Figure 4.2 a) R_U as a function of capillary/skimmer voltage difference for 9 monosaccharides. As capillary/skimmer voltage increases, ion-neutral collisions become increasingly energetic and a greater amount of internal energy is imparted into ions. b) Hypothetical isomerization reaction coordinate of a kinetically trapped solution-phase structure to a more gas-phase favorable tridentate structure.

The lowest onset voltage was observed for 6dGlc and is likely due to the absence of the sterically bulky hydroxymethyl group. How the lack of a hydroxymethyl group may affect ring-puckering activation energies are discussed in Chapter 3.1 and 3.3, and potential isomerization schemes for 6dGlc were proposed in Figure 3.7. Generally, increasing R_U values are observed for monosaccharides that begin with low R_U values. Man, 2dGlc and 4dGlc begin with high R_U values and minimal R_U change is observed with increasing voltages. Monosaccharides with high R_U values tend to form favorable tri- and tetradentate structures in the solution phase; therefore, if majority tri- and tetradentate structures are released by ESI then isomerization to other tri- or tetradentate structures will not change the measured R_U values. Only slight R_U changes are observed for the monosaccharides with high R_U values. Above 80 V, Man R_U increases and 4dGlc R_U decreases. For 2dGlc, there is an R_U rise and fall across the voltage range. A similar trend was observed for Gal. It is possible that a decreasing R_U results from isomerization of a tridentate structure into a bidentate structure, but this trend is not well understood. Also, as the capillary/skimmer voltage difference was increased, fragment ions are observed in the mass spectrum. It could be hypothesized that tridentate ions have a lower ε_o for fragmentation due to increased ring strain, thus, the proportion of bidentate structures in the ion trap increases. At least four replicate experiments were made for each monosaccharide with small standard deviations at each data point, but further experimental and theoretical investigation would be required to tease out details of the decreasing R_U values.

It should be noted that the isomerization of $[\text{Monosaccharide+Li}]^+$, and the resultant R_U change, could not be replicated using resonance excitation within the ion trap. Resonance excitation/activation is used generally for CID in the ion trap; instead, attempts to induce isomerization with low excitation amplitudes failed. It was originally hypothesized that imparting internal energy into the ion should induce ring puckering and observable R_U changes regardless of if it were within the ion optics or the ion trap. Upon further consideration, there are multiple differences in the two activation schemes which may be the reason for the discrepancy. Between the capillary and skimmer cone, ions are activated by a few relatively energetic collisions with nitrogen gas as they are transmitted through. During resonance excitation, ions are first trapped and isolated in the ion trap and subsequently excited by an on-resonance ac waveform to induce many, relatively low-energy collisions with helium gas. Because nitrogen is more massive than helium, an ion-nitrogen collision will impart more internal energy than an ion-helium collision. To summarize, in the ion optics, a few large steps of internal energy are quickly imparted into the ions as they traverse the capillary/skimmer region (a few ms). During resonance excitation CID in the ion trap, many small steps of internal energy are imparted into the ions during a relatively long activation time of 40 ms.

Activation of [Monosaccharide+Li]$^+$ ions may induce isomerization or dissociation. The first step for dissociation of lithiated hexoses was proposed to be ring opening at the anomeric center[33]. If the ε_o is greater for ion isomerization than for ring opening/dissociation, then during resonance excitation in the ion trap we may only observe ion dissociation. Conversely, if large energy steps are imparted into an ion, there may be excess ε for both isomerization and dissociation pathways. If one (or a few) collision(s) raises ion $\varepsilon > \varepsilon_o$ of both isomerization and dissociation, there is excess energy for both pathways; the reaction with the fastest rate will be observed in greatest abundance. Though some fragmentation is observed to occur in the ion optics, it can be hypothesized that the reaction rate of dissociation is slower because ring opening requires hydrogen transfer from O2 to O1. Isomerization may only require disrupting hydrogen bonds (not breaking covalent O-H bonds) and forming another Li-O coordination.

4.2 Water Adduction during Ion Accumulation in the Ion Trap

In previous sections we have discussed some elements of the entrance ion optics (Figure 4.1) that use voltages, and the resultant electric fields, to focus and transmit an ion beam into the quadrupole ion trap mass analyzer. The ion optics voltages can be set to optimize transmission of ions into the ion trap, or to completely block ion transmission. Because ions are continuously being generated at the ESI source, blocking ion transmission during MS^n (while the ion trap is performing mass analysis and other functions) is necessary for successful analysis. Inability to block ions from entering the trap would cause unwanted space-charge effects (high charge density) that lead to ion-ion repulsion, incorrect *m/z* determination and generally poor-quality mass spectra. Also, ions entering the trap at all times would negate the possibility of isolating and manipulating an *m/z* value of interest using MS^n, as well as likely convolute the spectrum. Therefore, ions are only transmitted into the ion trap for a short time, known as the trap accumulation time (one to hundreds of milliseconds), prior to performing the MS^n

experiment. At all times, other than the trap accumulation time, ion transmission is blocked. The trap accumulation time can be held constant, or the Bruker algorithm known as 'ion charge control' (ICC) can modulate the trap accumulation time based on ion flux to maintain a consistent number of ions for all MS events.

Ion flux generated by ESI is dependent on various parameters; for example, analyte concentration and ionization efficiency, etc.[83, 84]. Also, notably, the electrospray solvent affects the ESI process. Ionization efficiency is generally greater with methanol as an electrospray solvent than water; methanol has a lower vaporization temperature and a lower surface tension. Nebulization of methanol for ESI generates smaller initial droplet sizes than for water due to differences in surface tension. The smaller initial droplet sizes of methanol aid ion ejection (transfer from solution to gas phase) and lower vaporization temperature expedites droplet and ion-cluster desolvation, both of which result in a higher ion flux to the trap. Because most of the water adduction experiments in this dissertation thus far have used water an as electrospray solvent, lower ion fluxes resulted in relatively long accumulation times.

If the trap accumulation time is sufficiently long, $[\text{Hexose+Li}]^+$ ions that enter the ion trap early in the trap accumulation segment can adduct a water molecule during accumulation, prior to further MS^n steps. The *m/z* intensity ratio i187 / (i187 + i205) of glucose observed in a full scan MS experiment was monitored at incremented accumulation times (without ICC) for three different solvent systems (Figure 4.3). It should be noted that the ratios in Figure 4.3 are calculated in a similar manner to final R_U values reported in previous sections but are experimentally different; they are diagnostic ratios measured during a full scan MS experiment where no scan delay is applied. Lithium chloride salt was used, instead of lithium acetate, for the same reason as discussed in Chapter 3.4. Using short, static accumulation times denies ample time for many $[\text{Hexose+Li}]^+$ ions (*m/z* 187) to adduct a water molecule during accumulation and prior to detection; the ratio i187 / (i187 + i205) remains high because few *m/z* 187 ions are converted to *m/z* 205 by way of water adduction. As accumulation time is varied from 10 to 50 ms in increments of 10 ms, small decreases in the ratio are observed (Figure 4.3). For longer, static accumulation times (100 ms and greater) there is ample time to generate *m/z* 205 by water adduction; the ratio i187 / (i187 + i205) begins to decrease due to reaction of *m/z* 187 to 205. Greater decreases in the ratio are observed for large accumulation time increments. With ICC on, the trap accumulation time is modulated based on ion flux, so the ratio depends on electrospray solvent. Using water and water/methanol electrospray solvent systems the maximum allowable accumulation time of 300 ms (user defined) was reached for every MS scan event. For methanol, the average accumulation time was near 30 ms. The concentrations of Glc and LiCl were equimolar in each solvent system; therefore, the unique accumulation times are a result of ESI solvent composition causing different ion fluxes and ionization efficiencies. The "ICC on" data points for water and water/methanol closely resemble the ratios observed when a static accumulation time of 300 ms was applied. Similarly, the methanol "ICC on" ratio resembles the 30 ms static accumulation time data point.

Multiple data points for methanol at long accumulation times are missing in Figure 4.3 due to the high ion flux with methanol. Accumulation times of 200 ms or longer are not viable when using methanol as seen by the large error bar at 200 ms and missing data points for 300, 500 and 1000 ms. Near 200 ms, the charge capacity of the trap is reached, and ion-ion interactions (space charging) begin to degrade the spectral quality. Mass spectral peaks broaden, and mass-to-charge ratios shift to artificially high values.

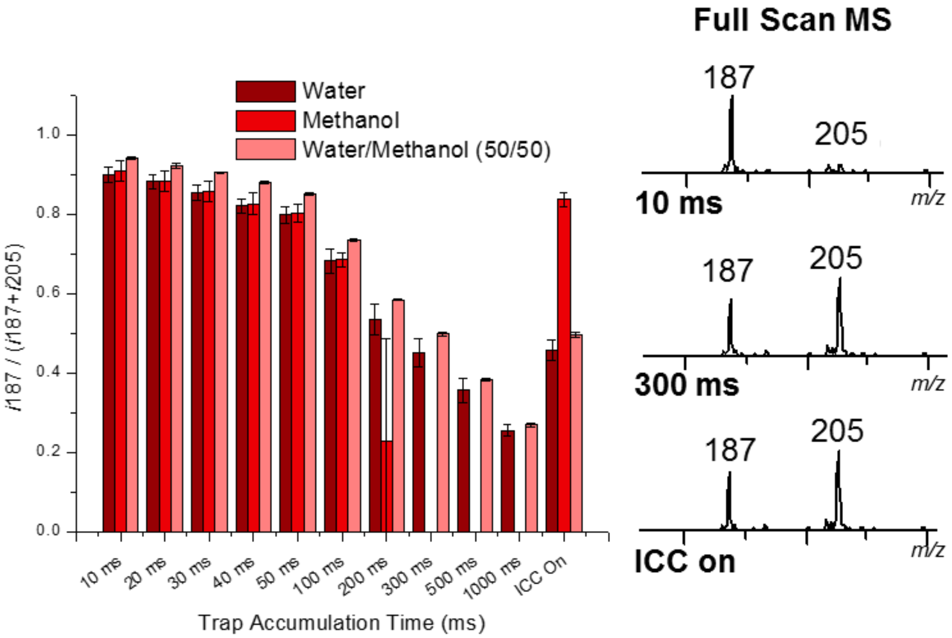

Figure 4.3 (left) Glc diagnostic ion ratio measured in the full scan mass spectrum as a function of ion trap accumulation time. The missing data points for MeOH at 200 through 1000 ms are explained in the body of the text. (right) Representative full scan mass spectra with water as the electrospray solvent for static accumulation times of 10 and 300 ms and dynamic accumulation time with ICC on.

The effects of trap accumulation time on the ratio i187 / (i187 + i205) observed in a full scan mass spectrum have been discussed (Figure 4.3). Trap accumulation time also affects the final R_U measured for Glc after isolation and application of a 1000 ms scan delay (Figure 4.4). To measure the final R_U, [Glc+Li]$^+$ ions were accumulated in the trap for incremented times, then isolated and provided a 1000 ms scan delay time for water adduction. Isolation of *m/z* 187 after accumulation resulted in ejection (loss) of any *m/z* 205 formed during trap accumulation; therefore, isolation of *m/z* 187 acted to 'purify' the ions that remained unreacted during trap accumulation. With increasing trap accumulation times, more *m/z* 187 reacted to the *m/z* 205 ion population, which was subsequently lost upon isolation of *m/z* 187. As more *m/z* 205 was lost to the isolation step, there were fewer reactive ions in the trap during the scan delay and the measured final R_U was altered. At increasing accumulation times, the unreacted ions are 'purified', resulting in increased R_U values (Figure 4.4).

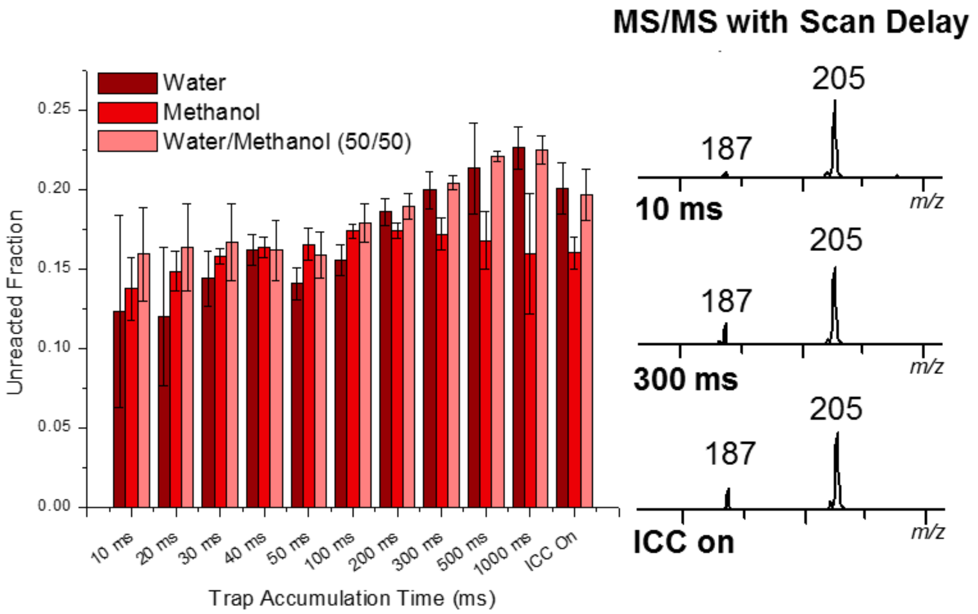

Figure 4.4 (left) Glc final R_U measured (with isolation and 1000 ms scan delay) as a function of ion trap accumulation time. (right) Representative MS/MS spectra after static accumulation times of 10 and 300 ms and dynamic accumulation time with ICC on. After accumulation, *m/z* 187 was isolated and a 1000 ms scan delay was applied to allow water adduction to occur.

Increasing R_U values as a function of trap accumulation time were observed for all three electrospray solvent compositions; the trend becomes more apparent as the static accumulation time is increased above 50 ms. With ICC on, the dynamic accumulation times for methanol, water and methanol/water averaged 75, 300 and 300 ms, respectively. The relatively shorter dynamic accumulation times for methanol are due to the differences in ion flux discussed earlier. It is common practice to operate the MS with ICC on. As seen in Figure 4.4, different electrospray solvents may result in distinct final R_U values based on the dynamic accumulation times set by ICC. The number of ions measured for methanol (ICC ≈ 200,000) may have been different than for water and water/methanol (ICC ≤ 200,000). Because the maximum allowable accumulation time (300 ms) was reached for water and water/methanol, the desired ICC limit of 200,000 may not have been reached. A higher ICC value means more ions in the trap and a greater ion density. Measuring more ions with methanol means a different distribution of lithium cationized Glc structures may have been accumulated. Also, a greater ion density could increase ion-ion interactions and ion energy, which affects the water adduction reaction rate (discussed in Chapter 4.3). Regardless of these two considerations, the long accumulation times (>300 ms) required for water and water/methanol to reach ICC ≈ 200,000 would heighten the trend observed in Figure 4.4. Hypothetically, if water and water/methanol required 600 ms to reach ICC ≈ 200,000, a larger fraction of *m/z* 187 would adduct to 205 before isolation. This increased purification of unreacted structures means the remaining ions at *m/z* 187 after isolation would result in a higher R_U.

The expected R_U increase is not observed in Figure 4.4 for methanol beyond a 200 ms accumulation time, rather a decrease is observed. The decrease is hypothesized to be due to space charging during trap accumulation, similar to what was observed during the full scan MS experiment in Figure 4.3. As the charge capacity of the trap is reached, ion-ion interactions increase the energy and velocity of ions during the trap accumulation step. Raising ion energies and velocities either prevents ions from adducting a water molecule or breaks some Li-H_2O bonds that form during accumulation. A phenomenon similar to this will be discussed in the next section.

While the R_U differences in Figure 4.4 were purposeful artifacts of the experimental design, they show it may not be proper to compare water adduction data from dissimilar, or uncontrolled, experiments. The current experiments suggest that electrospray solvent affects water adduction metrics through modulation of trap accumulation time. As with any other MS-based study, calibration and controls must be used.

4.3 Drive rf Voltage Amplitude during the Scan Delay

Ion trap mass analyzers are used to stabilize, manipulate, and controllably destabilize ions using alternating current voltages oscillating at radio frequencies (rf). The 'drive' rf voltage (781 kHz) applied to the center electrode (Figure 4.5a) of the Bruker HCT ion trap generates a stabilizing (trapping) quadrupolar electric field. A variable frequency 'auxiliary' rf voltage can be applied to the end cap to create a dipolar electric field for ion manipulation, activation or ejection. The drive rf frequency is fixed, but the drive rf voltage peak-to-peak amplitude (V_{rf}) is changed to adjust the stability, trajectory, and frequency of ion motion. The V_{rf} applied dictates the trapping forces acting on an ion. At a given V_{rf}, each *m/z* value has a distinct trapping q_z value, a parameter of the Mathieu equation[85–87]. The q_z value of an ion is inversely proportional to *m/z* and is proportional to the frequency and velocity of ion motion by some factor. Increasing the V_{rf} will raise the q_z of all *m/z* values; therefore, increasing the frequency and velocity of all ion motion. The V_{rf} is changed during a mass spectrometry experiment and can be monitored to visualize the ion trap scan function (Figure 4.5b-c). A photo of an ion trap MS/MS scan function is shown in Figure 4.5c. Following the previous scan function, the V_{rf} is lowered to empty the ion trap by destabilizing all ions; the electric field is reduced to minimize the trapping forces felt by ions. During ion accumulation, the V_{rf} level is optimized, using the 'trap drive' parameter, for effective trapping of the *m/z* range of interest. Isolation is the first mass-to-charge selective step in the scan function. The V_{rf} is raised to eject ions with a lower *m/z* than the ions being isolated and various auxiliary waveforms can be used to aid in the isolation step[88–91]. After isolation, a scan delay (one to hundreds of milliseconds) is applied to collisionally cool ions to the center of the trap prior to the analytical scan. The analytical scan is a linear ramp of V_{rf} for the controlled destabilization of sequential *m/z* values and detection of ions. The simplest way to eject ions is by boundary ejection when they reach $q_z = 0.908$. More commonly, because of performance improvements, resonance ejection is employed to eject ions at a lower q_z, where an auxiliary rf voltage is applied and an ion is ejected when its frequency of motion comes into resonance with the auxiliary rf frequency. Forgoing any further in-depth discussion about quadrupole ion trap fundamentals, we will relate the drive rf voltage amplitude, V_{rf}, during the scan delay (used to control water adduction reaction time) to the water adduction ion/molecule reaction results.

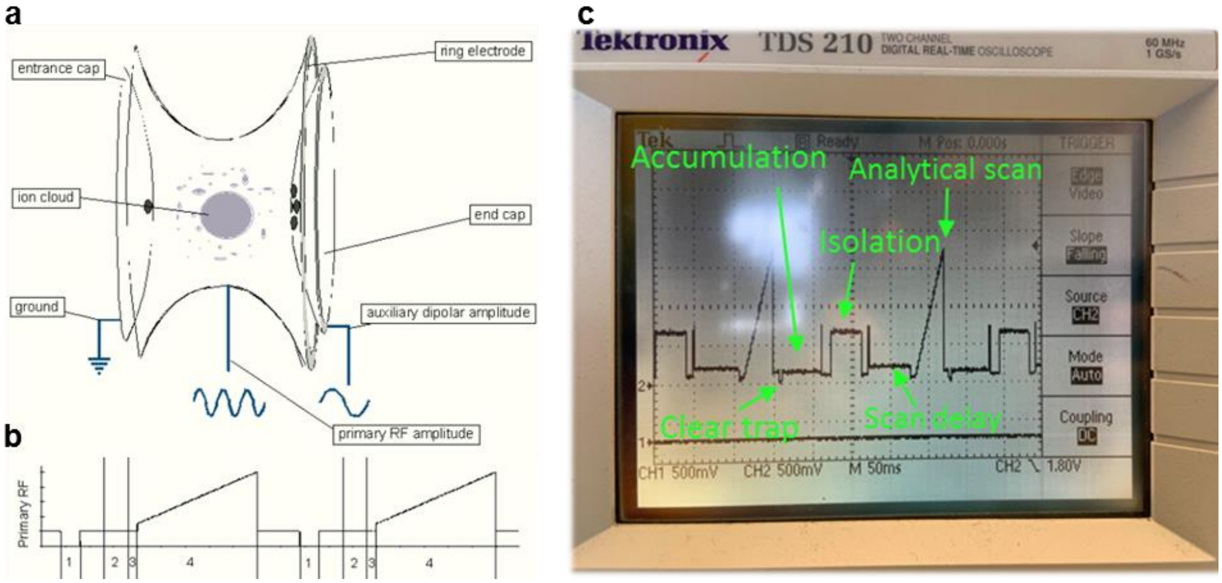

Figure 4.5 a) Schematic of a quadrupole ion trap. b) Illustration of V_{rf} amplitude during important steps of the ion trap scan function for an MS experiment: 1, clear all ions from trap; 2, accumulate ions in trap; 3, scan delay; 4, analytical scan/mass analysis. c) Photo of the ion trap drive rf voltage (V_{rf}) amplitude measured as a function of time during an MS/MS experiment. V_{rf} was monitored using an oscilloscope at the J11 pin of the Bruker ion trap rf board.

The scan delay was originally intended to provide time for collisional cooling of the ions to the center of the ion trap. The ion packet in center of the trap assures reproducibility of the analytical scan which is necessary for accurate and precise assignment of *m/z* values. We have used the scan delay in an unorthodox manner, for controlling the water adduction reaction time of $[M+Li]^+$ ions. Because of effects on reactant $[M+Li]^+$ ion energy (q_z, frequency, velocity, etc.), the V_{rf} level during the scan delay will affect the water adduction ion/molecule reaction. The V_{rf} level during the scan delay is determined by the mass-to-charge range defined in the MS method. More specifically, the 'scan begin' value sets the lowest *m/z* of the scan range, on which the V_{rf} during the scan delay is dependent. During the scan delay, V_{rf} is stepped to adjust the q_z value of the lowest *m/z* to just below the q_{eject} for resonance ejection. The V_{rf} step quickly destabilizes and ejects ions below the range of interest. The scan delay time allows collisional cooling of the remaining trapped ions and, following the delay, the analytical scan (linear ramp of V_{rf}) is initiated to immediately eject the ions at the 'scan begin' *m/z* value. The V_{rf} level during the scan delay was monitored at two different 'scan begin' values, where the low end of the scan range was set to either *m/z* 15 or 150 (Figure 4.6).

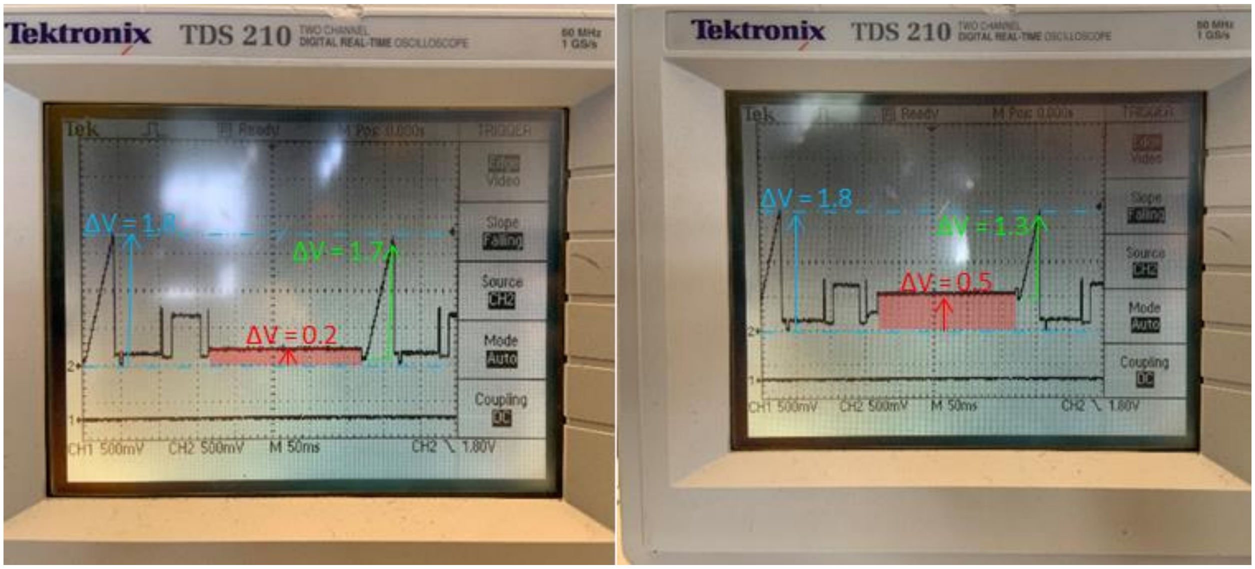

Figure 4.6 Scan begin value effect on V_{rf} during scan delay. MS/MS scan functions with a static accumulation time followed by isolation of *m/z* 187 and a 200 ms scan delay (red) was applied prior to the analytical scan (green). The range for the analytical scan was set from *m/z* 15 to 500 (left) and *m/z* 150 to 500 (right). The V_{rf} amplitude during the scan delay and linear voltage ramp of the analytical scan are both affected by the 'scan begin' value. The V_{rf} was monitored using an oscilloscope at the J11 pin of the Bruker ion trap rf board. The measured V_{dc} values are a rectified and attenuated signal of the peak-to-peak drive rf voltage (V_{rf}). On the left, the ΔV_{dc} of 1.7 V represents the linear V_{rf} ramp from 150 (to eject *m/z* 15) to 4850 V_{rf} (to eject *m/z* 500).

The water adduction final R_U of Glc was measured at incremented 'scan begin' values (Figure 4.7). The low end of the scan range was adjusted from *m/z* 15 to 187 and the upper limit was held constant at *m/z* 500. For each scan range ions were accumulated, *m/z* 187 ($[Glc+Li]^+$) was isolated and a 1000 ms scan delay was applied for water adduction prior to detection.

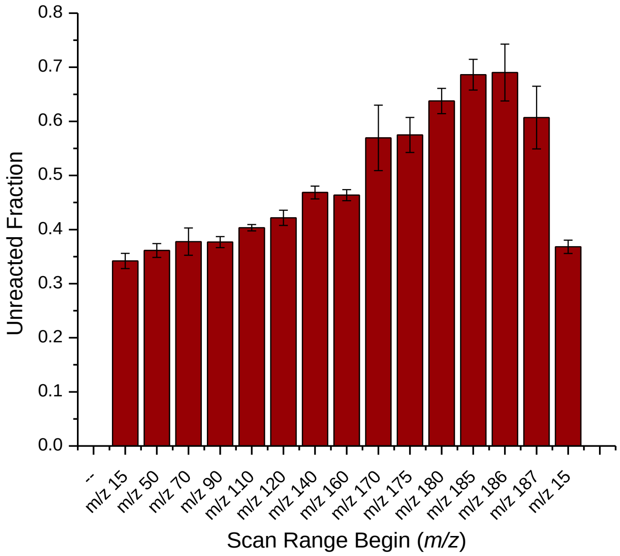

Figure 4.7 R_U values for Glc measured after 1000 ms scan delay at various 'scan begin' values. The low end of the *m/z* range was incremented from *m/z* 15 to 187 and the upper end of the range was held at *m/z* 500.

The measured R_U value for Glc is lowest at a scan begin value of *m/z* 15 (first and last data points in Figure 4.7) and is observed to positively correlate with an increasing scan begin value. The R_U of Glc rises until a scan begin value of *m/z* 186. When the scan begin value is set to *m/z* 187, the R_U of Glc is observed to decrease. Because the $[Glc+Li]^+$ ion is *m/z* 187, identical to the low end of the mass range, it is hypothesized that enough energy is imparted into $[Glc+Li]^+$ ions during the scan delay to eject them from the ion trap. When *m/z* 187 ions are ejected from the trap, the measured ratio i187 / (i187 + i205) will decrease – as observed in Figure 4.7 for a scan begin value of *m/z* 187. The q_z value of *m/z* 187 during the scan delay can be calculated as a function of 'scan begin' value using the relationship,

$$q_1 m_1 = q_2 m_2$$

where $q_1 = q_{eject} = 0.784$ (the q_z value of the first *m/z* to be ejected by the analytical scan), m_1 = variable (*m/z* set by the 'scan begin' value), q_2 = unknown (q_z value of the reacting ion) and $m_2 = 187$ (*m/z* of reacting ion). See Table 4.1.

Table 4.1 Estimated q_2 value of a $[\mathrm{Glc+Li}]^+$ ion during the ion trap scan delay as a function of 'scan begin' value (m_1)

m_1	q_2
15	0.063
50	0.210
70	0.293
90	0.377
110	0.461
120	0.503
140	0.587
160	0.671
170	0.713
175	0.734
180	0.755
185	0.776
186	0.780
187	0.784

Increasing the scan begin value raises V_{rf} during the scan delay to set the q_1 value of m_1 near or equal to $q_{eject} = 0.784$. Consequently, the q_2 value of $[\mathrm{Glc+Li}]^+$ ions increase – raising the frequency of ion motion and average ion kinetic energy. The q_z value can be related to V_{rf} and kinetic energy can be related to ion velocity with the following equations:

$$q_z = \frac{8zeV_{rf}}{m(r_0^2 + 2z_0^2)\Omega^2}$$

$$KE = \frac{mv^2}{2}$$

where m is the mass of an ion, z is the nominal charge on an ion, e is the electron charge, V_{rf} is the drive rf voltage amplitude, r_0 is the radius of the ring electrode in meters, $2z_0$ is the distance between the end-cap electrodes measured along the axis of the trap in meters, and Ω is the radial frequency of the drive rf, KE is kinetic energy and v is velocity. As seen in the equation, V_{rf} and q_z are positively correlated; an increase in Vrf will increase average ion KE in the trap. Therefore, higher scan begin values raise both V_{rf} and ion velocity during the water adduction reaction time (scan delay). This simplified relationship between q_z and KE does not account for ion-neutral collisions or ion-ion interactions and is a rudimentary estimate of how drive rf voltage amplitude affects ion velocity/energy. At higher velocities, ion trajectory will be further from the center of the ion trap and ion-neutral interaction energies may rise. Greater $[Glc+Li]^+$ ion velocities either results in fewer interactions with water molecules that form stable Li-H_2O bonds or some stable Li-H_2O bonds that do form are dissociated before detection. Both scenarios can contribute to the raised R_U at 1000 ms.

This phenomenon of drive rf voltage during the scan delay introduced a curious artifact into water adduction data for a CID product ion of $[Glc+Li]^+$. The dissociation chemistry and water adduction to CID product ions of lithium cationized hexoses will be discussed in detail in Chapter 6, but here a short story that relates to the *m/z* 67 ($[C_2H_4O_2+Li]^+$) CID product ion of $[Glc+Li]^+$ is discussed. The $[C_2H_4O_2+Li]^+$ product ion has only two oxygen atoms and can only form bidentate Li-O coordinations. Curiously, $[C_2H_4O_2+Li]^+$ was observed to have an R_U value > 0.4 after 1000 ms of reaction time; this observation contradicts our mechanistic understanding of the water adduction R_U. All $[C_2H_4O_2+Li]^+$ ions should react in the ion trap because only bidentate Li-O coordinations exist. Water adduction curves were generated at various 'scan begin' values for $[C_2H_4O_2+Li]^+$ by measuring the ratio i67 / (i67 + i85) for 0 to 7000 ms reaction times (Figure 4.8).

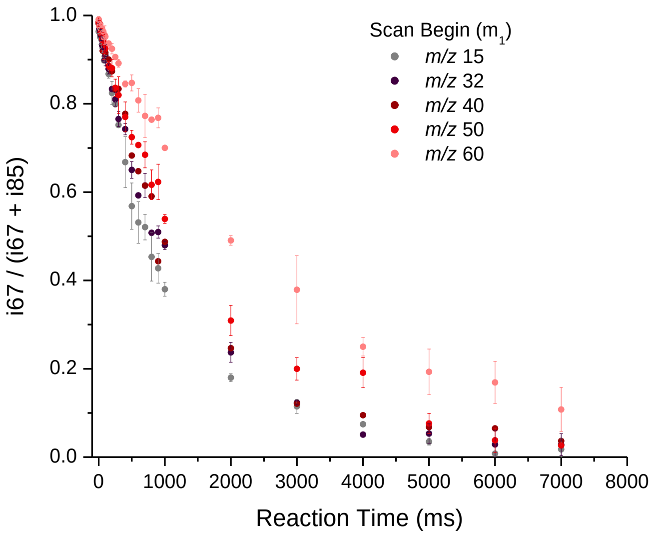

Figure 4.8 Water adduction curves for $[C_2H_4O_2+Li]^+$ at various scan begin (m_1) values. At a scan begin (m_1) of *m/z* 15, the q_2 value of *m/z* 67 is low during the scan delay. At a scan begin (m_1) of *m/z* 60, the q_2 value of *m/z* 67 is high during the scan delay, higher estimated velocity for the reacting ion.

The scan begin value alters the water adduction reaction rate. When scan begin (m_1) was set to *m/z* 15, the ratio i67 / (i67 + i85) decreases significantly more relative to $m_1 = 60$ at short reaction times. At $m_1 = 60$, the q_2 value of the reacting ion is elevated and fewer interactions that result in formation of stable Li-H_2O bonds occur between $[C_2H_4O_2+Li]^+$ and water, or stable Li-H_2O bonds that do form are dissociated. When provided long reaction times (6000 or 7000 ms), $[C_2H_4O_2+Li]^+$ was observed to completely react for m_1 = 15, 32, 40 and 50, but even after a 7000 ms reaction time at $m_1 = 60$, the ratio i67 / (i67 + i85) did not reach zero. Hypothetically, if $[C_2H_4O_2+Li]^+$ completely reacts after more than 7000 ms while $m_1 = 60$, then it is likely that only the reaction rate is affected and stable Li-H_2O bonds are not being dissociated. This experiment highlights that certain MS instrument parameters can introduce artifacts into data, and in this case an artifact that contradicted the fundamental mechanism of the water adduction ion/molecule reaction. The $[C_2H_4O_2+Li]^+$ ions, in fact, do completely react in accordance with our understanding of the water adduction mechanism, but at a reduced reaction rate due to less frequent interactions. Accordingly, low *m/z* ions may have artificially slow reaction rates due to relatively high q_z values during the scan delay. Duly, it may not be proper to compare water adduction reaction rates for reacting ions of different *m/z* ratios unless they are set to have the same q_z value.

4.4 Summary

For any analytical measurement the experimental parameters, user defined or not, will affect the instrument response. Any measurement with electrospray ionization and mass spectrometry involves many complex, compounding variables that dictate the experimental results. Chapter 4 highlights a few of the experimental and instrument parameters that are known to affect the results of the water adduction ion/molecule reaction. These parameters and their effects must be understood and considered during experiment design, data analysis, data interpretation and drawing conclusions. If the water adduction ion/molecule reaction were to be used for sugar identification in a cross-platform or cross-laboratory scenario (less well-controlled than confinement to a single MS instrument and laboratory), then some form of calibration must be comprised. This calibration would be similar to that for a quantitative LC-MS/MS measurement, where standards of known identity and quantity are analyzed to determine the expected response range for a specific instrument platform, set of instrument parameters and experimental design. It may be that a calibration for the water adduction ion/molecule reaction could simply consist of R_U and reaction rate measurements of known, pure hexoses and other pure carbohydrate standards under controlled experimental conditions.

CHAPTER 5: PRE- AND POST-IONIZATION SEPARATION OF CARBOHYDRATE STRUCTURAL CONFORMATIONS

5.1 Ion Mobility Spectrometry and Ion-Neutral Collision Cross Sections

Ion mobility spectrometry (IMS) is a post-ionization separation that occurs on the millisecond timescale and separates ions based on what is commonly described as their shape-to-charge ratio, where shape loosely refers to cross-sectional area. IMS can be thought of as gas-phase electrophoresis. There are multiple types of IMS instrumentation[23, 92], but, generally, ions are under the influence an electric field and undergo collisions with a neutral drift gas. Larger ions have larger cross-sectional areas and undergo more collisions with gas molecules. Larger ions, therefore, have a slower drift velocity and take longer than a smaller ion to traverse the IMS separation region to the detector. IMS analysis provides values of ion mobility (K), a characteristic value that is related to the drift velocity of an ion through an electric field. K is related to the three-dimensional structure of an ion, and therefore the collision cross-section (CCS) of the ion-neutral collision can be calculated using the Mason-Schamp equation[93]. Measured CCS values are reported as an area in angstroms ($Å^2$) and can be theoretically modeled using DFT optimized structures and CCS determination algorithms[94, 95].

Here, a modified Waters Synapt G2-Si Q-cIM-ToF mass spectrometer was used to study the gas-phase structures of lithium cationized mono- and disaccharides. The ESI-quadrupole-cyclic ion mobility (cIM)-TOF MS system is described in Chapter 2.7 and shown in Figure 2.3. The cIM separation is a cyclic traveling wave ion guide and uses a separation technology known as traveling wave IMS. For a cIM separation, a small packet of ions is injected into the cIM separation region and can be subjected to 1 or more passes around the cyclic ion guide and then directed towards the TOF for mass analysis and detection. Mass-to-charge specific arrival time distributions (ATDs) can be extracted from the IMS-MS data. More passes through the cIM device provide better resolution of ions with differing CCS values (Figure 5.1). In practice, the number of passes around the cIM device is limited by the 'racetrack' effect, where ions of higher K (high drift velocity, low CCS) can 'lap' ions of low K (low drift velocity, high CCS). For example, after 20 ms of separation time, ion A makes 1.75 passes and ion B makes 1 pass in the cIM. Ion A has a higher K value than ion B. But if ion detection begins as ion B finishes its first pass (ion B arrival time = 20 ms), ion A will be measured to have an arrival time = 25 ms. Without prior knowledge of the ion mobilities the experiment results would wrongly suggest that ion A has a lower mobility than ion B. Therefore, ATDs can become convoluted if high K ions 'lap' the low K ions.

The quadrupole prior to the cIM enables *m/z* selection prior to the cIM for mass-to-charge specific ion mobility separations if desired. Pre-cIM (between quadrupole and cIM) and post-cIM ion storage elements are positioned in the system ion path just before, and beyond, the cIM separation region, respectively. Dissociation of ions can be collisionally induced prior to the cIM separation, or prior to the TOF analyzer. At any time during the cIM separation, ions of a distinct mobility can be routed to the pre- or post-cIM storage for secondary IMS experiments and/or CID, or detection. Because the cIM is coupled to a TOF analyzer, there is no ion trap to do water adduction. The pre- or post-cIM storage can be used to store ions, but water adducted ions were not detected. It is likely that some water adduction could occur in the pre- or post-cIM storage, but the Li-H_2O bonds do not survive transfer from the ion storage devices or acceleration into the TOF separation region.

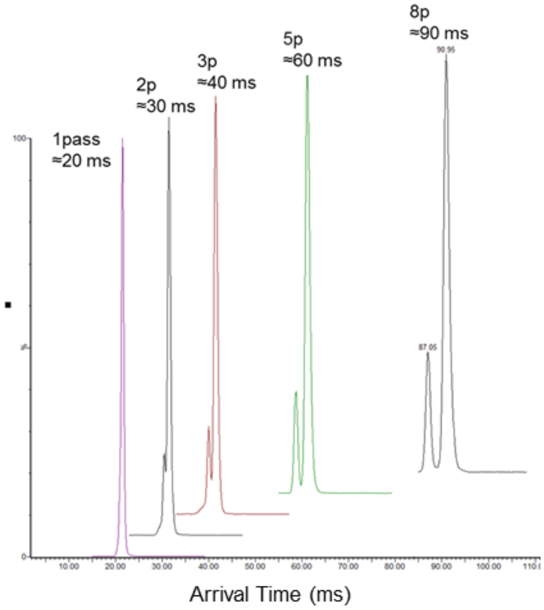

Figure 5.1 Increasing number of cIM passes improves feature resolution for [Fructose+Li]$^+$. After five passes, the two peaks are nearly baseline resolved. A single pass takes about 10 ms. The arrival time after pass 1 is 20 ms due to additional time (10 ms) required for ion accumulation in the pre-cIM storage device before separation.

Ion mobility spectrometry (IMS) is one of many tools that aid in deconvolution of isomeric carbohydrate structures. Isomeric carbohydrates may exist as various gas phase conformations, such as different anomers or different metal cationization sites. Metal cationization of carbohydrates has improved IMS separations[26], but many IMS systems lack the resolving power to separate monosaccharides. The cIM system used here was able to resolve multiple features for a single lithium cationized hexose epimer for the first time but could not separate the different epimers from one another. Recently, high resolution IMS techniques have resolved multiple features for a reducing polysaccharide[25, 56]. In these previous studies it was argued that the IMS resolved features are due to separation of the alpha and beta anomers. Another possible structural variant of gas-phase metal cationized sugars is the location of cation coordination (e.g. hexoses have 6 oxygen atoms available to coordinate to a metal cation in different places). Relating to sites of metal cationization, a previous study reported differences in ATDs for polysaccharides upon coordination with various metal cations[96]. The polysaccharides were found to have unique distributions of gas-phase conformations when coordinated to different metal cations. Multiple unique IMS features were observed for each metal-polysaccharide combination and the IMS separated gas-phase conformations had different CID characteristics.

Here, we investigate IMS separation of monosaccharides and disaccharides, with the goal of understanding whether anomers, or metal cationization sites are the reason for feature separation. Liquid chromatographic (solution phase) and cIM (gas phase) separations were used to parse out the various solution- and gas-phase structural conformations of mono- and dissacharides. IMS, hydrophilic interaction (HILIC) liquid chromatography, CID and theoretical data presented herein for mono- and disaccharides is not entirely consistent with the hypothesis that IMS feature resolution is solely due to separation of anomers, posing the question: does IMS resolve anomers, different cationization sites, or a convolution of the two?

5.2 HILIC LC Separation and CID of Hexose Anomers

Measuring individual anomers of each hexose can help explain the features observed in cIM ATDs. HILIC chromatography was used to separate hexose anomers prior to the Bruker HCT ion trap MS system. To test the ability of HILIC for separation of anomers, 1,5-Anhydroglucitol (1dGlc, glucose that has been deoxygenated at the C1 position) was injected onto the HILIC column. As expected, a single chromatographic peak was detected for 1dGlc because it lacks an anomeric center and cannot exist as multiple anomers. All other hexoses produced two peaks, one for each anomer (Figure 5.2). Separation of hexose anomers was further confirmed by retention order matching of pure α- and β-Glc to an equilibrated mixture of Glc anomers in aqueous solution. The pure anomers were individually injected immediately after being dissolved in water to minimize mutarotation prior to analysis. In Figure 5.2, the peak ratios for each hexose match the anomeric ratio measured by NMR[8]. Based on peak assignment by anomeric ratio (relative peak area), the α-anomer of Gal and Man elute before their respective β-anomer. For all three hexoses the α-anomer is more weakly retained on the column (shorter retention time).

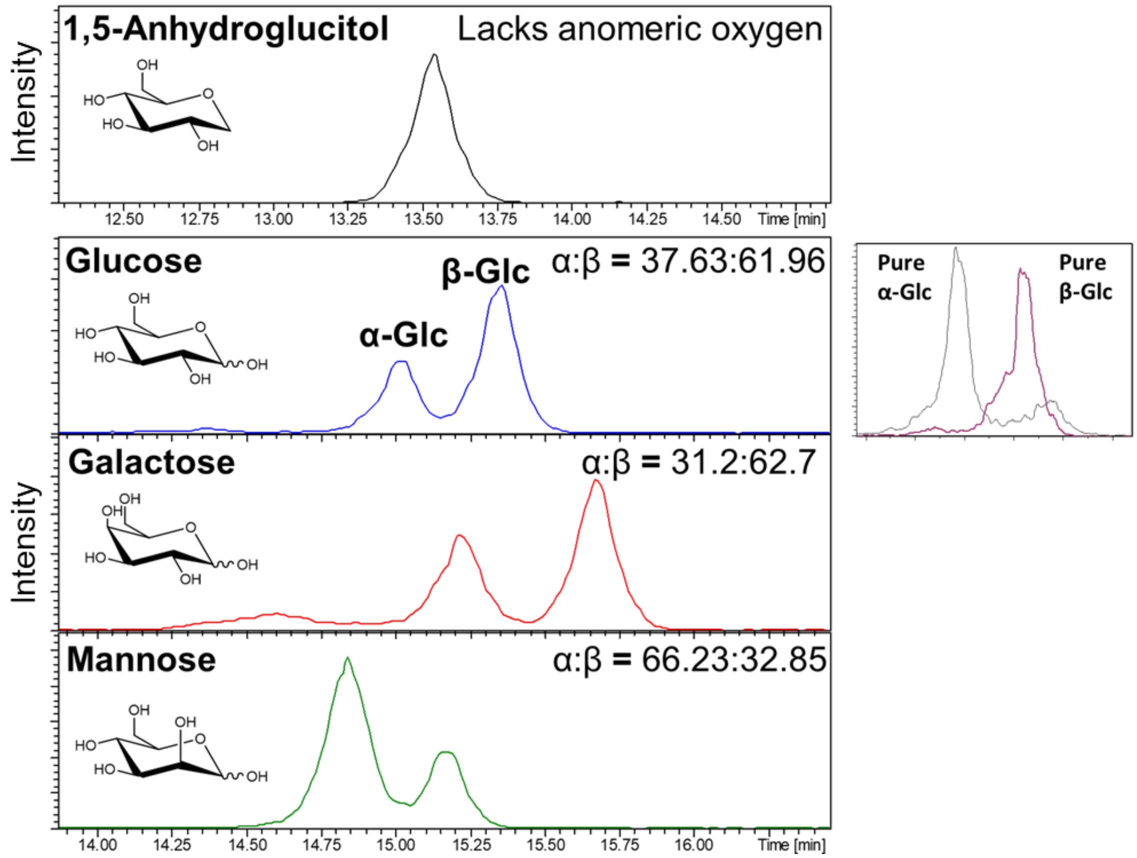

Figure 5.2 HILIC LC separation of hexose anomers. 1,5-Anhydroglucitol lacks an anomeric center, therefore a single peak was observed. Pure Glc anomers were injected and retention order matched with injection of Glc equilibrated to its favorable anomeric ratio.

Anomer assignment can be aided by the CID product ion spectra of the species eluting under each chromatographic peak. The CID product ion spectra for the anomers of Glc, Gal and Man as separated by HILIC LC are shown in Figure 5.3. The CID product ion spectrum for the HILIC LC separated α-Glc is consistent with that for the cIM separated feature peak 2 (Figure 5.6b). An ion trap MS was used for CID of the HILIC separated anomers. For the cIM separated features beam-type CID was used, the spectra were not expected to be identical between the two instruments. α-Glc has a higher abundance of *m/z* 169 (dehydration) and a lower abundance of *m/z* 127 (cross-ring cleavage). α-Glc also has greater abundances of *m/z* 109 and 91 which are sequential water losses from *m/z* 127. CID of the β-Glc anomer results in a greater relative abundance of the *m/z* 127 cross-ring cleavage product ion and less sequential water loss (*m/z* 109 and 91).

The CID product ion spectra for HILIC separated Gal anomers are also consistent with the cIM separated features. α-Gal in Figure 5.3 has a relatively low abundance of the *m/z* 127 cross-ring cleavage, matching post-cIM dissociation spectrum of Gal Peak 2 in Figure 5.6c. In both the post-cIM CID spectrum and the post-HILIC LC CID spectrum β-Gal formed a greater abundance of the *m/z* 127 cross-ring cleavage product ion.

The HILIC LC separated peaks for Man were assigned to be anomers based on relative retention order (α-anomer eluting first) and relative peak ratio. β-Man had a greater abundance of dehydration than α-Man (Figure 5.3). The O2 of Man is axially oriented above the pyranose ring (in the *trans* orientation relative to the α-anomer C1 hydroxyl and *cis* relative to the β-anomer C1 hydroxyl)[97]. O1 and O2 of β-Man have a shorter distance between them, opposite the phenomenon for Glc and Gal, resulting in more dehydration product ion for β-Man.

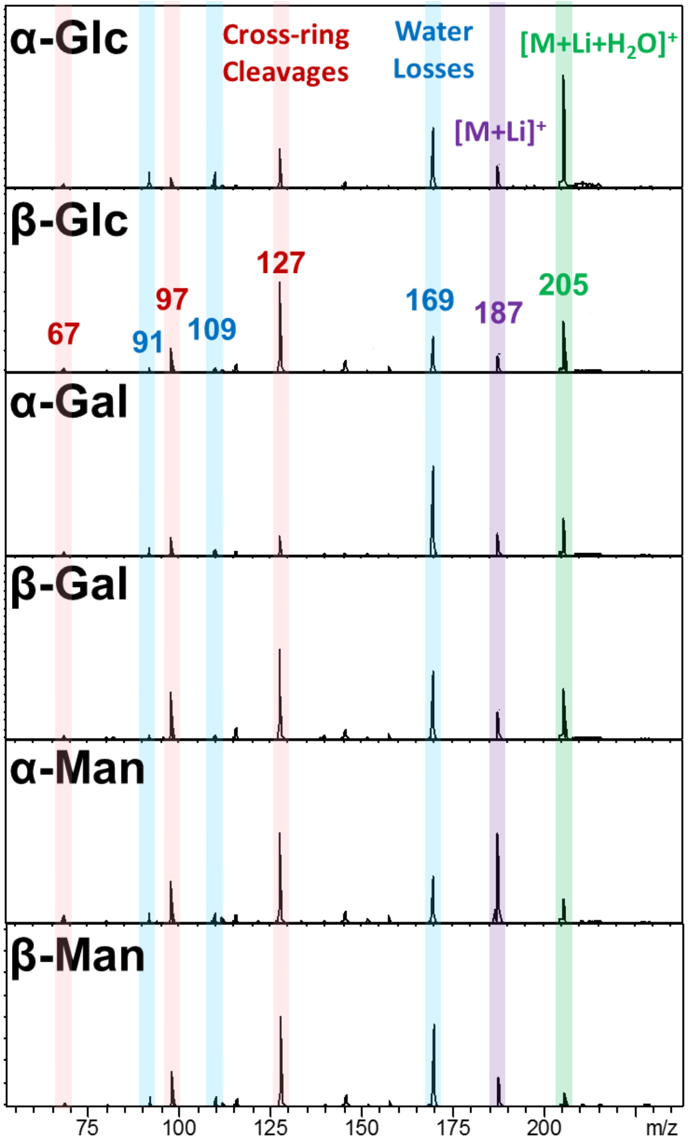

Figure 5.3 Ion trap CID product ion spectra of HILIC-LC separated hexose anomers.

5.3 Cyclic Ion Mobility of Lithium Cationized Hexoses

The ATDs for five hexoses were individually measured, and multiple features were resolved for some of them. The ATDs of two anomerically-locked methylglucosides (only exist as a single anomer) after 5 passes in the cIM are shown in Figure 5.4. After 5 passes, α- and β-methylglucoside had arrival time centroids at 55.87 and 52.24 ms, respectively. A later arrival time for α-methylglucoside is consistent with the larger CCS. The theoretical CCS calculation protocol is outline in Chapter 2.8. All ion structures were optimized with the B3LYP functional and the 6-311++(d,p) basis set with diffuse parameters,++, and polarization parameters, (d,p). Additionally, the natural population analysis (NPA) method for partial charge derivation was chosen based on a previous study[98]. This previous study explored the influence of the DFT functional, basis set and partial charge distribution on theoretical CCS value determination for monosaccharides. The B3LYP functional with the 6-31G and 6-31G+ basis sets were found to be satisfactory for estimation of CCS values. Table 5.1 lists the relative Gibbs free energies, estimated Boltzmann abundances of lithium cationized β-methylglucoside structures and their theoretical CCS values. Literature CCS values for the sodium cationized Glc, Gal and Man have been reported to be 147.32, 142.39, and 141.83 Å^2, respectively[99]. It is expected that lithium cationized monosaccharide CCS values would be slightly lower than sodium cationized ions.

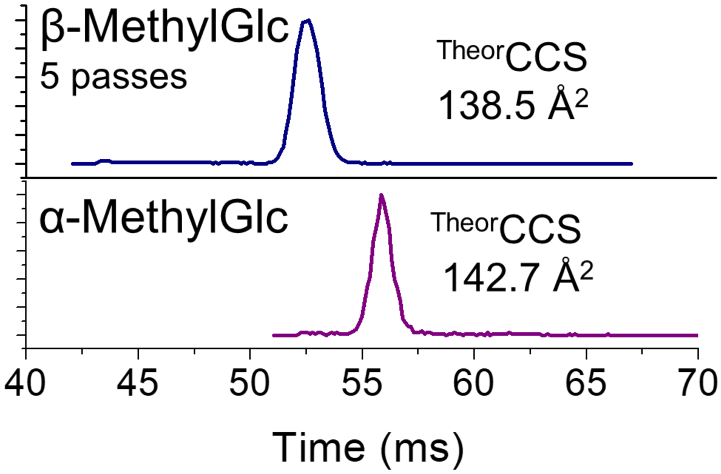

Figure 5.4 Individually measured ATDs after 5 passes in the cIM for the anomerically-locked methylglucosides.

Table 5.1 Relative energies and Boltzmann abundances of lithium cationized β-methylglucoside structures

Li-O Coord.	ΔΔG (kcal/mol)	% Abundance	Theor CCS (Å^2)
6-R-1	0.00	58.49	133.5
4-6	0.63	20.35	144.4
2-3	0.86	13.78	147.3
3-4	1.32	6.42	145.8
1-2	2.45	0.96	142.0

For the anomerically-locked methylglucosides, a single feature was observed in the ATD. The various Li-O coordinations for β-MeGlc were estimated to have a range of CCS values from 133.5 (6-R-1 coordination) to 147.2 (2-3 coordination) Å^2 which equates to a 9.5% difference in CCS. A 5% CCS difference is generally considered experimentally resolvable by IMS devices with less resolving power than the cIM used here. Because the Boltzmann abundance of β-MeGlc(6-R-1) and β-MeGlc(4-6) were both estimated to be significant, it was expected that at least two IMS features would be resolved for β-MeGlc based on their theoretical CCS values. This disagreement between experiment and theory is not yet understood but is under continual investigation. A previous study concluded that unambiguous determination of theoretical CCS values for structural models of monosaccharides, and generalized to other molecular classes, is more difficult than commonly believed[98]. For all hexoses studied here, a similar statement could be made about the mismatch between theoretical CCS values of different Li-O coordination structures and experimental results.

The cIM experiments were performed on Glucose (Glc), galactose (Gal), and Mannose (Man) that exist as a mixture of the alpha and beta anomers in solution. Two peaks were observed in the ATDs for Glc and Gal, but only a single peak was observed for Man (Figure 5.5).

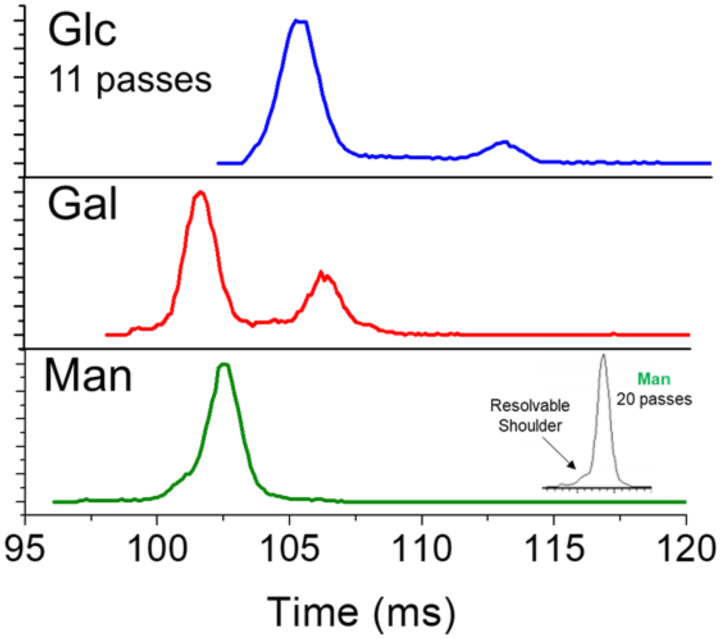

Figure 5.5 ATDs after 11 passes in the cIM for the three lithiated hexoses studied. (inset) After 20 passes for Man a low abundance feature was resolved.

The two cIM features for Glc have the greatest separation. It may be reasoned that the two peaks are the Glc anomers, but the ratio of the Glc ATD peaks do not match the anomeric ratio as measured by NMR (α:β = 37.63 : 61.96)[8]. Post-cIM dissociation of the $[Glc+Li]^+$ species that constitute each peak lends insight into the identity of the species (Figure 5.6a-b). Dehydration of $[Glc+Li]^+$ (product ion at *m/z* 169) upon CID requires H-atom transfer from O2 to O1[33]. The distance between O2 and O1 is shorter for α-Glc, resulting in a lower energy barrier for H-atom transfer and dehydration[97, 100]. Peak 2 for Glc undergoes more dehydration indicated by a larger relative abundance of *m/z* 169 in the post-cIM dissociation spectrum (Figure 5.6b). The $[Glc+Li]^+$ species under peak 2 in the Glc ATD also has a larger abundance of subsequent water losses from cross-ring cleavages (e.g. *m/z* 127 loses one or two waters to produce *m/z* 109 or 91). Glc peak 2 readily loses water upon post-cIM dissociation, suggesting it may be α-Glc, but the relative peak abundances do not unequivocally support the hypothesis of anomer separation.

The two ATD peaks for Gal roughly match the known anomeric ratio of Gal (α:β = 31.2 : 62.7, the remaining 6% being furanose ring anomers). Just as for Glc, the distance between O1 and O2 is shorter for α-Gal and greater water loss is expected. In Figure 5.6c a difference in dehydration product ion abundance is observed between each Gal peak. Peak 2 water loss, *m/z* 169, constitutes a greater fraction of the total product ion abundance. Another difference is the higher abundance of the cross-ring cleavage at *m/z* 127 for Gal peak 1 which matches the ion trap CID spectrum of β-Gal (Figure 5.3).

A single peak was detected for Man in the ATD after 11 passes through the cIM (Figure 5.5). After 20 passes, a low relative abundance (< 5%) feature could be resolved as a shoulder on the main Man peak (Figure 5.5 inset). The low abundance feature had a shorter arrival time, and, therefore, a smaller CCS value. The pyranose anomeric ratio of Man is α:β = 66.23 : 32.85, with less than 1% furanose structure in aqueous solution. Because the peak ratio does not match the Man anomeric ratio, the resolvable feature is likely not separation of Man anomers.

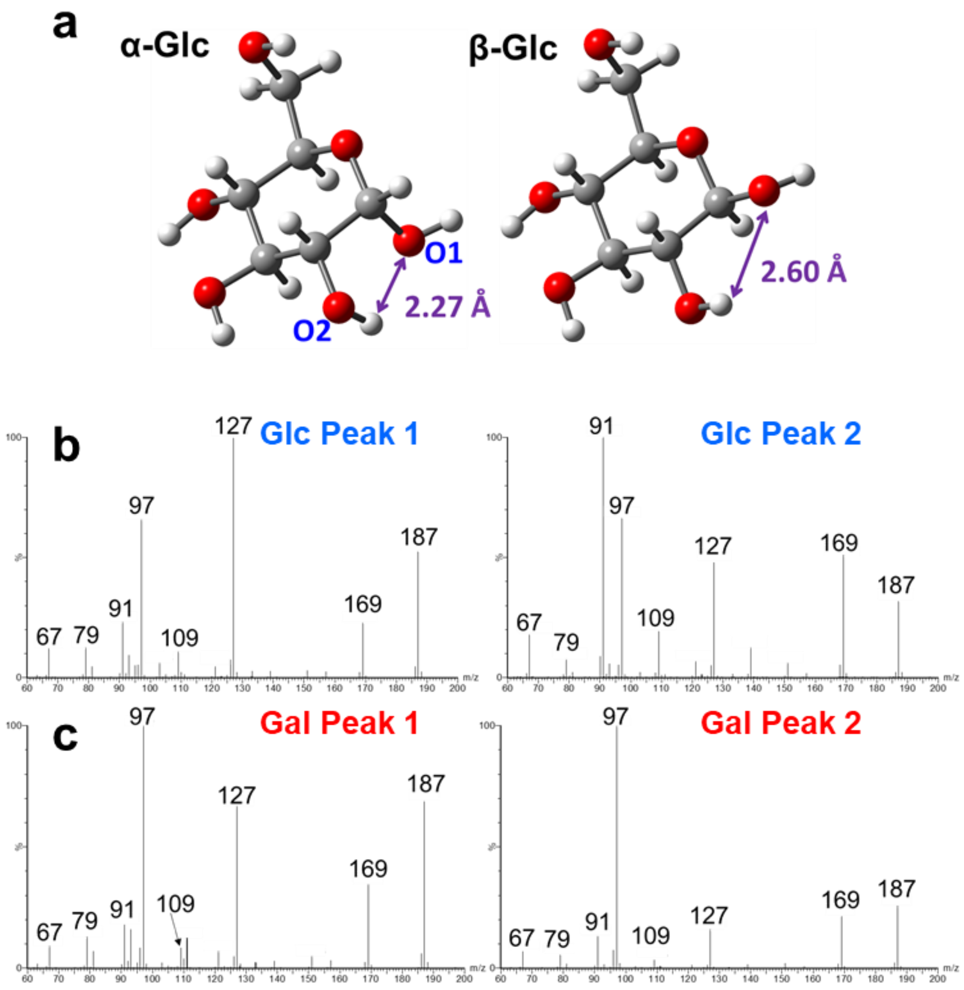

Figure 5.6 a) The distance between the O2 bound hydrogen and O1 is shorter for α-Glc than for β-Glc. b,c) Post-cIM dissociation spectra for mobility resolved species of Glc and Gal.

5.4 cIM and HILIC LC of Reducing and Non-reducing Disaccharides

Ten-pass ATDs of 2 non-reducing and 6 reducing disaccharides were individually measured (Figure 5.7). Non-reducing disaccharides do not have an anomeric center and exist as a single form. A single peak was observed in the ATD for both non-reducing lithium cationized disaccharides (trehalose and sucrose). Reducing disaccharides contain an anomeric center and can exist as either the α- or β-anomer. For 4 of the 6 reducing sugars two peaks were observed in the ATD. The remaining two reducing sugars (cellobiose and lactose) only produced a single feature in the ATD. Cellobiose and lactose have identical reducing ends with a β(1→4)Glc glycosidic linkage, but differ in their non-reducing monosaccharide subunit.

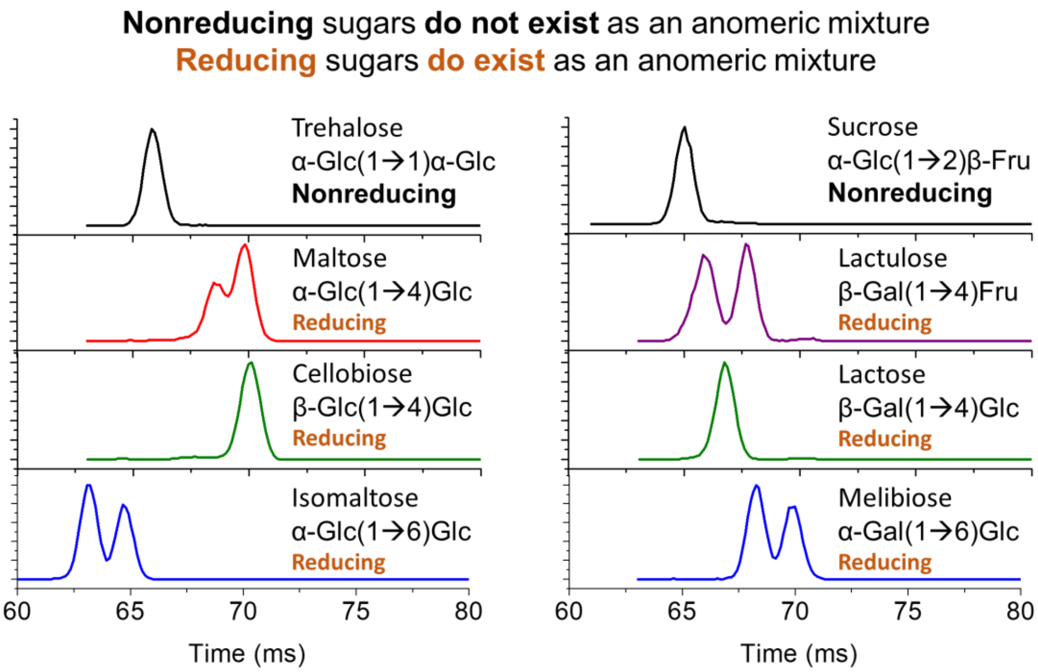

Figure 5.7 ATDs for 2 non-reducing and 6 reducing lithium cationized disaccharides.

Individual HILIC LC separations of trehalose, cellobiose and lactose were used to complement the cIM ATDs (Figure 5.8). The non-reducing trehalose produced a single chromatographic peak (consistent with the cIM ATD). Cellobiose and lactose each produced two peaks in the HILIC chromatogram, likely due to separation of the two anomers. The cellobiose anomeric ratio has been reported to be α:β = 42.2 : 57.8 [101], which roughly matches the peak ratio observed in the chromatogram. For lactose, the anomeric ratio has been reported as α:β = 62.7:37.3 by polarimetry[102], and NMR measurements varied greatly based on conditions[103]. Separation of two peaks for cellobiose and lactose by HILIC is inconsistent with the cIM ATDs that show a single feature for gas-phase separation of lithium cationized cellobiose and lactose. This could mean that the anomers do not have CCS differences large enough to be separated by IMS, or that the (1→4)Glc linkage promotes a lithium cationization site(s) that generate unresolvable gas-phase structures with similar CCS.

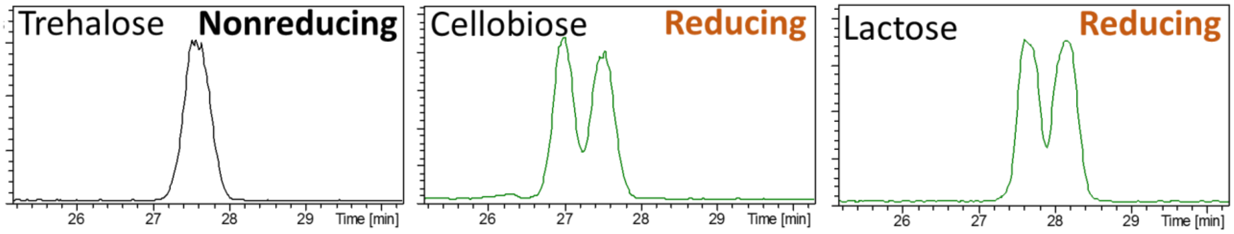

Figure 5.8 HILIC chromatograms of 1 non-reducing and 2 reducing disaccharides.

5.5 Summary

High resolution cyclic ion mobility resolved multiple features for lithium cationized mono- and disaccharides. Most IMS systems lack the resolving power to separate multiple features for a hexose, but sufficient resolving power was achieved with the cIM by allowing many passes around the separation region. The data acquired for Gal suggests that the cIM ATD features are anomers. Feature assignment for Gal was evidenced by ATD features mirroring the known Gal anomeric ratio and comparison of CID product ion spectra of both cIM separated and HILIC separated species.

For Glc, the two cIM separated features were not suggested to be anomers due to the peak ratio. The Glc cIM features were not confidently assigned as anomers, although, their CID product ion spectra were similar to the CID product ion spectra for HILIC LC separated Glc anomers. A low abundance resolvable shoulder was observed for Man after 20 cIM passes, for which the identity is unknown. Because of its low abundance, it is unlikely that the resolvable shoulder was one of the Man anomers. Man did produce two peaks when subjected to separation by HILIC LC that were assigned as anomers.

The two non-reducing disaccharides studied produced a single cIM ATD feature, likely due to the lack of an anomeric center. Four of six reducing disaccharides produced two cIM ATD features. The remaining 2 reducing disaccharides (cellobiose and lactose) had the same reducing end monosaccharide subunit and glycosidic linkage position, (1→4)Glc. Evidence that cellobiose and lactose both exist as a mixture of anomers was provided by HILIC LC separation, but cIM of cellobiose and lactose only produced a single ATD feature.

The data for mono- and disaccharides presented here is neither fully consistent with the claim that ion mobility separation of different metal cationization sites is observed, nor with the claim that solely separation of carbohydrate anomers is observed. Gas and liquid-phase separations alongside computational data has shown that the reason for IMS resolution of multiple features for metal cationized carbohydrates remains unclear. The accurate prediction of theoretical CCS values for carbohydrates remains difficult because of the many possible gas-phase conformations. Based on lithium cationized monosaccharide theoretical CCS values, separation of different Li-O coordination structures was expected but not observed.

Thank you to Andy Baker and Waters Corporation

for the opportunity run studies with the cIM system.

CHAPTER 6: UNVEILING THE ISOMERIC COMPLEXITY OF LITHIATED HEXOSE PRODUCT IONS

6.1 Introduction to Dissociation Technologies for Gas-phase Carbohydrates

The challenge of comprehensive carbohydrate structural elucidation remains unsolved, and a single MS-based workflow that can identify the stereochemistry of polysaccharide glycosidic linkages and each monosaccharide subunit is still sought after. Some success for carbohydrate structural elucidation has been found using MS-based techniques for dissociation of gas-phase carbohydrate ions. Polysaccharides with varying glycosidic linkage stereochemistries have been shown to yield different product ions, or product ion abundances, upon dissociation in the gas phase. Subtle differences in polysaccharide stereochemistry can be parsed, for example, by energetic interactions with an electron during electron-transfer or electron-capture dissociation[104, 105]. While electron-activated dissociation techniques are recognized for providing structural information that is complementary to CID, collisional activation is the most common method for dissociating gas-phase ions. Carbohydrate CID pathways can vary based on precursor ion type (e.g. deprotoned vs metal cationized)[33, 106, 107] and stereochemistry[108, 109]. While current dissociation methods provide information about polysaccharide glycosidic linkage position, they fail to identify glycosidic linkage anomericity and the isomeric configuration of the individual monosaccharide subunits. Due to this limitation, recent efforts have been towards understanding monosaccharide dissociation chemistry to better identify polysaccharide composition[33, 97, 100, 110–112].

Despite the success of the recent monosaccharide dissociation pathway studies, evidence described in this study suggests there is another degree of complexity to monosaccharide dissociation chemistry that remains to be unveiled. Previous studies have alluded to monosaccharide product ion isomeric heterogeneity[110, 113] and in this study we expand on previous efforts. Each type of hexose dissociation pathway is known, but there is high potential to form isomeric product ions that are difficult to differentiate. Four hexose epimers, glucose (Glc), mannose (Man), galactose (Gal), and talose (Tal) were chosen to illustrate the complexity of dissociation. Hexoses are a class of monosaccharide building blocks with the molecular formula $C_6H_{12}O_6$ and have three stereocenters (excluding the anomeric center) to produce eight diastereomers (epimers). Each hexose isomer exists primarily as a six-membered pyranose ring (Figure 6.1a) in solution, where each epimer can be described by the orientations (equatorial or axial) of their hydroxyl groups around the pyranose ring. Glc contains equatorial hydroxyl groups at the C2, C3 and C4 positions, Man has a single axial group at C2, Gal has a single axial group at C4, and Tal has two axial groups at the C2 and C4 positions.

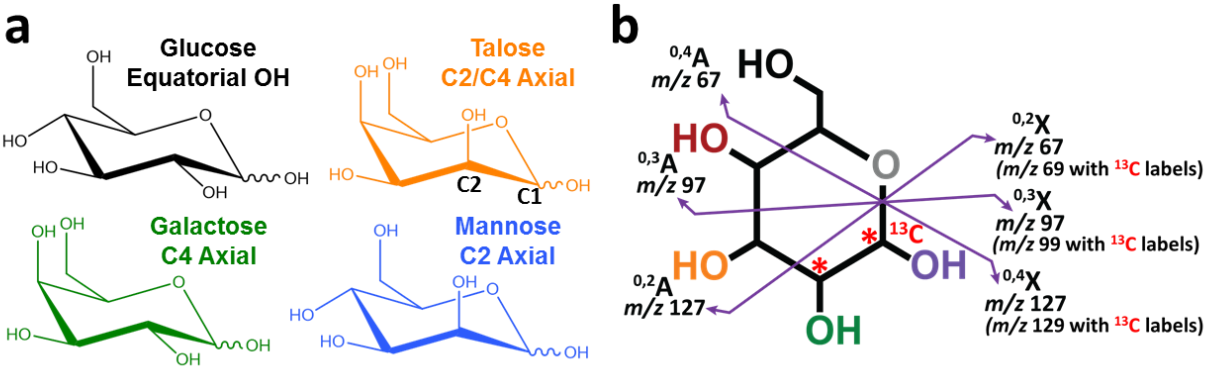

Figure 6.1 a) Pyranose form of four epimeric hexoses and hexose carbon numbering. b) Hexose cross-ring cleavage notation and lithiated product ion mass-to-charge values with and without carbon-13 labels at the C1 and C2 positions (reducing end).

The oxygen atoms of a hexose molecule favorably coordinate to metal cations during ESI to generate [Hexose+Cation]$^+$ and formation of multiple different coordination sites has been shown using computational data, ion/molecule reactions or spectroscopy [46–49, 61, 114]. Moreover, IMS-MS has also previously revealed that metal cation coordination site influences carbohydrate conformer CID pathways [96]. The unique oxygen atom arrangements of each hexose epimer can accommodate different sites of metal cation coordination, with some coordinations being unique to a single epimer. The cation-oxygen coordinations formed during ESI may be bi-, tri- or tetradentate in the gas phase[48, 61, 114]. Unique epimer stereochemistries that create different cation coordination sites may also direct different gas-phase hexose ion dissociation pathways. Additionally, different metal cations (e.g. sodium, lithium, silver) can promote disparate CID behaviors.

CID of sodiated carbohydrates does not provide much structural information. The critical internal energy, ε_o, required to break the Na-O coordinations (desodiation energy) is lower than the ε_o for many other dissociation pathways of $[\text{Hexose+Na}]^+$. Desodiation produces a neutral hexose and a bare Na^+ cation. Thus, no hexose CID product ion is formed and the hexose is not detected. If a lithium salt is added to the ESI solution, Li^+ outcompetes adventitious Na^+ to form $[\text{Hexose+Li}]^+$. Li-O coordinations of a hexose are more stable than Na-O coordinations, resulting in a higher ε_o required to neutralize $[\text{Hexose+Li}]^+$ by way of cation loss. Therefore, fragmentation efficiency of $[\text{Hexose+Li}]^+$ is greater than that of $[\text{Hexose+Na}]^+$. Due to a higher yield of product ions, structural analyses by collisional activation are often performed on lithiated carbohydrates.

CID of $[\text{Hexose+Li}]^+$ produces dehydration and cross-ring cleavage product ions (Figure 6.1b). The same nominal mass-to-charge CID product ions are observed for the epimers Glc, Man, Gal, and Tal but slight variations in the relative abundances at the MS/MS level are an indication that the dissociation processes are not identical. Further complicating product ion identification, the ion population within each nominal *m/z* product ion contains isomeric species.

Through ^{18}O labeling experiments, other groups have shown that hexose dehydration product ions form via loss of oxygen atoms from various carbons, not only the reducing end anomeric carbon[110]. Constitutional isomers also form during cross-ring cleavage, where the lithium cation is retained by either the reducing (X ion) or non-reducing (A ion) end of the hexose (Figure 6.1b). Hexoses labeled with carbon-13 at the C1 and/or C2 position(s) can be used to mass resolve X and A type product ions[115]. Based on the proposed structures (Figure 6.6) [33], other hexose product ion structural variants may involve *cis* vs. *trans* carbon-carbon double bonds, and each unique product ion structure may exist with multiple different lithium cation coordinations.

Hexose dissociation mechanisms have been of recent interest, but this current work shows hexose dissociation chemistry is more complex than has been postulated in literature. Although CID of hexoses is well-studied there has been few analytical methods able to differentiate isomeric product ions, therefore the complete array of hexose product ions is largely unknown. In this study, previous efforts are expanded by investigating how the stereochemistry of four isomeric hexose epimers affect lithium cation coordination, CID pathways and product ion structure. We use CID in tandem with the water adduction ion/molecule reaction to probe the Li-O coordination characteristics of lithiated hexose CID product ions. CID-water adduction to hexoses and ^{13}C-hexoses, along with our understanding of reacted and unreacted lithiated structures, enables novel investigation of hexose dissociation chemistry, unveiling the isomeric complexity of lithiated hexose product ions.

6.2 Collision-Induced Dissociation of Unlabeled and ^{13}C-Labeled Hexose Epimers

The CID product ion spectra of unlabeled hexose epimers, $[Hexose+Li]^+$, show identical nominal mass-to-charge product ions. The dehydration (B-type) product ion is detected at *m/z* 169 and cross-ring cleavage product ions (A- or X-type) are detected at *m/z* 127, 97 and 67

(Figure 6.2). The water adduct, $[\text{Hexose+Li+H}_2\text{O}]^+$, detected at *m/z* 205 is an ion/molecule reaction product ion and will be discussed in later sections. Although the same product ions are detected for each hexose epimer, their relative abundances are different for the epimers Glc, Man, All, Gal and Tal (Table 6.1). Slight differences in CID product ion abundances do not promote confident identification or differentiation of hexose epimers, but different product ion ratios do imply that each hexose undergoes a unique set of dissociation processes. Using various MS/MS techniques it possible to parse out some of these differences in $[\text{Hexose+Li}]^+$ dissociation.

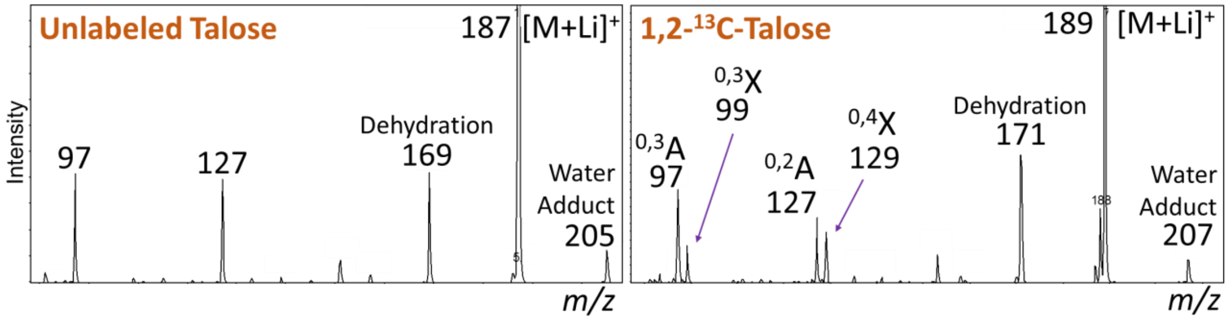

Figure 6.2 CID product ion spectra of two lithiated hexoses: unlabeled Tal (left) and 1,2-$^{13}C_2$-talose (right). The intact unlabeled Tal (*m/z* 187) and its dehydration CID product and water adduct at *m/z* 169 and 205, respectively, are shifted +2 Da for 1,2-^{13}C-Tal. Cross-ring cleavage of 1,2-^{13}C-Tal either produces an unlabeled cross-ring cleavage product ion or a +2 Da cross-ring cleavage product ion.

For all CID experiments an activation time of 40 ms was used. Energy-resolved CID showed that the optimal fragmentation amplitude was 0.28 V for all hexose epimers to achieve the highest fragmentation efficiencies. The fragmentation efficiencies of each epimer is different (Table 6.1), indicating varying levels of ion loss during CID. It is worth noting that the water adduct is not a CID product ion, rather a product of the water adduction ion/molecule reaction, and therefore is only considered when calculating MS/MS efficiency. Fragmentation, MS/MS and collection efficiencies listed in Table 6.1 were calculated following previously discussed methodology[116]. The collection efficiency is a measure of ion loss during the experiment and was calculated as follows,

$$Collection\ Efficiency = \frac{P + \sum F}{P_0}$$

where P_0 is the ion current (MS peak area) of the parent ion measured after isolation without an ion activation step or before any ion loss was observed. P is the peak area of the parent ion after isolation and activation, and $\sum F$ is the sum of all product ion peak areas (CID and/or water adduction product ions). The fragmentation efficiency is a measure of parent ion conversion to a dissociation (CID) product ion and was calculated using the following equation.

$$Fragmentation\ Efficiency = \frac{\sum F_{CID}}{P + \sum F_{CID}}$$

The MS/MS efficiency is a measure of conversion of parent ion to any product ion, whether it be a dissociation, or a water adduction, product ion.

$$MS/MS\ Efficiency = \frac{\sum F}{P_0}$$

Glucose had the highest fragmentation efficiency of 18.65% followed by Gal (16.22%), Man (8.44%) and Tal (4.89%). Lower fragmentation efficiencies are observed for hexoses that form greater amounts of tri- and tetradentate Li-O coordinations, but the fragmentation amplitude for optimal conversion to product ions is similar for all hexoses. It can be hypothesized that only certain $[Hexose+Li]^+$ structures (e.g., bidentate) will convert to measurable CID product ions. Glc/Gal form more bidentate structures than Man/Tal. Tridentate structures may have a high critical internal energy, ε_o, required for ring opening, such that ions gain enough kinetic energy to be ejected from the ion trap before ion internal energy exceeds ε_o. Ejection of $[\text{Hexose+Li}]^+$ will reduce the collection efficiency (as observed for Tal).

Subtle differences in product ion abundance ratios for each hexose were measured. For example, the ratio of cross-ring cleavages at *m/z* 97 to 127 for Glc was 2.6:8.1, whereas for Tal the ratio is closer to equal abundance at 1.5:1.4. Another example of stereochemical influence on dissociation is dehydration characteristics of hexoses. Dehydration of $[\text{Hexose+Li}]^+$ involves H atom transfer from O2 to O1[33], and is therefore dependent on the geometry between O1 and O2. O1 and O2 are in the *cis* configuration for α-Glc and in the *trans* configuration for β-Glc. With a shorter distance between O1 and O2 in the *cis* configuration, the dehydration activation barrier of α-Glc was observed to be smaller than that of sodiated β-Glc[117]. The lithiated product ion spectra of HILIC separated anomers of Glc, Gal and Man are shown in Figure 5.3, highlighting differences in dehydration characteristics for each.

Table 6.1 CID of unlabeled hexose epimers. Yield of each ion type as a percentage of the initial parent ion population at the optimal hexose CID settings

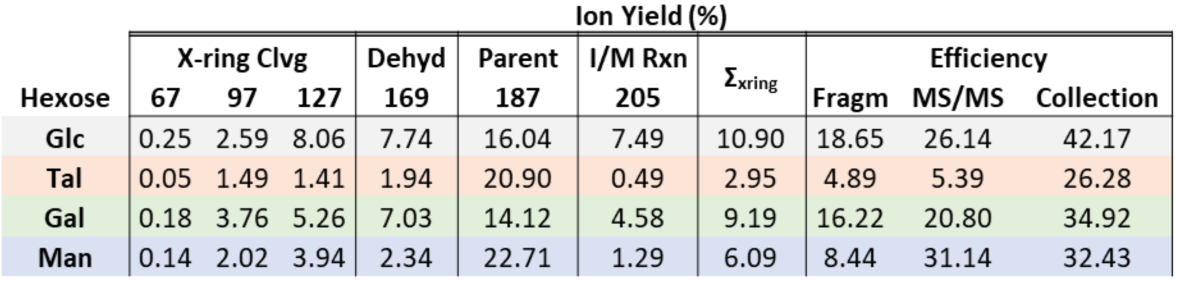

	Ion Yield (%)									
	X-ring Clvg			Dehyd	Parent	I/M Rxn	Σ_{xring}	Efficiency		
Hexose	67	97	127	169	187	205		Fragm	MS/MS	Collection
Glc	0.25	2.59	8.06	7.74	16.04	7.49	10.90	18.65	26.14	42.17
Tal	0.05	1.49	1.41	1.94	20.90	0.49	2.95	4.89	5.39	26.28
Gal	0.18	3.76	5.26	7.03	14.12	4.58	9.19	16.22	20.80	34.92
Man	0.14	2.02	3.94	2.34	22.71	1.29	6.09	8.44	31.14	32.43

Ion yield was calculated as the ratio F/P_0, where F is the specific product ion peak area
$\sum_{xring}$ = sum of all cross-ring cleavage ion yields

To ensure confident inferences can be made about hexose dissociation chemistry, the carbon-13 labeled and unlabeled hexose CID characteristics were compared. All unlabeled hexoses produced the same nominal mass-to-charge cross-ring cleavages of $[\text{A+Li}]^+$ and

$[X+Li]^+$, but for 1-$^{13}C_1$-hexoses and 1,2-$^{13}C_2$-hexoses, mass shifted $[^{13}C_1\text{-}X+Li]^+$ and $[^{13}C_2\text{-}X+Li]^+$ cross-ring cleavage ions are also observed. Because the carbon-13 labels are at the C1 and/or C2 positions, the reducing end X ions are observed as heavy (carbon-13 labeled) product ions and the A ions (non-reducing end) are observed as the light (unlabeled) product ions (Figure 6.1). Energy-resolved CID of unlabeled Glc, Gal, Man and Tal exhibited similar CID characteristics to their respective carbon-13 labeled hexoses. In Figure 6.3a all CID product ion yields, and the water adduct ion yield of Glc and 1,2-$^{13}C_2$-Glc are plotted as a function of fragmentation amplitude. The unfilled circles in Figure 6.3a represent the percent yield of the product ions for unlabeled $[Glc+Li]^+$, and the filled squares represent the corresponding $[1,2\text{-}^{13}C_2\text{-}Glc+Li]^+$ product ions. For $[1,2\text{-}^{13}C_2\text{-}Glc+Li]^+$ cross-ring cleavages, both unlabeled (light, A ions) and carbon-13 labeled (heavy, X ions) product ions were formed and their peak areas were summed to match the mixture of light A and light X ions formed by $[Glc+Li]^+$. The percent yield of each product ion for $[Glc+Li]^+$ and $[1,2\text{-}^{13}C_2\text{-}Glc+Li]^+$ are comparable at each fragmentation amplitude, as seen by comparing the unfilled circles and the filled squares of corresponding color in Figure 6.3a. Identical product ion yields during energy-resolved CID indicates that dissociation characteristics of $[1,2\text{-}^{13}C_2\text{-}Glc+Li]^+$ can be used to make inferences about dissociation of $[Glc+Li]^+$. The product ion yield comparisons of Glc, Gal, Man and Tal to their respective ^{13}C-hexoses are shown in Figure 6.3a-d.

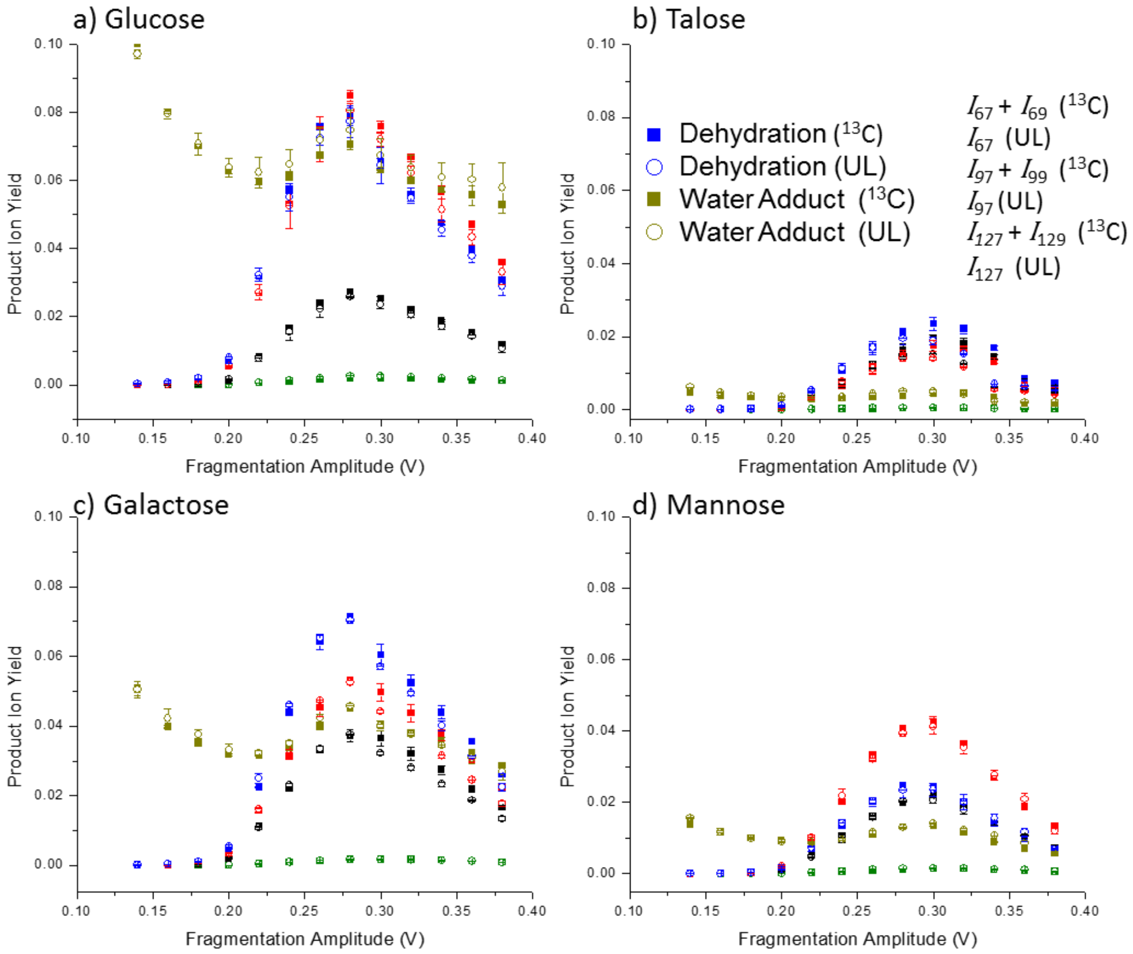

Figure 6.3 Comparison of CID product ion yields for unlabeled (UL) and carbon-13 labeled (^{13}C) hexoses. Filled markers represent product ions generated from ^{13}C-hexoses, and unfilled markers represent product ions generated from unlabeled hexoses.

Identification of A and X cross-ring cleavage ions using ^{13}C-hexoses relies on accurate regiospecific carbon-13 labelling. NMR confirmed the carbon-13 positions on 1-$^{13}C_1$-Gal and 1,2-$^{13}C_2$-Glc (Figure 6.4 and 6.5). To confirm C1 labeling for both 1,2-$^{13}C_2$-Glc and 1-$^{13}C_1$-Gal, the measured chemical shifts were compared to literature values[8], and C2 labeling of 1,2-$^{13}C_2$-Glc was confirmed using peak splitting patterns. Peak splitting is not typically observed for natural carbon-13 abundance NMR experiments but was readily observed for 1,2-$^{13}C_2$-Glc because C1 and C2 are 99% enriched carbon-13.

Because carbon-13 is localized to the hexose reducing anomeric center (C1 or C1/C2), we can make good inferences about which cross-ring cleavage product ions are forming. Table 6.2 is a list of all hypothetically possible hexose cross-ring cleavages and the pyranose ring atoms that they contain. Cross-ring cleavage notation is based on which ring atoms are contained in the product ion structure and which two pyranose ring bonds are broken. The pyranose ring bonds are labeled from the 0th bond through the 5th bond (Figure 6.6), where the 0th bond is the C1-O bond from the reducing carbon (C1, anomeric carbon) to the ring oxygen and the 5th bond is the C5-O pyranose ring bond. If the anomeric carbon is contained in the product ion it is an X ion. If the anomeric carbon is not contained in the product ion it is an A ion. For example, the ^{0,4}X ion involves dissociation of the 0th and 4th pyranose ring bonds and incorporates the C1, C2, C3 and C4 ring atoms. The mechanism of cross-ring cleavage during CID and resultant product ion structures are illustrated in Figure 6.6 based on the previously proposed mechanism[33]. The proposed first step to hexose cross-ring cleavage is ring opening at the anomeric center (0th bond cleavage) followed by 1,2-hydride shift(s) and ring C-C bond cleavage. Dissociation of the 0th bond involves hydrogen transfer from the C1 hydroxyl to the ring oxygen which has a lower activation barrier than a C-C bond cleavage for ring opening. In the current study, only cross-ring cleavage pathways that begin with ring opening at the anomeric center were considered. Distinctly, [1,2-$^{13}C_2$-Glc+Li]$^+$ and [1,2-$^{13}C_2$-Tal+Li]$^+$ generate mass-resolved [A+Li]$^+$ and [$^{13}C_2$-X+Li]$^+$ ions. [1-$^{13}C_1$-Gal+Li]$^+$ and [1-$^{13}C_1$-Man+Li]$^+$ generate mass-resolved [A+Li]$^+$ and [$^{13}C_1$-X+Li]$^+$ ions. Based on these considerations, for [1,2-$^{13}C_2$-Glc+Li]$^+$ and [1,2-$^{13}C_2$-Tal+Li]$^+$, *m/z* 127 represents the ^{0,2}A product ion, *m/z* 129 represents ^{0,4}X, *m/z* 97 represents ^{0,3}A, *m/z* 99 represents ^{0,3}X, *m/z* 67 represents ^{0,4}A, and *m/z* 69 represents ${}^{0,2}X$. For $[1\text{-}{}^{13}C_1\text{-Gal+Li}]^+$ and $[1\text{-}{}^{13}C_1\text{-Man+Li}]^+$, the X ions are observed as *m/z* 128, 98 and 68. As seen in Figure 6.2 both X and A cross-ring cleavage ions are observed upon CID of $[1,2\text{-}{}^{13}C_2\text{-Tal+Li}]^+$.

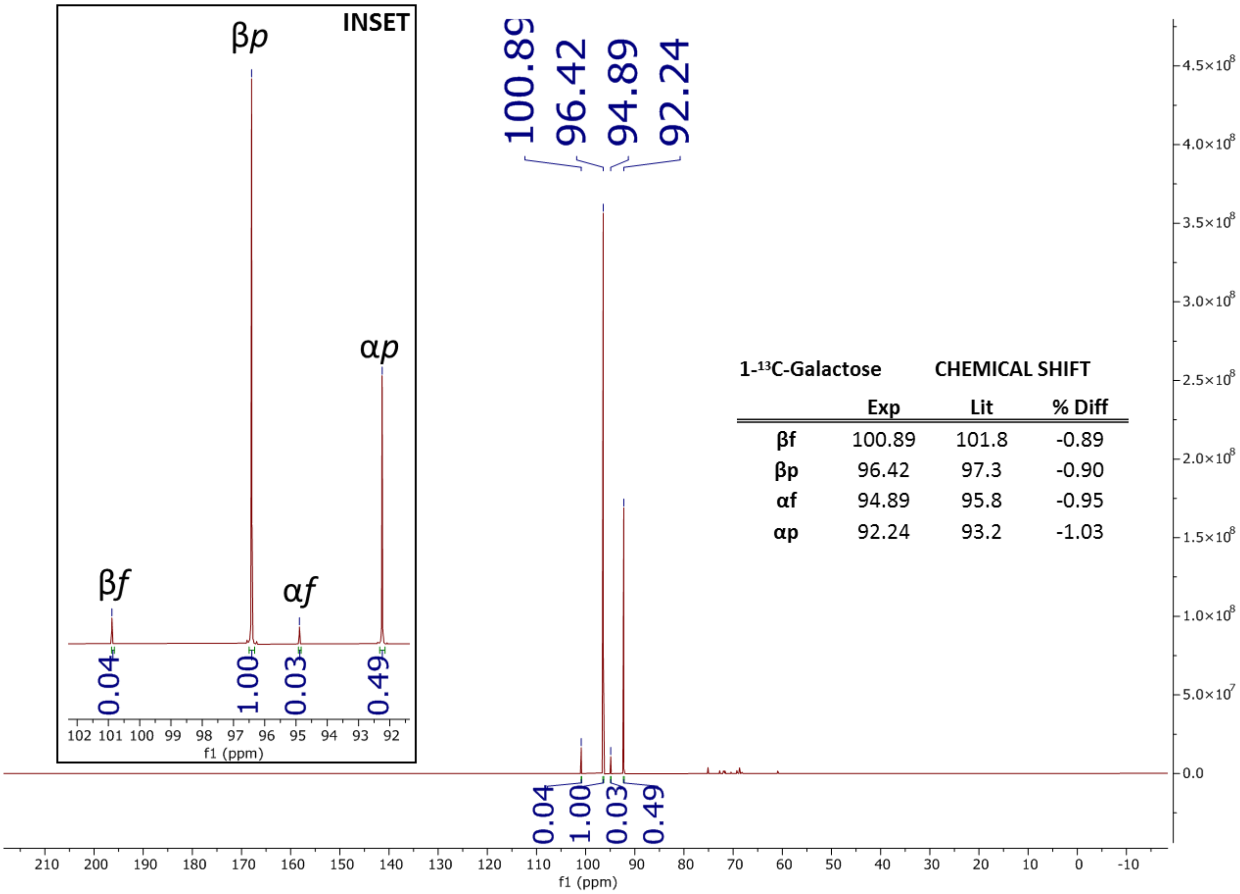

$1\text{-}{}^{13}C$-Galactose	CHEMICAL SHIFT		
	Exp	Lit	% Diff
βf	100.89	101.8	-0.89
βp	96.42	97.3	-0.90
αf	94.89	95.8	-0.95
αp	92.24	93.2	-1.03

Figure 6.4 $1\text{-}{}^{13}C_1$-Galactose carbon NMR spectrum with proton decoupling – 13C{H1} 1D. Chemical shifts in the range of 92 to 102 ppm for the carbon-13 enriched C1 of the α/β-pyranose and α/β-furanose structures were matched to previously measured literature values[8]**. Natural abundance carbon-13 C2-C6 peaks are observed in the 60 to 80 ppm range**

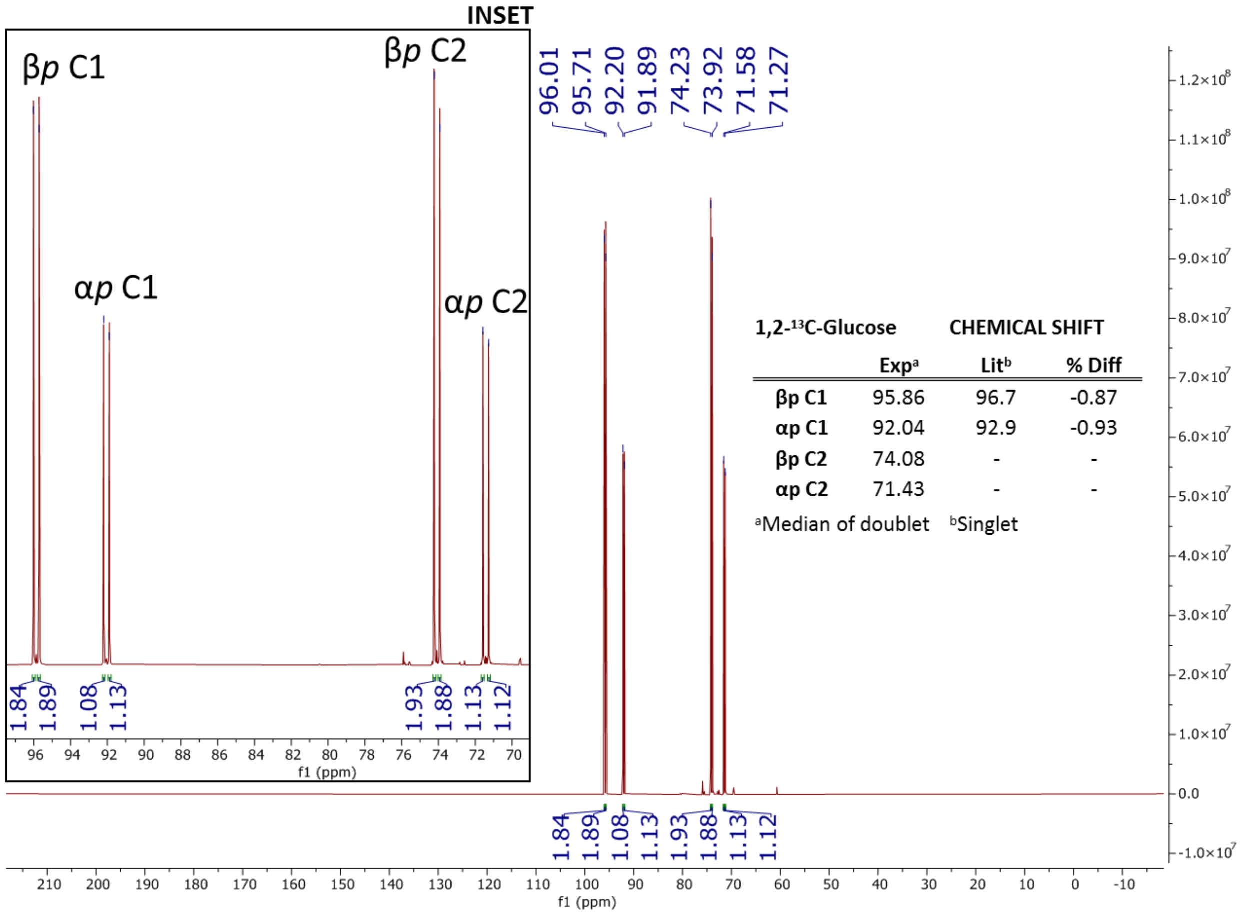

1,2-¹³C-Glucose	CHEMICAL SHIFT		
	Exp[a]	Lit[b]	% Diff
βp C1	95.86	96.7	-0.87
αp C1	92.04	92.9	-0.93
βp C2	74.08	-	-
αp C2	71.43	-	-

[a]Median of doublet [b]Singlet

Figure 6.5 1,2-$^{13}C_2$-Glucose carbon NMR spectrum with proton decoupling – 13C{H1} 1D. Chemical shifts of the carbon-13 enriched C1 of the α/β-pyranose structures were calculated as the median of the doublet peak and matched to previously measured literature values[8]**. The carbon-13 enriched C2 of the α/β-pyranose peaks were observed within the expected 60-80 ppm range. The C1 carbon-13 label was confirmed by chemical shift. The C2 carbon-13 label was confirmed by the doublet peaks that were observed due to splitting of adjacent 99% enriched carbon-13 atoms. Natural abundance carbon-13 C3-C6 peaks are observed in the 60 to 80 ppm range**

Table 6.2 List of all hypothetically possible lithiated hexose cross-ring cleavages

Product Ion	Molecular Formula	*m/z* [M+Li]+	Neutral Loss	Ring Atoms Contained
${}^{0,2}A_1$	$C_4H_8O_4Li$	127	60	C3,C4,C5,O
${}^{0,2}X_1$	$C_2H_4O_2Li$	67	120	C1,C2
${}^{0,3}A_1$	$C_3H_6O_3Li$	97	90	C4,C5,O
${}^{0,3}X_1$	$C_3H_6O_3Li$	97	90	C1,C2,C3
${}^{0,4}A_1$	$C_2H_4O_2Li$	67	120	C5,O
${}^{0,4}X_1$	$C_4H_8O_4Li$	127	60	C1,C2,C3,C4
${}^{1,3}A_1$	$C_2H_4O_2Li$	67	120	C2,C3
${}^{1,3}X_1$	$C_4H_8O_4Li$	127	60	C1,C4,C5,O
${}^{1,4}A_1$	$C_3H_6O_3Li$	97	90	C2,C3,C4
${}^{1,4}X_1$	$C_3H_6O_3Li$	97	90	C1,C5,O
${}^{1,5}A_1$	$C_5H_{10}O_4Li$	141	46	C2,C3,C4,C5
${}^{1,5}X_1$	CH_2O_2Li	53	134	C1,O
${}^{2,4}A_1$	$C_2H_4O_2Li$	67	120	C3,C4
${}^{2,4}X_1$	$C_4H_8O_4Li$	127	60	C1,C2,C5,O
${}^{2,5}A_1$	$C_4H_8O_3Li$	111	76	C3,C4,C5
${}^{2,5}X_1$	$C_2H_4O_3Li$	83	104	C1,C2,O
${}^{3,5}A_1$	$C_3H_6O_2Li$	81	106	C4,C5
${}^{3,5}X_1$	$C_3H_6O_4Li$	113	74	C1,C2,C3,O

The initial Li-O coordinations formed by $[\text{Hexose+Li}]^+$ may impact dissociation pathways and, specifically, cross-ring cleavage. The hexose oxygen atoms that preferentially retain the lithium cation after cross-ring cleavage dictate whether an A or X ion is observed. The effect of hexose stereochemistry and, therefore, initial Li-O coordinations on cross-ring cleavage was studied by monitoring the A and X ion abundances of each cross-ring cleavage type for the four carbon-13 labeled hexoses. For a specific hexose epimer and a given cross-ring cleavage pathway, the amount of X and A ions formed is reflected by the relative abundance of heavy and light product ions. The X ion yield is expressed as,

$$X\ Ion\ Yield = \frac{I_X}{I_X + I_A}$$

where I_X is the MS peak area of the heavy product ion (X ion) and I_A is the MS peak area of the light product ion (A ion). For example, $[\mathrm{Glc+Li}]^+$ produces a cross-ring cleavage ion at *m/z* 127, but $[1,2\text{-}^{13}\mathrm{C}_2\text{-}\mathrm{Glc+Li}]^+$ produces cross-ring cleavage ions at *m/z* 127 and 129 of differing abundances. The X ion yield for Glc can then be calculated from the MS peak areas of *m/z* 127 and 129. The reducing end yield was determined for each epimer. These types of calculations are possible for cross-ring cleavages due to the regiospecific carbon-13 labels and cannot be used for dehydration product ions.

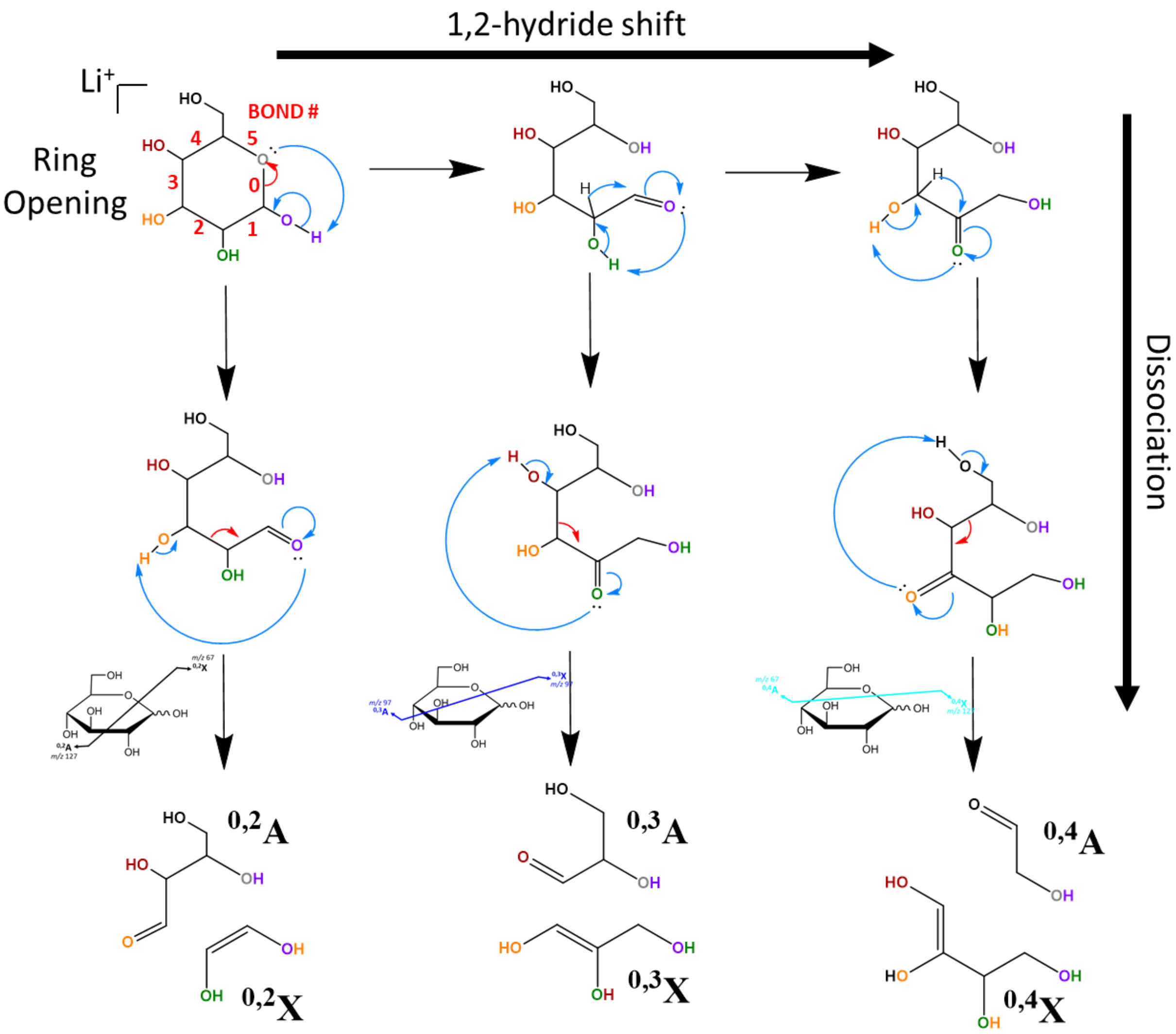

Figure 6.6. **Mechanism of hexose cross-ring cleavage illustrated based on the previously proposed mechanism**[33]. **Pyranose ring bond numbers are labeled in red on the hexose molecule at the top left of the figure.**

The X ion yield for *m/z* 127 versus 129 (^{0,2}A versus ^{0,4}X) of four hexose epimers are summarized in Figure 6.7. The mass spectra insets at the top of Figure 6.7 show relative abundances of ^{0,2}A and ^{0,4}X peaks. The ^{0,4}X ion yields measured here with ^{13}C-hexoses closely matches values measured for Glc, Gal and Man using ^{18}O-labeling at the anomeric center in a previous study[110]. The Tal ^{0,4}X product ion yield is reported for the first time in this current study. The ^{0,4}X ion yield (Yield$_{0,4X}$) for Glc is 0.104 and increases for axial epimers Man, Gal and Tal to 0.167, 0.292 and 0.447, respectively. The C2 axial hydroxyl of Man, C4 axial hydroxyl of Gal and C2/C4 axial hydrolxyls of Tal increase the ^{0,4}X ion yield during CID. The proposed ^{0,4}X ion structure contains the C1, C2, C3 and C4 ring atoms and the accompanying hydroxyl groups. An increasing abundance of ^{0,4}X ions relative to ^{0,2}A ions for Man, Gal and Tal may mean that C2 and C4 axial hydroxyl groups contribute to dissociation pathways specific to ^{0,4}X ion formation, or improve retention of the lithium cation to the ^{0,4}X structure. The C2/C4 axial hydroxyl groups of Man, Gal and Tal were previously found to contribute to a large portion of the favorable Li-O coordinations for intact $[\text{Hexose+Li}]^+$ (Chapter 3.1) [48]. Hexose stereochemistry had a lesser effect on the X ion yield when comparing *m/z* 97 and 99 (^{0,3}A versus ^{0,3}X) ions, where the ^{0,3}X yield (Yield$_{0,3X}$) was near 0.30 for all hexoses. X ion yields at multiple fragmentation amplitudes were generally consistent (Figure 6.8). ^{0,4}X and ^{0,3}X ion yields lend insight to the types of cross-ring cleavage product ions forming, and aid in understanding the water adduction characteristics of these product ions.

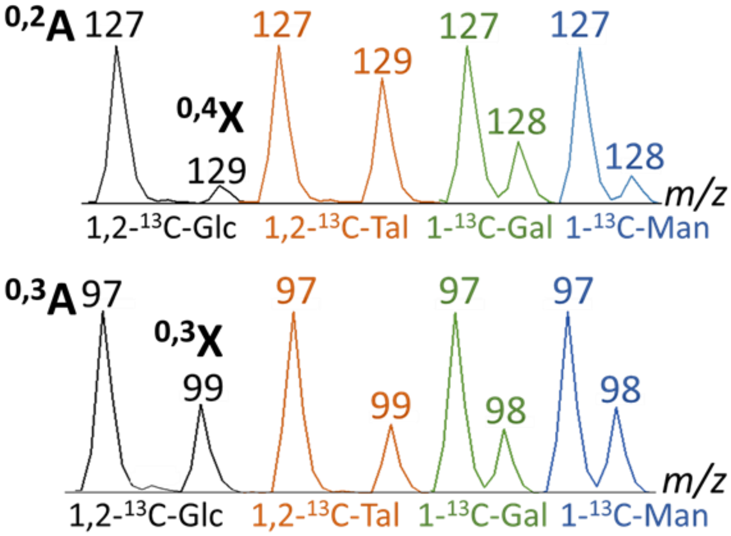

	Yield	
	^{0,3}X	^{0,4}X
1,2-^{13}C-Glucose	0.341 ± 0.006	0.104 ± 0.004
1,2-^{13}C-Talose	0.296 ± 0.005	0.447 ± 0.006
1-^{13}C-Galactose	0.271 ± 0.003	0.292 ± 0.005
1-^{13}C-Mannose	0.336 ± 0.001	0.167 ± 0.007

Figure 6.7 Product ion mass spectra insets of four carbon-13 labeled hexoses showing the formation of (top) ^{0,2}A and ^{0,4}X ions and (middle) ^{0,3}A and ^{0,3}X ions. The ^{0,3}X and ^{0,4}X ion yields calculated for each hexose epimer are listed in the table at the bottom of the figure.

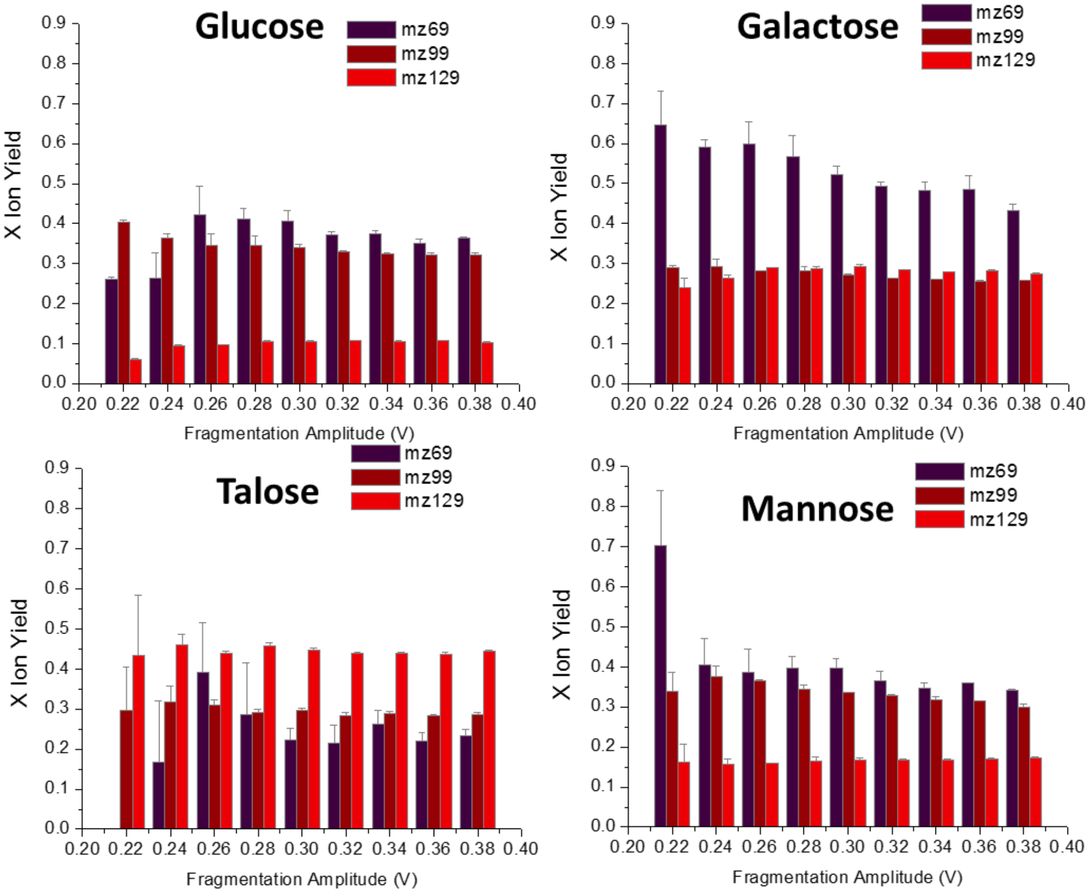

Figure 6.8. **X ion yields as a function of fragmentation amplitude. The ^{0,2}X ion is detected at *m/z* 69, the ^{0,3}X ion is *m/z* 99 and the ^{0,4}X ion is *m/z* 129.**

CID measurements thus far have been made on both the α- and β-hexose anomers. It was shown that hexose anomeric configuration affects the dehydration dissociation pathway (Figure 5.3). Does hexose anomeric configuration also affect cross-ring cleavage pathways? Carbon-13 hexose anomers were separated by HILIC-LC with a post-column infusion of lithium acetate, ionized by ESI and subjected to CID. The X ion yields of α-Glc, β-Glc, α-Man, β-Man, α-Gal, β-Gal, one Gal feature with an unassigned identity, and three unidentified Tal features were determined from the product ion spectra generated as each feature eluted from the LC column (Figure 6.9).

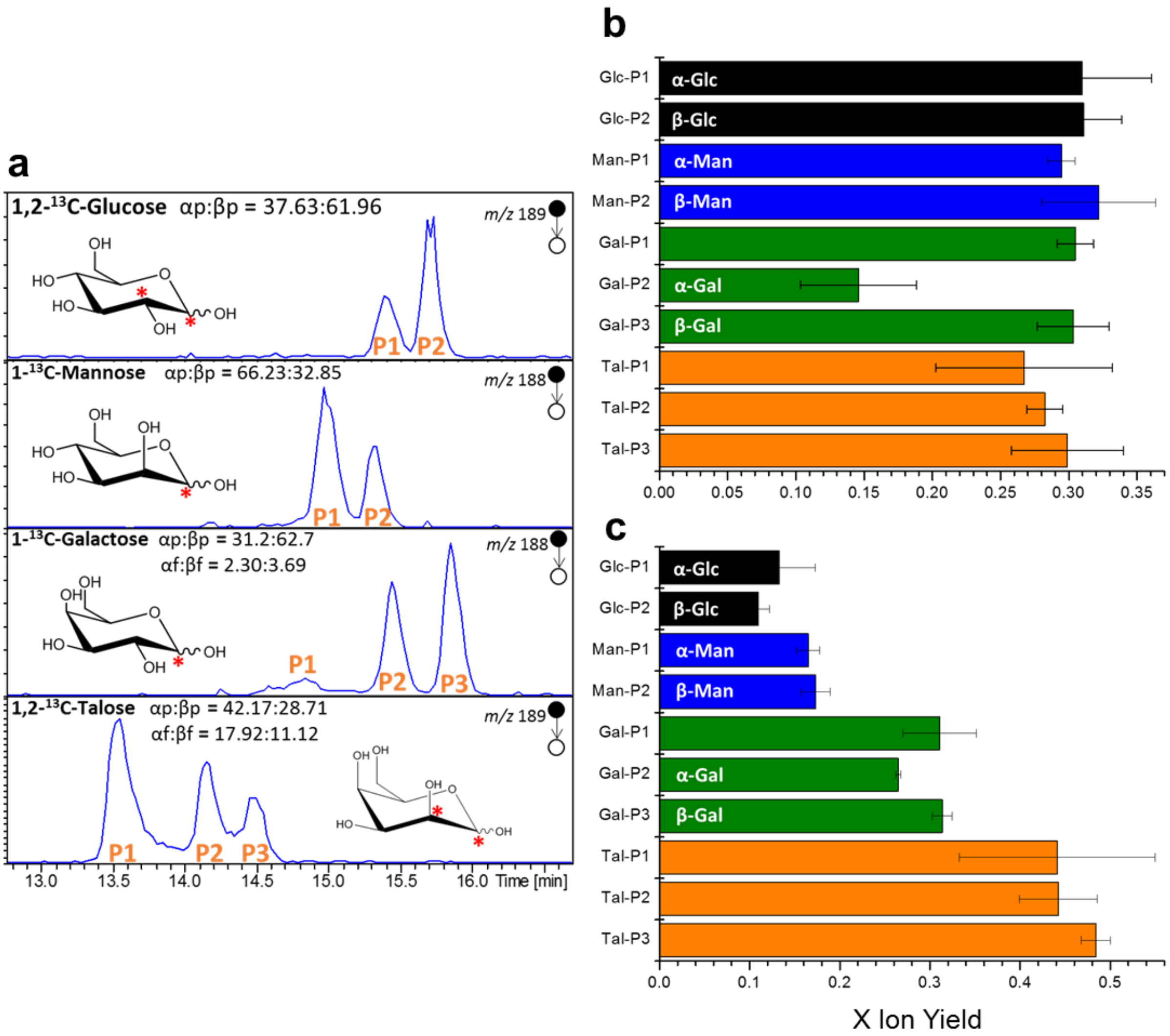

Figure 6.9 a) Chromatographic separations of hexose anomers using zwitterionic HLIC-LC. Some features for Gal and Tal remain unidentified; the third peak for each is hypothesized to be the furanose ring structure. b) ^{0,3}X ion yield and c) ^{0,4}X ion yield for each hexose anomer or structural feature.

For Glc, the anomer identities were assigned by retention time matching to pure α-Glc (or β-Glc) individually onto the chromatographic column. Also, the chromatographic peak area ratio roughly matches the expected anomeric ratio in solution of Glc. For Man and Gal, the anomer identities were assigned using the known anomeric ratio in solution, supported by the observation that α-anomers generally elute first. The unidentified peak 1 (P1) in the Gal chromatogram is hypothesized to be the furanose anomers. In aqueous solution, Gal was measured by NMR to be near 6% furanose in aqueous equilibrium[8]. Tal has significant amounts of the furanose and pyranose anomers which can explain the three chromatographic features, but the peaks remain unidentified.

In almost all cases, the ^{0,3}X and ^{0,4}X ion yields for the chromatographic separated anomers (Figure 6.9b-c) match the values from direct infusion measurements on the anomeric mixtures (Figure 6.7). The ^{0,3}X ion yields are all near 0.30 and 0,4X ion yields vary for each hexose, just as observed in Figure 6.7. Because cross-ring cleavage first requires ring opening at the anomeric center, which then allows free rotation of C-C bonds, X ion yields may not be impacted by anomeric configuration. α-Gal is the only structure that exhibits disparate cross-ring cleavage behavior; both the ^{0,3}X and ^{0,4}X ion yields are decreased. The axial C4 hydroxyl of Gal may promote formation of the respective A ions for α-Gal. The anomeric C1 hydroxyl of α-Gal is down and axial, opposite the plane of the ring from the C4 axial hydroxyl. Therefore, the axial C4 hydroxyl may dominate retention of the lithium cation upon cross-ring cleavage and direct formation of the ^{0,2}A and ^{0,3}A ions that contain the C4 hydroxyl group (Figure 6.6). Conversely, the anomeric C1 hydroxyl of β-Gal is equatorial and on the same side of the ring as the axial C4 hydroxyl. Both the C1 and C4 hydroxyls may coordinate to the lithium cation and compete for charge retention upon cross-ring cleavage to dictate whether the A or X ion forms.

The proposed structures for each cross-ring cleavage product ion (Figure 6.6) are trioses and tetroses, some of which are purchasable in liquid or solid form. Lithiated glyceraldehyde is isomeric to the ^{0,3}X and ^{0,3}A hexose cross-ring cleavages ($C_3H_6O_3Li^+$), so CID spectra of each were compared to assess structural similarities or differences. The CID (MS/MS) spectrum of [Glyceraldehyde+Li]$^+$ and CID (MS^3) spectra of ^{0,3}X and ^{0,3}A cross-ring cleavages from [1,2-

$^{13}C_2$-Glc+Li]$^+$ are shown in Figure 6.10. Upon CID of glyceraldehyde, no dissociation product ions of significant abundace are observed and the only measurable product ion is the water adduct. CID of the ^{0,3}A ion from 1,2-$^{13}C_2$-Glc is similar to [Glyceraldehyde+Li]$^+$ in that only a water adduct ion was observed. The ^{0,3}A ion structure has been proposed to form with an aldehyde moeity (Figure 6.6) [33], matching the structure of glyceraldehyde. But, the disparity in the relative abundance of *m/z* 97 and 115 indicates that the two ion populations have different water adduction reaction rates. Conversely, the ^{0,3}X ion from 1,2-$^{13}C_2$-Glc, which has been proposed to form as a vicinal enediol, had a measurable water loss and water adduct ion, indicating structural differences from glyceraldehyde. Different CID spectra were observed for the ^{0,2}A and ^{0,4}X ions of [1,2-$^{13}C_2$-Glc+Li]$^+$; consecutive water losses and the water adduct were observed for both the ^{0,2}A and ^{0,4}X ions, but additional neutral losses that correlate to CH_2O and $C_2H_4O_2$ were observed for the ^{0,2}A ion. MS^3 experiments identical to those shown here for 1,2-$^{13}C_2$-Glc were done for 1,2-$^{13}C_2$-Tal and the results were comparable.

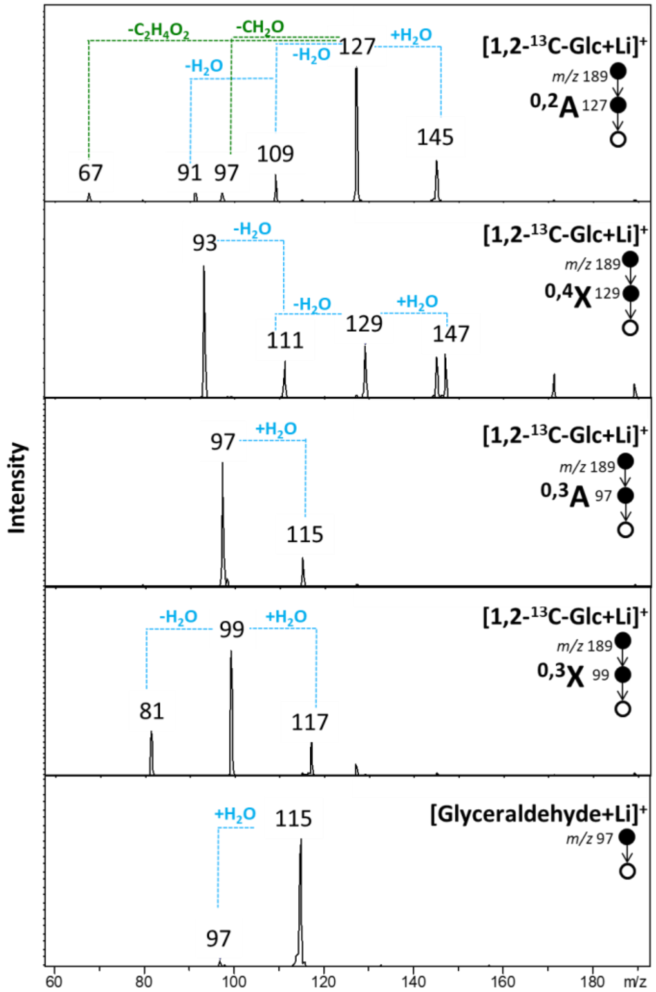

Figure 6.10 CID product ion spectra of lithiated 1,2-$^{13}C_2$-Glc cross-ring cleavage ions and lithiated glyceraldehyde. Spectra were averaged for 15 minutes.

6.3 Water Adduction to Unlabeled Hexose Product Ions

Unique water adduction unreacted fractions (R_U) were measured for the intact $[Hexose+Li]^+$ ions of the unlabeled hexose epimers (Figure 6.11). Glc with only equatorial hydroxyl groups has the lowest unreacted fraction, $R_{U(187)} = 0.284 \pm 0.002$. Axial hydroxyl groups increase the unreacted fractions for Gal (C4 axial, $R_{U(187)} = 0.377 \pm 0.015$), Man (C2 axial, $R_{U(187)} = 0.770 \pm 0.002$) and Tal (C2/C4 axial, $R_{U(187)} = 0.952 \pm 0.007$). DFT calculations suggest that axial hydroxyl groups increase the number of $[Hexose+Li]^+$ tri- and tetradentate

Li-O coordinations, as well as improve their stability. The C2 axial hydroxyl of Man and Tal greatly contribute to tri- and tetradentate coordinations that are detected as unreacted $[Hexose+Li]^+$ ions. Just as intact hexoses can be distinguished by the water adduction ion/molecule reaction, so can some of their CID product ions (Figure 6.11). Dehydration (*m/z* 169) and cross-ring cleavage (*m/z* 97 and 127) product ions had measurable R_U values, implying the existence of both reacted and unreacted product ion structures with Li-O coordinations of varying denticity. Conversely, the *m/z* 67 cross-ring cleavage ($C_2H_4O_2Li^+$) did not have a measurable R_U because it can only form bidentate Li-O coordinations (Figure 4.8 and Figure 6.15).

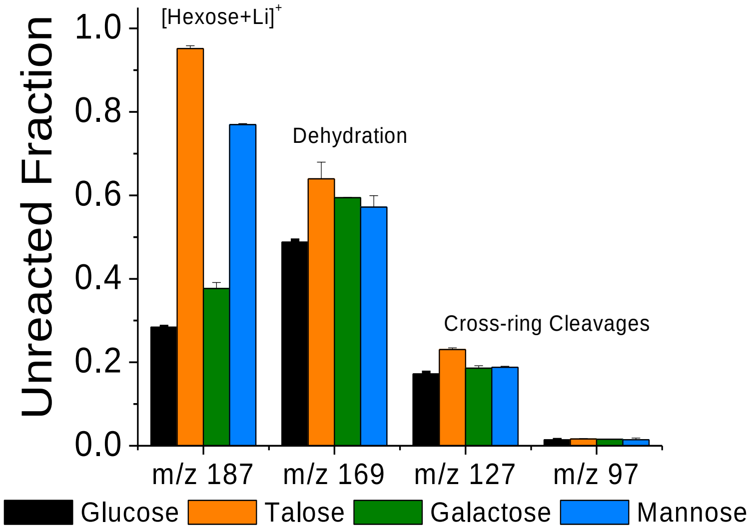

Figure 6.11 Unreacted fraction (R_U) measurements of unlabeled $[Hexose+Li]^+$ for four epimeric hexoses, and their dehydration and cross-ring cleavage CID product ions.

Unreacted fractions for the dehydration product ions were shifted from the intact hexoses. Tal ($R_{U(169)}$ = 0.639 ± 0.040) and Man ($R_{U(169)}$ = 0.572 ± 0.027) dehydration product ions have lower R_U values than their respective $[Hexose+Li]^+$ ions, meaning that the loss of an oxygen atom eliminates some tri- and tetradentate coordinations. Dehydration of Glc and Gal increased $R_{U(169)}$ compared to $R_{U(187)}$, which may initially seem counterintuitive considering the loss of an oxygen atom. Among the previously proposed dehydration ion structures for Glc and Gal are 1,2- and 1,3-anhydropyranoses, where the ether bridge (C-O-C bond) that forms a bicyclic structure can orient an oxygen atom above the pyranose ring. Because of the ether bridge, the lithium cation may now be positioned towards the center of the pyranose ring where it can coordinate to the ring oxygen and hydroxymethyl group to form tri- or tetradentate structures. The same effect is seen with axial hydroxyl groups of intact $[Hexose+Li]^+$, where the lithium is preferentially positioned towards the center of the pyranose ring and coordinates many oxygen atoms.

Cross-ring cleavage R_U values decrease with fewer number of oxygen atoms. The unreacted fraction for *m/z* 127 product ions represent a mixture of $^{0,2}A$ and $^{0,4}X$ ions with the molecular formula $C_4H_8O_4Li^+$. $R_{U(127)}$ for Tal (0.230 ± 0.005) was greatest followed by Man (0.188 ± 0.003), Gal (0.186 ± 0.006), and Glc (0.172 ± 0.004). The elevated $R_{U(127)}$ for unlabeled Gal, Man and Tal, relative to Glc, correlates to greater $^{0,4}X$ ion yields (Figure 6.7) and the R_U measurements of mass resolved $^{0,4}X$ and $^{0,2}A$ ions, on which more detail is provided in the next section. The near 0.20 unreacted fractions for *m/z* 127 cross-ring cleavage ions means the 4 carbon chain is flexible enough to favorably form tri- or tetradentate Li-O coordinations. $R_{U(97)}$ values for Glc, Tal, Gal and Man were all near 0.015; *m/z* 97 cross-ring cleavage ions were observed to almost completely react. The $R_{U(97)}$ values represent a mixture of unlabeled $^{0,3}A$ and $^{0,3}X$ ions ($C_3H_6O_3Li^+$). Excess strain would be placed on the $C_3H_6O_3Li^+$ ion to form a tridentate Li-O coordination; therefore, tridentate coordinations are unfavorable structures for the $^{0,3}A$ and

^{0,3}X cross-ring cleavages. The near equivalent ^{0,3}X ion yields for the four hexoses, as measured by CID of ^{13}C-Hexoses (Figure 6.7), may explain why the $R_{U(97)}$ values are also near equivalent.

6.4 Water Adduction to Mass Resolved A and X Cross-ring Cleavages

Mass resolution of A and X cross-ring cleavages enables water adduction to subsets of ions that are otherwise measured as an isomeric mixture. The mass-resolved A and X ion $R_{U(0,2A)}$ and $R_{U(0,4X)}$ values were greater than $R_{U(0,3A)}$ and $R_{U(0,3X)}$, which was expected based on $R_{U(127)}$ versus $R_{U(97)}$ from the unlabeled product ions. In all cases, the water adduction R_U of mass resolved A and X ions were nonidentical (Figure 6.12), and the linear combination of $R_{U(0,2A)}$ and $R_{U(0,4X)}$ is a close approximation of the $R_{U(127)}$ for the unlabeled cross-ring cleavage mixture. The linear combination must incorporate the A and X ion yields (Yield) and $R_{U(0,2A)}$ and $R_{U(0,4X)}$ values. For example, the ^{0,2}A and ^{0,4}X ions from [1,2-$^{13}C_2$-Tal+Li]$^+$ had values of $R_{U(0,2A)} = 0.164$ and $R_{U(0,4X)} = 0.333$. The ion yields measured by CID of [1,2-$^{13}C_2$-Tal+Li]$^+$ were $Yield_{0,2A} = 0.502$ and $Yield_{0,4X} = 0.498$. And thus, the linear combination is calculated as follows.

$$Estimated\ R_{U(127)} = \left(R_{U(0,2A)} \times Yield_{0,2A}\right) + \left(R_{U(0,4X)} \times Yield_{0,4X}\right)$$

$$Estimated\ R_{U(127)} = (0.164 \times 0.553) + (0.333\ \times 0.447)$$

$$Estimated\ R_{U(127)} = 0.239$$

The unlabeled mixture of these ions from [Talose+Li]$^+$ was measured to be $R_{U(127)} = 0.230$, near the average of $R_{U(0,2A)}$ and $R_{U(0,4X)}$ because the abundance ratio of the ^{0,2}A and ^{0,4}X ions is close to 50:50. In Table 6.3 the mass resolved ^{0,2}A and ^{0,4}X R_U values and ion yield values, and their linear combinations (estimated mixture R_U) are provided alongside the measured R_U for the unlabeled (UL) mixture. The estimated R_U values closely match the measured $R_{U(127)}$ for the unlabeled hexose, and $R_{U(127)}$ always falls between the $R_{U(0,2A)}$ and $R_{U(0,4X)}$ values for mass-resolved A and X ions. These linear combinations further suggest that each unlabeled hexose forms similar amounts of A and X ions as its ^{13}C-hexose counterpart.

Table 6.3 Measured R_U and ion yield for mass-resolved ^{0,2}A and ^{0,4}X ions, linear combination estimated R_U of the ion mixture, and the measured R_U for the unlabeled (UL) mixture.

Hexose	*m/z*	Ion(s)	R_U	Yield	Note
$^{13}C_2$-Glc	127	^{0,2}A	0.169	0.896	Mass resolved ion
	129	^{0,4}X	0.239	0.104	Mass resolved ion
	-	-	**0.176**	-	Estimated mix
Glc	127	^{0,2}A + ^{0,4}X	**0.172**	-	Measured UL mix
$^{13}C_2$-Tal	127	^{0,2}A	0.169	0.553	Mass resolved ion
	129	^{0,4}X	0.333	0.447	Mass resolved ion
	-	-	**0.239**	-	Estimated mix
Tal	127	^{0,2}A + ^{0,4}X	**0.230**	-	Measured UL mix
$^{13}C_1$-Gal	127	^{0,2}A	0.146	0.708	Mass resolved ion
	129	^{0,4}X	0.314	0.292	Mass resolved ion
	-	-	**0.195**	-	Estimated mix
Gal	127	^{0,2}A + ^{0,4}X	**0.186**	-	Measured UL mix
$^{13}C_1$-Man	127	^{0,2}A	0.187	0.833	Mass resolved ion
	129	^{0,4}X	0.256	0.167	Mass resolved ion
	-	-	**0.198**	-	Estimated mix
Man	127	^{0,2}A + ^{0,4}X	**0.188**	-	Measured UL mix

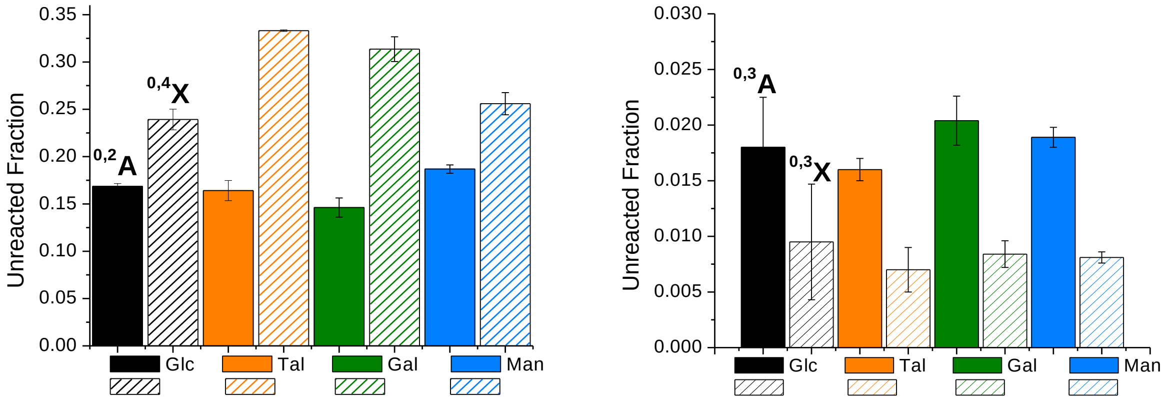

Figure 6.12 R_U values measured for mass-resolved ^{0,2}A, *m/z* 127, and ^{0,4}X, *m/z* 128 or 129, ions (left) and mass resolved ^{0,3}A, *m/z* 97, and ^{0,3}X, *m/z* 98 or 99, ions (right). Note the y-axis scale difference, where the ^{0,2}A and ^{0,4}X ($C_4H_8O_4Li^+$) product ions have higher R_U values than ^{0,3}A and ^{0,3}X ($C_3H_6O_3Li^+$) ions.

As discussed, there is disparity in the water adduction characteristics for mass-resolved A and X ions. Differences in covalent structure lead to unique capabilities for Li-O coordination. Upon dissociation of $[Hexose+Li]^+$, A ions are proposed to form with an aldehyde functional group and saturation with respect to carbon-carbon bonds, whereas X ions are proposed to from a (*cis* or *trans*) vicinal enediol that prevents rotation about the carbon-carbon double bond and increases structural rigidity (Figure 6.6). While intramolecular keto-enol tautomerism may occur in the gas phase, it is unlikely to occur if the lithium cation is coordinated between the vicinal hydroxyl groups. For all hexoses, $R_{U(0,4X)}$ was greater than $R_{U(0,2A)}$ indicating greater amounts of tridentate Li-O coordinations. The ^{0,4}X ion contains atoms C1 through C4 and the accompanying O1-O4 atoms, where the C3/C4 double bond may be in the *cis* or *trans* configuration. Considering both double bond configurations, DFT suggests that the ^{0,4}X ion can assume 9 possible Li-O coordinated structures, three of which are tridentate Li-O coordinations (Figure 6.13). The tridentate structures are more favorable in the gas phase than the bidentate structures, but bidentate structures must form based on the experimentally low R_U values. The results suggest that the most favorable product ions do not always form, and kinetic trapping of bidentate structures may occur. $R_{U(0,4X)}$ measured for Tal (0.333 ± 0.010) and Gal (0.314 ± 0.013) were significantly greater than for Glc (0.239 ± 0.011) and Man (0.256 ± 0.012). The C4 axial hydroxyl group of Gal/Tal increased both ^{0,4}X product ion yield and $R_{U(0,4X)}$, affecting the abundance and structure of ^{0,4}X ions. It is possible that the C4 axial hydroxyl group enables intact [Hexose+Li]$^+$ structures that invoke alternate dissociation pathways. For example, coordination of lithium to the C4 axial hydroxyl of [Hexose+Li]$^+$ may direct a certain double bond stereochemistry in the ^{0,4}X ion or specific tridentate coordination. Conversely, for the ^{0,2}A ions two tridentate structures and two bidentate structures were determined using DFT (Figure 6.13, right).

$C_3H_6O_3Li^+$ ions almost completely react in the ion trap. ^{0,3}A ions from each hexose epimer have $R_{U(0,3A)}$ values ranging 0.016 to 0.0204, and ^{0,3}X ions have $R_{U(0,3X)}$ values ranging from 0.007 to 0.0095. DFT calculations suggest that the ^{0,3}X ion can only form bidentate coordinations with lithium (Figure 6.14, left). The ^{0,3}X ion contains hexose ring atoms C1, C2 and C3 with a double bond between C2-C3. Therefore, the ^{0,3}X ion molecular rigidity prevents all three oxygen atoms from coordinating lithium, corroborating the very low experimental R_U. Conversely, the ^{0,3}A ion contains atoms C4, C5, and C6 and is proposed to form as an aldehyde; therefore, structural flexibility allows a tridentate Li-O coordination (Figure 6.14, right). The tridentate structure, again, is more favorable than the bidentate structures. A higher measured R_U for ^{0,3}X would be expected if the most favorable product ions formed upon dissociation.

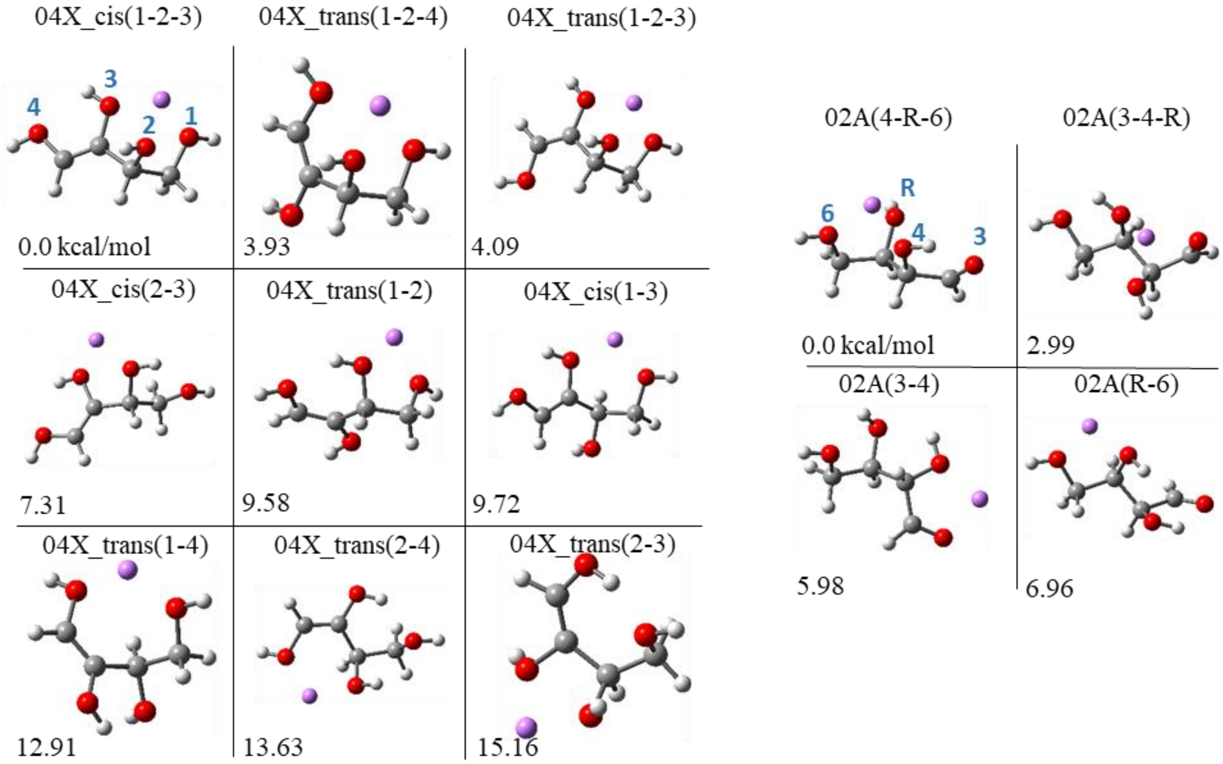

Figure 6.13 Gas-phase DFT optimized structures for lithiated ^{0,4}X (left) and ^{0,2}A (right) cross-ring cleavage ions (*m/z* 127). Relative Gibbs free energies are expressed in kcal/mol. Blue oxygen atom labels correlate to the oxygen atom positions from the intact hexose. Structure naming convention consists of *IonType_DoubleBondConfiguration(OyxgenAtomsLiCoordinates)*.

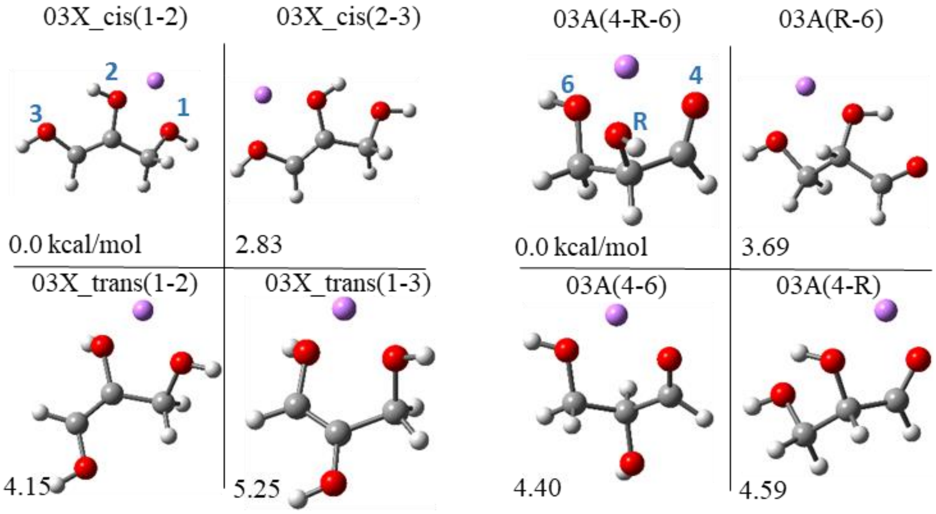

Figure 6.14 Gas-phase DFT optimized structures for lithiated ^{0,3}X (left) and ^{0,3}A (right) cross-ring cleavage ions (*m/z* 97). Relative Gibbs free energies are expressed in kcal/mol. Blue oxygen atom labels correlate to the oxygen atom positions from the intact hexose. Structure naming convention consists of *IonType_DoubleBondConfiguration(OyxgenAtomsLiCoordinates)*.

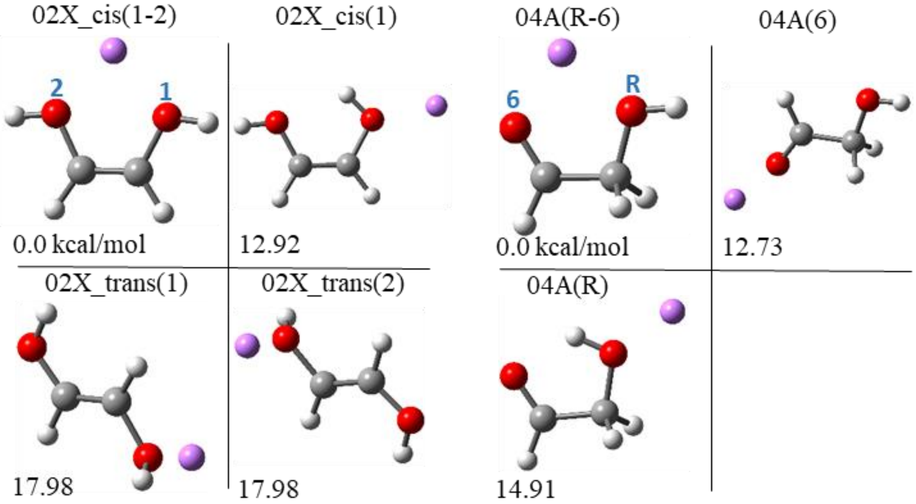

Figure 6.15 Gas-phase DFT optimized structures for lithiated ^{0,3}X (left) and ^{0,3}A (right) cross-ring cleavage ions (*m/z* 67). Relative Gibbs free energies are expressed in kcal/mol. Blue oxygen atom labels correlate to the oxygen atom positions from the intact hexose. Structure naming convention consists of *IonType_DoubleBondConfiguration(OyxgenAtomsLiCoordinates)*.

6.5 Summary

Stereochemistry affects the lithium cation coordination sites available on a hexose molecule and, as a result, hexose dissociation chemistry. The epimers Glc, Tal, Gal and Man were found to have differences in CID product ion formation and structure. Additionally, each product ion type was found to be a mixture of different covalent structures (^{0,2}A versus ^{0,4}X ion yield), and multiple sites and denticity of lithium-oxygen coordinations (R_U). The isomeric heterogeneity of CID product ions generated from four hexose epimers was measured using CID and the water adduction ion/molecule reaction. CID of a lithiated hexose in an ion trap generates lithiated dehydration and cross-ring cleavage product ions. Structural changes upon dehydration were probed based on unreacted fraction changes between intact [Hexose+Li]$^+$ and dehydration product ion. Cross-ring cleavage behavior between the four hexose epimers was not identical. CID of 1-^{13}C-hexoses and 1,2-^{13}C-hexoses generated mass-resolved A and X cross-ring cleavage ions. The yields of ^{0,3}X and ^{0,3}A ions were similar for each hexose epimer, but the ^{0,2}A and ^{0,4}X ion yields were different and correlated to axial hydroxyl group positions. Water adduction separated two subsets of CID product ion structures, $[M+Li]^+$ and $[M+Li+H_2O]^+$, lending insight to the types of lithium-oxygen coordinations each ion type forms. All intact $[Hexose+Li]^+$ ions and lithiated CID product ions had measurable unreacted fractions indicating two types of ion structures: bidentate Li-O coordinations that result in measurable water adducts and tri- or tetradentate Li-O coordinations that do not result in a measurable water adduct. Water adduction to each type of mass-resolved A and X ions revealed structural differences within a given hexose epimer, as well as some differences across the epimers.

CHAPTER 7: SUMMARY AND FUTURE DIRECTIONS

7.1 General Summary

This dissertation has focused on understanding the structures and chemistry of gas-phase lithium cationized carbohydrates produced during electrospray ionization. When stored in a low-energy quadrupole ion trap MS, gas-phase lithium cationized carbohydrates will adduct a water molecule. This water adduction ion/molecule reaction can differentiate multiple groups of isomeric monosaccharides with known stereochemistries. Density functional theory calculations aided understanding of the experimental results and provided mechanistic insights to the ion/molecule reaction. Mechanistic insights on the water adduction ion/molecule reaction (unreacted fraction and reaction rate) were discussed in Chapter 3. Ions with bidentate lithium-oxygen coordinations are observed to adduct a water molecule, whereas ions with tri- or tetradentate coordinations are not. The effect of hexose and inositol stereochemistry on lithium-oxygen coordination denticity and water adduction metrics were discussed in Chapter 3.1 and 3.2. In Chapter 3.3, monosaccharide gas-phase lithium cation affinities were correlated to their unreacted fractions to support the claim that lithium-oxygen coordination denticity impacts the water adduction unreacted fraction. The strength of Li-H_2O bonds that various hexoses form upon water adduction were probed using collision-induced dissociation and discussed in Chapter 3.4. Hexoses that form more tri- and tetradentate lithium-oxygen coordinations during ESI have, on average, weaker Li-H_2O bonds upon water adduction in the ion trap. Higher denticity lithium-oxygen coordinations, and weaker Li-H_2O bonds, correlate to higher unreacted fractions and slower reaction rates.

In Chapter 4 the effects of the Bruker HCT quadrupole ion trap instrument parameters on the water adduction results were covered. In Chapter 4.1, dc accelerating voltages were intentionally used to induce isomerization of lithium cationized monosaccharides in the entrance ion optics of the MS. Increasing unreacted fractions were measured for some monosaccharides as an increasing amount of internal energy was imparted into ions in the optics. Changing unreacted fractions were hypothesized to be due to pyranose ring puckering to boat and/or skew boat conformations that create tri- or tetradentate lithium-oxygen coordinations. In Chapters 4.2 and 4.3, MS instrument parameters that may introduce artifacts into water adduction data were studied. In Chapter 4.2, water adduction during the ion trap accumulation time can affect the results was discussed, and Chapter 4.3 discussed how ion energy during reaction (during the scan delay) can affect the water adduction reaction rate and measured unreacted fraction. Well controlled experimental conditions are necessary when comparing data and a calibration protocol will be required when the water adduction experiment is implemented cross-platform or cross-laboratory.

Chapter 5 addresses the uncertainty about whether carbohydrate features resolved by ion mobility spectrometry are due to separation of the alpha and beta anomers, or due to different metal cationization sites. The results of HILIC liquid chromatography (condensed phase) or cyclic ion mobility (gas-phase) separations paired with collision-induced dissociation experiments in some respects agree, and in some respects disagree, with the hypothesis of ion mobility anomer separation. Therefore, ion mobility resolution of gas-phase carbohydrate ions may be a result of anomer separation but anomers are not always resolved.

In Chapter 6 the dissociation chemistry of hexoses was shown to be far more complex than previously postulated, and the potential for water adduction to expand our understanding of gas-phase carbohydrate structure and chemistry was demonstrated. Collision-induced dissociation of regiospecifically synthesized carbon-13 enriched hexoses and the water adduction ion/molecule reaction highlighted the formation of isomeric product ions upon dissociation of lithium cationized hexoses. Upon dissociation, hexoses formed product ions with various lithium coordination sites as probed by water adduction. Cross-ring cleavage of each lithium cationized hexose epimer produced conformational isomers, and the cross-ring cleavage characteristics varied for each hexose epimer.

7.2 CID-Water Adduction for *de novo* Carbohydrate Structure Elucidation

Glycans are the most structurally diverse natural biopolymers[7] and have many characteristic features that affect structure and biological activity of proteins[118–121]. Recently it was discovered that glycans modify small RNAs, changing the outlook on RNA localization and function[122]. Listed in Figure 7.1 are the requirements for complete glycan structural characterization roughly in order of increasing analytical challenge. Enzymatic linkage of multiple classes of monosaccharides can occur, and each class contains multiple stereoisomers. As the saccharide chain is lengthened the glycosidic linkage can occur via one of five monosaccharide hydroxyl groups, resulting in either linear or branched polymer chains. Additionally, due to the monosaccharide anomeric center the glycosidic linkage can be in the α- or β-configuration.

Mass-to-charge ratio alone informs of the number of monosaccharides and provides insight into class composition; however, while mass spectrometry is an extremely powerful analytical technique, the area it is most challenged with is differentiating isomers and especially stereoisomers. To gain further structural information tandem mass spectrometry (MS/MS) methods are used.

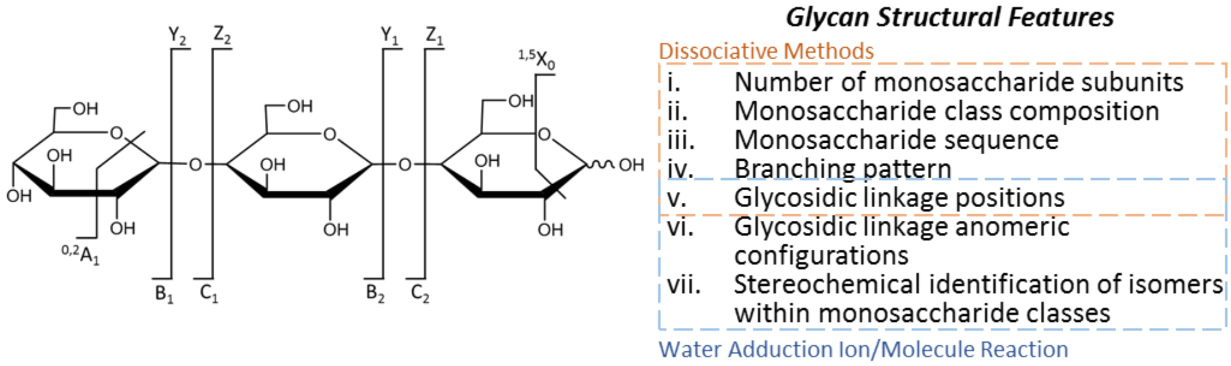

Figure 7.1 Domon-Costello nomenclature for glycan dissociation, and structural features required for complete glycan characterization. Only 1→4 linkages are shown in this linear glycan structure, and linakge anomeric configuration is not depicted. Additionally, the three hexoses shown are Glc molecules, but monosaccharide class and/or hydroxyl stereochemistry can vary.

Tandem mass spectrometry involves multiple stages of mass selection often with ion dissociation between MS steps. Dissociation of glycans produces structurally informative glycosidic bond cleavage ions (B, C, Y and Z) and cross-ring cleavage (A and X) ions. Glycosidic cleavages provide information about monosaccharide sequence and branching patterns, whereas cross-ring cleavages reveal linkage position information. CID has generated glycosidic linkage-type dependent fragments, elucidated branching patterns, and identified monosaccharide connectivity[28–30, 35, 36, 108, 123, 124].

Dissociative techniques have not yet been able to distinguish stereochemical features of glycans (Figure 7.1 vi and vii), but the water adduction molecule has been shown to be sensitive to monosaccharide stereochemistry and disaccharide glycosidic linkage stereochemistry[46, 47, 49]. With the technology to identify all glycan structural features, the next challenge is to efficiently sequence glycans from the available data. Annotating MS/MS spectra and determining the associated glycan sequence manually is time-consuming and impractical for glycomics experiments which produce large amounts of data. Two strategies for automated glycan sequencing have been employed in previous software: database spectral matching[125–127] and *de novo* sequencing[128–130]. Many *de novo* sequencing strategies employ machine/deep learning to extract structural patterns in large datasets for glycan sequencing at low computational cost. Despite their calculable success, automated sequencing strategies have been limited by the incomplete set of glycan structural features (e.g. lack of stereochemical information) available in MS/MS data. This limitation can be addressed by incorporating water adduction ion/molecule reaction metrics into datasets used for *de novo* glycan sequencing.

Machine/deep learning neural networks have been applied to mass spectrometry data for structural prediction based on product ion spectra for various compound classes[131, 132], and multiple data pretreatment methods for extracting chemical information from mass spectra have been investigated[133]. These past studies concluded that predictive power of neural networks would increase by supporting MS/MS dissociation data with experimental data from complementary techniques. A recent study trained a neural network with a differential ion mobility spectrometry-MS dataset[134]. This neural network accurately determined condensed phase molecular properties (e.g., cell permeability, solubility) of molecules with ten different classes of structural topologies, demonstrating the benefits of a dataset assembled from complementary technologies. Building on the success of this recent report, the aim is to train a neural network to assign structural features to, and identify, unknown polysaccharides obtained by enzymatic cleavage from peptides, and to improve the completeness of glycan structural characterization.

A large collection of data is required to properly train and test a deep learning algorithm. Thus, a database of CID MS^n spectra, with associated water adduction reaction metrics and differential ion mobility spectrometry parameters, should be acquired for many polysaccharide standards of known structures. CID-water adduction has previously been shown to differentiate disaccharides[49]. Also, in Chapter 6 of this dissertation it was shown that CID and water adduction to lithium cationized product ions of hexose epimers produces different results. Therefore, large lithium cationized carbohydrates can be dissociated to their individual monosaccharide subunits, and dissociation product ions of those monosaccharides. Then at each stage of MS^n, unique CID-water adduction information can be acquired as a part of the large database. Differential ion mobility spectrometry (DIMS) can be used to separate ions prior to the MS[135], and the compensation field required to transmit ions can be used as an identifier similar to chromatography retention time or arrival time during cyclic ion mobility. As discussed in Chapter 5, cIM is a separation in time where ions have some travel time to the detector and only a small packet of ions can be injected into the cIM device for each separation. DIMS is a separation in space, does not require injection of a small packet of ions and can be used as a constant filter for transmission of ions of interest. The compensation field required to transmit a polysaccharide through the DIMS will be one aspect of the database. Coupling DIMS to the ion trap MS will also allow for separation of polysaccharides from biological interferences when real samples are analyzed.

To generate the database, polysaccharide standards will be transmitted through DIMS at their characteristic compensation field and subjected to CID-water adduction experiments. Water adduction to lithiated polysaccharides is not observed, so dissociation of the polysaccharide parent ion to monosaccharide (or smaller) product ions via MS^n is necessary. While it is difficult to determine which monosaccharide retains the lithium cation after dissociation (without heavy-isotope labeling experiments), the proposed MS^n experiments (Figure 7.2) hypothetically have enough product ion redundancy to measure all monosaccharides within a polysaccharide structure. Heavy-water labeling of mono- and disaccharides has shown that the metal cation (sodium or lithium) is retained by the reducing end upon CID with 5 to 30% abundance[110]. Retention of the lithium cation by both the reducing and non-reducing ends suggests that all monosaccharide subunits should be measurable with CID experiments. Water adduction can probe oxygen atom orientation (anomeric and stereochemical configuration) because the lithium can be coordinated by different groups of oxygen atoms in molecular space. The water adduction characteristics of a molecule are dependent on the types of lithium-oxygen coordinations that form during ionization and dissociation. Illustrated in Figure 7.2 is a small subset of the available MS^n experiments showing the monosaccharide coverage for a generic trisaccharide. Each colored box represents the product ion formed if lithium is retained by that part of the structure. There are two boxes per color to represent isomeric product ions formed from the non-reducing or the reducing ends.

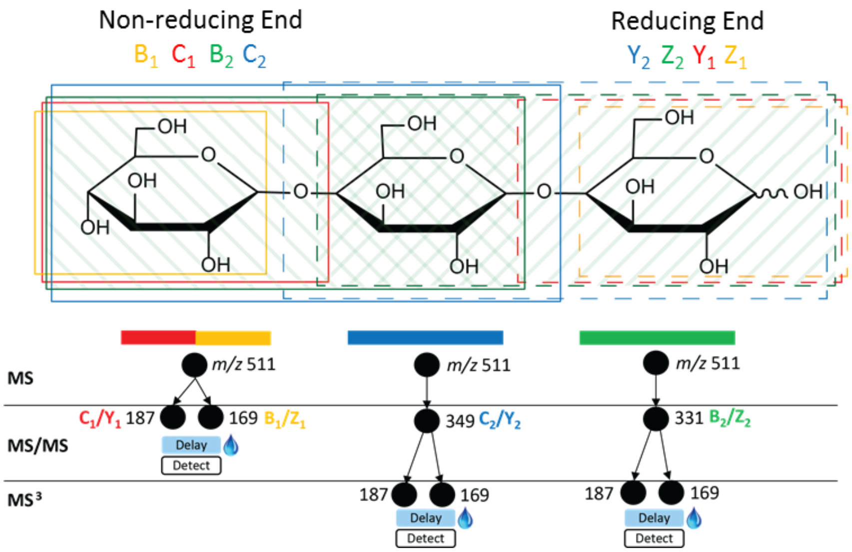

Figure 7.2 Three MS^n experiments that allow redundant measurement of each monosaccharide subunit, shown by the coverage of colored boxes. Each box is a lithium cationized product ion at the MS/MS level. The *m/z* 349 product ion (blue, C_2 or Y_2) is a lithium cationized disaccharide from either the non-reducing (solid line) or reducing (dashed line) end. The green patterned infill depicts measurement redundancy between the B_2/Z_2 ions (the same type of overlap exists for the C_2/Y_2 ions).

While cross-ring cleavages of polysaccharides also occur upon CID, only glycosidic cleavages will be considered for the purpose of this explanation; however, similar experiments should be done for cross-ring cleavage ions and will be an important part of the overall database. With regard to the glycosidic cleavage, once *m/z* 511, $[M+Li]^+$, is isolated in the quadrupole ion trap it is collisionally dissociated to *m/z* 349, 331, 187 and 169, and these are detected (MS/MS). An identical experiment is performed, but then allows the *m/z* 187 and 169 product ions to react with water prior to detection. Barring any subsequent dissociation events, the ion populations of *m/z* 187 and 169 at the MS/MS level represent the outer monosaccharide subunits. The abundance of these C_1/Y_1 and B_1/Z_1 ions, among others in the MS/MS spectrum, prior to water adduction will be indicative of trisaccharide features *i* through *v* outlined in Figure 7.1. The water adduction reaction rates and unreacted fractions of the C_1/Y_1 and B_1/Z_1 product ions will encode information about the anomeric configurations and positions of both glycosidic linkages, as well as for the stereochemistry of the outer monosaccharides.

Re-isolation of *m/z* 349 (MS^3) and dissociation to *m/z* 187 and 169 should allow measurement of the internal monosaccharide subunit. The product ions yielded from CID of *m/z* 349 and 331 have significant overlap regarding the monosaccharides that can be measured. While these experiments may produce redundant information, they provide information about all parts of the polysaccharide structure. The CID-water adduction MS^n experiments available for a given polysaccharide significantly exceeds the three examples described here, highlighting the potential to generate thousands of features (data points) for the deep learning algorithm.

A successful neural network requires acquisition of high-quality data, preprocessing of the data, selection of the correct modeling architecture for the task, and training of the neural network using the preprocessed data. For dataset acquisition, the DIMS separation space (dispersion and compensation fields) and CID-water adduction metrics should be mapped for a large group of polysaccharide standards similar to a previous study[129]. Preprocessing of the data entails extracting and converting raw data to a clean and consistent format, data normalization, and providing identifiers for polysaccharides and the MS^n experiment each data piece was generated from. Finding the right modeling architecture and training method will be an iterative process.

A shallow network architecture, typical of machine learning networks, contains an input layer, a hidden layer, and an output layer (Figure 7.3). Many hidden layers stitched together is known as a deep neural network. Additional hidden layers allow the network to learn increasingly complex and abstract representations of the input data. Because of the complex intricacies of glycan structural features, a deep learning neural network should be used.

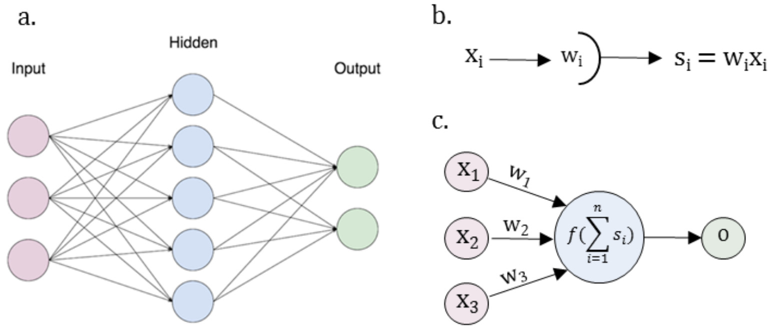

Figure 7.3 a) Architecture of a feed-forward artificial neural network. b) Weighting of inputs prior to the neuron. c) All inputs feed into every neuron in the hidden layer for transformation.

Training neural networks involves repeatedly exposing the network to a training dataset until the desired outcome is reached. A fraction of the available dataset is not used for training, but used as a test dataset that the network must successfully characterize. There are two general learning types for neural networks: supervised or unsupervised (Figure 7.4). Supervised learning is merely a template matching scheme, and therefore is limited in the predictions it can make. To overcome template matching, the input data can be repeatedly passed through the network until outputs have stabilized. In this unsupervised learning process, the network creates its own unique representation of the dataset (Figure 7.4b).

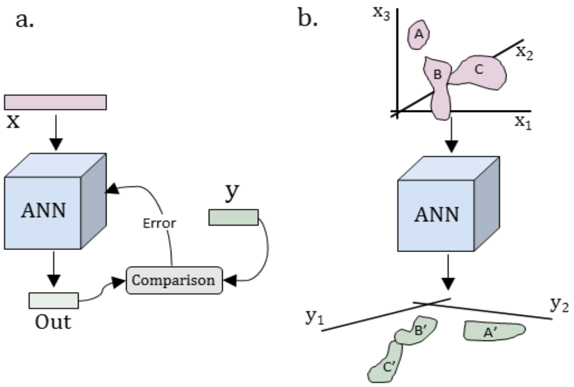

Figure 7.4 a) A schematic of supervised learning. b) Unsupervised learning where the neural network learns a unique representation of the input data.

Unsupervised training is fit for glycan characterization due to the difficulty of recognizing structural features in the DIMS-CID-Water Adduction data. It is reasonable to manually recognize patterns in the data for disaccharides[49], but analyzing larger saccharides manually quickly becomes unattainable. Output data from deep learning neural networks can be converted into a spectral network to visualize data clustering. One of the past limitations of neural networks from a scientific point of view is that the important chemical parameters leading to the output could not be determined. New algorithms allow one to look at individual hidden nodes to potentially glean such information and thus logically improve the system.

Data from CID and water adduction ion/molecule reaction experiments are uniquely embedded with structural information that can identify all necessary glycan features for complete structural characterization. While a human may interpret such data and determine the structure of a polysaccharide, a neural network can extract patterns and features in the dataset and use it to *de novo* determine the structure of unknown polysaccharides much faster and more reliably than the human. Therefore, a deep learning algorithm that takes advantage CID-water adduction data could be a powerful tool for *de novo* glycan sequencing that extends beyond the capabilities of current analytical techniques.

7.3 Anomerically-locked Methyl Pyranosides for Mechanistic Studies

A pyranose is a six-membered ring consisting of five carbon atoms and one oxygen atom. An intramolecular hemiacetal forms the pyranose ring upon reaction of the hydroxyl group on C5 with C1 (see Figure 7.5 for carbon numbering). The cyclic hemiacetal can ring open to form the linear conformation of Glc, followed by rotation about the C1-C2 bond and re-cyclization. Mutarotation, shown in Figure 7.5, is the interconversion between the α and β anomer of a carbohydrate.

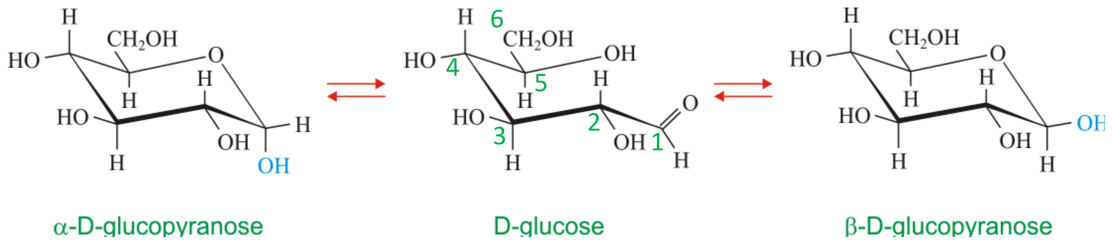

Figure 7.5 Mutarotation of Glc occurs upon pyranose ring opening in protic solvent.

Any carbohydrate containing a hemiacetal is known as a reducing sugar and can ring open in protic solvent. If the OH group at C1 is replaced with an OR group, forming an acetal, the sugar becomes non-reducing. A non-reducing sugar is locked in the cyclic form and is unable to mutarotate. This section proposes the locking of the anomeric configuration of hexopyranoses *via* the reaction in Figure 7.6 to study lithium cationization and water adduction characteristics of individual hexose anomers. Theoretical and experimental studies similar to those described in Chapters 3.1 and 3.2 can be done using anomerically-locked methyl pyranoside molecules to gain further water adduction mechanistic insights. Theoretical DFT data provides information about the Li-O coordinations formed by each hexose anomer, but generally the experimental water adduction data is acquired using a mixture of hexose anomers. Therefore, experiments using anomerically-locked methyl pyranosides are better suited for comparison to theoretical DFT data. Both methyl glucopyranosides, α-methylglucoside and β-methylglucoside, were used previously in the Glish lab to study the water adduction characteristics of Glc anomers[48].

Some anomerically-locked methyl hexopyranosides can be purchased from chemical vendors. Both methyl glucopyranosides, α-methylglucoside and β-methylglucoside, are relatively affordable. The methyl galactopyranoside anomers are available but are relatively expensive. The α-methyl mannopyranoside is inexpensive to purchase but β-methyl mannopyranoside is not at all available for purchase from any chemical vendors as of this writing. Other methyl hexopyranosides (All, Tal, Alt, Gul, Ido) are also not currently available for purchase. A previous IMS study on methyl pyranosides required synthesis of these molecules[136]. Because of the wide unavailability of the methyl pyranosides, a simple one-pot synthesis scheme is proposed here and was tested.

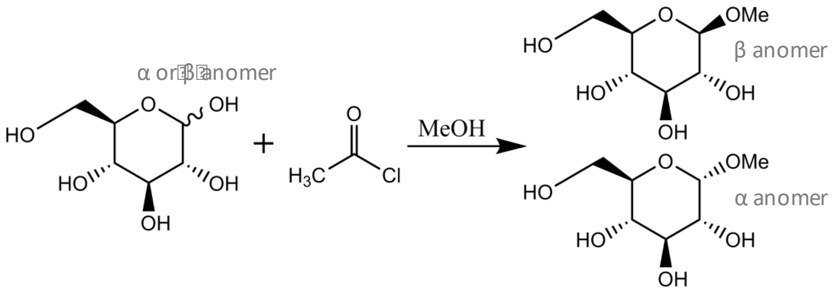

Figure 7.6 Reaction of a mixture of Glc anomers with acetyl chloride in methanol to produce anomerically-locked methyl glucopyranosides.

Synthesis of methyl pyranoside derivatives is done in a scintillation vial. To the scintillation vial was added methanol ($[\text{sugar}]_0 = 0.2$ M). Acetyl chloride (0.05 equivalent) was added dropwise and stirred for 30 minutes at room temperature and upon reacting with methanol anhydrous hydrochloric acid is produced in catalytic amount. This step is taken to limit water in the reaction solution because it will regenerate the starting sugar and reduce methyl pyranoside yield. The appropriate sugar (1 equivalent) was added and the mixture was stirred at 65 °C for 16 hours. Methyl pyranoside product was concentrated by evaporating solvent under nitrogen. This method can be easily scaled down to derivatize milligram amounts of sugars. The reaction was tested using Glc and yield was assessed by analyzing the lithium cationized methyl glucopyranoside with ESI-MS. Trace amounts of underivatized sugar remained (less than 2% relative abundance). The synthesized methyl glucopyranoside water adduction metrics matched those of Glc because even though the derivatized anomers could not mutarotate, they were still in a mixture together at the same anomeric ratio as Glc. To reach the goal of analyzing individual anomers, a purification step will be necessary.

Alpha and beta methyl pyranoside anomers can possibly be purified using HILIC liquid chromatography. The zwitterionic ZIC-cHILIC and ZIC-HILIC columns (Merck SeQuant, Sweden) with 5 μm particles and dimensions 150 x 4.6 mm have previously been shown to separate Glc and other hexose anomers (Chapter 2.6, Figure 5.2)[21]. Thus far, separation of methyl pyranosides has not been achieved with the ZIC-HILIC or ZIC-cHILIC column, and 18- or 40-minute gradients of water/acetonitrile or water/acetone. Separation of the methyl pyranosides has proven difficult because the orientation of the anomeric methoxy (-OR) group is the only structural difference and the methyl group does not favorably interact with a HILIC column. Though separation has not yet been achieved, it may be possible with further method development. Once separation of the anomers is achieved, the mobile phase containing analytes can be sent to the mass spectrometer for analysis or fraction collected into different vials to isolate each anomer for later analysis.

Through derivatization to lock anomeric configuration and subsequent purification, separate solutions of the alpha and beta anomer for any hexopyranose sugar can be collected. The purified methyl pyranose anomers can be electrosprayed with lithium salt and their water adduction unreacted fractions and reaction rates measured. Experimental data for individual anomers describes how much each anomer contributes to the total unreacted fraction. Since the only structural difference is stereochemistry at the anomeric center, differences in unreacted fraction are easily assigned to a specific coordination site. Additionally, DFT calculations provide theoretical data for individual anomers, which improves ease of comparison between theoretical and experimental data.

7.4 Structural Differentiation of Glycolipids using CID and Water Adduction

The structural intricacies of carbohydrates have been discussed in detail in this dissertation. Lipids are another molecular class with tremendous structural diversity[137, 138]. In biology, carbohydrates are often conjugated to lipids. These glycolipids combine the isomeric and stereochemical intricacies of both molecular classes[139]. Few analytical techniques are capable of complete carbohydrate or lipid structural elucidation; this holds especially true for glycolipids. Multiple lipid classes are found as glycoconjugates in biology, such as glycerolipids, glycerophospholipids and sphingolipids[140]. The carbohydrate moiety can be one of the various inositol or hexose isomers or a more complex glycan such as in a ganglioside (Figure 7.7). Glycoglycerolipid headgroups have high structural diversity that relate to the wide scope of glycolipid function in plants and bacteria[141], and inositol derivatized glycerolipids are known nervous system regulators[142]. Many mass spectrometry-based technologies have found use in lipidomics, glycomics and glycolipid studies[138, 143–146]. The use of ion/ion reactions for improved structural elucidation of glycerophospholipids highlighted the potential for gas-phase ion chemistry in these related fields[147, 148]. Glycolipids are amenable to electrospray ionization and subsequent tandem-MS analysis; therefore, dissociation and ion/molecule reactions in a quadrupole ion trap may be able to elucidate subtle glycolipid structural differences that were previously unattainable.

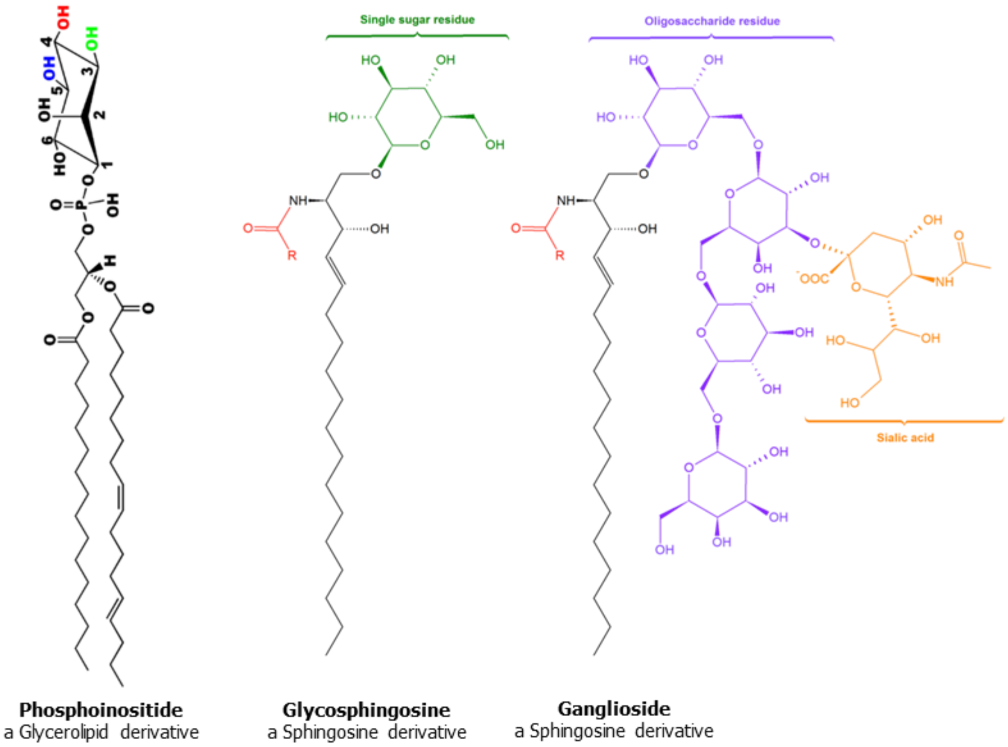

Figure 7.7 Three example glycolipids. Left) Phosphoglycerolipid with an inositol headgroup; The hydroxyl groups at the 3, 4 and/or 5 positions of the inositol can be phosphorylated to alter lipid function. Middle) A sphingosine derived glycolipid with a monosaccharide. Right) Ganglioside, a sphingosine derived glycolipid with a complex glycan.

Glucosphingosine (GluSph) and galactosphingosine (GalSph) are biomarkers for the lysosomal Gaucher and Krabbe diseases, respectively. GluSph was measured in human blood plasma and urine using reversed-phase LC-MS/MS[149], and both GluSph and GalSph could be separated from one another by HILIC-LC and measured using MS/MS[150]. There is potential to quickly differentiate and identify the lipid and carbohydrate moieties of glycolipids using DIMS and CID-water adduction in an ion trap, similar to the workflow proposed in Chapter 7.2. Proof of principle experiments were done to confirm that lithium cationization, dissociation and water adduction could be achieved for glycolipids. Three glycolipids were used: the two isomers GluSph and GalSph, also called psychosine, and one phosphoinositide, PI(8:0/8:0).

One micromolar PI(8:0/8:0) was ionized by electrospray from a solution of methanol/chloroform/water (66.5/30/3.5) with 0.1% formic acid and 100 µM lithium acetate additives. With all instrument parameters set to analyze positive ions, $[PI(8:0/8:0)+Li]^+$ was detected at *m/z* 593, and CID and water adduction product ions were detected after MS/MS experiments (Figure 7.8a-e). CID of *m/z* 593 generated the lithium cationized inositol at *m/z* 187, the lithium cationized phosphoinositol at *m/z* 267, and a product ion at *m/z* 327 which was due to neutral loss of the phosphoinositol group (Figure 7.8b). MS^3 of *m/z* 267 showed that the phosphoinositol group adducted water to form *m/z* 285, and further dissociated to *m/z* 169, 187 and 249, water loss (Figure 7.8c). Lastly, for the *m/z* 593 ion, Figures 7.8d,e display insets of the MS/MS spectrum with no scan delay and 1000 ms scan delay for water adduction. With 1000 ms scan delay the ion population shifts to higher *m/z* values due to water adduction. The water adduction characteristics of the product ions in the MS/MS and MS^3 spectra should be unique to the phosphoinositol headgroup stereochemistry and may even unique to the entire PI(8:0/8:0) molecule. Water adduction to *m/z* 187 should be compared to pure *myo*-inositol.

An ion corresponding to the proposed formula $[PI(8:0/8:0)-H+2Li]^+$ was detected at *m/z* 599 (Figure 7.8a), where the of 6 Da difference may be from removal of a proton and addition of a second lithium. The *m/z* 599 ion has different behavior than *m/z* 593 upon CID and water adduction, possibly adding another experiment to gain structural information (Figure 7.9). Only the phosphoinositol headgroup at *m/z* 273 (similar +6 Da, minus a hydrogen and add a lithium) and sequential water loss product ions were observed upon CID of *m/z* 599. CID-water adduction characteristics of both *m/z* 593 and 599 may prove useful for glycolipid structural elucidation.

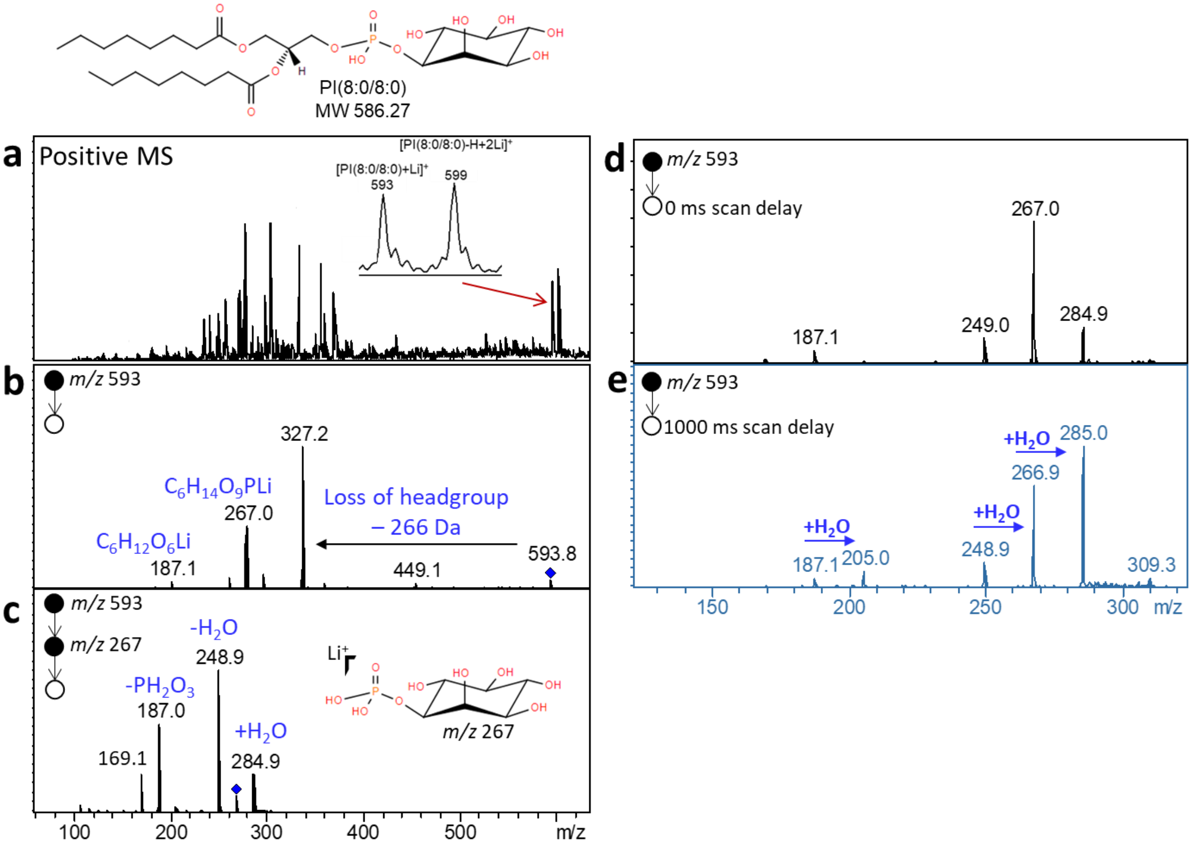

Figure 7.8 Full scan MS of PI(8:0/8:0) and CID-water adduction of *m/z* 593. a) Full scan mass spectrum of a solution containing PI(8:0/8:0), where *m/z* 593 and 599 correspond to [PI(8:0/8:0)+Li]$^+$ and, proposedly, [PI(8:0/8:0)-H+2Li]$^+$, respectively. b) MS/MS CID product ion spectrum of *m/z* 593. c) MS3 CID product ion spectrum of the lithium cationized phosphoinositol headgroup. d) Inset of the MS/MS CID spectrum of *m/z* 593 with no scan delay added. e) Inset of the MS/MS CID spectrum of *m/z* 593 with a 1000 ms scan delay added to allow more time for water adduction.

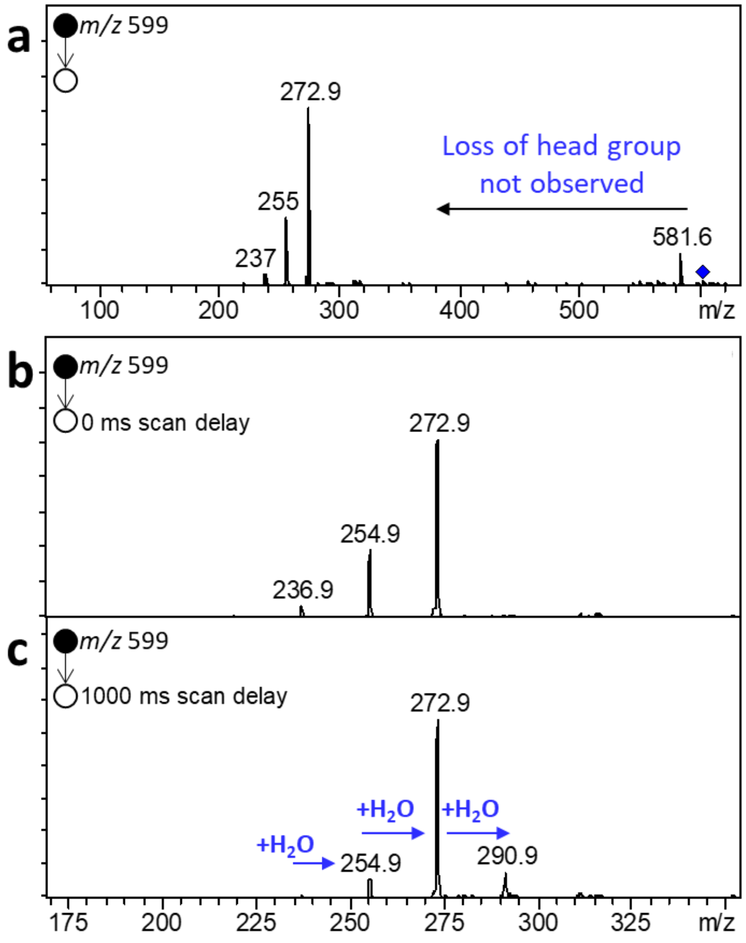

Figure 7.9 CID-water adduction of *m/z* 599 from PI(8:0/8:0). a) MS/MS CID product ion spectrum of *m/z* 599 which was proposed to be [PI(8:0/8:0)-H+2Li]$^+$. Insets of the MS/MS CID product ion spectrum at b) 0 ms scan delay and c) 1000 ms scan delay to allow more time for water adduction.

Next, solutions of 2 µg/mL GlcSph and GalSph were prepared in methanol/dichloromethane/water (50/45/5) with 100 µM LiAc and ionized by ESI. CID-water adduction experiments were used to differentiate the isomers GlcSph and GalSph. CID of [GlcSph+H]$^+$ and [GlcSph+H]$^+$ produced similar product ion spectra (Figure 7.10a,b, and CID of [GlcSph+Li]$^+$ and [GlcSph+Li]$^+$ also produced similar spectra (Figure 7.10c,d). Water adduction to the product ions was used to differentiate the two glycolipids.

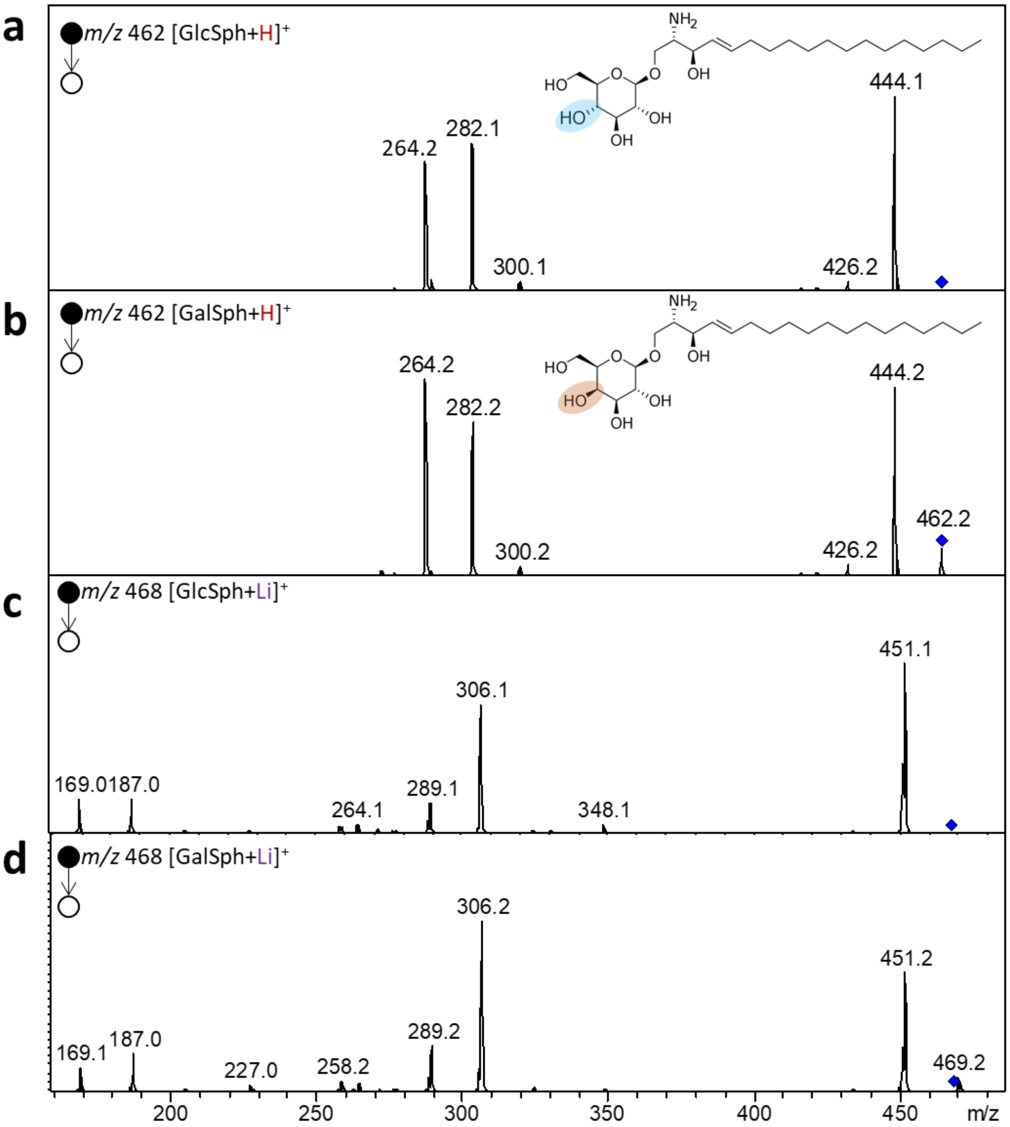

Figure 7.10 MS/MS product ion spectra of GlcSph and GalSph. Similar MS/MS product ion spectra were observed for protonated a) GlcSph and b) GalSph, and of lithium cationized c) GlcSph and d) GalSph. GlcSph has an equatorial hydroxyl group at the C4 position of the hexose, and GalSph has an axial hydroxyl group.

After CID of the lithium cationized GlcSph, or GalSph, the scan delay time can be varied for water adduction measurements of the hexose head moiety. The two isomers could be differentiated by the ratios of *m/z* 169, 187 and 205 product ions at the MS/MS level with various scan delay times for water adduction. After long or short scan delay times of 10 ms or 1000 ms (Figure 7.11) the ratios of product ions *m/z* 169, 187 and 205 could be used to differentiate GlcSph and GalSph. The *m/z* 169 ions can adduct water to *m/z* 187, and *m/z* 187 can adduct water to *m/z* 205. The MS peak area of each product ion was normalized to the *m/z* 187 peak area and plotted for both glycolipids.

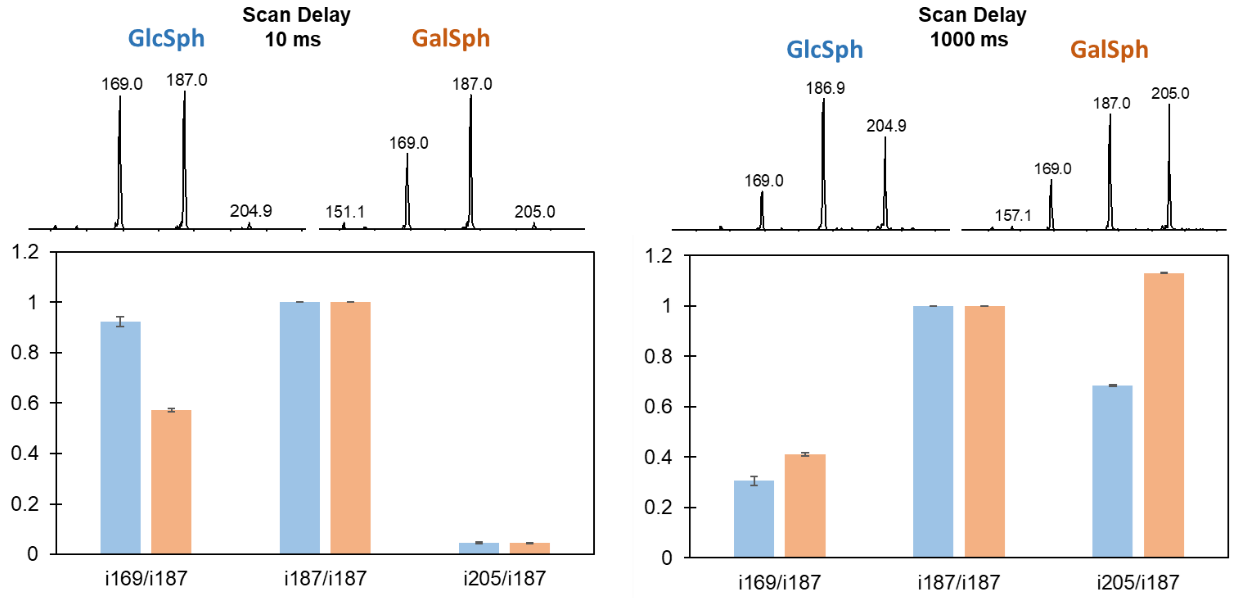

Figure 7.11 MS/MS level CID-water adduction product ion ratios for GlcSph and GalSph at (left) 10 ms and (right) 1000 ms delay times. All MS peak areas were normalized to the peak area of *m/z* 187.

At a short reaction time (10 ms scan delay) the ratio of 169 to 187 was different between GlcSph and GalSph, suggesting differences in dissociation and/or water adduction. The scan delay was incremented and as reaction time was increased, the population of product ions began to shift towards *m/z* 187 and *m/z* 205 as more ions adducted water molecules. At 1000 ms scan delay, the *m/z* 169 product ions are only unreacted ions, and the *m/z* 187 ion population consisted of unreacted *m/z* 187 or *m/z* 169 that adducted a water. The *m/z* 205 population consisted of *m/z* 187 ions plus water. GlcSph and GalSph product ion ratios were different at a 1000 ms scan delay due to differences in water adduction characteristics.

The types of Li-O coordinations and gas-phase structures that the hexose moieties assume after CID of the glycolipid can be probed by comparing CID-water adduction of glycolipids to pure hexose water adduction characteristics. More specifically, CID could be used to release the either the Glc or Gal hexose from GlcSph or GalSph, and subsequent isolation and water adduction (MS^3 experiment) for complete R_U and rate measurements. The R_U and reaction rates for GlcSph and GalSph hexose moieties can be compared to that of pure Glc and Gal. Similarities or differences of the R_U and reaction rate between the pure hexoses and glycolipid hexoses could hold information about ion structure.

These proof of principle experiments show that lithium cationization and CID-water adduction can be extended to glycolipid analysis. Two glycosphingosine isomers (GlcSph and GalSph) could be differentiated based on water adduction to the hexose moieties after CID. CID-water adduction was also shown to be amenable to phosphoinositide analysis using PI(8:0/8:0). Upon lithium cationization of PI(8:0/8:0), both $[PI(8:0/8:0)+Li]^+$ and $[PI(8:0/8:0)-H+2Li]^+$ were observed in the mass spectrum. Each ion type had unique CID characteristics, and water adduction to the phosphorylated inositol or inositol moieties could be used to differentiate isomeric inositol headgroups. Lithium cationization by ESI and CID-water adduction in an ion trap MS could prove useful for glycolipid structural elucidation.

REFERENCES

1. The Human Genome Project | NHGRI, https://www.genome.gov/human-genome-project
2. Wiśniewski, J.R., Zougman, A., Nagaraj, N., Mann, M.: Universal sample preparation method for proteome analysis. Nature Methods. 6, 359–362 (2009). https://doi.org/10.1038/nmeth.1322
3. Aebersold, R., Mann, M.: Mass-spectrometric exploration of proteome structure and function, (2016)
4. Nesvizhskii, A.I., Keller, A., Kolker, E., Aebersold, R.: A statistical model for identifying proteins by tandem mass spectrometry. Analytical Chemistry. 75, 4646–4658 (2003). https://doi.org/10.1021/ac0341261
5. Transforming Glycoscience. National Academies Press (2012)
6. Committee, N.R.C. (US): Transforming Glycoscience: A Roadmap for the Future. National Academies Press, Washington, DC (2012)
7. Ruhaak, L.R., Xu, G., Li, Q., Goonatilleke, E., Lebrilla, C.B.: Mass Spectrometry Approaches to Glycomic and Glycoproteomic Analyses. Chemical Reviews. acs.chemrev.7b00732 (2018). https://doi.org/10.1021/acs.chemrev.7b00732
8. Zhu, Y., Zajicek, J., Serianni, A.S.: Acyclic forms of [1-13C]aldohexoses in aqueous solution: Quantitation by 13C NMR and deuterium isotope effects on tautomeric equilibria. Journal of Organic Chemistry. 66, 6244–6251 (2001). https://doi.org/10.1021/jo010541m
9. Cremer, D., Pople, J.A.: A General Definition of Ring Puckering Coordinates. Journal of the American Chemical Society. 97, 1354–1358 (1975). https://doi.org/10.1021/ja00839a011
10. Mayes, H.B., Broadbelt, L.J., Beckham, G.T.: How sugars pucker: Electronic structure calculations map the kinetic landscape of five biologically paramount monosaccharides and their implications for enzymatic catalysis. Journal of the American Chemical Society. 136, 1008–1022 (2014). https://doi.org/10.1021/ja410264d
11. Williams, A.A., Darwanto, A., Theruvathu, J.A., Burdzy, A., Neidigh, J.W., Sowers, L.C.: Impact of sugar pucker on base pair and mispair stability. Biochemistry. 48, 11994–12004 (2009). https://doi.org/10.1021/bi9014133
12. Clay, M.C., Ganser, L.R., Merriman, D.K., Al-Hashimi, H.M.: Resolving sugar puckers in RNA excited states exposes slow modes of repuckering dynamics. Nucleic Acids Research. 45, (2017). https://doi.org/10.1093/nar/gkx525
13. Brisson, J.-R., Vinogradov, E., McNally, D.J., Khieu, N.H., Schoenhofen, I.C., Logan, S.M., Jarrell, H.: The application of NMR spectroscopy to functional glycomics. In: Methods in molecular biology (Clifton, N.J.). pp. 155–173. Humana Press (2010)

14. Duus, J.Ø., Gotfredsen, C.H., Bock, K.: Carbohydrate Structural Determination by NMR Spectroscopy: Modern Methods and Limitations †. Chemical Reviews. 100, 4589–4614 (2000). https://doi.org/10.1021/cr990302n

15. Drew, K.N., Zajicek, J., Bondo, G., Bose, B., Serianni, A.S.: 13C-labeled aldopentoses: Detection and quantitation of cyclic and acyclic forms by heteronuclear 1D and 2D NMR spectroscopy. (1998)

16. Veillon, L., Huang, Y., Peng, W., Dong, X., Cho, B.G., Mechref, Y.: Characterization of isomeric glycan structures by LC-MS/MS. ELECTROPHORESIS. 38, 2100–2114 (2017). https://doi.org/10.1002/elps.201700042

17. Zhou, S., Huang, Y., Dong, X., Peng, W., Veillon, L., Kitagawa, D.A.S., Aquino, A.J.A., Mechref, Y.: Isomeric Separation of Permethylated Glycans by Porous Graphitic Carbon (PGC)-LC-MS/MS at High Temperatures. Analytical Chemistry. 89, 6590–6597 (2017). https://doi.org/10.1021/acs.analchem.7b00747

18. Tang, Y., Wei, J., Costello, C.E., Lin, C.: Characterization of Isomeric Glycans by Reversed Phase Liquid Chromatography-Electronic Excitation Dissociation Tandem Mass Spectrometry. Journal of the American Society for Mass Spectrometry. 29, 1295–1307 (2018). https://doi.org/10.1007/s13361-018-1943-9

19. Yan, J., Shi, S., Wang, H., Liu, R., Li, N., Chen, Y., Wang, S.: Neutral monosaccharide composition analysis of plant-derived oligo- and polysaccharides by high performance liquid chromatography. Carbohydrate polymers. 136, 1273–80 (2016). https://doi.org/10.1016/j.carbpol.2015.10.028

20. Yan, J., Ding, J., Jin, G., Duan, Z., Yang, F., Li, D., Zhou, H., Li, M., Guo, Z., Chai, W., Liang, X.: Profiling of Human Milk Oligosaccharides for Lewis Epitopes and Secretor Status by Electrostatic Repulsion Hydrophilic Interaction Chromatography Coupled with Negative-Ion Electrospray Tandem Mass Spectrometry. Analytical Chemistry. (2019). https://doi.org/10.1021/acs.analchem.9b00687

21. Hetrick, E.M., Kramer, T.T., Risley, D.S.: Evaluation of a hydrophilic interaction liquid chromatography design space for sugars and sugar alcohols. Journal of Chromatography A. 1489, 65–74 (2017). https://doi.org/10.1016/J.CHROMA.2017.01.072

22. Ruiz-Matute, A.I., Hernández-Hernández, O., Rodríguez-Sánchez, S., Sanz, M.L., Martínez-Castro, I.: Derivatization of carbohydrates for GC and GC-MS analyses. Journal of Chromatography B: Analytical Technologies in the Biomedical and Life Sciences. 879, 1226–1240 (2011). https://doi.org/10.1016/j.jchromb.2010.11.013

23. May, J.C., McLean, J.A.: Ion Mobility-Mass Spectrometry: Time-Dispersive Instrumentation. Analytical Chemistry. 87, 1422–1436 (2015). https://doi.org/10.1021/ac504720m

24. Gray, C.J., Thomas, B., Upton, R., Migas, L.G., Eyers, C.E., Barran, P.E., Flitsch, S.L.: Applications of ion mobility mass spectrometry for high throughput, high resolution

glycan analysis. Biochimica et Biophysica Acta - General Subjects. 1860, 1688–1709 (2016). https://doi.org/10.1016/j.bbagen.2016.02.003

25. Nagy, G., Attah, I.K., Garimella, S.V.B., Tang, K., Ibrahim, Y.M., Baker, E.S., Smith, R.D.: Unraveling the isomeric heterogeneity of glycans: ion mobility separations in structures for lossless ion manipulations. Chemical Communications. (2018). https://doi.org/10.1039/C8CC06966B

26. Zheng, X., Zhang, X., Schocker, N.S., Renslow, R.S., Orton, D.J., Khamsi, J., Ashmus, R.A., Almeida, I.C., Tang, K., Costello, C.E., Smith, R.D., Michael, K., Baker, E.S.: Enhancing glycan isomer separations with metal ions and positive and negative polarity ion mobility spectrometry-mass spectrometry analyses. Analytical and Bioanalytical Chemistry. 409, 467–476 (2017). https://doi.org/10.1007/s00216-016-9866-4

27. McLuckey, S.A., Goeringer, D.E.: SPECIAL FEATURE:TUTORIAL Slow Heating Methods in Tandem Mass Spectrometry. Journal of Mass Spectrometry. 32, 461–474 (1997). https://doi.org/10.1002/(SICI)1096-9888(199705)32:5<461::AID-JMS515>3.0.CO;2-H

28. Asam, M.R., Glish, G.L.: Tandem mass spectrometry of alkali cationized polysaccharides in a quadrupole ion trap. Journal of the American Society for Mass Spectrometry. 8, 987–995 (1997). https://doi.org/10.1016/S1044-0305(97)00124-4

29. Gray, C.J., Schindler, B., Migas, L.G., Pičmanová, M., Allouche, A.R., Green, A.P., Mandal, S., Motawia, M.S., Sánchez-Pérez, R., Bjarnholt, N., Møller, B.L., Rijs, A.M., Barran, P.E., Compagnon, I., Eyers, C.E., Flitsch, S.L.: Bottom-Up Elucidation of Glycosidic Bond Stereochemistry. Analytical Chemistry. 89, 4540–4549 (2017). https://doi.org/10.1021/acs.analchem.6b04998

30. Kolli, V., Dodds, E.D.: Energy-resolved collision-induced dissociation pathways of model N-linked glycopeptides: Implications for capturing glycan connectivity and peptide sequence in a single experiment. Analyst. 139, 2144–2153 (2014). https://doi.org/10.1039/c3an02342g

31. Hofmeister, G.E., Zhou, Z., J.A., L.: Linkage position determination in lithium-cationized disaccharides: Tandem mass spectrometry and semiempirical calculations. Journal of American Chemical Society. 113, 5964–5970 (1991). https://doi.org/10.1021/ja00016a007

32. Bythell, B.J., Abutokaikah, M.T., Wagoner, A.R., Guan, S., Rabus, J.M.: Cationized Carbohydrate Gas-Phase Fragmentation Chemistry. Journal of the American Society for Mass Spectrometry. 28, 688–703 (2017). https://doi.org/10.1007/s13361-016-1530-x

33. Abutokaikah, M.T., Frye, J.W., Tschampel, J., Rabus, J.M., Bythell, B.J.: Fragmentation Pathways of Lithiated Hexose Monosaccharides. Journal of The American Society for Mass Spectrometry. 29, 1627–1637 (2018). https://doi.org/10.1007/s13361-018-1973-3

34. Bythell, B.J., Rabus, J.M., Wagoner, A.R., Abutokaikah, M.T., Maître, P.: Sequence Ion Structures and Dissociation Chemistry of Deprotonated Sucrose Anions. Journal of The

American Society for Mass Spectrometry. (2018). https://doi.org/10.1007/s13361-018-2065-0

35. Adamson, J.T., Håkansson, K.: Infrared multiphoton dissociation and electron capture dissociation of high-mannose type glycopeptides. Journal of Proteome Research. 5, 493–501 (2006). https://doi.org/10.1021/pr0504081

36. Khatri, K., Pu, Y., Klein, J.A., Wei, J., Costello, C.E., Lin, C., Zaia, J.: Comparison of Collisional and Electron-Based Dissociation Modes for Middle-Down Analysis of Multiply Glycosylated Peptides. Journal of the American Society for Mass Spectrometry. 29, 1075–1085 (2018). https://doi.org/10.1007/s13361-018-1909-y

37. Guttman, M., Scian, M., Lee, K.K.: Tracking hydrogen/deuterium exchange at glycan sites in glycoproteins by mass spectrometry. Analytical chemistry. 83, 7492–7499 (2011). https://doi.org/10.1021/ac201729v

38. Kostyukevich, Y., Kononikhin, A., Popov, I., Nikolaev, E.: In-ESI source hydrogen/deuterium exchange of carbohydrate ions. Analytical Chemistry. 86, 2595–2600 (2014). https://doi.org/10.1021/ac4038202

39. Uppal, S.S., Beasley, S.E., Scian, M., Guttman, M.: Gas-Phase Hydrogen/Deuterium Exchange for Distinguishing Isomeric Carbohydrate Ions. Analytical Chemistry. 89, 4737–4742 (2017). https://doi.org/10.1021/acs.analchem.7b00683

40. Liyanage, O.T., Quintero, A. V., Hatvany, J.B., Gallagher, E.S.: Distinguishing Carbohydrate Isomers with Rapid Hydrogen/Deuterium Exchange-Mass Spectrometry. Journal of the American Society for Mass Spectrometry. 22, jasms.0c00314 (2020). https://doi.org/10.1021/jasms.0c00314

41. Madhusudanan, K.P.: Tandem mass spectra of ammonium adducts of monosaccharides: Differentiation of diastereomers. Journal of Mass Spectrometry. 41, 1096–1104 (2006). https://doi.org/10.1002/jms.1085

42. Zhu, X., Sato, T.: The distinction of underivatized monosaccharides using electrospray ionization ion trap mass spectrometry. Rapid Communications in Mass Spectrometry. 21, 191–198 (2007). https://doi.org/10.1002/rcm.2825

43. Fouquet, T., Charles, L.: Distinction and quantitation of sugar isomers in ternary mixtures using the kinetic method. Journal of the American Society for Mass Spectrometry. 21, 60–7 (2010). https://doi.org/10.1016/j.jasms.2009.09.002

44. Nagy, G., Pohl, N.L.B.: Monosaccharide Identifcation as a First Step toward de Novo Carbohydrate sequencing: Mass Spectrometry Strategy for the Identifcation and Differentiation of Diastereomic and Enantiomeric Pentose Isomers. Anal Chem. 87, 4566–4571 (2015). https://doi.org/10.1021/acs.analchem.5b00760

45. Nagy, G., Pohl, N.L.B.: Complete hexose isomer identification with mass spectrometry. Journal of the American Society for Mass Spectrometry. 26, 677–85 (2015). https://doi.org/10.1007/s13361-014-1072-z

46. Campbell, M.T., Chen, D., Glish, G.L.: Identifying the D-Pentoses Using Water Adduction to Lithium Cationized Molecule. Journal of The American Society for Mass Spectrometry. 28, 1420–1424 (2017). https://doi.org/10.1007/s13361-017-1656-5

47. Campbell, M.T., Chen, D., Wallbillich, N.J., Glish, G.L.: Distinguishing Biologically Relevant Hexoses by Water Adduction to the Lithium-Cationized Molecule. Analytical Chemistry. 89, 10504–10510 (2017). https://doi.org/10.1021/acs.analchem.7b02647

48. Campbell, M.T.: DISTINGUISHING CARBOHYDRATE ISOMERS WITH ION-MOLECULE REACTIONS AND INSIGHTS INTO METAL CATIONIZATION, (2018)

49. Campbell, M.T., Chen, D., Glish, G.L.: Distinguishing Linkage Position and Anomeric Configuration of Glucose–Glucose Disaccharides by Water Adduction to Lithiated Molecules. Analytical Chemistry. 90, 2048–2054 (2018). https://doi.org/10.1021/acs.analchem.7b04162

50. Williams, J.D., Cox, K.A., Cooks, R.G., McLuckey, S.A., Hart, K.J., Goeringer, D.E.: Resonance Ejection Ion Trap Mass Spectrometry and Nonlinear Field Contributions: The Effect of Scan Direction on Mass Resolution. Analytical Chemistry. 66, 725–729 (1994)

51. Son, M.H., Graham Cooks, R.: Selective Injection and Isolation of Ions in Quadrupole Ion Trap Mass Spectrometry Using Notched Waveforms Created Using the Inverse Fourier Transform. Wiley (1994)

52. Guan, S., Marshall, A.G.: Stored waveform inverse Fourier transform axial excitation/ejection for quadrupole ion trap mass spectrometry. Analytical Chemistry. 65, 1288–1294 (1993). https://doi.org/10.1021/ac00057a029

53. Guan, S., Marshall, A.G.: Stored Waveform Inverse Fourier Transform (SWIFT) Ion Excitation in Trapped-Ion Mass Spectrometry: Theory and Applications. International Journal of Mass Spectrometry and Ion Processes. 157/158, 5–37 (1996)

54. Graham Cooks, R., Patrick, J.S., Kotiaho, T., McLuckey, S.A.: Thermochemical determinations by the kinetic method. Mass Spectrometry Reviews. 13, 287–339 (1994). https://doi.org/10.1002/mas.1280130402

55. Cooks, R.G., Koskinen, J.T., Thomas, P.D.: The kinetic method of making thermochemical determinations. Journal of Mass Spectrometry. 34, 85–92 (1999). https://doi.org/10.1002/(SICI)1096-9888(199902)34:2<85::AID-JMS795>3.0.CO;2-#

56. Ujma, J., Ropartz, D., Giles, K., Richardson, K., Langridge, D., Wildgoose, J., Green, M., Pringle, S.: Cyclic Ion Mobility Mass Spectrometry Distinguishes Anomers and Open-Ring Forms of Pentasaccharides. Journal of the American Society for Mass Spectrometry. (2019). https://doi.org/10.1007/s13361-019-02168-9

57. Ropartz, D., Fanuel, M., Ujma, J., Palmer, M., Giles, K., Rogniaux, H.: Structure Determination of Large Isomeric Oligosaccharides of Natural Origin through Multipass and Multistage Cyclic Traveling-Wave Ion Mobility Mass Spectrometry. Analytical Chemistry. 91, 12030–12037 (2019). https://doi.org/10.1021/acs.analchem.9b03036

58. Frisch, M.J., Trucks, G.W., Schlegel, H.B., Scuseria, G.E., Robb, M.A., Cheeseman, J.R., Scalmani, G., Barone, V., Mennucci, B., Petersson, G.A.: Gaussian 09, Revision D. 01; Gaussian: Wallingford, CT, USA, 2009. There is no corresponding record for this reference. (2009)

59. Becke, A.D.: A new mixing of Hartree-Fock and local density-functional theories. The Journal of Chemical Physics. 98, 1372–1377 (1993). https://doi.org/10.1063/1.464304

60. Stephens, P.J., Devlin, F.J., Chabalowski, C.F., Frisch, M.J.: Ab Initio calculation of vibrational absorption and circular dichroism spectra using density functional force fields. Journal of Physical Chemistry®. 98, 11623–11627 (1994). https://doi.org/10.1021/j100096a001

61. Mayes, H.B., Tian, J., Nolte, M.W., Shanks, B.H., Beckham, G.T., Gnanakaran, S., Broadbelt, L.J.: Sodium ion interactions with aqueous glucose: Insights from quantum mechanics, molecular dynamics, and experiment. Journal of Physical Chemistry B. 118, 1990–2000 (2014). https://doi.org/10.1021/jp409481f

62. Angyal, S.J.: Complexes of Sugars with Cations. Advances in Chemistry, ACS. 17, 32 (1973)

63. Bose-Basu, B., Zhang, W., Kennedy, J.L.W., Hadad, M.J., Carmichael, I., Serianni, A.S.: 13C-Labeled Idohexopyranosyl Rings: Effects of Methyl Glycosidation and C6 Oxidation on Ring Conformational Equilibria. Journal of Organic Chemistry. 82, 1356–1370 (2017). https://doi.org/10.1021/acs.joc.6b02399

64. Crawford, T., Glish, G.L.: Distinguishing Unique Structures of Hexoses using Differential Ion Mobility Spectrometry-Mass Spectrometry. In: Poster presented at the American Society for Mass Spectrometry Annual Conference. June 2020. University of North Carolina at Chapel Hill (2020)

65. Siddiqui, N., Singh, V., Deshmukh, M.M., Gurunath, R.: Structures, stability and hydrogen bonding in inositol conformers. Physical Chemistry Chemical Physics. 17, 18514–18523 (2015). https://doi.org/10.1039/c5cp02690c

66. Baercor, T., Mayerfn, P.M.: Statistical Rice-Ramsperger-Kassel-Marcus quasiequilibrium theory calculations in mass spectrometry. Journal of the American Society for Mass Spectrometry. 8, 103–115 (1997). https://doi.org/10.1016/S1044-0305(96)00212-7

67. Crawford, T., Glish, G.L.: Influence of Electrospray and Nanoelectrospray on Lithiated Monosaccharide Homodimer Structures Monitored by Differential Ion Mobility Spectrometry - Mass Spectrometry Introduction ESI vs nESI with Transport Gas Modifiers High and Low Energy Optics. In: Poster presented at the American Society for Mass Spectrometry Annual Conference. June 2019. Atlanta, GA. University of North Carolina at Chapel Hill (2019)

68. Nagy, G., Pohl, N.L.B.: Monosaccharide identification as a first step toward de novo carbohydrate sequencing: Mass spectrometry strategy for the identification and

differentiation of diastereomeric and enantiomeric pentose isomers. Analytical Chemistry. 87, 4566–4571 (2015). https://doi.org/10.1021/acs.analchem.5b00760

69. Wooke, Z., Nagy, G., Barnes, L.F., Pohl, N.L.B.: Development of a Post-Column Liquid Chromatographic Chiral Addition Method for the Separation and Resolution of Common Mammalian Monosaccharides. Journal of The American Society for Mass Spectrometry. 419–425 (2018). https://doi.org/10.1007/s13361-018-2095-7

70. Sannes-Lowery, K., Griffey, R.H., Kruppa, G.H., Speir, J.P., Hofstadler, S.A.: Multipole Storage Assisted Dissociation, A Novel In-Source Dissociation Technique for Electrospray Ionization Generated Ions. Rapid Communications in Mass Spectrometry. 12, 1957–1961 (1998)

71. Sannes-Lowery, K.A., Hofstadler, S.A.: Characterization of multipole storage assisted dissociation: Implications for electrospray ionization mass spectrometry characterization of biomolecules. Journal of the American Society for Mass Spectrometry. 11, 1–9 (2000). https://doi.org/10.1016/S1044-0305(99)00110-5

72. Håkansson, K., Axelsson, J., Palmblad, M., Håkansson, P.: Mechanistic Studies of Multipole Storage Assisted Dissociation. Journal of the American Society for Mass Spectrometry. 11, 210–217 (2000)

73. Wu, X., Oleschuk, R.D., Cann, N.M.: Characterization of microstructured fibre emitters: in pursuit of improved nano electrospray ionization performance. The Analyst. 137, 4150 (2012). https://doi.org/10.1039/c2an35249d

74. Konermann, L., Ahadi, E., Rodriguez, A.D., Vahidi, S.: Unraveling the mechanism of electrospray ionization. Analytical Chemistry. 85, 2–9 (2013). https://doi.org/10.1021/ac302789c

75. Musah, R.A., Cody, R.B., Domin, M.A., Lesiak, A.D., Dane, A.J., Shepard, J.R.E.: DART-MS in-source collision induced dissociation and high mass accuracy for new psychoactive substance determinations. Forensic Science International. 244, 42–49 (2014). https://doi.org/10.1016/j.forsciint.2014.07.028

76. Lee, S.H., Choi, D.W.: Comparison between Source-induced Dissociation and Collision-induced Dissociation of Ampicillin, Chloramphenicol, Ciprofloxacin, and Oxytetracycline via Mass Spectrometry. Toxicol. Res. 29, 107–114 (2013). https://doi.org/10.5487/TR.2013.29.2.107

77. Breuker, K., McLafferty, F.W.: Stepwise evolution of protein native structure with electrospray into the gas phase, 10-12 to 102 s. Proceedings of the National Academy of Sciences. 105, 18145–18152 (2008). https://doi.org/10.1073/pnas.0807005105

78. Silveira, J.A., Clemmer, D.E., Servage, K.A., Pierson, N.A., Fort, K.L., Kim, D., Russell, D.H.: From Solution to the Gas Phase: Stepwise Dehydration and Kinetic Trapping of Substance P Reveals the Origin of Peptide Conformations. Journal of the American Chemical Society. 135, 19147–19153 (2013). https://doi.org/10.1021/ja4114193

79. Dixit, S.M., Polasky, D.A., Ruotolo, B.T.: Collision induced unfolding of isolated proteins in the gas phase: past, present, and future. Current Opinion in Chemical Biology. 42, 93–100 (2018). https://doi.org/10.1016/j.cbpa.2017.11.010

80. Warnke, S., Seo, J., Boschmans, J., Sobott, F., Scrivens, J.H., Bleiholder, C., Bowers, M.T., Gewinner, S., Schöllkopf, W., Pagel, K., von Helden, G.: Protomers of Benzocaine: Solvent and Permittivity Dependence. Journal of the American Chemical Society. 137, 4236–4242 (2015). https://doi.org/10.1021/jacs.5b01338

81. Xia, H., Attygalle, A.B.: Untrapping Kinetically Trapped Ions: The Role of Water Vapor and Ion-Source Activation Conditions on the Gas-Phase Protomer Ratio of Benzocaine Revealed by Ion-Mobility Mass Spectrometry. Journal of the American Society for Mass Spectrometry. 28, 2580–2587 (2017). https://doi.org/10.1007/s13361-017-1806-9

82. Patrick, A.L., Cismesia, A.P., Tesler, L.F., Polfer, N.C.: Effects of ESI conditions on kinetic trapping of the solution-phase protonation isomer of p-aminobenzoic acid in the gas phase. International Journal of Mass Spectrometry. 418, 148–155 (2017). https://doi.org/10.1016/j.ijms.2016.09.022

83. Bruins, A.P.: Mechanistic aspects of electrospray ionization. Journal of Chromatography A. 794, 345–357 (1998). https://doi.org/10.1016/S0021-9673(97)01110-2

84. Cech, N.B., Enke, C.G.: Practical implications of some recent studies in electrospray ionization fundamentals. Mass Spectrometry Reviews. 20, 362–387 (2002). https://doi.org/10.1002/mas.10008

85. March, R.E.E.: An introduction to quadrupole ion trap mass spectrometry. Journal of Mass Spectrometry. 32, 351–369 (1997). https://doi.org/10.1002/(SICI)1096-9888(199704)32:4<351::AID-JMS512>3.0.CO;2-Y

86. COOKS, R.G., GLISH, G.L., MCLUCKEY, S.A., Kaiser, R.E.: Ion Trap Mass Spectrometry. Chemical and Engineering News. 69, 26–41 (1991). https://doi.org/10.1021/cen-v069n012.p026

87. March, R.E.: Quadrupole ion trap mass spectrometry: Theory, simulation, recent developments and applications. Rapid Communications in Mass Spectrometry. 12, 1543–1554 (1998)

88. McLuckey, S.A.S.A., Goeringer, D.E.D.E., Glish, G.L.G.L.: Selective ion isolation/rejection over a broad mass range in the quadrupole ion trap. Journal of the American Society for Mass Spectrometry. 2, 11–21 (1991). https://doi.org/10.1016/1044-0305(91)80056-D

89. Soni, M.H., Cooks, R.G.: Selective Injection and Isolation of Ions in Quadrupole Ion Trap Mass Spectrometry Using Notched Waveforms Created Using the Inverse Fourier Transform. Analytical Chemistry. 66, 2488–2496 (1994). https://doi.org/10.1021/ac00087a013

90. Hilger, R.T., Santini, R.E., Luongo, C.A., Prentice, B.M., McLuckey, S.A.: A method for isolating ions in quadrupole ion traps using an excitation waveform generated by

frequency modulation and mixing. International Journal of Mass Spectrometry. 377, 329–337 (2015). https://doi.org/10.1016/j.ijms.2014.06.029

91. Snyder, D.T., Cooks, R.G.: Ion Isolation in a Linear Ion Trap Using Dual Resonance Frequencies. Journal of the American Society for Mass Spectrometry. 27, 1906–1913 (2016). https://doi.org/10.1007/s13361-016-1494-x

92. Michelmann, K., Silveira, J.A., Ridgeway, M.E., Park, M.A.: Fundamentals of trapped ion mobility spectrometry. Journal of the American Society for Mass Spectrometry. 26, 14–24 (2014). https://doi.org/10.1007/s13361-014-0999-4

93. Stow, S.M., Causon, T.J., Zheng, X., Kurulugama, R.T., Mairinger, T., May, J.C., Rennie, E.E., Baker, E.S., Smith, R.D., McLean, J.A., Hann, S., Fjeldsted, J.C.: An Interlaboratory Evaluation of Drift Tube Ion Mobility-Mass Spectrometry Collision Cross Section Measurements. Analytical Chemistry. 89, 9048–9055 (2017). https://doi.org/10.1021/acs.analchem.7b01729

94. Larriba, C., Hogan, C.J.: Ion mobilities in diatomic gases: Measurement versus prediction with non-specular scattering models. Journal of Physical Chemistry A. 117, 3887–3901 (2013). https://doi.org/10.1021/jp312432z

95. Shrivastav, V., Nahin, M., Hogan, C.J., Larriba-Andaluz, C.: Benchmark Comparison for a Multi-Processing Ion Mobility Calculator in the Free Molecular Regime. J. Am. Soc. Mass Spectrom. (2017). https://doi.org/10.1007/s13361-017-1661-8

96. Zhu, F., Glover, M.S., Shi, H., Trinidad, J.C., Clemmer, D.E.: Populations of Metal-Glycan Structures Influence MS Fragmentation Patterns. J. Am. Soc. Mass Spectrom. 26, 25–35 (2015). https://doi.org/10.1007/s13361-014-1000-2

97. Huynh, H.T., Phan, H.T., Hsu, P.J., Chen, J.L., Nguan, H.S., Tsai, S.T., Roongcharoen, T., Liew, C.Y., Ni, C.K., Kuo, J.L.: Collision-induced dissociation of sodiated glucose, galactose, and mannose, and the identification of anomeric configurations. Physical Chemistry Chemical Physics. 20, 19614–19624 (2018). https://doi.org/10.1039/c8cp03753a

98. Migas, L.G., Gray, C.J., Flitsch, S.L., Barran, P.E.: A Careful Consideration of the Influence of Structure, Partial charges and Basis Sets on Collision Cross Sections of Monosaccharides when Comparing Values from DFT Calculated Conformers to those Obtained Experimentally. 6–31 (2017). https://doi.org/10.1101/162305

99. Zheng, X., Aly, N.A., Zhou, Y., Dupuis, K.T., Bilbao, A., Paurus, V.L.L., Orton, D.J., Wilson, R., Payne, S.H., Smith, R.D., Baker, E.S.: A structural examination and collision cross section database for over 500 metabolites and xenobiotics using drift tube ion mobility spectrometry. Chem. Sci. 8, 7724–7736 (2017). https://doi.org/10.1039/C7SC03464D

100. Chen, J.-L., Nguan, H.S., Hsu, P.-J., Tsai, S.-T., Liew, C.Y., Kuo, J.-L., Hu, W.-P., Ni, C.-K.: Collision-induced dissociation of sodiated glucose and identification of anomeric

configuration. Physical Chemistry Chemical Physics. 19, 15454–15462 (2017). https://doi.org/10.1039/C7CP02393F

101. Srisa-nga, S., Flood, A.E.: Mutarotation Rates and Equilibrium of Simple Carbohydrates. (2004)

102. Fox, P.F., Uniacke-Lowe, T., McSweeney, P.L.H., O'Mahony, J.A.: Dairy chemistry and biochemistry, second edition. (2015)

103. Jawad, R., Elleman, C., Vermeer, L., Drake, A.F., Woodhead, B., Martin, G.P., Royall, P.G.: The measurement of the β/α anomer composition within amorphous lactose prepared by spray and freeze drying using a simple 1H-NMR method. Pharmaceutical Research. 29, 511–524 (2012). https://doi.org/10.1007/s11095-011-0575-6

104. Yu, X., Jiang, Y., Chen, Y., Huang, Y., Costello, C.E., Lin, C.: Detailed Glycan Structural Characterization by Electronic Excitation Dissociation. Anal. Chem. 85, (2013). https://doi.org/10.1021/ac402886q

105. Tang, Y., Pu, Y., Gao, J., Hong, P., Costello, C.E., Lin, C.: De Novo Glycan Sequencing by Electronic Excitation Dissociation and Fixed-Charge Derivatization. Analytical Chemistry. 90, 3793–3801 (2018). https://doi.org/10.1021/acs.analchem.7b04077

106. Rabus, J.M., Abutokaikah, M.T., Ross, R.T., Bythell, B.J.: Sodium-cationized carbohydrate gas-phase fragmentation chemistry: influence of glycosidic linkage position †. Phys. Chem. Chem. Phys. 19, 25643 (2017). https://doi.org/10.1039/c7cp04738j

107. Rabus, J.M., Simmons, D.R., Maître, P., Bythell, B.J.: Deprotonated carbohydrate anion fragmentation chemistry: Structural evidence from tandem mass spectrometry, infra-red spectroscopy, and theory. Physical Chemistry Chemical Physics. 20, 27897–27909 (2018). https://doi.org/10.1039/c8cp02620c

108. Hsu, H.C., Liew, C.Y., Huang, S.P., Tsai, S.T., Ni, C.K.: Simple method for de novo structural determination of underivatised glucose oligosaccharides. Scientific Reports. 8, 5562 (2018). https://doi.org/10.1038/s41598-018-23903-4

109. Hsu, H.C., Liew, C.Y., Huang, S.-P., Tsai, S.-T., Ni, C.-K.: Simple Approach for De Novo Structural Identification of Mannose Trisaccharides. https://doi.org/10.1007/s13361-017-1850-5

110. Tsai, S.T., Chen, J.L., Ni, C.K.: Does low-energy collision-induced dissociation of lithiated and sodiated carbohydrates always occur at anomeric carbon of the reducing end? Rapid Communications in Mass Spectrometry. 31, 1835–1844 (2017). https://doi.org/10.1002/rcm.7961

111. Shen, Y.-H., Tsai, S.-T., Liew, C.Y., Ni, C.-K.: Mass spectrometry-based identification of carbohydrate anomeric configuration to determine the mechanism of glycoside hydrolases. Carbohydrate Research. (2019). https://doi.org/10.1016/j.carres.2019.03.004

112. Chiu, C.C., Huynh, H.T., Tsai, S.T., Lin, H.Y., Hsu, P.J., Phan, H.T., Karumanthra, A., Thompson, H., Lee, Y.C., Kuo, J.L., Ni, C.K.: Toward Closing the Gap between Hexoses

and N-Acetlyhexosamines: Experimental and Computational Studies on the Collision-Induced Dissociation of Hexosamines. Journal of Physical Chemistry A. 123, 6683–6700 (2019). https://doi.org/10.1021/acs.jpca.9b04143

113. Mookherjee, A., Uppal, S.S., Guttman, M.: Dissection of Fragmentation Pathways in Protonated N-Acetylhexosamines. Analytical Chemistry. 90, 11883–11891 (2018). https://doi.org/10.1021/acs.analchem.8b01963

114. Voss, J.M., Kregel, S.J., Fischer, K.C., Garand, E.: IR-IR Conformation Specific Spectroscopy of Na + (Glucose) Adducts. Journal of the American Society for Mass Spectrometry. 29, 42–50 (2018). https://doi.org/10.1007/s13361-017-1813-x

115. Jiang, W., Wysocki, V.H., Dodds, E.D., Miesfeld, R.L., Scaraffia, P.Y.: Differentiation and quantification of C1 and C2 13 C-labeled glucose by tandem mass spectrometry. Analytical Biochemistry. 404, 40–44 (2010). https://doi.org/10.1016/j.ab.2010.04.035

116. Yost, R.A., Enke, C.G., McGilvery, D.C., Smith, D., Morrison, J.D.: High efficiency collision-induced dissociation in an RF-only quadrupole. International Journal of Mass Spectrometry and Ion Physics. 30, 127–136 (1979). https://doi.org/10.1016/0020-7381(79)80090-X

117. Chen, J.L., Nguan, H.S., Hsu, P.J., Tsai, S.T., Liew, C.Y., Kuo, J.L., Hu, W.P., Ni, C.K.: Collision-induced dissociation of sodiated glucose and identification of anomeric configuration. Physical Chemistry Chemical Physics. 19, 15454–15462 (2017). https://doi.org/10.1039/c7cp02393f

118. Van Den Steen, P., Rudd, P.M., Dwek, R.A., Opdenakker, G.: Concepts and principles of O-linked glycosylation. Critical Reviews in Biochemistry and Molecular Biology. 33, 151–208 (1998). https://doi.org/10.1080/10409239891204198

119. Helenius, A., Aebi, M.: Intracellular functions of N-linked glycans. (2001)

120. Rudd, P.M., Wormald, M.R., Dwek, R.A.: Glycosylation and the immune system. (2001)

121. Ohtsubo, K., Marth, J.D.: Glycosylation in Cellular Mechanisms of Health and Disease, (2006)

122. Ryan Flynn, A.A., Pedram, K., Malaker, S.A., Villalta, P.W., Carette, J.E., Bertozzi Correspondence, C.R., Flynn, R.A., Batista, P.J., Smith, B.A., Johnson, A.G., George, B.M., Majzoub, K., Bertozzi, C.R.: Small RNAs are modified with N-glycans and displayed on the surface of living cells In brief Identification of stable mammalian RNAs decorated with glycan structures opens up a new dimension for regulatory control of RNA localization and function by post-transcriptional modification. Small RNAs are modified with N-glycans and displayed on the surface of living cells. Cell. 184, 1–16 (2021). https://doi.org/10.1016/j.cell.2021.04.023

123. Sun, S., Huang, C., Wang, Y., Liu, Y., Zhang, J., Zhou, J., Gao, F., Yang, F., Chen, R., Mulloy, B., Chai, W., Li, Y., Bu, D.: Toward Automated Identification of Glycan Branching Patterns Using Multistage Mass Spectrometry with Intelligent Precursor Selection. Anal. Chem. 21, 1 (2018). https://doi.org/10.1021/acs.analchem.8b03967

124. Mechref, Y.: Use of CID/ETD Mass Spectrometry to Analyze Glycopeptides. Current Protocols in Protein Science. 68, (2012). https://doi.org/10.1002/0471140864.ps1211s68

125. Ceroni, A., Maass, K., Geyer, H., Geyer, R., Dell, A., Haslam, S.M.: GlycoWorkbench: A tool for the computer-assisted annotation of mass spectra of glycans. Journal of Proteome Research. 7, 1650–1659 (2008). https://doi.org/10.1021/pr7008252

126. Campbell, M.P., Peterson, R., Mariethoz, J., Gasteiger, E., Akune, Y., Aoki-Kinoshita, K.F., Lisacek, F., Packer, N.H.: UniCarbKB: Building a knowledge platform for glycoproteomics. Nucleic Acids Research. 42, (2014). https://doi.org/10.1093/nar/gkt1128

127. Horlacher, O., Jin, C., Alocci, D., Mariethoz, J., Müller, M., Karlsson, N.G., Lisacek, F.: Glycoforest 1.0. Analytical Chemistry. 89, 10932–10940 (2017). https://doi.org/10.1021/acs.analchem.7b02754

128. Kumozaki, S., Sato, K., Sakakibara, Y.: A Machine Learning Based Approach to de novo Sequencing of Glycans from Tandem Mass Spectrometry Spectrum. In: IEEE/ACM Transactions on Computational Biology and Bioinformatics. pp. 1267–1274. Institute of Electrical and Electronics Engineers Inc. (2015)

129. Hong, P., Sun, H., Sha, L., Pu, Y., Khatri, K., Yu, X., Tang, Y., Lin, C.: GlycoDeNovo – an Efficient Algorithm for Accurate de novo Glycan Topology Reconstruction from Tandem Mass Spectra. J. Am. Soc. Mass Spectrom. 28, 2288–2301 (2017). https://doi.org/10.1007/s13361-017-1760-6

130. Ju, F., Zhang, J., Bu, D., Li, Y., Zhou, J., Wang, H., Wang, Y., Huang, C., Sun, S.: De novo glycan structural identification from mass spectra using tree merging strategy. Computational Biology and Chemistry. 80, 217–224 (2019). https://doi.org/10.1016/j.compbiolchem.2019.03.015

131. Varmuza, K.: Pattern recognition in analytical chemistry. (1980)

132. Curry, B., Center, S.S., Rumelhart, D.E.: MSnet: A Neural Network That Classifies Mass Spectra. (1990)

133. Justice, J.B., Isenhour, T.L.: Information Content of Mass Spectra as Determined by Pattern Recognition Methods. (1974)

134. Walker, S.W.C.C., Anwar, A., Psutka, J.M., Crouse, J., Liu, C., Le Blanc, J.C.Y.Y., Montgomery, J., Goetz, G.H., Janiszewski, J.S., Campbell, J.L., Hopkins, W.S.: Determining molecular properties with differential mobility spectrometry and machine learning. Nature Communications. 9, 5096 (2018). https://doi.org/10.1038/s41467-018-07616-w

135. Shvartsburg, A.A.: Differential Ion Mobility Spectrometry. CRC Press, Boca Raton (2008)

136. Li, H., Giles, K., Bendiak, B., Kaplan, K., Siems, W.F., Hill, H.H.: Resolving Structural Isomers of Monosaccharide Methyl Glycosides Using Drift Tube and Traveling Wave Ion Mobility Mass Spectrometry. Anal. Chem. 84, 3231–3239 (2012). https://doi.org/10.1021/ac203116a

137. Bou Khalil, M., Hou, W., Zhou, H., Elisma, F., Swayne, L.A., Blanchard, A.P., Yao, Z., Bennett, S.A.L., Figeys, D.: Lipidomics era: Accomplishments and challenges. Mass Spectrometry Reviews. 29, 877–929 (2010). https://doi.org/10.1002/mas.20294

138. Wenk, M.R.: The emerging field of lipidomics. Nature Reviews Drug Discovery. 4, 594–610 (2005). https://doi.org/10.1038/nrd1776

139. Kirschbaum, C., Greis, K., Mucha, E., Kain, L., Deng, S., Zappe, A., Gewinner, S., Schöllkopf, W., von Helden, G., Meijer, G., Savage, P.B., Marianski, M., Teyton, L., Pagel, K.: Unravelling the structural complexity of glycolipids with cryogenic infrared spectroscopy. Nature Communications. 12, (2021). https://doi.org/10.1038/s41467-021-21480-1

140. Malhotra, R.: Membrane Glycolipids: Functional Heterogeneity: A Review. Biochemistry & Analytical Biochemistry. 1, (2012). https://doi.org/10.4172/2161-1009.1000108

141. Hölzl, G., Dörmann, P.: Structure and function of glycoglycerolipids in plants and bacteria, (2007)

142. Raghu, P., Joseph, A., Krishnan, H., Singh, P., Saha, S.: Phosphoinositides: Regulators of Nervous System Function in Health and Disease, (2019)

143. O'Brien, R.E., Laskin, A., Laskin, J., Liu, S., Weber, R., Russell, L.M., Goldstein, A.H., O'Brien, R.E., Laskin, A., Laskin, J., Liu, S., Weber, R., Russell, L.M., Goldstein, A.H.: Molecular characterization of organic aerosol using nanospray desorption/electrospray ionization mass spectrometry: CalNex 2010 field study. Atmospheric Environment. 68, 265–272 (2013). https://doi.org/http://dx.doi.org.libproxy.lib.unc.edu/10.1016/j.atmosenv.2012.11.056

144. Wojcik, R., Webb, I.K., Deng, L., Garimella, S.V.B., Prost, S.A., Ibrahim, Y.M., Baker, E.S., Smith, R.D.: Lipid and glycolipid isomer analyses using ultra-high resolution ion mobility spectrometry separations. International Journal of Molecular Sciences. 18, (2017). https://doi.org/10.3390/ijms18010183

145. Wuhrer, M.: Glycomics using mass spectrometry. Glycoconjugate Journal. 30, 11–22 (2013). https://doi.org/10.1007/s10719-012-9376-3

146. Veillon, L., Zhou, S., Mechref, Y.: Quantitative Glycomics. Presented at the (2017)

147. Randolph, C.E., Blanksby, S.J., McLuckey, S.A.: Toward Complete Structure Elucidation of Glycerophospholipids in the Gas Phase through Charge Inversion Ion/Ion Chemistry. Analytical Chemistry. 92, 1219–1227 (2020). https://doi.org/10.1021/acs.analchem.9b04376

148. Randolph, C.E., Shenault, D.S.M., Blanksby, S.J., Mcluckey, S.A.: Structural Elucidation of Ether Glycerophospholipids Using Gas- Phase Ion/Ion Charge Inversion Chemistry. (2020). https://doi.org/10.1021/jasms.0c00025

149. Mirzaian, M., Wisse, P., Ferraz, M.J., Gold, H., Donker-Koopman, W.E., Verhoek, M., Overkleeft, H.S., Boot, R.G., Kramer, G., Dekker, N., Aerts, J.M.F.G.: Mass spectrometric

quantification of glucosylsphingosine in plasma and urine of type 1 Gaucher patients using an isotope standard. Blood Cells, Molecules, and Diseases. 54, 307–314 (2015). https://doi.org/10.1016/j.bcmd.2015.01.006

150. Sidhu, R., Mikulka, C.R., Fujiwara, H., Sands, M.S., Schaffer, J.E., Ory, D.S., Jiang, X.: A HILIC-MS/MS method for simultaneous quantification of the lysosomal disease markers galactosylsphingosine and glucosylsphingosine in mouse serum. Biomedical Chromatography. 32, (2018). https://doi.org/10.1002/bmc.4235